

N73-18123[#]

2070

900-597
PLANETARY QUARANTINE
ANNUAL REVIEW
SPACE TECHNOLOGY AND RESEARCH
July 71 - July 72
February, 1973

Approved By:

Daniel M. Taylor
D. M. Taylor, Supervisor
Life Sciences Research

Alan R. Hoffman
A. R. Hoffman, Supervisor
Planetary Quarantine Analysis

R. H. Green
R. H. Green, Assistant Manager
Planetary Quarantine and Civil Systems

JET PROPULSION LABORATORY
CALIFORNIA INSTITUTE OF TECHNOLOGY
PASADENA, CALIFORNIA

Distribution

Caird, H.	111-118
Flitton, D. D. (2)	111-208
Green, R. H. (3)	233-208
Goddard, F. E., Jr. (4)	180-700
Hess, D. S.	233-208
Small, J. G. (3)	180-703
Taylor, D. M. (62)	233-206

Distribution

Caird, H.	111-118
Flitton, D. D. (2)	111-208
Green, R. H. (3)	233-208
Goddard, F. E., Jr. (4)	180-700
Hess, D. S.	233-208
Small, J. G. (3)	180-703
Taylor, D. M. (62)	233-206

PREFACE

This document contains a report on Research and Advanced Development at the Jet Propulsion during the period July, 1971 to July, 1972 sponsored by the Planetary Quarantine branch of the NASA Office Space Science and Applications.

Page intentionally left blank

CONTENTS

I	PLANETARY QUARANTINE CONSTRAINTS (STRATEGIES) FOR ADVANCED MISSIONS <i>Gonzalez, C. C.</i>		1-1
	1.1	INTRODUCTION	1-1
	1.2	SIGNIFICANT ACCOMPLISHMENTS	1-1
		1.2.1 Tasks Conducted	1-1
		1.2.2 Meaning of Results to Planetary Quarantine . .	1-20
	1.3	PROBLEM AREAS	1-21
	1.4	FUTURE ACTIVITIES	1-21
		1.4.1 Work Planned for Next Six Months	1-21
		1.4.2 Additional Required Work	1-22
	1.5	PUBLICATIONS	1-22
	1.6	PRESENTATIONS	1-23
II	PLANETARY QUARANTINE CONSTRAINTS FOR UNMANNED PLANETARY SAMPLE RETURN MISSIONS <i>Miller, L. W.</i>		2-1
	2.1	INTRODUCTION	2-1
	2.2	SIGNIFICANT ACCOMPLISHMENTS	2-2
		2.2.1 Trajectory Analysis and Strategies	2-2
		2.2.2 Spacecraft Contamination Transfer	2-7
		2.2.3 Terrestrial Quarantine Analysis	2-14
		2.2.4 Research Areas and Technology Developments	2-16
	2.3	PROBLEM AREAS	2-16
	2.4	FUTURE ACTIVITIES	2-17
	2.5	PUBLICATIONS	2-17
	2.6	PRESENTATIONS	2-17
III	NATURAL SPACE ENVIRONMENT STUDIES <i>Taylor, D. M. and C. F. Hagen</i>		3-1
	3.1	INTRODUCTION	3-1
	3.2	SIGNIFICANT ACCOMPLISHMENTS	3-1
		3.2.1 Effect of Planetary Trapped Radiation Belt on Microorganisms	3-1

CONTENTS (contd)

	3.2.2	Effect of Solar Wind Protons on Microorganisms	3-15
	3.2.3	Effect of Space Vacuum on Microorganisms . . .	3-19
	3.2.4	Probability of Growth in Planetary Atmospheres	3-25
	3.3	RELEVANCY TO PLANETARY QUARANTINE	3-32
	3.4	PROBLEM AREA	3-34
	3.5	FUTURE ACTIVITIES	3-34
	3.5.1	Effect of Planetary Trapped Radiation Belt on Microorganisms	3-34
	3.5.2	Effect of Solar Wind Radiation on Microorganisms	3-34
	3.5.3	Effect of Space Vacuum on Microorganisms . . .	3-34
	3.5.4	Probability of Growth in Planetary Atmospheres	3-35
	3.6	PUBLICATIONS	3-35
	3.7	PRESENTATIONS	3-35
		REFERENCES	3-36
IV		POST LAUNCH RECONTAMINATION STUDIES <i>Nazares, R. and J. Barenholtz</i>	4-1
	4.1	INTRODUCTION	4-1
	4.2	SIGNIFICANT ACCOMPLISHMENTS	4-2
	4.2.1	Particle Adhesion Force Study	4-2
	4.2.2	Meteoroid Impact Study	4-6
	4.2.3	Spaceflight Recontamination Analysis	4-20
	4.3	FUTURE ACTIVITIES	4-29
	4.4	PRESENTATIONS	4-30
		REFERENCES	4-31
V		SPACECRAFT MICROBIAL BURDEN ESTIMATION AND PREDICTION <i>Hoffman, R.R.</i>	5-1
	5.1	INTRODUCTION	5-1

CONTENTS (contd)

5.2	SIGNIFICANT ACCOMPLISHMENTS	5-1
5.2.1	Microbial Burden Prediction Model	5-1
5.2.2	Analysis of the Mariner '71 Microbial Data ...	5-3
5.3	PROBLEM AREAS	5-19
5.4	FUTURE ACTIVITIES	5-19
5.5	PUBLICATIONS	5-19
5.6	PRESENTATIONS	5-19
VI	SPACECRAFT CLEANING AND DECONTAMINATION TECHNIQUES	6-1
	SUBTASK I - MECHANICAL REMOVAL OF SPACECRAFT MICROBIAL BURDEN <i>Schneider, H.W.</i>	6.1-1
6.1	INTRODUCTION AND SCOPE	6.1-1
6.2	APPROACH	6.1-3
6.2.1	Test Apparatus	6.1-3
6.2.2	Experimental Techniques	6.1-3
6.3	ACCOMPLISHMENTS	6.1-7
6.3.1	Vacuum Cleaning with Brushes	6.1-7
6.3.2	Vacuum Cleaning with Air Flow Only	6.1-12
6.3.3	Injection of Solvents into the Vacuum Flow	6.1-17
6.4	AERODYNAMICAL CONSIDERATIONS AND DISCUSSIONS	6.1-22
6.4.1	Effect of Reynolds Number	6.1-23
6.4.2	Assessment of Drag Force	6.1-26
6.5	PULSATORY EFFECTS	6.1-30
6.6	SUMMARY AND CONCLUSIONS	6.1-31
6.6.1	Potential for Improvement	6.1-33
6.7	PROBLEMS ENCOUNTERED	6.1-36
6.8	FUTURE ACTIVITIES	6.1-37

CONTENTS (contd)

SUBTASK II – THERMAL RESISTANCE OF MICROBIAL POPULATIONS OCCURRING IN SPACECRAFT ASSAY AREAS . .		6.2-1
<i>Wardle, M.D.</i>		
6.1	INTRODUCTION	6.2-1
6.2	SIGNIFICANT ACCOMPLISHMENTS	6.2-1
6.3	FUTURE ACTIVITIES	6.2-1
6.4	PUBLICATIONS	6.2-1
6.5	PRESENTATIONS	6.2-4
SUBTASK III – VERIFICATION OF USSR HYDROGEN PEROXIDE DECONTAMINATION . .		6.3-1
<i>Wardle, M.D.</i>		
6.1	INTRODUCTION	6.3-1
6.2	APPROACH	6.3-1
6.3	SIGNIFICANT ACCOMPLISHMENTS	6.3-1
6.4	FUTURE ACTIVITIES	6.3-2
6.5	PRESENTATIONS	6.3-2
SUBTASK IV – PLASMA CLEANING AND DECONTAMINATION TECHNIQUES . .		6.4-1
<i>Taylor, D.M.</i>		
6.1	INTRODUCTION	6.4-1
6.2	SIGNIFICANT ACCOMPLISHMENTS	6.4-1
6.3	FUTURE ACTIVITIES	6.4-1
APPENDIX		
A	ANALYSIS OF MICROBIAL BURDEN DATA . .	A-1
<i>Efrom, B.</i>		

TABLES

1-1	Conclusions from large impactable analyses	1-5
1-2	Atmospheric parameters	1-9
1-3	Summary of representative properties for major satellites of the outer planets	1-11
1-4	Spacecraft breakup: pressures and ballistic coefficients	1-18
2-1	Comparison of quarantine implications between conjunction and opposition class missions	2-3
2-2	Error and navigation analysis	2-6
2-3	Comparisons between contamination sources and control methods for planetary and terrestrial quarantine	2-10
3-1	Analysis of variance of test results (constant dose rate)	3-7
3-2	Effect of electron energy and dose on spacecraft bacterial isolates exposed to vacuum	3-9
3-3	Effect of electron energy, dose, and temperature on spores of spacecraft bacterial isolates exposed to vacuum	3-11
3-4	Analysis of variance of test results (constant dose)	3-12
3-5	Effect of electron energy and dose rate (300 krad)	3-15
3-6	Solar wind (1 au)	3-16
3-7	Analysis of variance of 3 keV proton test	3-17
3-8	Limits of environmental factors governing microbial growth	3-29
4-1	Force model verification test matrix	4-3
4-2	Test facility capabilities	4-5
4-3	Particle adhesion force model verification experiment (preliminary data)	4-8
5-1	Number of samples with given non-heat shocked colony count	5-4
5-2	Number of samples with given heat shocked colony count	5-6

TABLES (contd)

5-3	Comparison of the numbers and types of microorganisms detected on Mariner-Mars 1971 spacecraft.....	5-7
5-4	Identification of heat shock cultures isolated from Mariner-Mars 1971 spacecraft.....	5-9
6-1	Comparison of Mariner '69 and '71 spore isolate $D_{125^{\circ}\text{C}}$ values	6.2-3

APPENDIX

A-1	Theoretical count proportions	A-4
A-2	Proportions of assays containing one or two clumps	A-6

FIGURES

1-1	$P_{C/I}$ vs ΔV for Earth-Jupiter leg	1-3
1-2	$P_{C/I}$ vs ΔV for Jupiter - Saturn leg J-S77	1-4
1-3	Jupiter closest approach distance of ejecta efflux	1-6
1-4	Closest approach of ejecta efflux at spacecraft-Jupiter encounter	1-7
1-5	Entry flow field diagram	1-13
1-6	Entry of 100μ plastic particle through molecular regime	1-16
1-7	Stagnation pressure vs time from entry angle 30°	1-17
2-1	Mars sample return trajectory options	2-4
2-2	Probability of Earth impact by biasing Mars departure aim point	2-8
2-3	Lander/ascent vehicle on surface of Mars	2-9
2-4	MSSR orbiter/bus	2-12
2-5	Earth return methods	2-13
2-6	Terrestrial quarantine allocation example-orbiter mode	2-15
3-1	Schematic of changed particle regions near Jupiter	3-3
3-2	Jovian trapped radiation belt	3-4
3-3	Effect of electron irradiation dose on spacecraft bacterial isolates exposed to vacuum	3-8
3-4	Effect of electron energy on spores of spacecraft bacterial isolates exposed to vacuum	3-10
3-5	Effect of electron irradiation dose rate on spacecraft bacterial isolates exposed to vacuum	3-14
3-6	Effect of 3 keV protons on spacecraft bacterial isolates exposed to vacuum	3-18
3-7	Test facility	3-20
3-8	Test chamber	3-22
3-9	Test fixture	3-23

FIGURES (contd)

3-10	Vacuum temperature resistance of spores of spacecraft isolates	3-24
3-11	Vacuum temperature resistance of nonsporeforming spacecraft isolates	3-26
3-12	Pressure vs temperature for the Jupiter model atmosphere	3-30
3-13	Zones of relative probability of growth in Jupiter atmosphere	3-33
4-1	Schematic diagram of test set-up	4-4
4-2	Acceleration time history	4-7
4-3	Shock spectrum ($Q = 20$)	4-7
4-4	Sample spacecraft geometry	4-21
4-5	Projected surface area	4-22
4-6	Photoelectric current density	4-23
4-7	Flow diagram of sun/shade and particle impact	4-26
4-8	Sun vector paralleled to polygon of spacecraft	4-27
4-9	Particles in the Sun and shade	4-28
4-10	Cauchy integral formula	4-28
4-11	Particle "hit" test	4-29
5-1	Comparison between estimates and prediction — total count — Mariner '71-2	5-2
5-2	Spacecraft configuration during first ESF encapsulation assay (Flight 2)	5-10
5-3	Distribution of microorganisms on back of Mariner 71 panel	5-11
5-4	Solar panel front raw count distribution Flight 2, panel all samples	5-13
5-5	Sampling of flight solar panel	5-14
5-6	Mean particle levels in SAF high bay. Particle/ Ft^3 /Week	5-15

FIGURES (contd)

5-7	Particle level in SAF tent. Particle/Ft ³ /Week	5-15
5-8	Reyneirs, high bay. Viable particles/Ft ³ of air/Week	5-16
5-9	Reyneirs tent. Viable particles/Ft ³ of air/Week	5-16
5-10	Total count/week in high bay	5-17
5-11	Total count/week in SAF tent	5-17
5-12	Relationship between viable and nonviable environmental fallout data	5-18
6-1	Schematic of vacuum flow simulator	6.1-4
6-2	Sable brush seen through sample plate (100x view)	6.1-9
6-3	Particulate surface vs brush stroke	6.1-10
6-4	Removal efficiency of 1/4 in. sable brush at 57 in. H ₂ O vacuum (count before and after one cm double stroke cleaned with brush)	6.1-11
6-5	Removal efficiency vs particle size and flow velocity	6.1-13
6-6	Removal efficiency vs particle size and flow velocity	6.1-14
6-7	Removal efficiency vs particle size and flow velocity	6.1-15
6-8	Maximum removal efficiencies at 0.02 mm stand-off and choked nozzle flow	6.1-16
6-9	Effect of stand-off from surface on removal efficiency at choked nozzle flow. Facility dust on glass, 35-45% RH	6.1-18
6-10	Maximum removal efficiencies achieved	6.1-19
6-11	Typical surface pressure profile with rounded test nozzle at choked flow condition	6.1-21
6-12	Frictional resistance vs Reynolds number	6.1-25

FIGURES (contd)

6-13	Calculated Stokes-drag at constant 230 microns stand-off from surface.	6.1-28
6-14	Removal efficiency vs stand-off for critical nozzle expansion	6.1-29
6-15	Particle adhesion and drag force vs size	6.1-35
6-1	Frequency distribution of $D_{125^{\circ}\text{C}}$ values for Mariner '71 spore isolates	6.2-2

APPENDIX

A-1	Histograms of burden distribution on non-zero assays categorized by percent zero cells	A-2
A-2	Distribution of large counts	A-5
A-3	Large counts in different cases compared to total cumulative distribution function (CDF)	A-9

900-597

SECTION I

PLANETARY QUARANTINE CONSTRAINTS (STRATEGIES)

FOR ADVANCED MISSIONS

SECTION I

PLANETARY QUARANTINE CONSTRAINTS (STRATEGIES)
FOR ADVANCED MISSIONS

NASA No. 193-58-61-01

Cognizance: C. C. Gonzalez

Associate Personnel: W. Stavro, W. Jaworski,
A. McRonald

1.1 INTRODUCTION

The objectives of this task are to perform analyses necessary to assess the impact of planetary quarantine on mission strategies; to determine the parameters to which this impact is most sensitive; and to identify problem areas which will require further research.

Current models of the atmospheres of Jupiter and Saturn indicate the possible existence of regions with conditions favorable for growth of terrestrial microorganisms (Section III, para. 3.4). To ensure that the environments of the outer planets are not altered biologically, a study was performed to identify planetary quarantine constraints and problem areas. Potential mission strategies compatible with both mission objective and planetary quarantine constraints were investigated.

Possible sources of contamination were identified and related to mission events, flight-path-control strategies, and interplanetary environments. Relevant parameters to which planetary quarantine analyses were considered most sensitive were selected and included in subsequent analyses. A preliminary allocation model was developed and analyses were performed to obtain probability of contamination values for the most significant sources. Potential problem areas in need of future research were identified.

1.2 SIGNIFICANT ACCOMPLISHMENTS

1.2.1 Tasks Conducted

1.2.1.1 Jupiter-Saturn Trajectory and Navigation Analyses. The trajectory and navigation analyses have been completed for typical multiplanet fly-by missions. Typical Jupiter-Saturn missions were selected; in particular, a

Mariner-Jupiter-Saturn 1977 opportunity. The trajectory and navigation analysis for an outer planet mission must take into account the fact that the heliocentric spacecraft velocities are greater than for a Mars mission. This means biasing fuel penalties will be greater. Also, the planetary impact radius is larger because of the more massive planets.

The analysis includes the impact of dropping the assumption that the probability of contamination, given impact ($P_{C/I}$), was equal to one. Although this assumption has been used on past missions, it may be conservative for outer planet missions. The probability of contamination (P_C) is equal to the product of $P_{C/I}$ and the probability of impact (P_I), equal to ($P_C = P_{C/I} \times P_I$). Hence, if $P_{C/I}$ is reduced in value from one, the allowable P_I will increase. Our previous analyses indicated that biasing introduces added fuel penalties to provide the velocity changes (ΔV) needed to remove the bias. However, as the allowable P_I increases, the bias required to satisfy planetary quarantine (PQ), and consequently the fuel penalties, decrease. The current analyses were performed in order to determine the variation of incremental velocity (fuel penalty) with $P_{C/I}$ for a mission using a five segment Titan launch vehicle. The effect of maneuver reliability and approach guidance accuracy was also considered.

Figure 1-1 shows the relationship between $P_{C/I}$ vs ΔV for the Earth-Jupiter leg and effect of the maneuver reliability. Figure 1-2 shows $P_{C/I}$ vs ΔV for the Jupiter-Saturn leg. Results are given for two separate approach guidance accuracies at Jupiter. Approach guidance accuracy is considered here because the location of the spacecraft relative to Jupiter determines where it crosses the Saturn aim plane.

The results for the analyses are summarized in Table 1-1.

1.2.1.2 Ejecta Efflux Analyses. An analysis was performed to determine the critical periods for particulate debris, or ejecta efflux, released from a spacecraft during a Jupiter-Saturn mission. A critical period is defined to be that portion of the trajectory when released debris will come closest to intersecting a planet. The purpose of the analysis was to develop the required analytical tools and apply them to a typical mission. It is expected that the determination of the probability of contamination due to ejecta efflux will be an appropriate

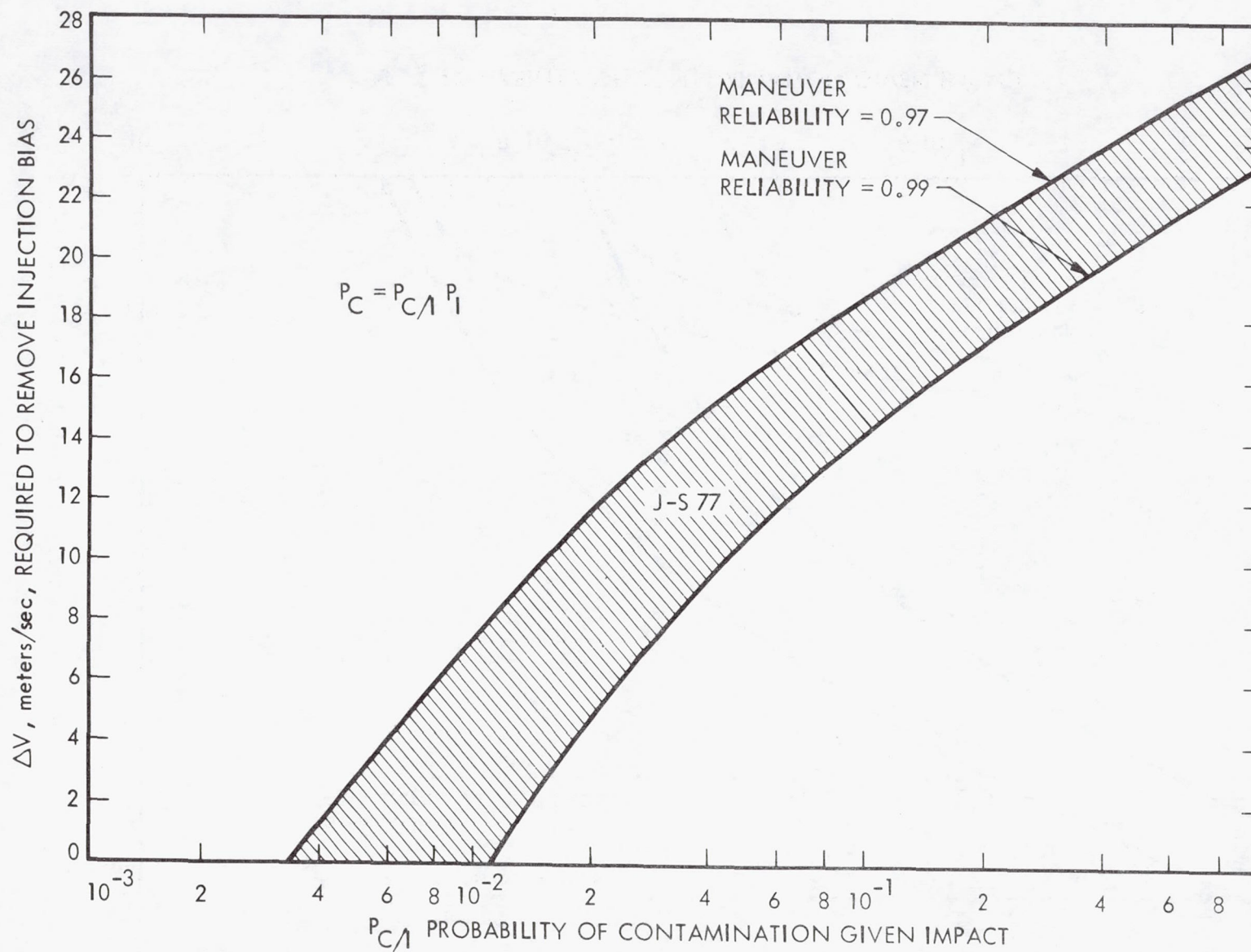


Fig. 1-1. $P_{C/I}$ vs ΔV for Earth-Jupiter leg

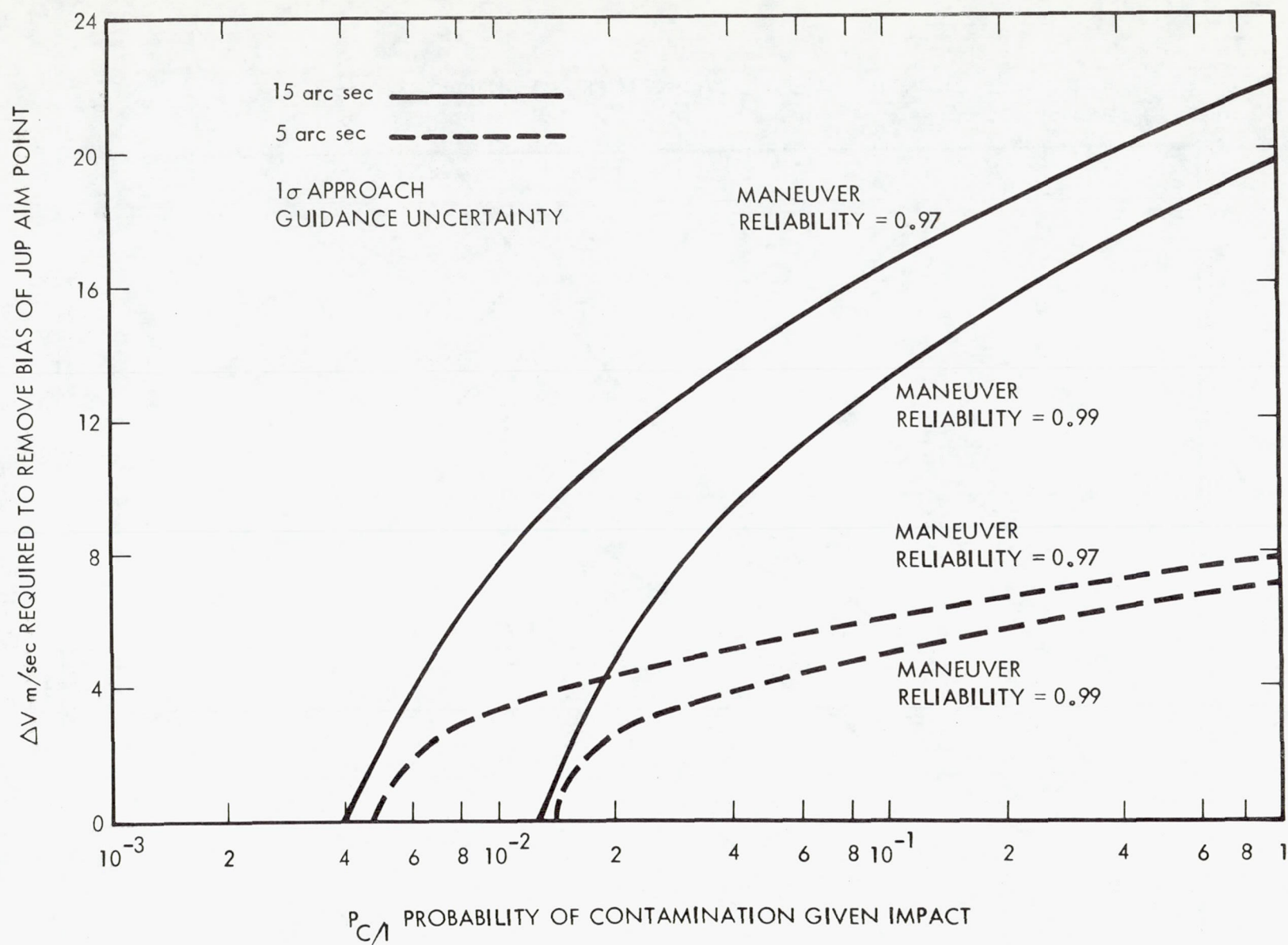


Fig. 1-2. $P_{C/I}$ vs ΔV for Jupiter - Saturn leg J-S77

Table 1-1. Conclusions from large impactable analyses

Dependence on $P_{C/I}$	Fuel load penalty
(1) $P_{C/I} = 1$	Significant*
(2) $P_{C/I} = 10^{-1}$	Significant but smaller*
(3) $P_{C/I} = 10^{-2}$	Existence depends on mission parameters
(4) $P_{C/I} = 10^{-3}$	None
*Fuel load penalty greater than 20%	

task for a specific flight project team. The particle size chosen ranged from 1-10 m, densities from 1-3 g/cm³, and ejection velocities from 0-10 msec⁻¹ with an isotropic distribution. The analysis for the Earth-Jupiter leg involved a point by point integration using the spacecraft position and velocity vectors at five day intervals. The particles were assumed to be ejected uniformly in all directions and acted upon by the gravitational forces of the Sun and planets and the solar pressure. When particles leave the spacecraft they follow an essentially rectilinear trajectory. Therefore, the closest distance of approach of the particles to the planet is a function of spacecraft/Sun/planet angle. Software was not available to perform the same analysis for the Jupiter-Saturn leg; however, an analysis by analogy was performed using the spacecraft/Sun/planet angle.

The results indicated that, for the particular mission analyzed, there were two critical periods in the Earth-Jupiter leg: one near the start of the asteroid belt; and one starting two days before encounter. The first critical period resulted in 18×10^6 km miss; the second, lasting about a day, resulted in impact. Figures 1-3 and 1-4 summarize the results. There were no critical periods in the Jupiter-Saturn leg.

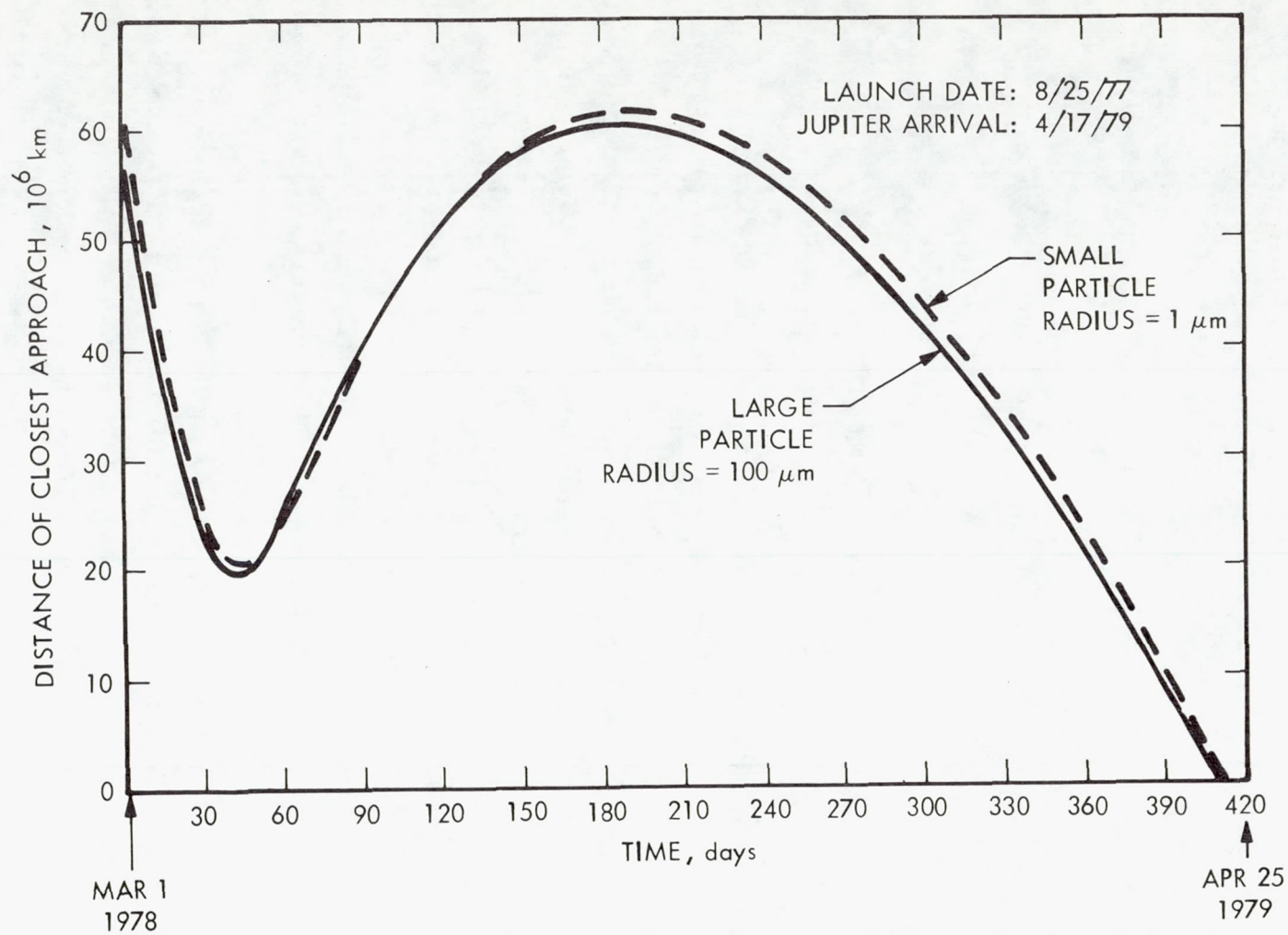


Fig. 1-3. Jupiter closest approach distance of ejecta efflux

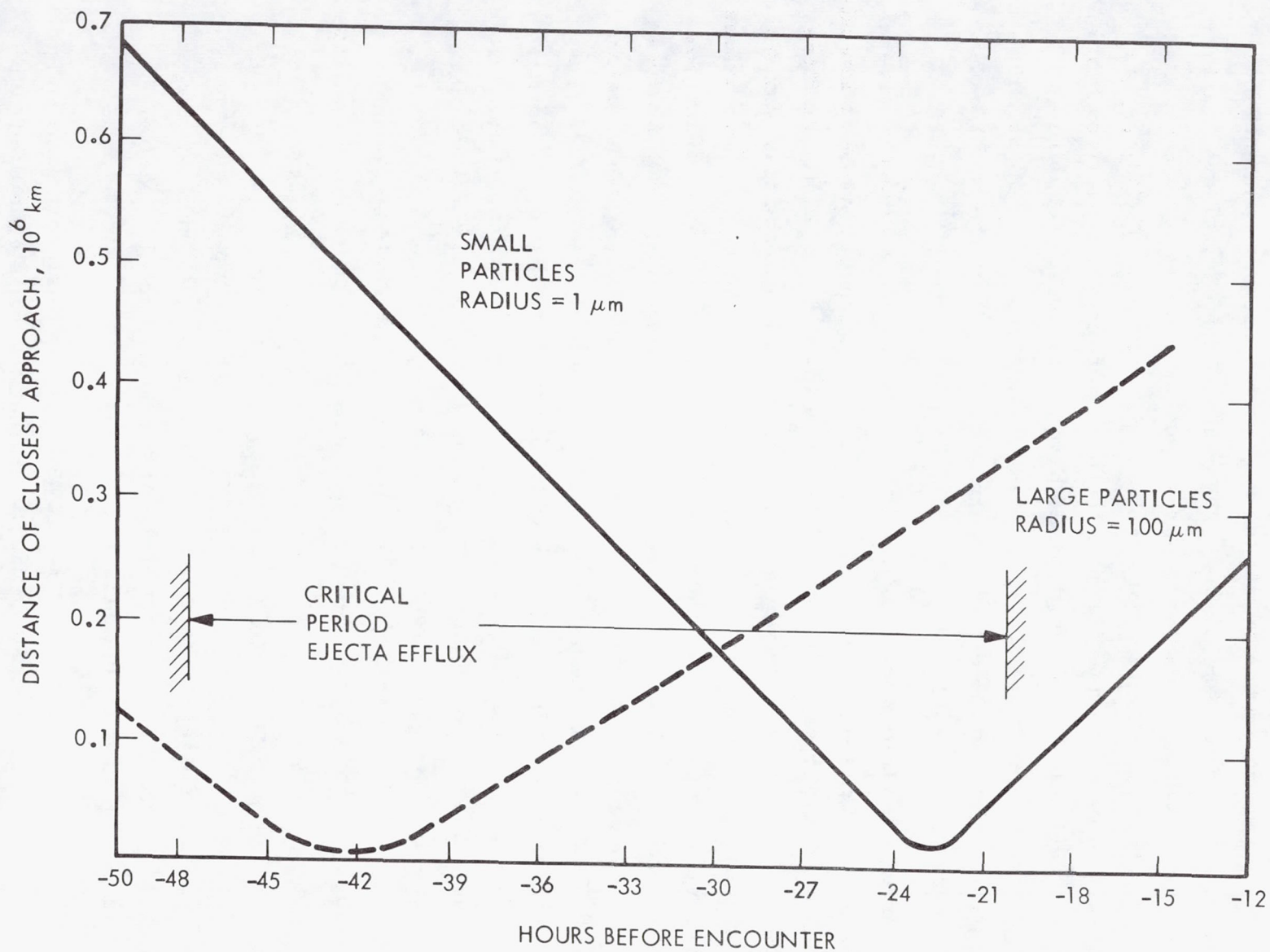


Fig. 1-4. Closest approach of ejecta efflux at spacecraft-Jupiter encounter

1.2.1.3 Natural Space Environments. Values of the parameters for the interplanetary and planetary environments of Jupiter and Saturn were provided for use in tasks designed to evaluate the impact of these environments on survival and growth of microorganisms. These environments include the interplanetary meteoroid environment, solar radiation, galactic cosmic rays, planetary trapped radiation, and atmospheric parameters. The atmospheric parameters are being used to consider the levels of the atmosphere of Jupiter and Saturn where microbial growth would have the greatest probability. Table 1-2 shows an example of the results. (In this case some of the atmospheric parameters for Jupiter and Saturn were taken from the NASA monograph nominal models.)

In addition to the above environments, preliminary values of several physical parameters for some satellites of the outer planets have been investigated. For the major satellites - Io, Europa, Ganymede, Callisto (Jupiter), Titan (Saturn), and Triton (Neptune) - some of the values associated with the orbits, atmospheres, and surfaces are presented in Table 1-3. These values are consistent with potential thin atmospheres in all cases except Titan, for which observational evidence strongly favors the reality of a methane atmosphere. Furthermore, convincing theoretical investigations of the structure and evolution of these bodies favors a surface composed of an H_2O ice crust overlying a liquid water interior, with which inhomogeneities in composition and terrain are to be associated. In particular, local disturbances associated with "geological" activity involving ice, water, and steam are possible (e.g., seepages and "icequakes"). From the perspective of Planetary Quarantine, it is imperative that these preliminary studies be complimented by thorough quantitative analyses of the likely environments of these and other planet satellites not yet investigated with these needs in mind.

1.2.1.4 Atmospheric Entry Heating Analysis. The objective of the atmospheric entry heating analysis task is to determine the effect of heat generated by the accidental entry of a spacecraft and related debris on microbial survival. Jupiter was chosen as the study planet.

Figure 1-5 gives a schematic representation of the entry of a body at hypersonic velocities into an atmosphere. A shock wave is generated by the

Table 1-2. Atmospheric parameters

Jupiter*			
Altitude (km)	Temperature (°K)	Pressure (atm)	Cloud composition
0.0(a)	189.1	1.00	NH ₃ Ice cloud base
-17.8	230.0	1.80	
-33.0	264.2	2.76	H ₂ O Ice cloud base
-96.7	395.8	10.0	
Saturn**			
0.0(a)	145.2	1.00	NH ₃ Ice cloud base
-67.5	210.0	3.00	
-109.9	250.0	5.10	Solid H ₂ H ₂ O-NH ₃ Solution cloud base
-138.1	275.9	6.92	
-175.5	309.9	10.0	

*Draft of NASA Space Vehicle Design Criteria Monograph "The Planet Jupiter (1970)." To be published as NASA SP-8069.

**Draft of NASA Space Vehicle Design Criteria Monograph "The Planet Saturn (1970)." To be published as NASA SP-80XX.

(a) Zero altitude is defined as the altitude where the pressure is 1 atmosphere.

Page intentionally left blank

Table 1-3. Summary of representative properties for major satellites of the outer planets

Parameters Satellites	Orbital parameters				Physical properties		Atmosphere*				Surface*			Other Environments
	Semi-major axis (10 ⁵ km)	Sideral period (days)	Eccentricity	Inclination to planetary equator (Deg)	Radius (km)	Mean density g/cm ³	Constituents	Surface pressure (N/m ²)	Temperature (°K)	Water-vapor pressure (N/m ²)	Constituents	Temperature (°K)	Activity	
Jupiter Io	4.23	1.769	0	0	1829	2.8	CH ₄ NH ₃	≤0.01	78-164	≤10 ⁻³	Water ice, NH ₃ hydrates, dust, organic compounds, frozen radicals (including predominantly H, C, N, O, Si, Fe, and other metals).	78-164	Local disturbances involving ice, water, steam, seepages and "icequakes."	Charged particles from Jupiters radiation belts
Europa	6.75	3.551	0.0003	0	1550	3.0	CH ₄ NH ₃	<0.01	82-165	<10 ⁻³	Same as Io	82-165	Same as Io	Same as Io
Ganymede	10.7	7.154	0.0015	0	2775	1.7	CH ₄ NH ₃	<0.01	82-167	<10 ⁻³	Same as Io	82-167	Same as Io	Same as Io except that only the upper limit proton model produces significant fluxes.
Callisto	18.9	16.689	0.0075	0	2500	1.5	CH ₄ NH ₃	<0.01	80-168	<10 ⁻³	Same as Io	80-168	Same as Io	Same as Ganymede
Saturn Titan	12.3	15.95	0.0291	0.33	2425	2.3	CH ₄ (mostly) H ₂ { Mixing He ratios NH ₃ ≤0.1	≥150	>89	Saturation	Same as Io with the addition of CH ₄ hydrates, and NH ₃ snow and frost, and liquid water if the atmospheric pressure is great enough.	≥89	Same as Io	<u>Small</u> amounts of charged particles from Saturn's radiation belts (no actual data for existence).
Neptune Triton	3.54	5.877	0	159.9	1890	4.6	CH ₄ Ar (possibly) NH ₃ Mixing ratios ≤0.1	~14	~70°	Saturation	Same as Io	~70	Same as Io	<u>Small</u> amounts of charged particles from Neptune's radiation belts (no actual data for existence).

*The atmosphere and surface entries are speculative.

Page intentionally left blank

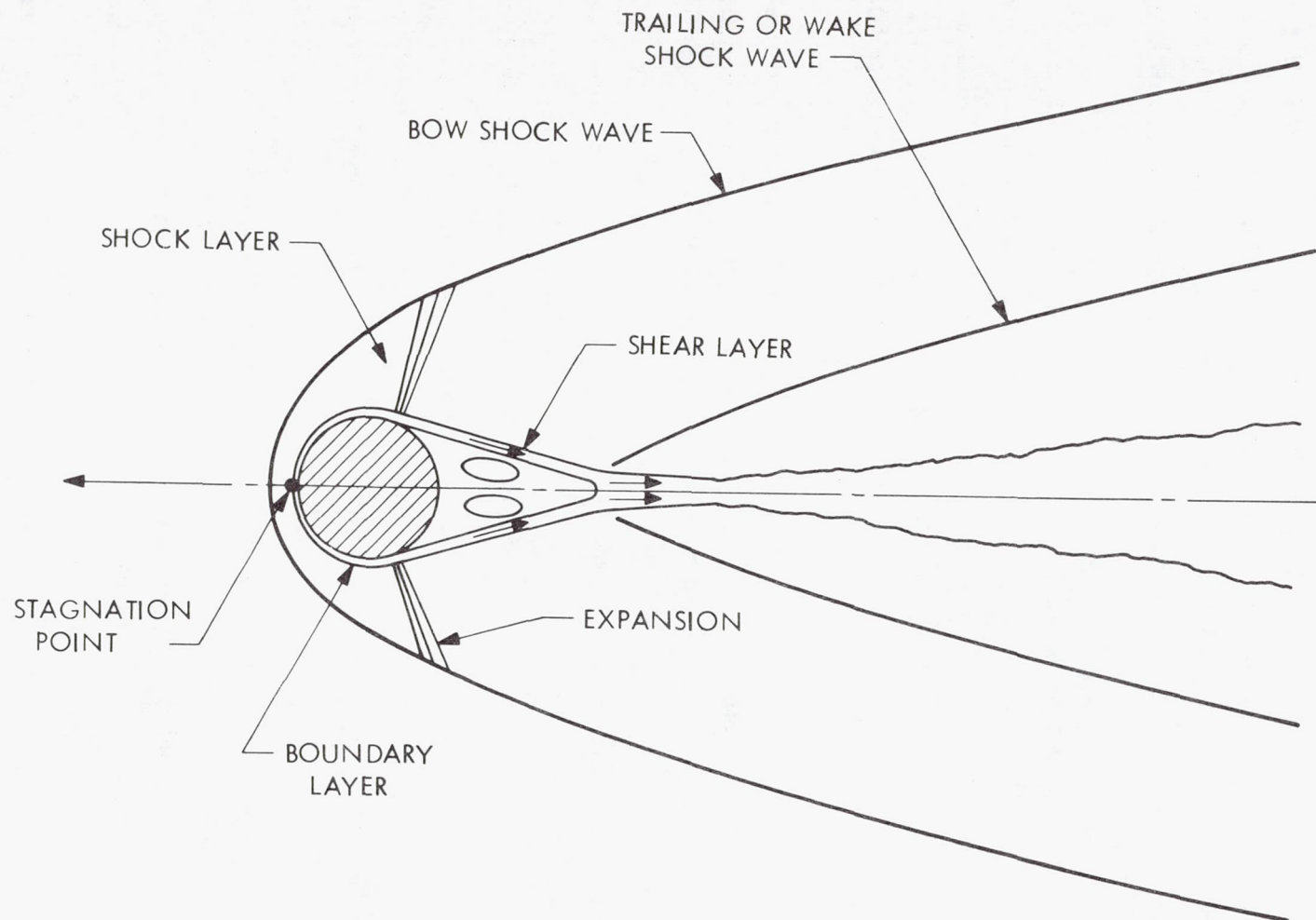


Fig. 1-5. Entry flow field diagram

body and a major part of it is intensely heated - like a meteor entering the Earth's atmosphere. The heat reaching the body is transferred by two mechanisms: cold wall convective and radiative heat.

Heat transferred by the convective mode is carried by individual gas molecules or atoms to the surface while the molecules in front of the body, in the shock layer, generate radiation which reaches the surface. Additional complexities arise from the blocking of the heat by the gas layer ablated from the surface.

The analyses are being performed in three stages. The first stage consisted of the aerodynamic analyses to determine the dynamic presence of a typical spacecraft and related components. These pressure loads were used to determine the time and mode of spacecraft breakup, thus identifying the components which would have to be analyzed. Heat loads transmitted to the spacecraft were not computed.

The second stage of the analysis consists of computing the convective and radiative heat fluxes to the surface of the spacecraft and components. Computations have been performed for entry angles of 3, 15 and 90°, ballistic coefficients ranging from 0.5 to 500 Kg/m², nose radii from 0.3 to 0.001 meters, and three atmospheric models. Such an analysis is called a cold wall analysis because the interaction of the body material with the heat flux is ignored. This interaction is the subject of the third stage in the analysis.

In this stage, the effect of the heat fluxes on the surface and their interaction with the vapors and materials released, as well as the thermal response of the body, will be determined. Thermal time histories will be provided.

The complex calculations identified are performed with the aid of computer programs. A number of routines were assembled combining aerodynamic calculations with routines calculating the chemistry and dynamics of the shock layer and heat transmitted. These very complex mechanisms required use of some approximating techniques. Finally, these routines were mated to set routines used to determine the thermal response of the spacecraft and its components. The results have not been obtained yet but initial checkout of the entire program has begun with some sample cases already run.

The calculations described above were performed for that portion of the entry called the continuum regime. The other entry regime considered is called the free molecular regime.

In the free molecular regime, a shock layer is not produced, but energy is transferred between gas atoms and molecules and an entering body via a "billiard ball collision" mode. An entering body will enter the free molecular regime before passing into the continuum regime. The analyses for the former is much simpler. However, most large bodies will receive a relatively small amount of heat there. This is not necessarily true in the case of small particles and light weight materials which remain in the free molecular regime for a longer period of time. Therefore, a free molecular regime analysis has been initiated for them. Small particles possess the additional feature of having a larger area to volume ratio and thus will radiate a larger percentage of heat absorbed.

Another phase of entry being considered is the skip entry. In this case, a body enters at a shallow angle, causing it to skip out and return again. This may happen several times before the body finally enters for the last time. Each time the body comes in contact with the atmosphere it is heated; however, once outside the atmosphere, it radiates the heat away. Figure 1-6 illustrates this case for a 10 μm plastic particle.

Figure 1-7 illustrates a sample of the results obtained for the spacecraft breakup due to dynamic pressure loads. The curves shown are plots of the stagnation pressure versus time from entry. The calculations were performed for a range of angles and ballistic coefficients. The example is for a 30° entry. Each curve represents the case for a body of a particular ballistic coefficient as indicated. The area enclosing the cross hatching indicates where various components of the spacecraft separate or collapse due to the forces. Finally, the distance scale on the bottom indicates that all of these events occur well above the zero of altitude, or that portion of the atmosphere where the probability of microbial survival and growth would be highest. Table 1-4 gives the pressure required for the occurrence of each event indicated in Fig. 1-7.

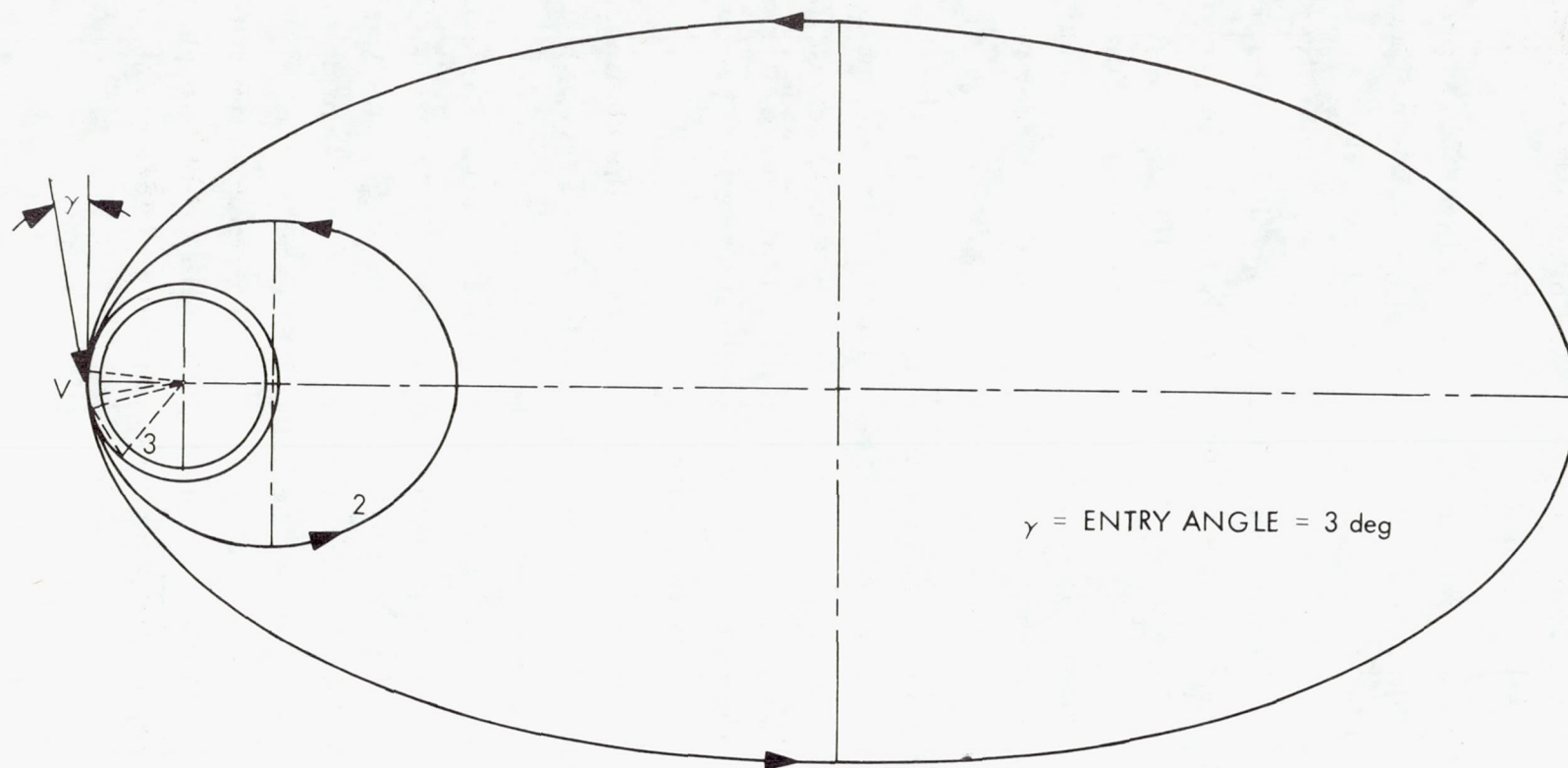


Fig. 1-6. Entry of 100μ plastic particle through molecular regime

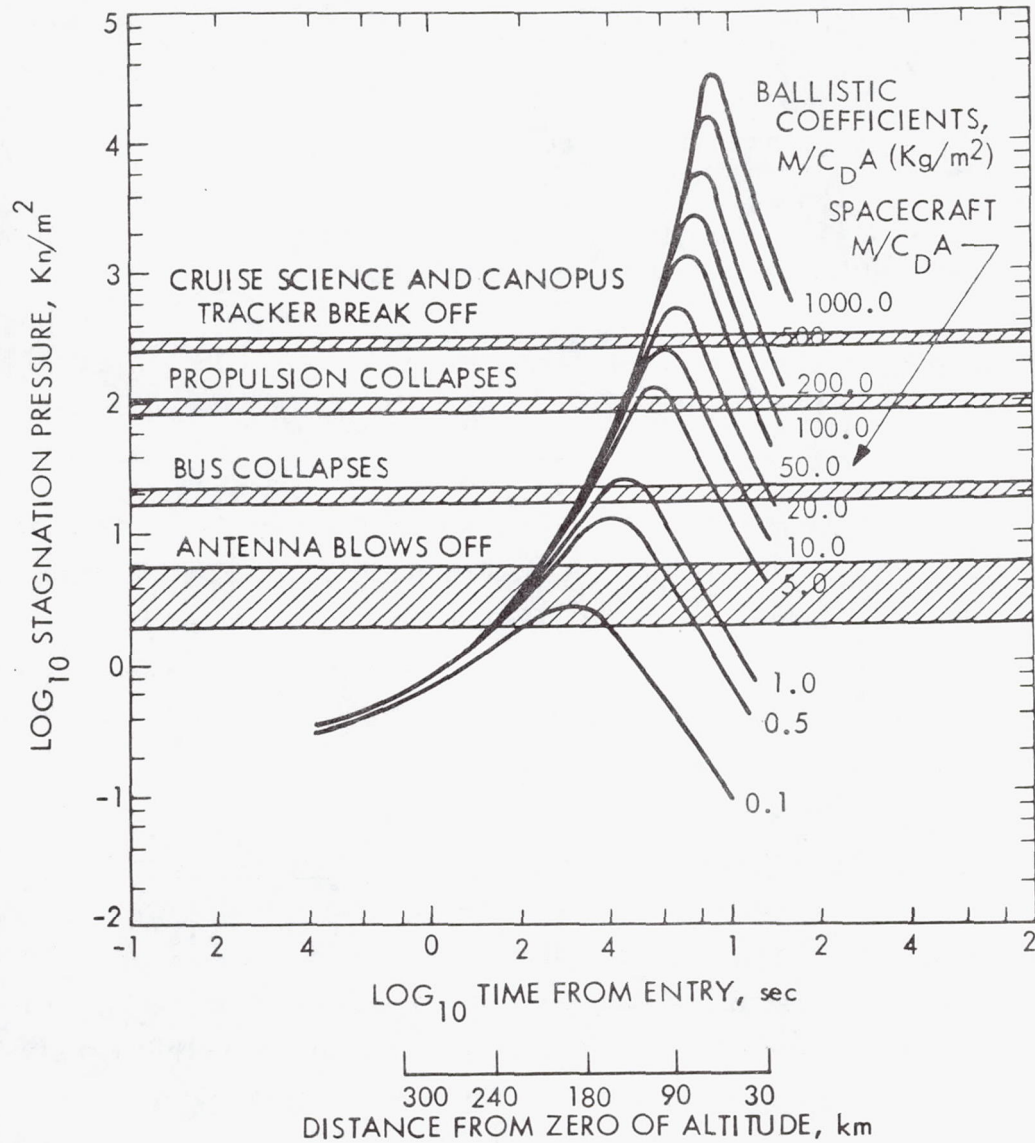


Fig. 1-7. Stagnation pressure vs time from entry angle 30°

Table 1-4. Spacecraft breakup: pressures and ballistic coefficients

Event	Pressure, kN/m^2	$M/C_D A$, kg/m^2
Original state	---	66
Antenna blows off spacecraft, reorients with scan platform down	2-6	365
Bus collapses, scan platform blows off	20	385
Propulsion system collapses, RTGs breakoff, bus continues to collapse	100	360
Cruise science and Canopus tracker breaks off	300	440

The results of the cold wall convective and radiative heat analysis have been investigated and it was determined that computer routine produced what appear to be reasonable values. However, until the last stages of the analyses (involving the materials response and thermal time histories in the body) are completed, the results obtained thus far cannot be interpreted in terms of microbial survivability.

1.2.1.5 Planetary Quarantine Considerations for Probe Missions. There are a number of implications on the mission and hardware design for Jupiter and Saturn atmosphere probe missions that result from PQ considerations which are imposed. As a result, a number of problem areas were identified. The following is a summary of the analyses required and possible constraints and problem areas to be encountered.

1. Heliocentric Mission Phase. Trajectory and navigation analyses must be performed which will include factors different (to demonstrate compliance with PQ constraints) from a pure fly-by such as type II trajectories and more exacting conditions for targeting at the planet.

PQ constraints may impose restrictions on the periapsis distance, which will in turn impact the minimum entry angle which can be achieved, and consequently the heat load on the probe.

2. Planet Centered Mission Phase-Deflected Spacecraft (bus) Mode.

If a deflected spacecraft mode is chosen, it must be demonstrated that the probability of being able to perform the deflection maneuver is high enough that the probability of impact does not exceed the PQ constraint.

3. Planet Centered Mission Phase-Deflected Probe Mode.

Survivable Probes - nonsterilized. Although a probe or components separated from it are not sterilized prior to launch, sufficient microbial burden reduction, might result from atmospheric entry heating to satisfy PQ constraints (probably 100% on surfaces). Also, it appears from the atmosphere models in Ref. 1 that the temperatures that exist below 100 atmospheres (300 atmospheres in the case of Saturn) of pressure will kill organisms. The restrictions on a nonsterilized probe depend on a number of factors.

If the probe survives intact to 100 atmospheres (300 atmospheres in the case of Saturn), it appears that only minor problems exist if (1) it is demonstrated that microorganisms present will be killed by the entry heating or (2) the following components are sterile: parachutes, aeroshells, covers, removable insulation, and deflection motor gases. The problems which must be considered are possible survival of microorganisms on the aft surface portions of the probe (in the entry wake), and possible escape of organisms through vents. If these problems can be resolved and if it can be demonstrated that the probe will survive to 100 (or 300) atmospheres, sterilization of the probe interior appears to be unnecessary.

Survivable Probes - sterilized. There are no mission restrictions (there are hardware implications involving materials compatibility) on probe if all components including aeroshells, covers, parachutes, and ejected gases are sterile or it can be shown that any microorganisms which they contain will not survive atmospheric entry heating.

Nonsurvivable Probes - nonsterilized and sterilized. In the case of nonsterilized and sterilized probes which do not survive to 100 (or 300) atmospheres (this includes both so called turbopause probes and probes that

survive only to 10-30 atmospheres), it must be demonstrated that as the probe is destroyed, the resultant components and debris are sufficiently heated throughout to destroy all microorganisms. (This is in addition to the special components cited for nonsterilized survivable probes.)

Finally, in the case of Saturn, it must be demonstrated that non-sterilized probe will not be affected by the ring particles in such a way that contamination is possible.

A general comment which should be made is that if a sterilized probe (or specified components) is used, the problem of recontamination from the spacecraft should be considered. The only restrictions that apply to the spacecraft are those cited for the heliocentric mission phase.

1.2.2 Meaning of Results to Planetary Quarantine

The results of the large impactable analyses indicate that considerable fuel savings can be effected if $P_{C/I}$ is several orders of magnitude less than one. $P_{C/I}$ is dependent on other factors such as the probability of microbial survival in the space and planetary environments, survival of the atmospheric entry heating, probability of growth, and initial spacecraft bio-burden. Therefore, if sufficient reduction can be achieved in any of these factors, fuel penalties may be made quite small.

The results of the ejecta efflux analyses indicate that two critical periods existed: one at the start of the asteroid belt; and one near encounter. Although the one at the asteroid belt resulted in a miss in this case, particles could conceivably come closer in the case of another Jupiter-Saturn mission. Figure 1-4 indicates that the critical period at encounter would result in impact by some of the particles. Actually, the probability of impact is a function of the physical parameters of the particles. In the case of the current analyses, sample ranges of size, density, and velocity distribution were chosen based on engineering judgment. The direction and magnitude of the ejection velocity is particularly important. It was found that up to some tens of meters/sec the results were close to those given in Fig. 1-4. Much higher velocities would cause some deviation; however, such velocities would be rare. In order to determine the probability of contamination of a planet by a small particle, an

analysis including probability of release of the particles along with its physical parameters would have to be performed by the appropriate mission analysis team.

The end result of the atmospheric entry heating analysis will be the identification of the spacecraft components and debris most likely to experience heating to temperatures low enough to allow microbes to survive. Thermal time histories will be plotted for these components.

1.3 PROBLEM AREAS

Two main problem areas have been encountered so far. The first area involves the lack of navigation and maneuver analysis data on multiple outer planet mission. The second area relates to the analyses required to determine the heat loads when a spacecraft enters the Jovian atmosphere. The analytical tools, mathematical treatments, and computer programs available to do the analyses, were quite involved and inappropriate as they stood. It was necessary to do considerable modification of these tools. Also, values of many of the required parameters are unavailable and have to be approximated.

1.4 FUTURE ACTIVITIES

1.4.1 Work Planned for Next Six Months

The following tasks will be initiated in the next six months.

1.4.1.1 Quarantine Analyses for Missions with Satellite Encounter. A trajectory analysis will be performed to determine the possible impact of any satellite quarantine (SQ) constraints on trajectory and navigation strategies. This will include possible ejecta efflux problems. Possible conflicts between satisfying SQ and PQ (for the primary planet) will also be considered and a PQ and SQ analysis model for satellite encounters will be developed.

1.4.1.2 Quantitative Analyses for Missions with Possible Saturn's Rings Encounters. The PQ significance of possible spacecraft impact of Saturn's rings due to accidental impact from a near ring encounter or due to impact

from an encounter intended to pass through an area of low particle density will be considered. The probability of accidental impact and catastrophic occurrences will also be considered.

1.4.1.3 Terrestrial Quarantine Constraints. Information will be developed to assist the Planetary Quarantine Office in developing NASA policy for defining terrestrial quarantine constraints.

The current task, Atmospheric Entry Heating Analysis, will be continued during the next six months. Internal response of selected spacecraft components will be determined and temperature versus time histories will be obtained. Small particle and light weight materials analysis will continue and components, including debris, and materials most likely to contain surviving microorganisms will be determined.

1.4.2 Additional Required Work

The following work is required to better understand the problems of planetary quarantine analyses for outer planet missions: Jupiter Orbiter, Jupiter, and Saturn Entry Probe Mission PQ Analysis.

A PQ analysis will be performed for orbiter missions similar to that for fly-by missions. The fact that an orbiter will spend a longer time in the vicinity of the planet coupled with different modes of entry into the planetary atmosphere from a fly-by requires a separate analysis for such a mission. A large impactable analysis will be performed for both the heliocentric and orbital phases. The orbit analysis will include orbit lifetimes. Ejecta efflux problems will also be considered and PQ analysis model will be developed.

A large impactable analysis will be performed for the heliocentric phase of probe missions. The impact of planetary quarantine on probe design will be considered and a PQ analysis model developed.

1.5 PUBLICATIONS

Stavro, W. and Gonzalez, C., "Flight Path and Mission Strategies to Satisfy Outer Planet Quarantine Constraints"; Paper presented at the AAS/AIAA Astrodynamics Specialists Conference, Ft. Lauderdale, Florida, August 17-19, 1971; Preprint No. AAS-71-319.

1.6 PRESENTATIONS

Gonzalez, C.; "Planetary Quarantine Constraints for Advanced Missions"; presented to NASA Semiannual Sterilization Technology Seminar, Cape Kennedy, Florida, January, 1972.

900-597

SECTION II

PLANETARY QUARANTINE CONSTRAINTS FOR UNMANNED
PLANETARY SAMPLE RETURN MISSIONS

SECTION II

PLANETARY QUARANTINE CONSTRAINTS FOR UNMANNED PLANETARY SAMPLE RETURN MISSIONS

NASA No. 193-58-62-02

Cognizance: L. W. Miller

Associate Personnel: D. M. Taylor, A. R. Hoffman,
W. Stavro

2.1 INTRODUCTION

The Earth return portion of a sample return mission has quarantine aspects which differ considerably from previous missions involving only the Earth out-bound strategy. To evaluate these quarantine aspects, a Space Research and Technology (SR&T) task was initiated whose objectives were to:

- (1) Perform analysis required to determine terrestrial quarantine constraints related to unmanned planetary sample return missions.
- (2) Determine mission strategies to achieve mission objectives while satisfying the constraints.
- (3) Identify required research necessary to assure compatibility of terrestrial quarantine constraints with mission success.

A variety of mission parameters were available for inclusion in this study. The broad context of these parameters consisted of: 1) Mars and comet missions; 2) 1980 versus 1990 launch opportunities; 3) new propulsion systems, i. e., chemical-nuclear, and/or solar electric; and 4) trajectories involving a direct return from the planet of interest to Earth or a Venus swingby. The inclusion of all these parameters would involve great difficulty in the synthesis of data and the derivation of a coherent analysis. For this reason, the study was focused on a particular type mission: the return portion of a Mars mission consisting of an ascent vehicle that docks with an orbiting bus which then returns to Earth. The sample container either returned by a direct re-entry capsule or by an Earth orbiting capsule which is transferred to a space shuttle.

The scope of the mission was structured as follows: 1) the study assumes life exists on Mars; 2) terrestrial quarantine (TQ) is defined to apply to Earth return; 3) the study terminates upon manned recovery of the sample; and 4) an avoidance of bringing back extraterrestrial life in an uncontrolled manner (controlled being inside the sample container, uncontrolled being outside the sample container).

Several terrestrial quarantine assumptions are significantly different from those used for the out-bound planetary quarantine analysis. First, the risk of widespread exposure to large segments of the Earth's population indicates that stricter quarantine measures will be imposed by terrestrial quarantine than those imposed by out-bound planetary quarantine missions - the rationale being the risk would present a potential for immense human disaster, even though the possibility for life forms from extraterrestrial areas appear very low. However, in actuality, knowledge of whether such life forms exist may not be known at the occasion of a sample return mission, and the reports obtained from precursor Viking or Russian flights indicating an absence of life would be taken as presumptive but not conclusive evidence.

Secondly, the modeling approach for out-bound missions is based on an assumption of a random distribution of contaminants over the spacecraft as opposed to discrete apportionment of contaminants related to terrestrial quarantine analysis inside the sample container and outside the sample container. The concern is focused on events which relate to bioburden outside the sample container and providing uncontrolled contamination. Such uncontrolled contamination would result from or be caused by:

- (1) Organisms randomly distributed on the spacecraft
- (2) Leaking of the sample container
- (3) Conditions leading to a possible break-up of the sample container

2.2 SIGNIFICANT ACCOMPLISHMENTS

2.2.1 Trajectory Analysis and Strategies

The parameter of interest in terrestrial quarantine analysis is the probability that the returning sample will accidentally impact the Earth.

However, whether impact will result in contamination or not is outside the realm of trajectory analysis.

For a Mars sample return mission, various mission mode options are available for the return portion. After the launch off the Martian surface, the vehicle carrying the sample can either return directly to Earth, or rendezvous with another Mars orbiting vehicle before returning to Earth. For the Mars-Earth transfer phase, the trajectory can be of a conjunction class, an opposition class, or may even have a Venus fly-by mode. At Earth the vehicle can either enter directly or go into an Earth orbit mode where the sample would be retrieved by a space shuttle or would re-enter from the Earth orbiter.

For the time being, attention will be focused on the Mars-Earth transfer trajectory, and the differences between the conjunction and opposition modes. Figure 2-1 shows the essential differences between the two modes. A summary of these differences and resulting quarantine implications are given in Table 2-1.

Table 2-1. Comparison of quarantine implications between conjunction and opposition class missions

Conjunction class	Opposition class
Trajectory	
Low Energy (minimum fuel loading) To achieve this, there needs to be a long stopover at Mars (approximately 1 yr) until the required celestial geometry is reached.	High Energy If the Mars stopover time is short, the return trajectory will require higher fuel loading.
Arrival Velocity	
Relatively low because of low energy.	Relatively high because of high energy.
Capture Area	
Larger due to lower Earth arrival velocity.	Smaller due to higher Earth arrival velocity.
Probability of Impact	
Relatively larger if due to a specific navigation error.	Relatively smaller if due to specific navigation error.

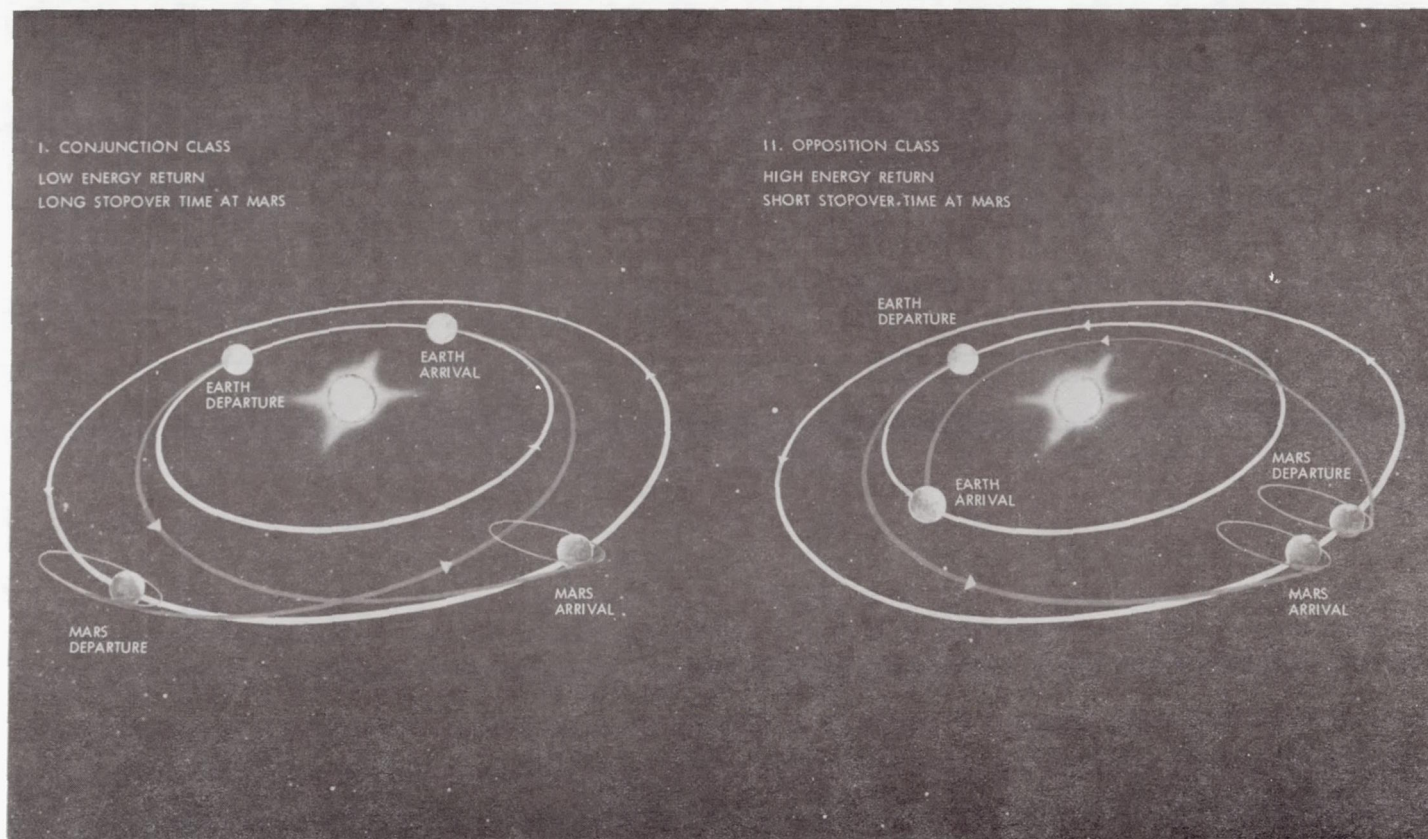


Fig. 2-1. Mars sample return trajectory options

In order to obtain a quantitative data sample for the analysis, the following was performed:

- (1) A 1981-82 Mars sample return mission was designed and the trajectory data for both opposition and conjunction class returns determined.
- (2) A maneuver plan was assumed for the return trajectories consisting of an injection out of Mars orbit maneuver and two trajectory correction maneuvers at 10 days past Mars launch and 20 days before Earth arrival.
- (3) The mapping matrices for the selected trajectories at the maneuver times were determined.
- (4) A 1 m/sec velocity error was mapped into the Earth aim-plane and the resulting 1 σ ellipse was determined for the three mentioned maneuvers. The numerical values are shown in Table 2-2.
- (5) The injection out of Mars orbit maneuver was used as a sample to examine the probability of Earth impact. The 1 m/sec error used is fairly representative of expected errors. An aim-point at Earth with a B-value of 100,000 kms was used, and a probability of impact calculated.

The probabilities of impact for these assumptions were 1.8×10^{-2} for the opposition class and 4.6×10^{-2} for the conjunction class. Thus the conjunction class results in a higher impact probability, as expected.

From a terrestrial quarantine point of view, the opposition class seems to be more desirable.

The numerical results obtained indicate that the impact probabilities calculated, although different, are still of the same order of magnitude; i.e., of the order 10^{-2} . A high maneuver correction reliability can reduce this probability (to produce uncontrolled accidental impact) by two additional orders of magnitude; i.e., an order of 10^{-4} . If it is assumed that accidental impact will result in contamination ($P_{C/I} = 1$), then an overall terrestrial quarantine constraint in the order of 10^{-4} can probably be satisfied. However, a very tight constraint of the order of 10^{-8} will result in severe quarantine violation.

Table 2-2. Error and navigation analysis

Maneuver Plan *	Conjunction	Opposition
Capability ellipse** for injection	$\sigma_1 = 213,300 \text{ km}$ $\sigma_2 = 3,200 \text{ km}$ $\theta = 172^\circ$ $P_{I_A} = 0.046$	$\sigma_1 = 63,540 \text{ km}$ $\sigma_2 = 5,930 \text{ km}$ $\theta = 180^\circ$ $P_{I_A} = 0.018$
Capability ellipse for maneuver 1	$\sigma_1 = 83,280 \text{ km}$ $\sigma_2 = 5,060 \text{ km}$ $\theta = 173^\circ$	$\sigma_1 = 51,000 \text{ km}$ $\sigma_2 = 8,130 \text{ km}$ $\theta = 179^\circ$
Capability ellipse for maneuver 2	$\sigma_1 = 1,760 \text{ km}$ $\sigma_2 = 1,713 \text{ km}$ $\theta = 167^\circ$	$\sigma_1 = 1,690 \text{ km}$ $\sigma_2 = 1,690 \text{ km}$ $\theta = 167^\circ$
Capture radius	14,250 km	8,100 km
<p>*First maneuver, Mars +10 days; second maneuver, Earth -20 days</p> <p>**Resulting 1σ ellipse in the Earth B-Plane due to a 1 m/sec error in the maneuver, for 100,000 Km B miss distance.</p>		

One method, used extensively in previous missions to satisfy quarantine constraints, biases the aim-point outward to reduce the impact probability. This was performed with a sample numerical example. The results are shown in Fig. 2-2. A significant result is that doubling the aiming distance from 100,000 to 200,000 kms, reduces the impact probability for the opposition class by two logs magnitude, but essentially does not change the impact probability for the conjunction class. These results again show that the opposition class returns are more favorable.

However, the most important conclusion of the above analyses is that a tight terrestrial quarantine constraint of the order of 10^{-8} cannot be satisfied by trajectory and navigation design alone.

Additional control methods that can be employed should be investigated. Table 2-3 summarizes control differences between out-bound flights which mainly rely on preflight control methods of trajectory design and decontamination, and sample return missions which rely on preflight methods of trajectory and spacecraft design and inflight monitoring methods.

2.2.2 Spacecraft Contamination Transfer

The study of spacecraft contamination transfer involves examining the sequence of possible events from which a contamination problem may evolve. A progression of these events includes: 1) the sample retrieval from the planet's surface and encapsulation into the sample container; 2) the lift-off and dynamic environment affecting contaminating events; 3) the docking maneuvers and dynamic events which could cause contamination; and 4) the Earth return method and respective vulnerabilities to contamination transfer. Some possible specific events will now be discussed.

A Mars descent/ascent vehicle is shown in Fig. 2-3. The container receives its samples from the rover by means of the sample transfer arm. During this time, contamination can occur by dust storms transferring particles to the spacecraft surfaces, malfunctions of the transfer arm, or the sample container.

Transfer of dust particles detached from the surface of the ascent vehicle to the bus surfaces can occur by means of vibration shakeoff, contact

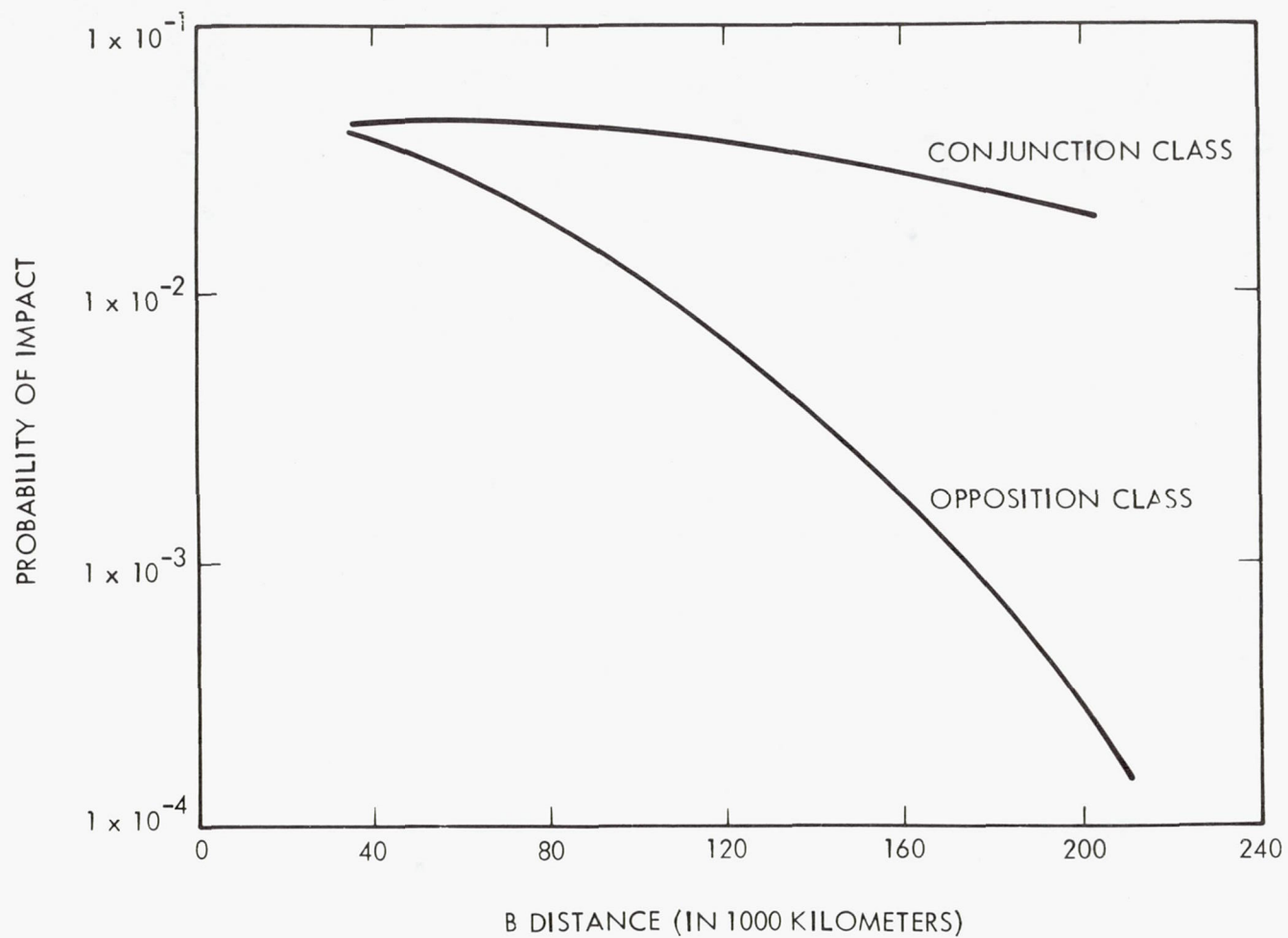


Fig. 2-2. Probability of Earth impact by biasing Mars departure aim point

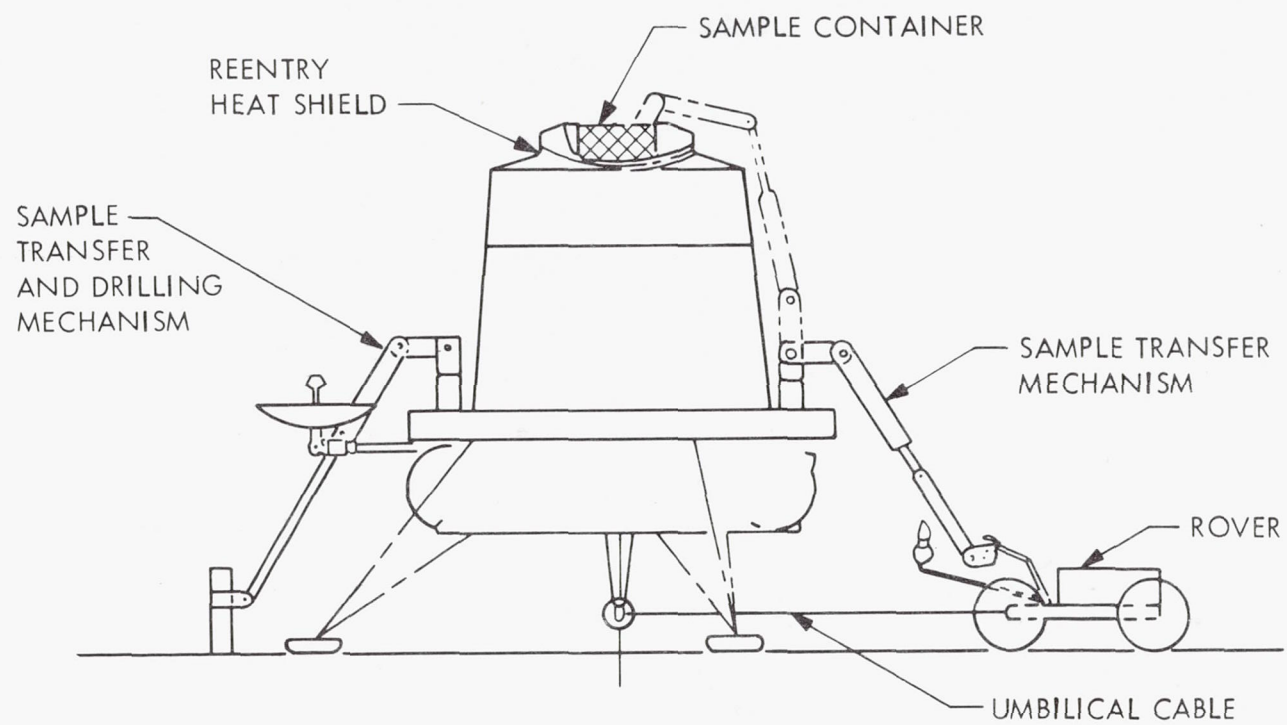


Fig. 2-3. Lander/ascent vehicle on surface of Mars

Table 2-3. Comparisons between contamination sources and control methods for planetary and terrestrial quarantine

Mission	Contamination	Contamination source	Control Method
Outbound mission	Earth organisms	Ejecta efflux Large impactables	Decontamination Sterilization Mission design
Sample return mission	Mars organisms outside sample container	Ejecta efflux Large impactables Sample container	Spacecraft design Mission design Container design

of docking surfaces (Fig. 2-4), and docking malfunctions causing contact of the spacecraft.

The possibility of contamination transfer to the inside of the bus must also be considered. Figure 2-5 depicts a typical Earth orbiter capsule and a direct Earth re-entry capsule. The direct re-entry capsule configuration has been shown in Figs. 2-3 and 2-4 and will be used as the basis for discussion of the contamination transfer mechanisms.

When the ascent vehicle docks with the bus, it is actually docking with the rear portion of the re-entry capsule. When the ascent vehicle disengages and falls away from the bus, the heat shield and sample container remain attached to the rear portion. These three parts make up the sample container.

The contamination on the sample container is trapped in the interior of the re-entry capsule, and the outside of the re-entry vehicle is free from contamination. Special seals and bioshields would be necessary to control possible problems at the conjunction of the heat shield and the rear portion, but the design is basically very good at handling contamination transfer problems.

By comparison, the orbiter design is poor at handling contamination transfer because the sample container is exposed. Thus, contamination on the container would easily transfer to other parts of the orbiter surfaces. In addition, the sample container is not as well protected against meteorite impact or problems arising from leakage. This design could be improved considerably by placing a shield over the sample container similar to the re-entry capsule design.

To summarize, spacecraft leaving Mars will be contaminated, and contamination transfer problems must be studied carefully. Spacecraft design will make a considerable difference in the magnitude of these problems. Spacecraft design considerations suggested by terrestrial quarantine to reduce these problems include the use of:

- (1) A sample container seal to minimize contamination and transfer of contaminants.
- (2) A leakage detection device.
- (3) On-board monitoring of contamination processes.

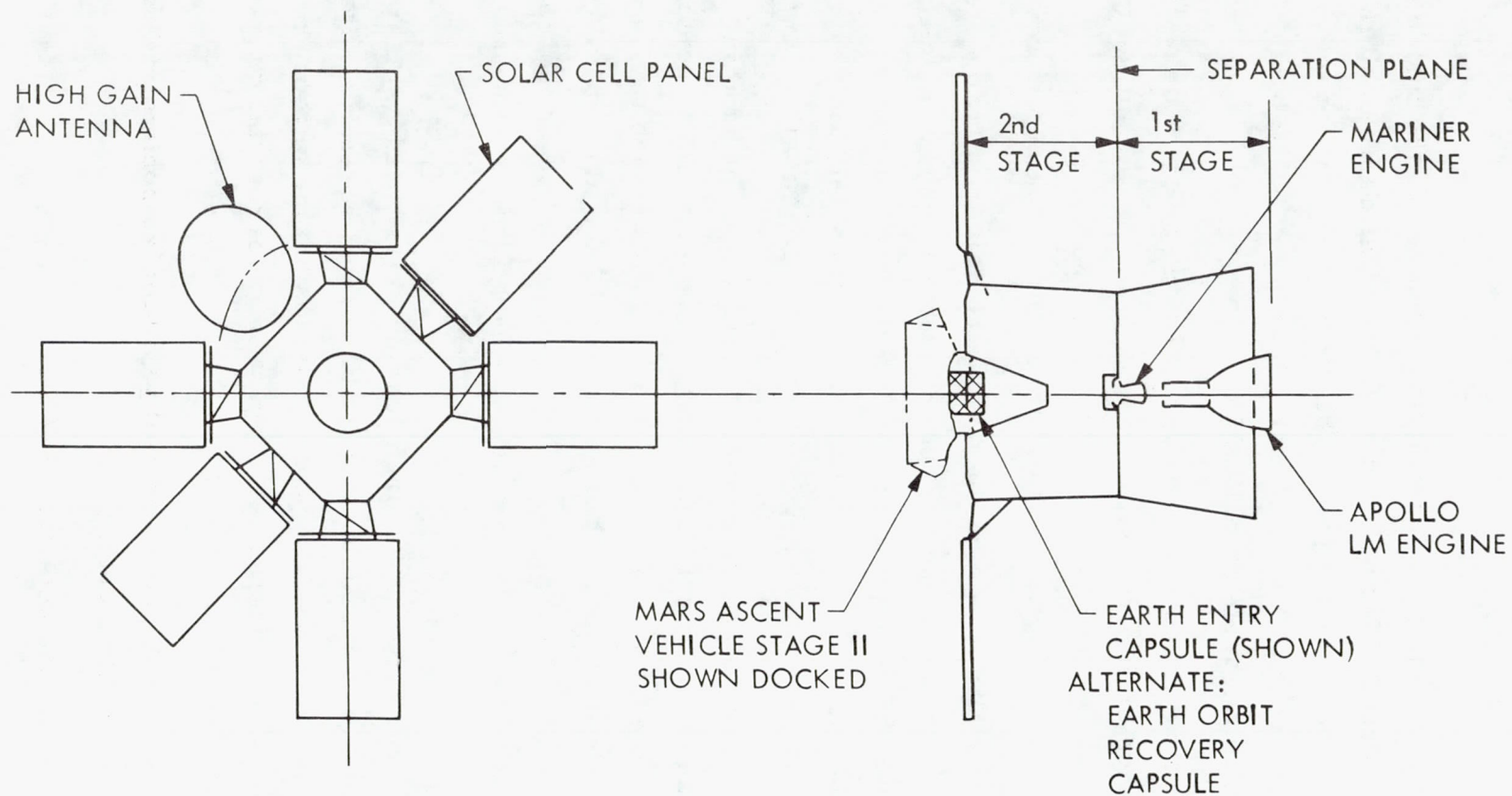


Fig. 2-4. MSSR orbiter/bus

BOTH VEHICLES ABOUT 300 lb

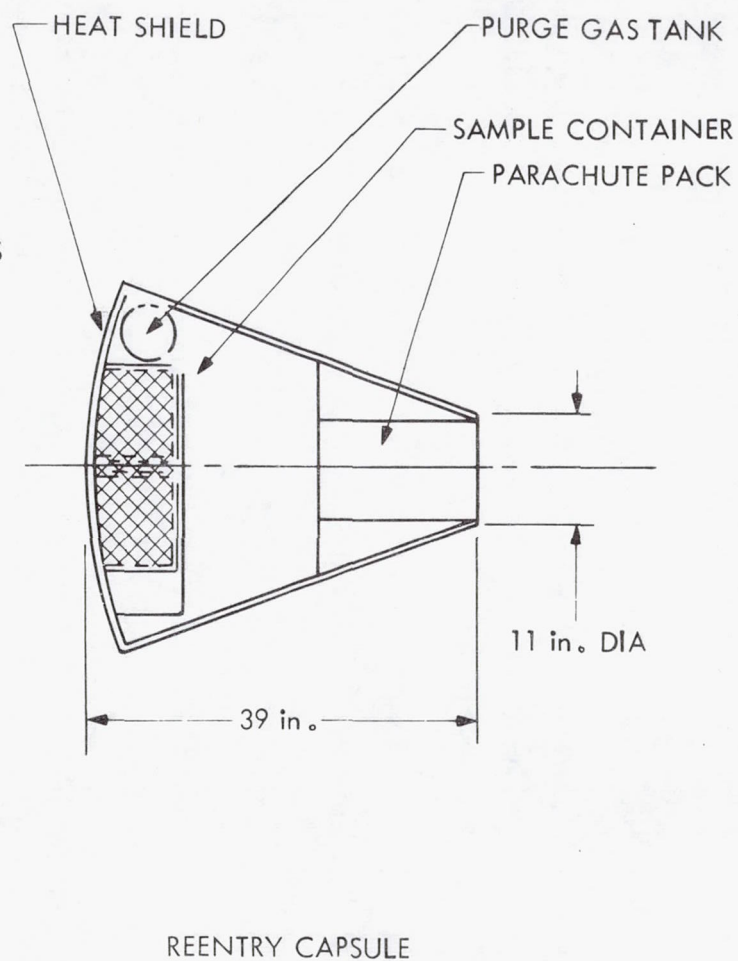
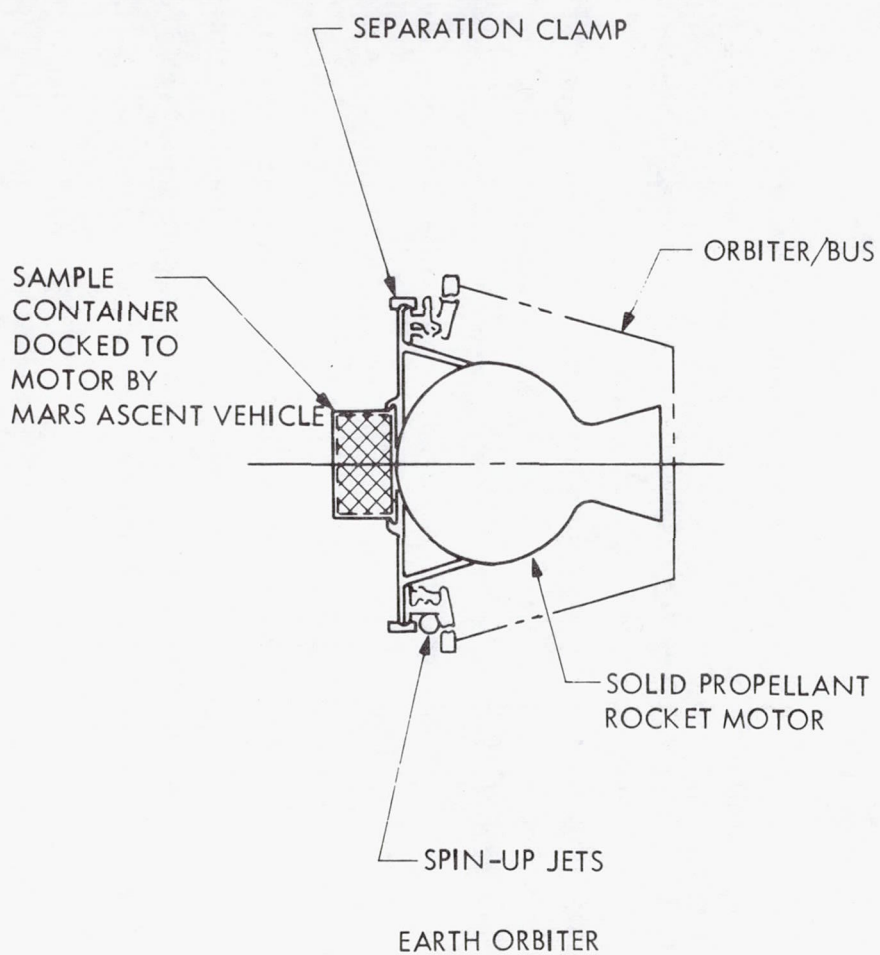


Fig. 2-5. Earth return methods

- (4) A sample container protected against meteorite impact.
- (5) A sample container capable of unaided atmospheric entry.

2.2.3 Terrestrial Quarantine Analysis

After appropriate consideration for the differences, the sample return missions are amenable to standard planetary quarantine analysis. The analysis is based on the model

$$\sum_i P_{c\text{Estimated}} \leq \sum_i P_{c\text{Allocated}} \leq P_c$$

where

P_c = the risk probability of contamination of the Earth biosphere (also called the TQ constraint).

$\sum_i P_{c\text{Allocated}}$ = the probability of contamination allocated to contamination from spacecraft parts expressed as the i^{th} ejecta efflux or large impactable source.

$\sum_i P_{c\text{Estimated}}$ = the probability of contamination that the analysis indicates would arise from the i^{th} ejecta efflux or large impactable source.

No previous work has been done on P_c for unmanned sample return missions, and for study purposes the values of P_c has been at 10^{-8} . This is several orders of magnitude lower than the values that have been assigned for out-bound flights such as Mariner 71, which had a value of 0.7×10^{-4} . The more stringent sample return value was assigned because of the subjective feeling that concern for possible contamination would be stronger because such a disaster potential exists.

The probability of contamination $P_{c\text{Allocated}}$ was broken down by an allocation model to cover the various sources of contamination. Fig. 2-6 shows this $P_{c\text{Allocated}}$ and $P_{c\text{Estimated}}$ relationship of the large impactables and the ejecta efflux to the TQ constraint. Only the Earth orbiter recovery mode is shown; however, both the Earth orbiter and direct re-entry capsule recovery

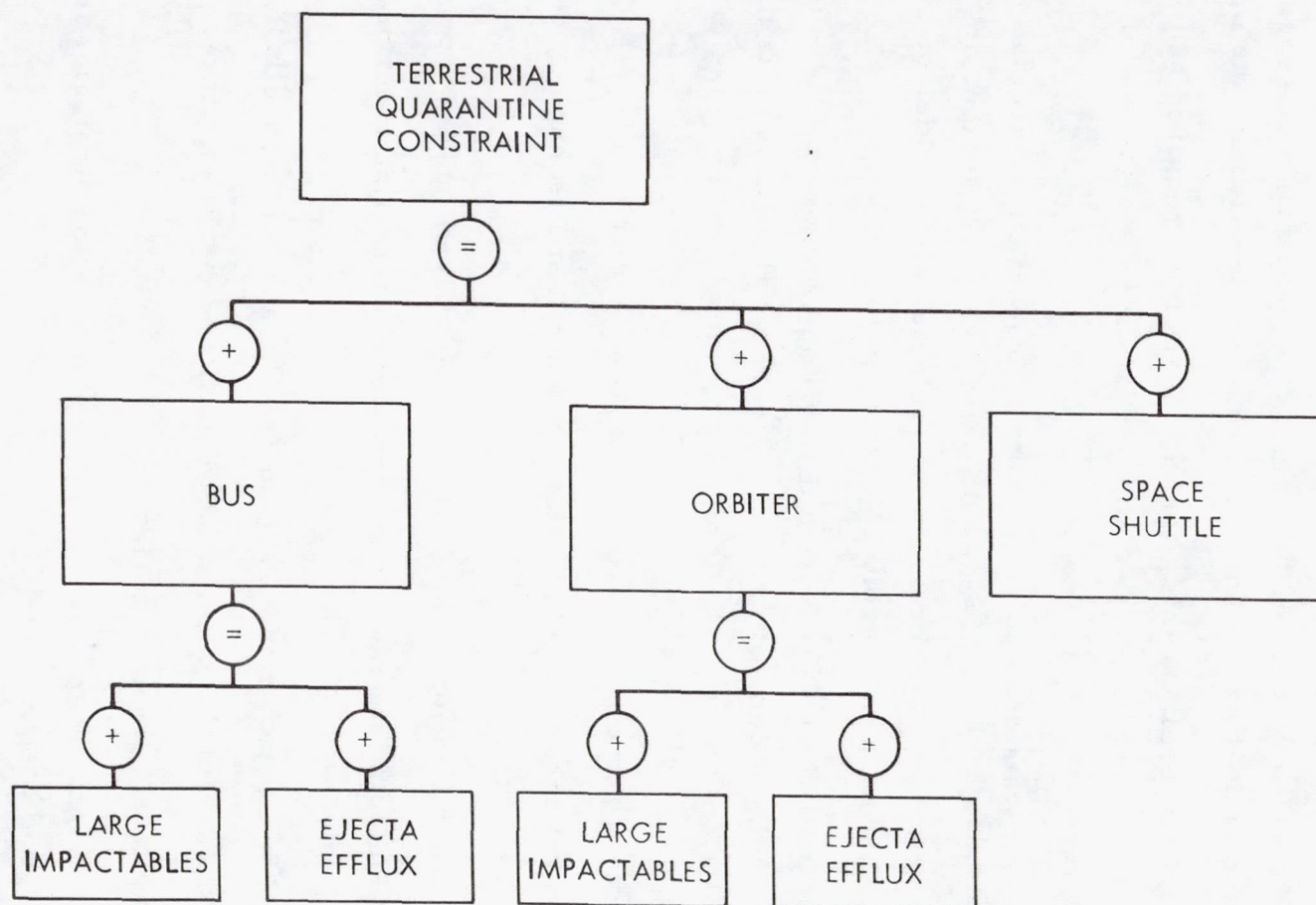


Fig. 2-6. Terrestrial quarantine allocation example-orbiter mode

options have the same tree structure. To perform the task of suballocating the contamination probability, a list of possible contaminating mechanisms was compiled.

The next step would be to compute the probabilities associated with each of the contaminating mechanisms', sum and to calculate the probability $P_{c\text{Estimated}}$. However, at this time, several of the required numbers are not available; particularly those estimating microorganism survival during Earth atmospheric re-entry.

The analysis does point up that the probabilities associated with the bus will be approximately the same for either recovery option, and that the major analysis effort should concentrate on determining which of the two options, the re-entry capsule or the orbiter/shuttle, is better.

The final report provides a discussion of other sample return missions, such as asteroid and comet missions. The general conclusion is that quarantine problems will be similar to those of a Mars sample return mission.

2.2.4 Research Areas and Technology Developments

Several areas where additional research and technology development are needed are as follows:

- (1) Sterilization methods for organisms with unknown properties.
- (2) Information needed by terrestrial quarantine from precursor missions.
- (3) Spacecraft contamination designs and sealing methods.
- (4) Terrestrial quarantine monitor and detection package.
- (5) Re-entry characteristics.
- (6) Investigation of trajectory and navigation strategies to minimize fuel loading penalties.

2.3 PROBLEM AREAS

The study could not be carried far enough to provide a bounding estimate on $P_{c\text{Estimated}}$, the capability to meet a TQ constraint. Additional work

is required in the areas of research and trajectory analysis, particularly on organism survival during re-entry and error analysis on Earth orbital insertion. While precise answers must await more defined mission sets, realistic preliminary estimates could be made by continuing work in these areas.

2.4 FUTURE ACTIVITIES

No further activities are planned under this task. However, additional work will continue under the Planetary Quarantine constraints for advanced missions task in preparing the following:

- (1) Terrestrial Quarantine constraints guidelines document for use with new sample return study contracts.
- (2) Terrestrial Quarantine provisions document.
- (3) Background material on definitions and considerations to aid in defining Terrestrial Quarantine policy.

2.5 PUBLICATIONS

"Terrestrial Quarantine Constraints for Unmanned Planetary Sample Return Missions Final Report." In publication.

2.6 PRESENTATIONS

Stavro, W., "Planetary Quarantine Constraints for Unmanned Planetary Sample Return Missions", presented at NASA Semiannual Sterilization Technology Seminar, San Francisco, California, January, 1972.

900-597

SECTION III

NATURAL SPACE ENVIRONMENT STUDIES

SECTION III
NATURAL SPACE ENVIRONMENT STUDIES

NASA No. 193-58-62-04

Cognizance: D. M. Taylor, C. A. Hagen (Bionetics)

Associate Personnel: J. Barengoltz, R. Berkman,
R. Gildersleeve (Bionetics),
G. Gonzalez, G. Renninger (Bionetics),
G. Smith (Bionetics), C. Smith (Bionetics),
and J. Yelinek (Bionetics)

3.1 INTRODUCTION

The objective of the Natural Space Environment Studies is to determine the probability of microorganisms surviving exposure to elements of the space environment such as rapid pressure changes, vacuum and temperature, and different types of solar, cosmic, and planetary trapped radiations. Twelve organisms randomly selected from over two hundred isolates, recovered at different assembly and test stages from Mariner Mars 71 spacecraft, and two comparative organisms, Bacillus subtilis var. niger and Staphylococcus epidermidis ATCC 17917, are being tested. Nine of the spacecraft isolates are sporeformers while three are nonsporeformers. These fourteen organisms are used in all experiments constituting a unified approach that examines the effects of a variety of factors of the natural space environment on the survival of a spacecraft microbial subpopulation.

An additional task area is directed toward an understanding of the underlying factors related to the probability of terrestrial microorganisms growing in the environment of a planet other than Earth.

3.2 SIGNIFICANT ACCOMPLISHMENTS

3.2.1 Effect of Planetary Trapped Radiation Belt on Microorganisms

3.2.1.1 Description of Study. With missions to Jupiter, the spacecraft will possibly be exposed for an extended duration to the Jovian trapped radiation belt. In this environment, the radiation type, energy, and flux vary depending

on the prediction model and the position within the environment. The trapped radiation belt of Jupiter is predicted by the model used in this study (Ref. 1) to be torus shaped (Fig. 3-1) and to extend approximately out along the equatorial plane as much as 30 Jupiter radii. The model contains both electrons and protons. The energy and flux levels of electrons and protons of the predicted model increase as the distance from the planet decreases (Fig. 3-2). The current model predicts electron energies as high as 20-MeV with a flux level up to 10^7 $e\text{ cm}^{-2}\text{ sec}^{-1}$ and proton energies greater than 400-MeV at flux levels greater than 10^8 $p\text{ cm}^{-2}\text{ sec}^{-1}$.

For any mission where the planetary quarantine analysis considers the effect of radiation environments on the probability of survival of microorganisms, there must be an understanding of two questions for these probabilities to be meaningful or useful: 1) What is the relationship of different types of radiation, energy levels, dose rates, and temperature on the survival of microorganisms; and 2) What is the relative radioresistance of microorganisms naturally occurring on spacecraft hardware.

3.2.1.2 Experimental Conditions.

1. Microbiology. Twelve microorganisms, randomly selected from over two hundred bacterial isolates recovered at different assembly and test stages from Mariner Mars '71 spacecraft, were used in these studies. Nine of the spacecraft isolates were sporeformers while three were nonsporeformers. For purposes of comparison, the sporeformer, Bacillus subtilis var. niger and the nonsporeformer Staphylococcus epidermidis ATCC 17917 were included in all tests.

The sporeforming isolates were sporulated in the liquid synthetic medium of Lazzarini and Santangelo (Ref. 2) modified by the addition of 1 - methionine and 1 - tryptophan (25 mg L^{-1}). The spores were washed seven times with sterile deionized water and finally resuspended in 95% ethanol. The nonsporeforming isolates were grown as lawns on Trypticase Soy Agar (TSA) with 48 hr incubation at 37°C after which the cells were harvested and washed four times with sterile deionized water and finally resuspended in sterile deionized water.

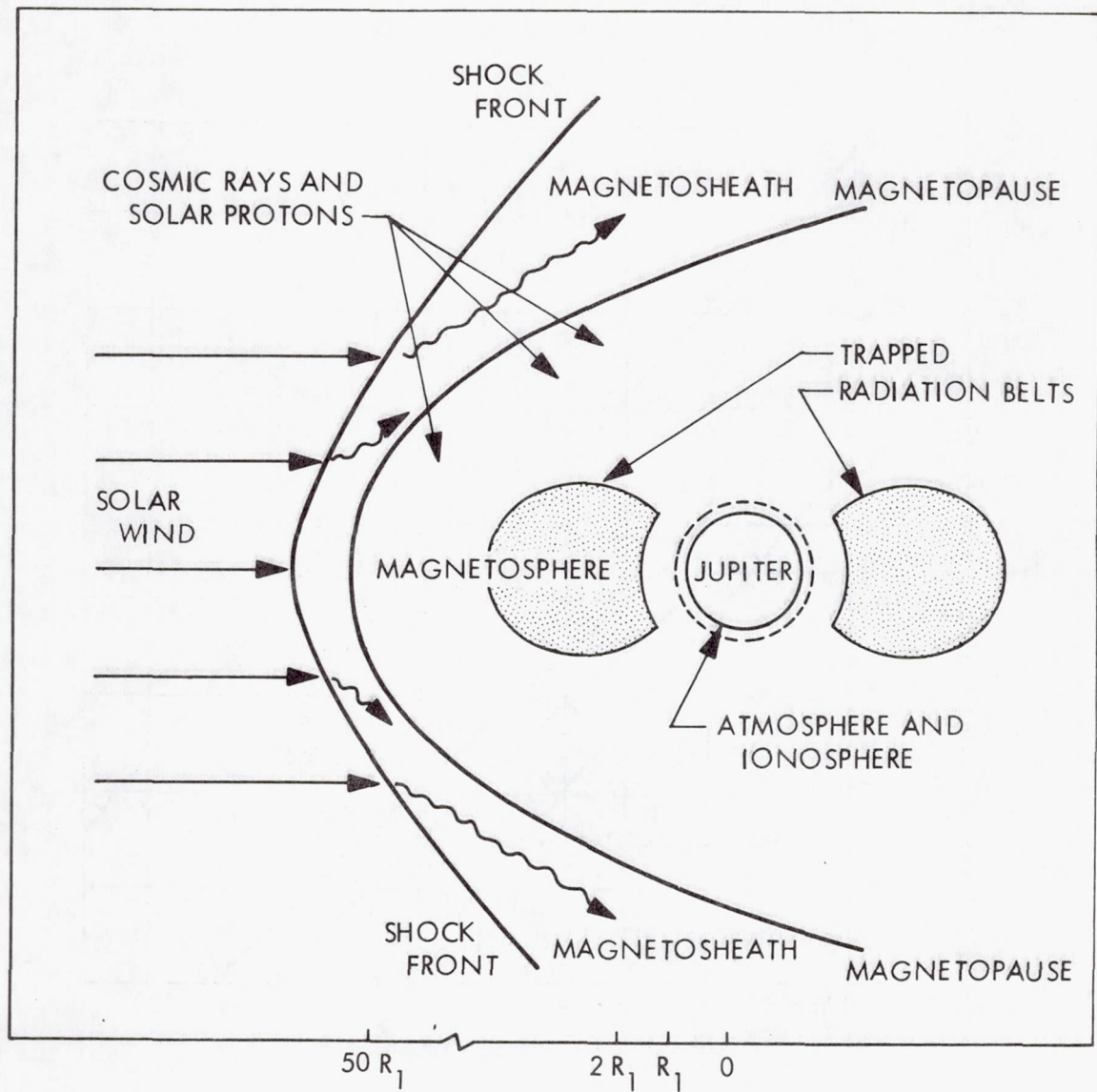


Fig. 3-1. Schematic of charged particle regions near Jupiter

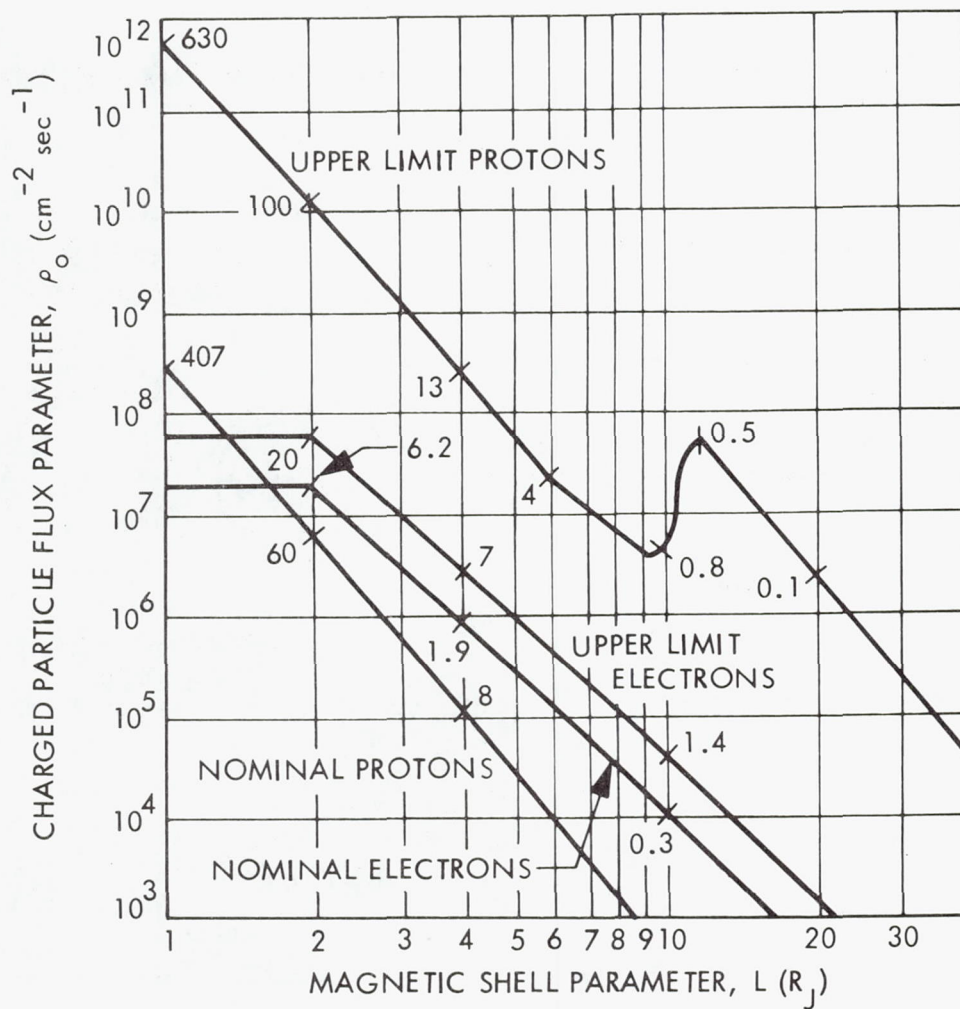


Fig. 3-2. Jovian trapped radiation belt

A planchet (sample holder) was inoculated with either 10^5 spores or 10^6 vegetative cells. The inoculum was allowed to air dry in an environmentally controlled room (45% relative humidity, 21°C). The planchets were placed into the test fixture and exposed to the selected test conditions. At the conclusion of a test, a planchet was assayed for viable microorganisms by placing the planchet into 10 ml of 0.1% sterile peptone water and insonating at 25 kHz for 12 min.

The insonated suspension was serially 10-fold diluted with the dilutions being plated in triplicate using the pour plate method with TSA as the recovery medium. The plates were incubated at either 25, 32, or 37°C , depending on the isolate. Viable cell counts were performed with the data subjected to an analysis of variance with the effect significantly different at the 0.05 level of probability.

2. Vacuum Equipment. A vacuum chamber was constructed from stainless steel tubing with aluminum face plates. The test fixture, a planchet retainer collar made from aluminum, was mounted to the chamber flange. Thermoelectric coolers, placed between the test fixture and flange, controlled temperatures across the test fixture so that one half of the fixture was maintained at 20°C while the other half of the fixture was maintained at -20°C . At the conclusion of a test, the chamber was backfilled from 10^{-6} torr to ambient pressure (760 torr) with dry nitrogen.

The vacuum chamber was constructed so that two flanges with test fixtures were employed for a test: one flange exposed to vacuum, temperature, and radiation, and the other flange exposed only to vacuum and temperature.

3. Radiation. The 2 MeV electrons were produced by a dynamitron, a direct current accelerator. The flux profile was established and the exposure was monitored with the use of Faraday cups. The 12 and 25 MeV electrons were produced by a LINAC operated at 15 pulses sec^{-1} and a pulse width of 2 to 3 μsec . The flux profile for the tests using the LINAC was established prior to each run with LiF thermoluminescent detectors (TLD). The magnitude of the flux in these maps and during the test runs was standardized by a center-mounted PIN diode.

The bacterial isolates were exposed to 2, 12, and 25 MeV electrons at 150, 300, and 450 krads with a flux level of $10^{10} \text{ e cm}^{-2} \text{ sec}^{-1}$. Additional

exposures were conducted with the same electron-energies at 300 krad with flux levels of 10^9 and 10^{11} e cm⁻² sec⁻¹.

3.2.1.3 Results. The analysis of variance performed on test data from 150, 300, and 450 krad at a flux level of 10^{10} e cm⁻² sec⁻¹ with electron energies of 2, 12, and 25 MeV is presented in Table 3-1. The effect of 150, 300, and 450 krad exposures at a flux level of 10^{10} e cm⁻² sec⁻¹ across all three energies of electrons on spores of B. subtilis and the sporeforming spacecraft subpopulation is shown in Fig. 3-3a. The mean survival fraction for the spacecraft isolates is plotted with those isolates exhibiting maximum and minimum resistance identified at each dose. The survival curve for B. subtilis indicates an approximate one log reduction of the initial population for each 150 krad exposure. The mean survival of the spacecraft isolate subpopulation indicates that these isolates were more resistant to electron irradiation than B. subtilis. The data showed that no individual isolate was the most or least resistant to all exposures.

The effect of electron irradiation at different doses on the nonspore-forming organisms is shown in Fig. 3-3b. The survival curve for S. epidermidis indicates that initial populations of this organism were reduced approximately two logs for each 150 krad exposure. The nonsporeforming isolates exhibited a greater resistance than S. epidermidis to the electron irradiation, with the resistance of isolate No. 5 being similar to spores of B. subtilis.

The sensitivity of the sporeforming and nonsporeforming isolates to dose was a function of electron energy (Table 3-2). At all doses, the spores were least resistant to 2 MeV electrons. The spores were also less resistant to 12 than to 25 MeV at 300 and 450 krad. The percent reduction of initial populations was greatest at the lowest electron energy for each additional 150 krad exposure.

The interaction between electron energy and exposure for the nonspore-forming isolates was different than that of the spore isolates (Table 3-2). It was found that electron energy did not affect the radiosensitivity of the isolates at 150 krad and that there was no significant difference between 2 and 25 MeV electrons at 300 krad. The nonsporeforming isolates were most sensitive to 12 MeV electrons at 300 and 450 krad and to 2 MeV electrons at 450 krad.

Table 3-1. Analysis of variance of test results (constant dose rate)

Source of variance	Spores		Nonsporeformers	
	Degrees of freedom	F ratio ¹	Degrees of freedom	F ratio ¹
Replications	3	***	3	-
Treatment	179	***	71	***
Isolate (A)	9	***	3	***
Temperature (B)	1	***	1	-
Dose (C)	2	***	2	***
Energy (E)	2	***	2	***
AB	9	-	3	-
AC	18	***	6	***
AE	18	***	6	***
BC	2	***	2	-
BE	2	***	2	-
CE	4	***	4	***
ABC	18	***	6	-
ABE	18	*	6	-
ACE	36	*	12	*
BCE	4	*	4	*
ABCE	36	-	12	-
Error	537		213	
Total	719		387	
¹ - = P > 0.05 *P < 0.05 **P < 0.01 ***P < 0.001				

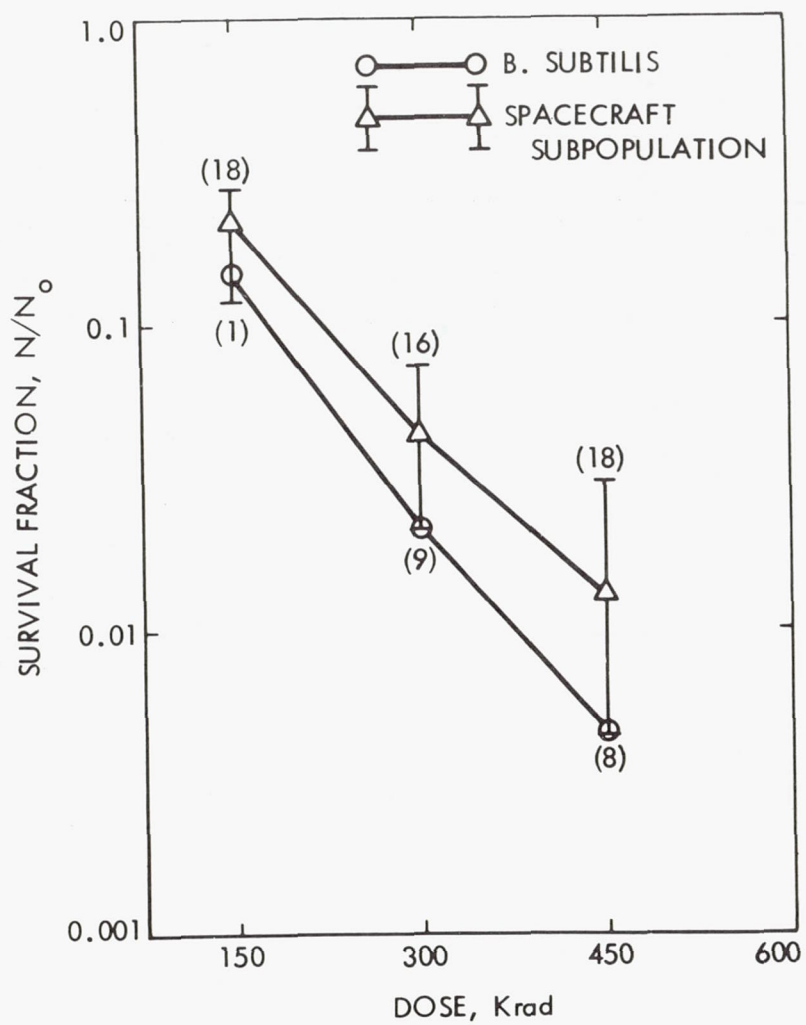


Fig. 3-3 a. Sporeformers

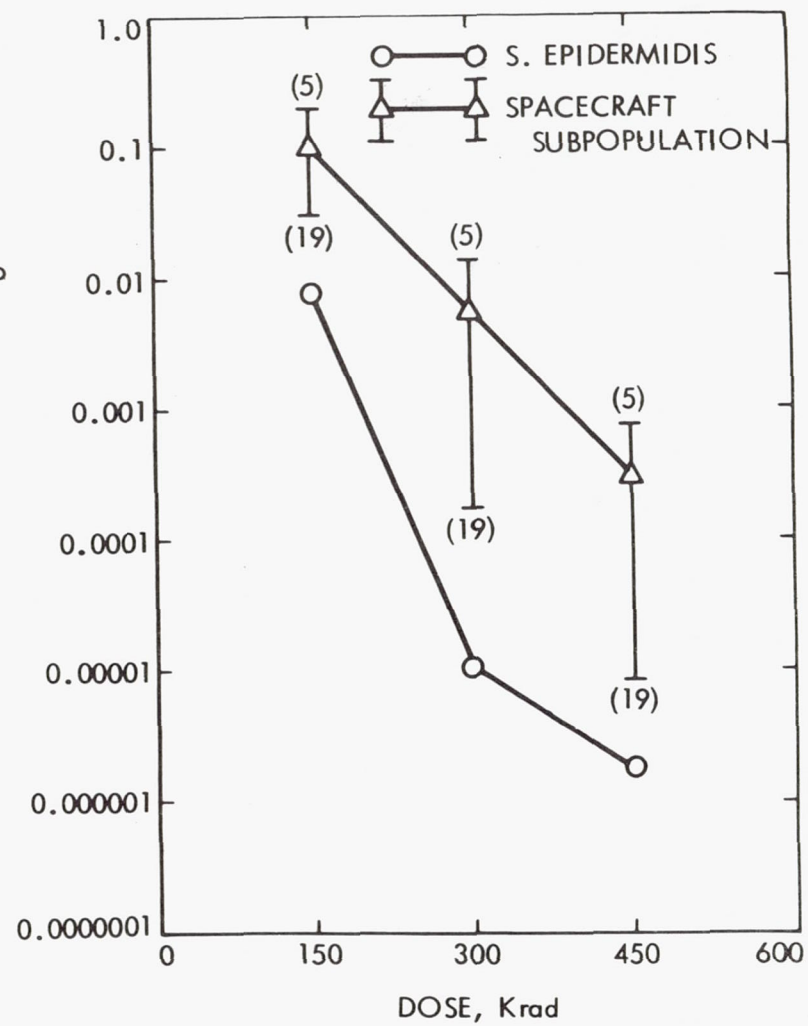


Fig. 3-3 b. Nonsporeformers

Fig. 3-3. Effect of electron irradiation dose on spacecraft bacterial isolates exposed to vacuum

Table 3-2. Effect of electron energy and dose on spacecraft bacterial isolates exposed to vacuum

Dose, krad	Electron energy, MeV		
	2	12	25
Spores			
150	10.80 ^{1,2} _e	27.90 _g	28.50 _g
300	0.70 _b	5.35 _d	13.90 _f
450	0.07 _a	2.53 _c	4.69 _d
Nonsporeformers			
150	2.40 _q	4.74 _q	7.52 _q
300	0.055 _p	0.013 _o	0.130 _p
450	0.011 _n	0.000 _m	0.070 _p
¹ Mean percent survival. ² Mean followed by same subscript letter not significantly different at 0.5 level of probability.			

The effect of electron energy was dependent on the individual isolates. This dependence for the sporeforming isolates is shown in Fig. 3-4. All spore isolates were significantly more sensitive to 2 MeV than to 12 or 25 MeV electrons. Exposure of the isolates to 12 and 25 MeV electron energies indicated that four of the ten isolates (Numbers 8, 11, 13, and 18) were not significantly affected by higher energy. This suggests that, for some organisms, the effect of electron energy does not increase beyond a particular energy level.

The radioresistance to electrons of only the sporeforming isolates was significantly increased at -20°C compared with 20°C (Table 3-3). This temperature effect on spores was influenced by both the dose and the electron energy. Survival was significantly greater at -20° than at 20°C with 300 and

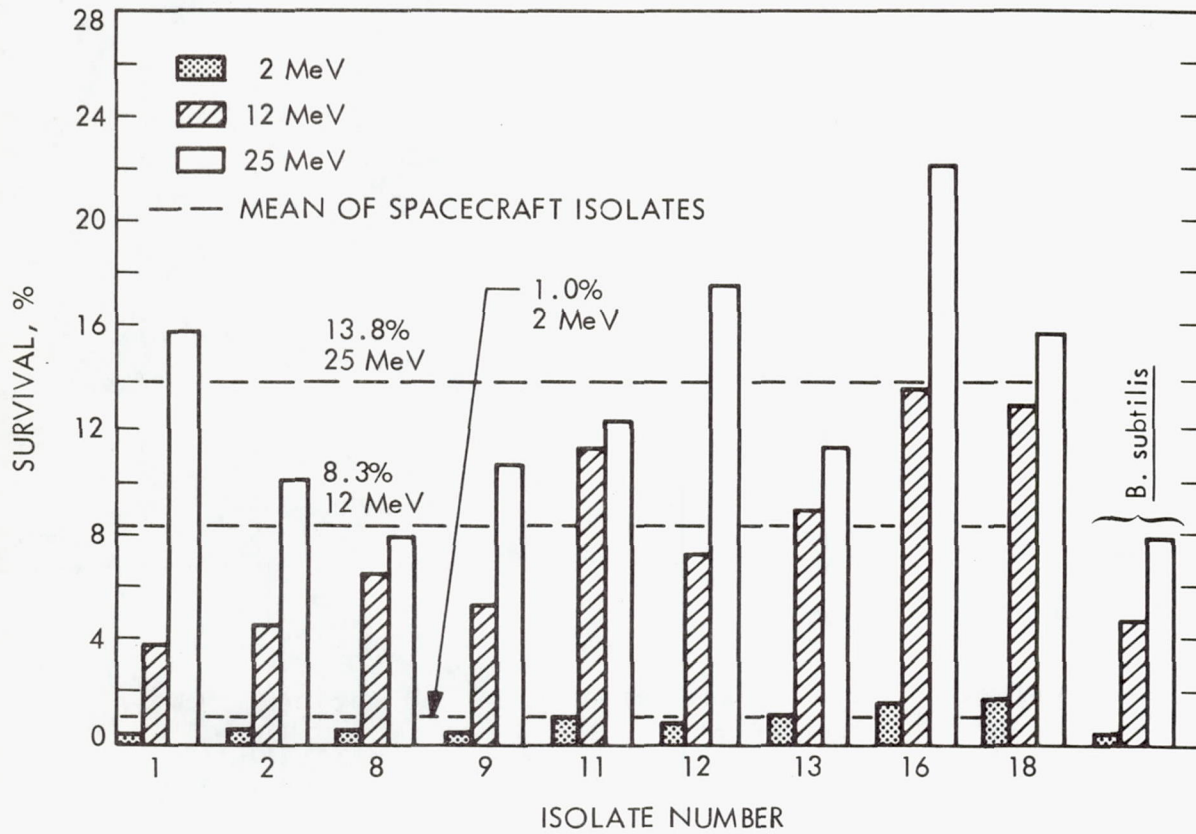


Fig. 3-4. Effect of electron energy on spores of spacecraft bacterial isolates exposed to vacuum

Table 3-3. Effect of electron energy, dose, and temperature on spores of spacecraft bacterial isolates exposed to vacuum

(a) Dose		
Dose, krad	Temperature, °C	
	+20	-20
150	19.8 ^{1,2} _e	21.4 _e
300	3.19 _c	4.35 _d
450	0.687 _a	3.01 _b
(b) Electron energy		
Electron energy, MeV	Temperature, °C	
	+20	-20
2	0.564 ^{1,2} _a	1.14 _b
12	5.86 _c	8.89 _d
25	13.01 _e	12.0 _e
¹ Mean percent survival. ² Means followed by same subscript letter not significantly different at 0.05 level of probability.		

450 krad doses (Table 3-3a). The data also indicated that with increasing electron energies temperature became less effective with no significant effect at 25 MeV (Table 3-3b).

The analysis of variance performed on test data from 300 krad at flux levels of 10^9 , 10^{10} , and 10^{11} e cm⁻² sec⁻¹ with electron energies of 2, 12, and 25 MeV is presented in Table 3-4. The effect of flux levels of 10^9 , 10^{10} , and

Table 3-4. Analysis of variance of test results (constant dose)

Source of variance	Spores		Nonsporeformers	
	Degrees of freedom	F ratio ¹	Degrees of freedom	F ratio ¹
Replications	3	*	3	-
Treatment	179	***	71	***
Isolate (A)	9	***	3	***
Temperature (B)	1	***	1	***
Flux (D)	2	***	2	***
Energy (E)	2	***	2	***
AB	9	*	3	-
AD	18	**	6	**
AE	18	***	6	***
BD	2	***	2	**
BE	2	***	2	*
DE	4	**	4	**
ABD	18	-	6	-
ABE	18	-	6	-
ADE	36	***	12	-
BDE	4	-	4	-
ABDE	36	-	12	-
Error	537		213	
Total	719		287	
¹ - = P > 0.05 *P < 0.05 **P < 0.01 ***P < 0.001				

$10^{11} \text{ e cm}^{-2} \text{ sec}^{-1}$ at 300 krad across all three electron energies on spores of B. subtilis and the sporeforming spacecraft subpopulation is shown in Fig. 3-5a. The mean survival fraction for the spacecraft isolates is plotted with those isolates exhibiting maximum and minimum resistance identified at each dose. The survival curve for B. subtilis indicates that a flux level of $10^{10} \text{ e cm}^{-2} \text{ sec}^{-1}$ was the most effective in reducing initial populations followed by 10^{11} and $10^9 \text{ e cm}^{-2} \text{ sec}^{-1}$. Spores of the spacecraft subpopulation responded to the different flux levels in a manner similar to that of B. subtilis but the spacecraft isolates were more resistant. The logarithmic response of the sporeformers to dose did not occur with flux.

The effect of electron irradiation at different fluxes on the nonspore-forming organisms is shown in Fig. 3-5b. A logarithmic response to flux occurred with S. epidermidis. After an initial 3.5 logs decrease with a flux of $10^9 \text{ e cm}^{-2} \text{ sec}^{-1}$, further 1.0 log reduction occurred at 10^{10} and $10^{11} \text{ e cm}^{-2} \text{ sec}^{-1}$. The nonsporeforming spacecraft isolate number 19, although slightly more resistant than S. epidermidis, responded in a similar logarithmic pattern. Isolate number 5 was the most resistant of the nonsporeforming spacecraft isolates to the different electron fluxes and survived almost as well as spores of B. subtilis. The response to the different flux levels was similar to that of the spores.

The sensitivity of the sporeforming isolates to flux was a function of electron energy as shown in Table 3-5. A $10^{10} \text{ e cm}^{-2} \text{ sec}^{-1}$ flux was most effective with 2 and 12 MeV electrons with no significant difference in effectiveness between 10^9 and $10^{11} \text{ e cm}^{-2} \text{ sec}^{-1}$ fluxes at the same electron energies. The 25 MeV electrons were least effective at all fluxes with no significance between 10^{10} and $10^{11} \text{ e cm}^{-2} \text{ sec}^{-1}$.

The response of the nonsporeforming isolates to flux was different than the sporeforming isolates. The maximum flux effect occurred with the 12 MeV electrons. The 12 MeV electrons at a flux level of $10^{11} \text{ e cm}^{-2} \text{ sec}^{-1}$ were the most effective. The least effective were the 25 MeV electrons at a $10^9 \text{ e cm}^{-2} \text{ sec}^{-1}$ flux.

The experimentation to date indicates that the radiosensitivity of the spacecraft subpopulation to electrons was a function of the individual isolate, the total exposure, and the electron energy and flux. The lowest energy (2 MeV)

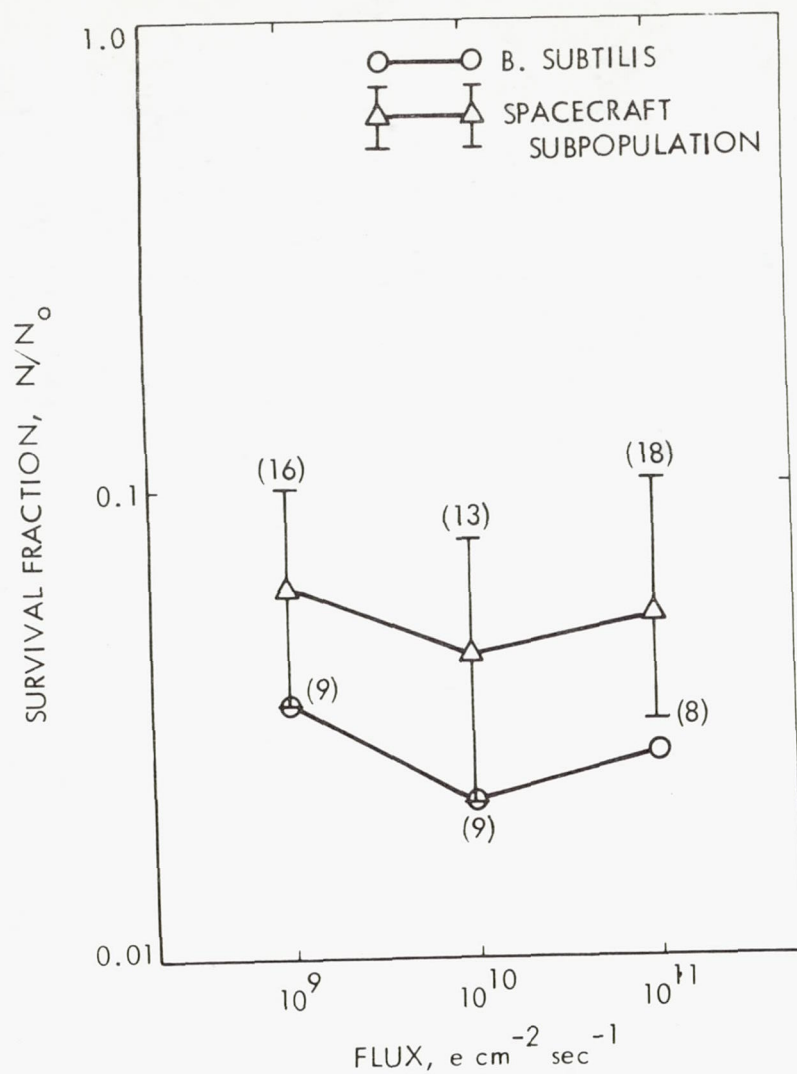


Fig. 3-5a. Sporeformers

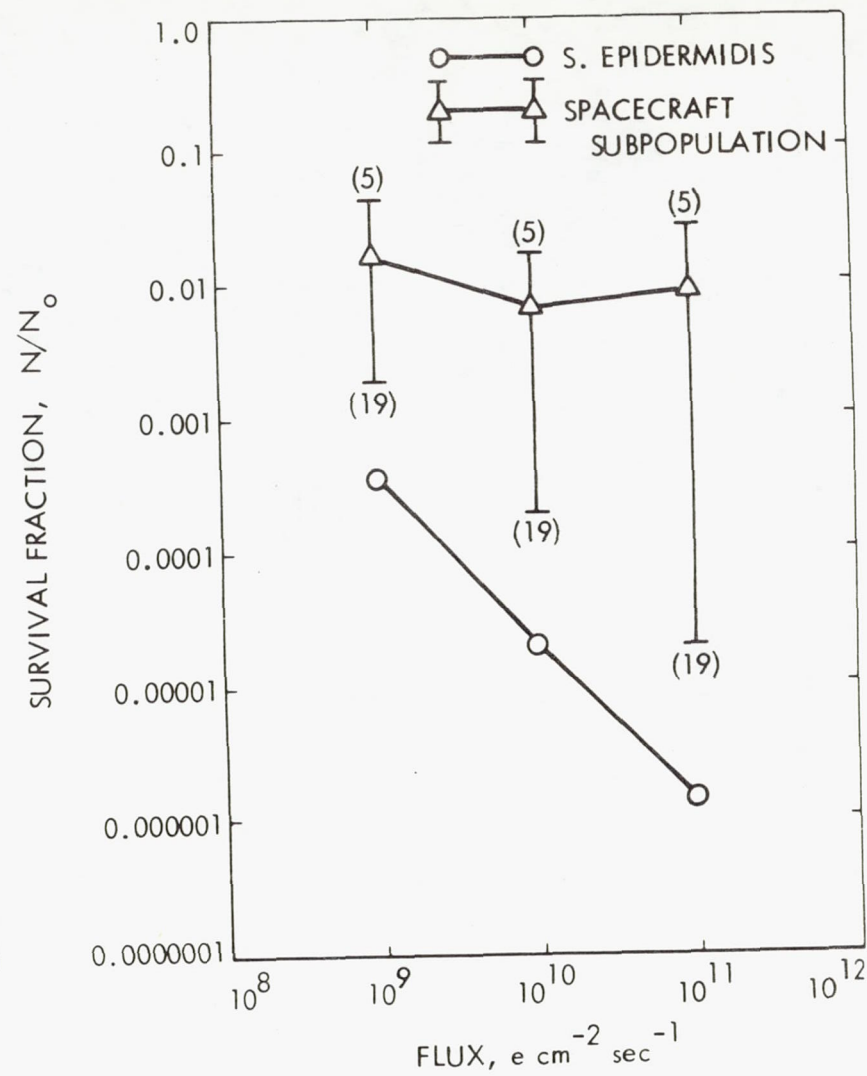


Fig. 3-5b. Nonsporeformers

Fig. 3-5. Effect of electron irradiation dose rate on spacecraft bacterial isolates exposed to vacuum

Table 3-5. Effect of electron energy and dose rate (300 krad)

Flux (e/cm ² sec)	Electron energy (MeV)		
	2	12	25
Spores			
10 ⁹	1.18 ¹ _b ²	8.62 _d	16.33 _f
10 ¹⁰	0.70 _a	4.77 _c	13.90 _{ef}
10 ¹¹	0.96 _b	8.50 _d	12.31 _e
Nonsporeformers			
10 ⁹	0.087	0.41 _{pq}	1.06 _q
10 ¹⁰	0.055 _{no}	0.013 _n	0.13
10 ¹¹	0.027 _n	0.002 _m	0.05 _n
¹ Percent survival.			
² Means follow by same subscript letter not significantly different.			

tested was the most effective in reducing initial populations of spacecraft bacterial isolates. With a constant electron flux (10^{10} e cm⁻² sec⁻¹), dose was effective in reducing initial spore populations 1 log and vegetative cells 1.5 logs for each 150 krad. With constant dose (300 krad), a 10^{10} e cm⁻² sec⁻¹ flux was most effective against spores, and a 10^{11} e cm⁻² sec⁻¹ flux was most effective against vegetative cells.

3.2.2 Effect of Solar Wind Protons on Microorganisms

3.2.2.1 Description of Study. The solar wind contains both electrons and protons with varying energies and flux levels, depending on the activity of the Sun and the distance from the Sun in the case of flux levels. Table 3-6 shows the predicted solar wind protons to be between 0.5 and 4 keV with fluxes between 2.6×10^8 and 1×10^{10} p cm⁻² sec⁻¹ at 1 AU for a quiet and maximum disturbed

Table 3-6. Solar wind (1 au)

Particle	Flux ¹ (cm ⁻² sec ⁻¹)		Energy (eV)	
	Quiet	Maximum disturbed	Quiet	Maximum disturbed
Protons	2.6×10^8	1×10^{10}	534	4000
Electron	1.7×10^9	2×10^{11}	13	130
¹ Decreases with distance squared ($1/R^2$).				

Sun, respectively. The solar wind electrons have energies between 0.013 and 0.13 keV with flux levels of 1.7×10^9 and 2×10^{11} e cm⁻² sec⁻¹ at 1 AU for a quiet and maximum disturbed Sun, respectively.

The present study was conducted to determine the possible effect of solar wind protons on the survival of microorganisms on exposed spacecraft surfaces. The study was limited to radiation with 3 keV protons which is representative of the higher energies of solar protons from an active Sun.

3.2.2.2 Experimental Conditions.

1. Microbiology. The same bacterial isolates and microbiological procedures presented in para. 3.2.1.2 were also used in the 3 keV proton experiments.

2. Vacuum Equipment. The same vacuum equipment described in para. 3.2.1.2 was also used in the 3 keV proton experiments.

3. Radiation. The 3 keV protons were generated as an essentially direct current beam by a radio-frequency ion source. The proton flux in the beam spot was established by a Faraday cup and was monitored by the source current. The spatial profile was determined by the properties of a scan system that was employed to cover the test plan.

The bacterial isolates were exposed to 3 keV protons at one dose (1.5×10^{13} p cm⁻²) and one flux (8.6×10^9 p cm⁻² sec⁻¹).

3.2.2.3 Results. An analysis of variance performed on the test data is presented in Table 3-7. The analysis of these data indicated that all organisms were significantly affected and that sensitivity was dependent upon isolate and temperature.

The percent survival of the spacecraft isolates and comparative organisms is represented as a histogram (Fig. 3-6). The percent survival ranged from 20.2% for S. epidermidis to 64.8% for spacecraft isolate No. 5, a nonsporeforming bacterium. The 45% survival of B. subtilis was approximately the same as the mean survival of the spacecraft subpopulation (45.3%). In contrast to the effect of electrons, there was no significant difference in the radiosensitivity of sporeforming and nonsporeforming isolates exposed to 3 keV protons. Temperature, although not shown in Fig. 3-6, was found to have a significant effect on the radioresistance across all organisms. Approximately 10% more survived irradiation at -20°C than at 20°C.

Table 3-7. Analysis of variance of 3 keV proton test

Source of variation	Degrees of freedom	Mean square	F ₁ ratio
Replications	3	677.5	2.57
Treatment	27	1,137.5	4.32**
Organisms (a)	13	1,378.2	5.26**
Temperature (b)	1	2,779.0	10.56***
(ab)	13	770.6	2.93*
Error	82	263.1	
Total	111		
*P < 0.05			
**P < 0.01			
***P < 0.001			

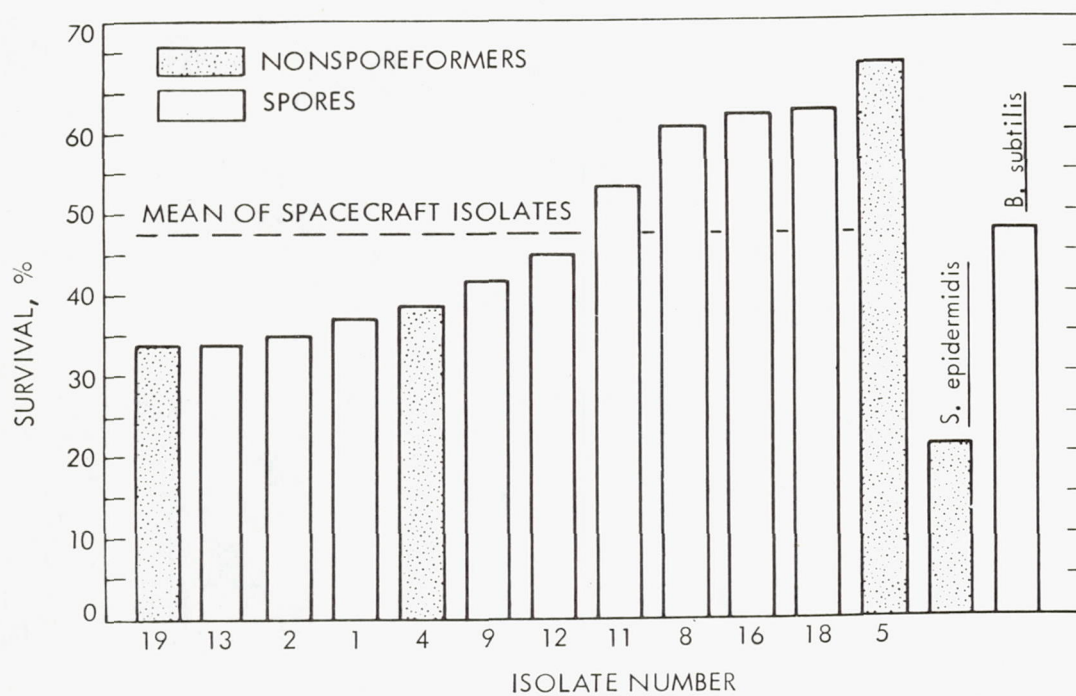


Fig. 3-6. Effect of 3 keV protons on spacecraft bacterial isolates exposed to vacuum

3.2.3 Effect of Space Vacuum on Microorganisms

3.2.3.1 Description of Study. The ultra-high vacuum and heat study was designed to examine the combined effects of space vacuum and spacecraft temperatures on the survival of microorganisms. Fourteen organisms were exposed to the test conditions. Nine of the organisms, isolated from MM'71 spacecraft, were sporeformers while three isolates were nonsporeformers. A sporeforming organism, Bacillus subtilis var. niger and nonsporeforming organism, Staphylococcus epidermidis ATCC 17917, were included in the tests for comparative purposes.

The initial establishment of the vacuum closely approximated the rapid pressure change that may be associated with a spacecraft during the launch stage. The pressure decreased from 750 torr to 10^{-5} torr during the first 20 min and to approximately 10^{-6} and 10^{-7} torr after ion pumping for 1 hr and 24 hr, respectively.

Vacuum exposures of the bacterial isolates to temperatures of -40, 25, 40, and 55°C were conducted for different durations of time up to 180 days to simulate the vacuum and temperature environment of a spacecraft during a typical mission to Mars.

3.2.3.2 Experimental Conditions.

1. Microbiology. The same bacterial isolates and microbiological procedures presented in para. 3.2.1.2 were also used to study the effects of space vacuum on the survival of microorganisms.

The test matrix for the space vacuum study differed from the radiation studies in that for the space vacuum study, the isolates were exposed to four temperatures (-40, 25, 40, and 55°C) while in a vacuum of approximately 10^{-8} torr for durations of 7, 14, 28, 56, and 180 days.

2. Vacuum Equipment. The test facility for the space vacuum study is shown in Fig. 3-7. The vacuum chambers are located on either side of the console that contains the recording and controlling equipment for the chambers.

The vacuum chambers were manufactured by mating 6 in. inside diameter 303 stainless steel tubing directly to 200 L sec⁻¹ ion pumps (Perkin-Elmer Corp.). Each chamber has a Freon 12 refrigeration system for the -40°C

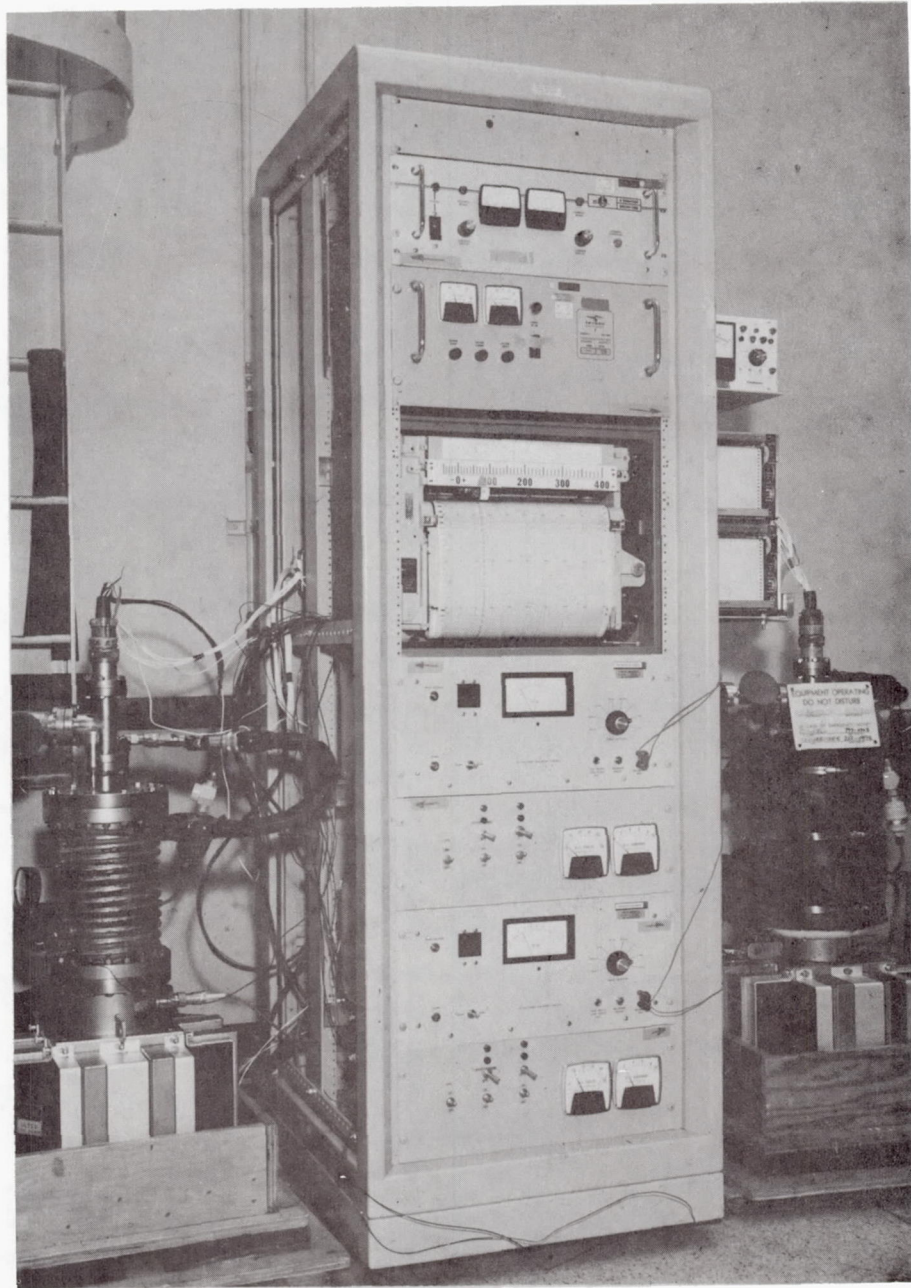


Fig. 3-7. Test facility

plate of the test fixture and also to cool the chamber wall. The copper cooling coils around the chamber wall are shown in Fig. 3-8.

The test fixture (Fig. 3-9) was made with four 8.75 x 3.50 in. stainless steel plates. Each plate had 84 holes to accommodate the inoculated planchets and planchets to which copper constantan thermocouples have been welded. Each chamber had nine thermocouples. Temperatures were recorded hourly during a test.

The temperatures of the 25, 40, and 55°C plates were established and maintained with printed circuit heater elements (Thermal Systems Division) affixed to the back sides of the plates with thermal conductive epoxy.

3.2.3.3 Results. The 180 day space vacuum test is in progress and for this reason only preliminary unanalyzed data will be presented. Figure 3-10 shows the space vacuum resistance of spores of two spacecraft isolates. The two isolates were selected to demonstrate differences in resistance of the spore-forming isolates to the test environments. For comparison, the space vacuum resistance of B. subtilis var. niger spores were included.

Spores of isolate 9 were relatively sensitive to the test environments. A temperature effect was noticed at 40 and 55°C after the shortest exposure of 7 days. Temperatures of -40 and 25°C were not found to greatly reduce spore viability.

The duration of exposure of spores to a particular temperature while under vacuum was significant for some of the isolates. Isolate 1, one of the more resistant of the sporeforming isolates to the test environments, demonstrates the effect of duration of exposure (Fig. 3-10). A temperature effect occurred at 40 and 50°C but it was not manifested until the 56 day exposure.

Spores of the comparative organism, B. subtilis var. niger, were affected both by temperature and the duration of the exposure. A temperature of 55°C decreased spore viability as early as 7 days and as the duration of the exposure was lengthened, a greater portion of the spores became nonviable.

In summary then, spores of isolate 1 decreased in viability at a temperature between 25 and 40°C but only after the longest exposure of 56 days. Spores of isolate 9 decreased in viability at a temperature between

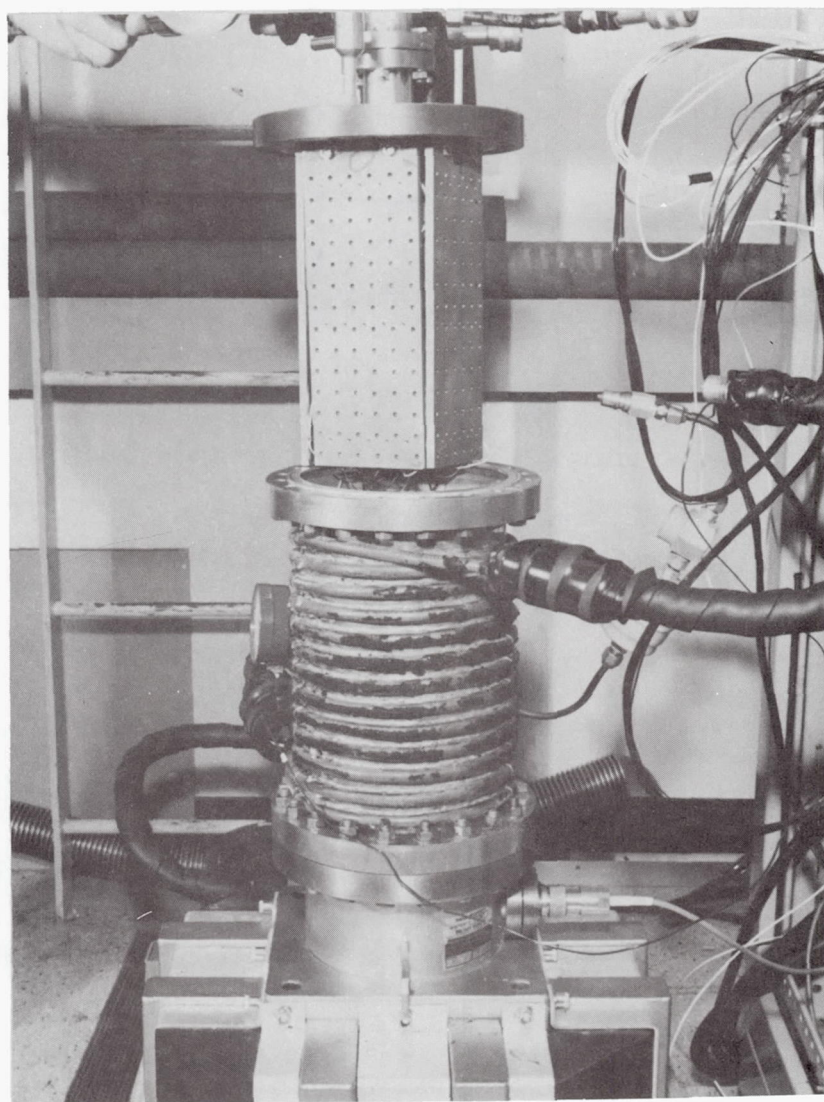


Fig. 3-8. Test chamber

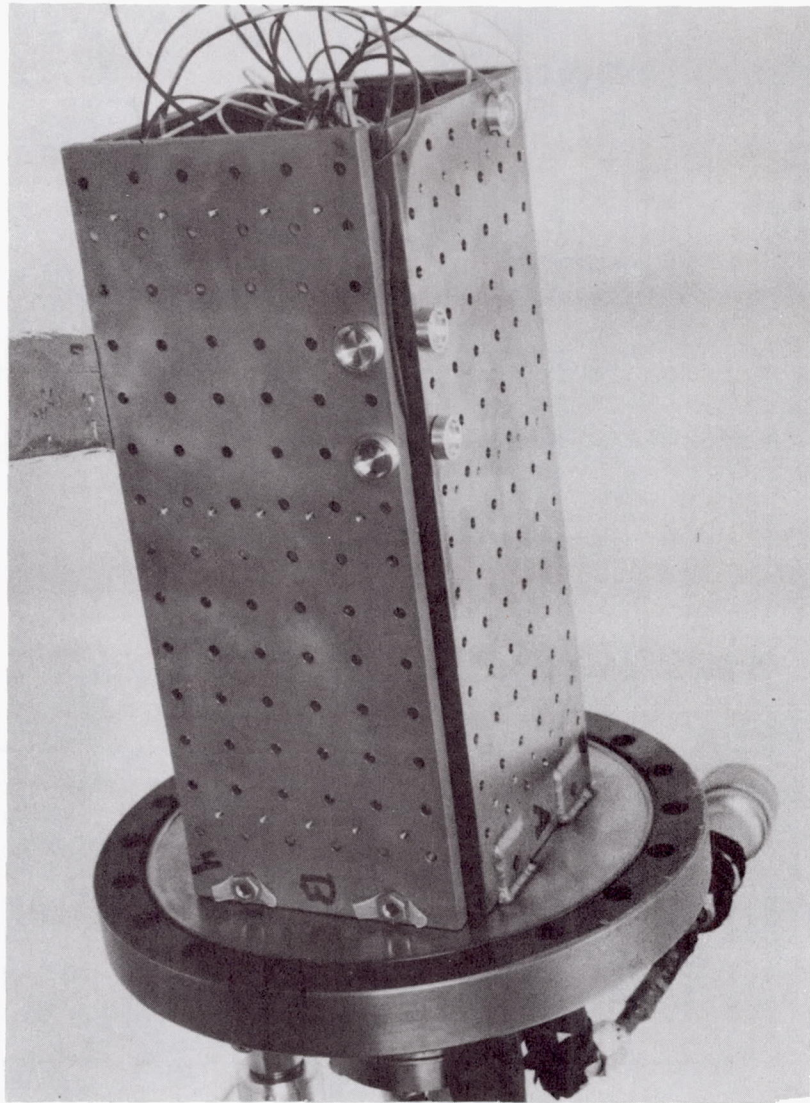


Fig. 3-9. Test fixture

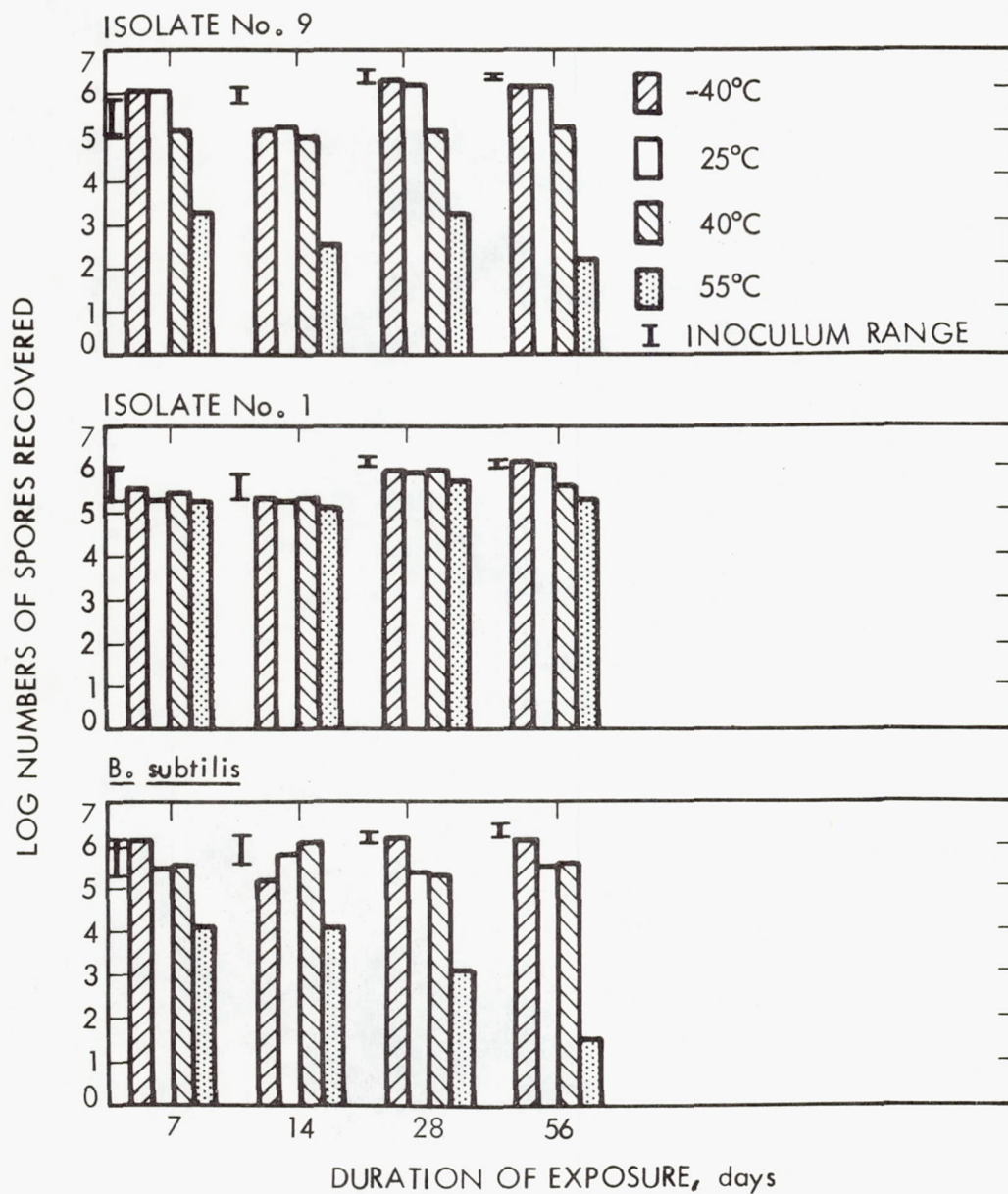


Fig. 3-10. Vacuum temperature resistance of spores of spacecraft isolates

25 and 40°C as early as a 7 day exposure. The critical temperature affecting spore viability of B. subtilis var. niger occurred between 40 and 55°C, as early as the shortest exposure of 7 days.

The reactions to the test environments of two of the nonsporeforming spacecraft isolates together with the comparative organism, S. epidermidis, are shown in Fig. 3-11. Isolate 19 was one of the more sensitive of the non-sporeforming isolates to the test conditions. Cells of this organism survived the vacuum environment best at 25°C and poorest at 55°C. A decrease in cell viability also occurred at -40°C.

Isolate 5 was the most resistant of the nonsporeforming spacecraft isolates to the test environments. Survival was best at -40°C and poorest at 55°C (Fig. 3-11).

The survival of the comparative organism, S. epidermidis, in the test environments was similar to the survival of isolate 19 (Fig. 3-11).

In summary, the cell viability of isolate 19 was best at 25°C. The lower cell viability at all other temperatures occurred as early as the 7 day exposure. Viability of isolate 5 was best at -40°C. The critical temperature for this organism occurred between 25 and 40°C as early as 7 days. With the exception of the 14 day exposure, the cell viability of the comparative organism S. epidermidis was best at -40°C. Exposure to all other temperatures resulted in decreased cell viability with all exposure durations.

3.2.4 Probability of Growth in Planetary Atmospheres

3.2.4.1 Description of Study. This task has been restricted to a study of the probability of growth (Pg) in the Jupiter atmosphere with emphasis on zones of relative probability of actual growth rather than mere survival. The approach to establishing Pg values was to assess the minimal needs of bacteria and to determine whether or not the Jupiter atmosphere can meet these needs. Each requirement was evaluated independently in terms of its growth supporting function and a Pg value assigned. Additionally, the possibility of there being present in the Jupiter atmosphere factors which, in the presence of the basic growth requirements, could prevent growth, was considered. An overall Pg picture based on the sum total of all factors was constructed, establishing zones of relatively high and low Pg.

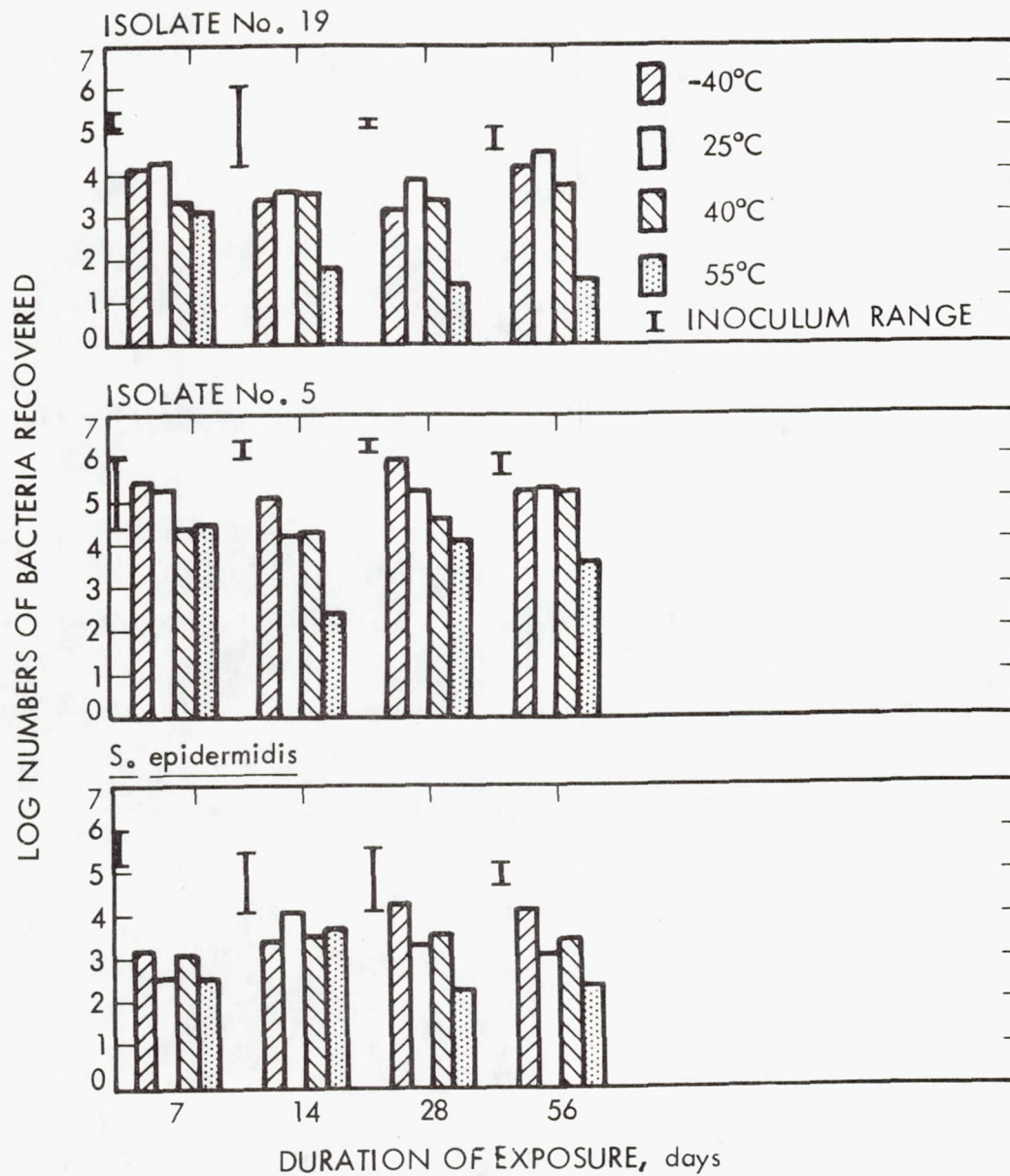


Fig. 3-11. Vacuum temperature resistance of nonsporeforming spacecraft isolates

The organisms considered in the task were bacteria rather than other life forms primarily because of their greater variety, higher adaptability, comparative ease of study in the laboratory, simple growth requirements in many cases, and the availability of extensive published literature on their physiological and morphological characteristics.

A literature review of how temperature, pressure, chemical composition and moisture affect the growth of bacteria was presented previously (Ref. 3). While the maximum and minimum limits of various parameters permitting growth were described, there were no attempts to assign Pg values on the basis of the limited data. The present report provides relative Pg values in terms of high, low, or nil probabilities of growth. Numerical Pg values still cannot be assigned with high reliability because: 1) determinations of temperatures, pressures and abundances are only tentative; 2) existing data of Jupiter atmosphere is insufficient; and 3) the Jupiter atmosphere is turbulent. Thus, even in generally hostile regions there might exist localized biospheres where growth could occur readily (Refs. 4, 5, and 6). There also can be extremely complex interactions between temperature, pressure, chemical composition, and other growth parameters that may affect the imposed limits; i.e., pressure can extend the upper temperature limits at which bacteria can grow (Ref. 7).

The present Pg study used "the law of limiting factors" as a basis to calculate high, low, or nil probabilities of growth. The law states that any one factor, if limiting for growth, will affect Pg even if all other required factors are optimal.

3.2.4.2 Discussion.

1. Minimal Growth Requirements of Bacteria. A concise review of the nutritional requirements of bacteria is given by Guirard and Snell (Ref. 8). For Pg purposes, the needs have been divided into 4 categories: 1) carbon source; 2) energy source; 3) salts; and 4) water.

While carbon is essential for growth, bacteria can utilize a wide variety of carbon compounds, including CO_2 , CH_4 , and all other naturally occurring carbon compounds.

As a source of energy, the heterotrophic bacteria invariably use the same compound which serves as the carbon source, whereas autotrophs derive energy from sunlight or by oxidation of inorganic compounds.

Bacteria require a large number of inorganic salts, either in relatively large quantity ($\text{SO}_4^{-2} \cdot \text{NH}_4^+$, PO_4^{-3} , etc.), or in trace amounts (Ni^{+2} , CO^{+2} , etc.). Many salts are required both as structural entities and as cofactors in enzyme systems.

The need for water requires little elaboration. It should be noted, however, that growth of microorganisms has been measured down to 11 percent relative humidity (Ref. 3).

2. Growth Limiting Factors. Even with all minimal growth requirements present, various other agents may still limit or prevent growth. Such inhibitory factors include radiation, temperature, pressure, and chemical agents. Radiation would include some of the visible and ultraviolet wavelengths. In the case of temperature, literature indicates that growth of Earth organisms cannot occur below about -20°C ; the upper temperature extreme is generally considered to be near 100°C with few exceptions. The effect of pressure on bacterial growth has not been studied in detail; however, growth of marine bacteria has been shown to occur at depths corresponding to 1000 atmospheres hydrostatic pressure. Organisms have also been shown to grow under a pressure of 0.01 atmosphere (Ref. 3).

Chemical inhibitors of growth include those of a highly toxic nature as well as those which are toxic only when present in great abundance. The former includes various metabolic inhibitors such as azide and cyanide; the latter, compounds which are competitive inhibitors and those which cause secondary effects. An example of the latter is ammonia, which if abundant, can raise the pH of aqueous suspensions to toxic levels.

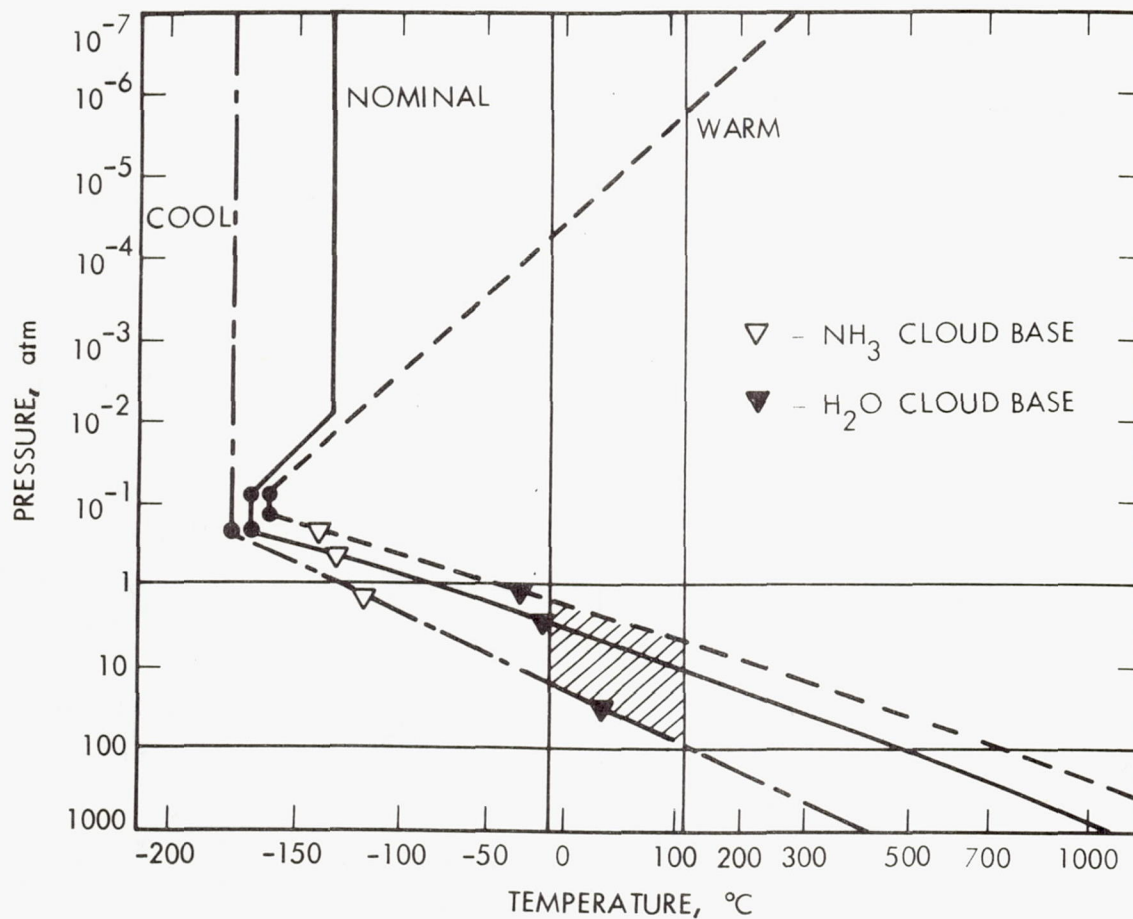
The minimum and maximum limits for some environmental factors are summarized in Table 3-8 (Ref. 3).

3. Pg in the Jupiter Atmosphere. There are three models for the Jupiter atmosphere: cool, nominal, and warm. Probability of growth in the atmosphere is dependent on three factors: pressure-temperature relationships, water, and the chemical profile of the atmosphere.

Table 3-8. Limits of environmental factors governing microbial growth

Environmental factors	Minimum/maximum limit
Moisture, A_w	0.11 0.999
Temperature, °C	-34, -18 93, 104
Pressure, atm	0.01 1000
Atmospheric composition	100% CO_2 100% O_2 5% NH_3 , 45% H_2 , 50% CH_4 15% NH_3 , 35% H_2 , 50% CH_4 15% NH_3 , 75% AIR 50% NH_3 , 50% CH_4 25% NH_3 , 25% CH_4 , 50% air

The pressure-temperature relationships for the three atmosphere models are shown in Fig. 3-12. The models predict both ammonia and water clouds (represented by open and closed circles, respectively). The cross-hatched area indicates a temperature-pressure range compatible with bacterial growth. A high P_g is associated with a temperature range from about 0 to 100°C and pressures between approximately 1 and 100 atmospheres. One atmosphere of pressure corresponds to an equatorial distance of approximately 71,400 km from the center of the planet. In addition, the band in which temperature and pressure are compatible with a high P_g is comparatively narrow, less than 300 km in depth. Future considerations of P_g will be limited to this region; i.e., the pressure region between 1 and 100 atmospheres.



From NASA Document "NASA SP 8069", December 1971.

Fig. 3-12. Pressure vs temperature for the Jupiter model atmosphere

While the cool, nominal, and warm models all predict aqueous clouds in the Jupiter atmosphere, only the cool model predicts the presence of liquid water. In the cool model, liquid water should be present within the band of 20 to 50 atmospheres pressure. In considering water as a limiting factor, a high P_g to the 20 to 50 atmosphere pressure region, and a low P_g to the remaining region between 1 and 100 atmospheres was assigned. However, in all three models, localized regions of high moisture content in the form of precipitation or condensation could exist even in low P_g regions.

In the region from 10 to 100 atmospheres, carbon is available as methane (CH_4). Ammonia gas is also present, although in regions below 10 atmosphere's pressure, the concentrations of methane and ammonia drop to below 0.7 and 0.2 moles/ m^3 , respectively. Based on the availability of these two compounds, a high P_g to the 10 to 100 atmosphere pressure region, and a low P_g to regions approaching 1 atmosphere were assigned.

An additional factor to consider in aqueous ammonia environments is pH. Present estimates of pH for the high P_g region range between 10.0 to pH 12.0. However, these estimates are tentative.

The other chemical constituents required for growth include several inorganic compounds such as sulfur, various divalent cations, and phosphates. Because knowledge of the existence of such compounds on Jupiter is vague, it is assumed they do exist along with other inorganic compounds required in trace amounts.

4. Growth Limiting Factors in the Jupiter Atmosphere. Radiation, chiefly in the ultraviolet wavelengths, does not pose a problem to microorganisms since most of it is dissipated before reaching the high P_g region. Other kinds of radiation (X-rays, cosmic rays, etc.) are not believed to be significant in considering P_g on Jupiter.

Temperature and pressure as growth limiting factors have been considered earlier in terms of a relatively narrow band in which growth could be possible. It is clear from Fig. 3-12 that organisms cannot grow below one atmosphere of pressure nor can they survive above 100 atmospheres of pressure.

Various chemical agents inhibitory to the growth of microorganisms may or may not be present in the Jupiter atmosphere. It was assumed that such agents will not prevent growth of microorganisms. The assumption is based both on the attributes of bacteria as described in para. 3.2.4.2 and on the assumption that inhibitory agents, if present, are present only in low concentration.

5. Pg for Jupiter. Pg for Jupiter is based on knowledge of Jupiter and the growth requirements of bacteria (Fig. 3-13). Zones of Pg are defined for individual parameters in terms of atmospheric pressure. The solid vertical lines represent zones of high Pg while the broken vertical lines represent zones of low Pg. The headings, chemical inhibitors and radiation, are represented by continuous solid lines, indicating that these factors should not limit bacterial growth. The discontinuity of other lines show that the parameters of temperature, availability of water, and chemical needs are, in part, limiting. For water, note that most of the pressure zone from 1 to 100 atmospheres is represented by a broken line indicating, for the most part, a low Pg. In accordance with "the law of limiting factors", the zone of high Pg is thus reduced to a minimum by a single factor - the availability of water.

The postulated high Pg zone is indicated by the cross-hatched band around 30 atmospheres. Were water not a limiting factor, the high Pg zone could have been widened to encompass a pressure zone from 10 to more than 50 atmospheres. Outside the 1 to 100 atmosphere range Pg is nil; growth outside this region is prevented by temperature extremes.

3.3 RELEVANCY TO PLANETARY QUARANTINE

The Natural Space Environment studies are directly related to Planetary Quarantine by providing data and conclusions as to how the natural space environment effects the survival of microorganisms. Certain summary statements, based upon results to date, can be made:

- (1) Electrons, with energies similar to those present in the trapped electron radiation belt of Jupiter, could be effective in reducing the bioburden of spacecraft but the probability of the spacecraft bacterial burden surviving the trapped electron belt of Jupiter would be a function of the location and time duration in the belt as well as the temperature of the spacecraft surface.

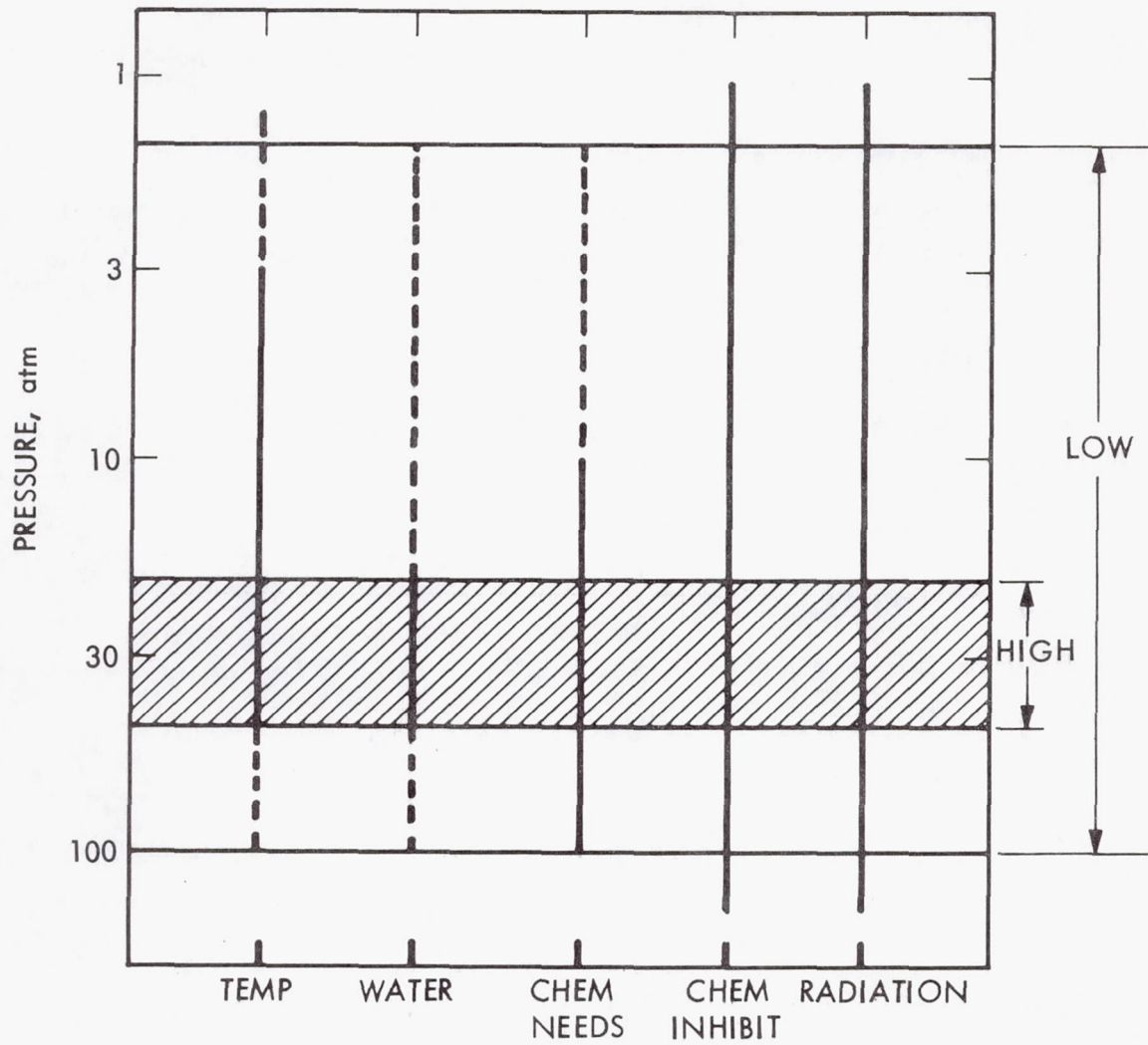


Fig. 3-13. Zones of relative probability of growth in Jupiter atmosphere

- (2) Initial studies with protons at an energy similar to those present in the solar wind could be considered as an additional factor to reduce bacterial burden on spacecraft surfaces.
- (3) Space vacuum in conjunction with normal operating temperatures of spacecraft is an additional factor that could reduce the surface bioburden of spacecraft.
- (4) Theoretical considerations that define possible zones for bacterial growth in nonterrestrial environments are related to planetary quarantine constraints of proposed future spacecraft missions to the outer planets.

3.4 PROBLEM AREA

The results of the launch pressure profile study (Planetary Quarantine Semiannual Review June 30, 1971, Section III, para. 3.5.1) indicate that viable spore count of some spacecraft isolates in the space vacuum study was greater after exposure to the test environment, which did not allow cellular proliferation, than before exposure. Similar results have been reported for other space vacuum simulation experiments (Refs. 9, 10, and 11). Experiments have been planned in an attempt to resolve this problem.

3.5 FUTURE ACTIVITIES

3.5.1 Effect of Planetary Trapped Radiation Belt on Microorganisms

The future activities will be to complete the test matrices for 12 and 25 MeV electrons at 150 and 450 krad and 10^9 and 10^{11} e cm⁻² sec⁻¹ fluxes, conduct studies with 2, 12, and 25 MeV protons, and continue data analyses of test results.

3.5.2 Effect of Solar Wind Radiation on Microorganisms

Future activities will involve studying the effect of dose and dose rate of 3 keV protons, lower proton energies, and solar wind electrons.

3.5.3 Effect of Space Vacuum on Microorganisms

Future activities will involve completion of 180 day exposure to space vacuum at -40, 25, 40, and 55°C, determining the distribution of resistance of spacecraft bacterial isolates to space vacuum and selected spacecraft temperatures, and completion of data analyses of test results.

3.5.4 Probability of Growth in Planetary Atmospheres

Future activities will involve the development of analytical approaches that utilize existing knowledge of maximum and minimum limits of environmental parameters to predict the probability of microbial growth in planetary atmospheres.

3.6 PUBLICATIONS

Taylor, D. M., et al, "A Re-evaluation of Material Effects on Microbial Release from Solids"; Life Sciences and Space Research, Vol. X, p. 23-28, 1972.

Gustan, E. A., et al, "Effects of Aeolian Erosion on Microbial Release from Solids"; Life Science and Space Research, Vol. X, p. 29-32, 1972.

3.7 PRESENTATIONS

The following presentations were made at the NASA Semiannual Sterilization Seminar, Cape Kennedy, Florida, January 1972.

Hagen, C. A. "The Effect of Planetary Trapped Radiation Belt on Microorganisms".

Hagen, C. A. "The Effect of Solar Wind Protons in Microorganisms".

The following presentations were made at the NASA Semiannual Sterilization Seminar, San Francisco, California, July 1972.

Taylor, D. M., "The Effect of Planetary Trapped Radiation Belt on Microorganisms".

Hagen, C. A., "The Effect of Space Vacuum on Microorganisms".

Taylor, D. M., "Probability of Growth in Planetary Atmospheres".

The following presentation was made at the annual meeting of the Committee on Space Research, Madrid, Spain, May 1972.

Taylor, D. M., "Survival of Bacterial Isolates Exposed to Simulated Jovian Trapped Radiation Belt Electrons and Solar Wind Protons".

REFERENCES

1. National Aeronautics and Space Administration; "The Planet Jupiter"; NASA SP-8069; Goddard Space Flight Center; Beltsville, Maryland, 1971.
2. Lazzarini, R. A., and Santangelo, E.; J. Bacterial: 94; 125; 1967.
3. Taylor, D. M., and Knittel, M; Planetary Quarantine Semiannual Review; JPL 900-556; 3-34; June 1971.
4. Newburn, R. L., Jr., and Gulkis, S.; Space Science Reviews; in the press; 1972.
5. The Planet Jupiter; NASA SP-8069; 1971.
6. Sagan, C.; Space Science Reviews: 11; 827; 1971.
7. Zobel, C. E.; Producers Monthly: 22; 12; 1958.
8. Guirard, B. M., and Snell, E. E.; The Bacteria, V. 4, I. C. Gunsalus and R. Y. Stanier eds.; p 33-93; 1962.
9. Imshenetsky, A. A., and Lysenki, S. V.; Life Sciences and Space Research Vol. III, M. Florkin ed.; 142-148; 1965.
10. Gustan, E. A., and Strandberg, D. A.; Boeing Company Report; D2-121029-1; 1970.
11. Silverman, G. J.; Planetary Quarantine, L. Hall ed.; 83-97; 1971.

900-597

SECTION IV

POST LAUNCH RECONTAMINATION STUDIES

SECTION IV
POST LAUNCH RECONTAMINATION STUDIES

NASA No. 191-58-62-03

Cognizance: R. Kazares, J. Barengoltz
Associate Personnel: C. Bauerle (Bionetics),
R. Gildersleeve (Bio-
netics), J. Yang

4.1 INTRODUCTION

The major objective of this task is to study the effects of typical mission environments on the distribution of particles on spacecraft surfaces. Specifically, the various migration mechanisms that result in particle redistribution will be investigated and quantified. The ultimate goal is to develop a methodology and a quantitative analytical tool for the evaluation of the recontamination hazard for various planetary missions and mission strategies.

In order to accomplish these objectives, the task has been divided into four major studies:

- 1) Launch Phase Recontamination Analysis
- 2) Particle Adhesion Force Study
- 3) Meteoroid Impact Study
- 4) Spaceflight Recontamination Analysis

The launch phase recontamination analysis is complete and has been previously reported. This analysis consists of a probabilistic model of the effects of the launch environments on the spacecraft and shroud which predicts release and migration.

The particle adhesion force study includes an analytical model and a test verification program. The model, previously reported, predicts the percent of particles removed as a function of surface acceleration, particle size, and relative humidity. The verification test facility has been constructed and preliminary data has been obtained.

The meteoroid impact study is also divided into an analytical and a test program. The analytical phase is concerned with the determination of the acceleration and velocity of a surface subjected to meteoroid impact. These quantities are required to determine whether a particle attached to the surface will be released. During this reporting period, the analytical solutions to three models designed to describe the various possible conditions have been obtained. The analytical solutions to two of the models represent new technology.

There is no test program underway in this task to directly investigate the surface response to meteoroid impact. Instead, arrangements have been made to obtain the data from a related experiment at Langley Research Center (LRC) when it becomes available.

The spaceflight recontamination analysis deals with the transport problem of the released particles during the flight phase. A general spacecraft geometry routine has been completed. The current effort is in the area of electrostatic force modeling and calculation.

4.2 SIGNIFICANT ACCOMPLISHMENTS

4.2.1 Particle Adhesion Force Study

The particle adhesion force study is currently concerned with the experimental verification of an analytical model previously completed and reported (Ref. 1). During this fiscal year a test facility for this purpose has been designed and fabricated, and preliminary test results have been obtained.

4.2.1.1 Test Plan. An overall test plan has been formulated to provide the needed data for the verification, or modification if necessary, of the particle adhesion force model. Tests will be performed at 1 atm and at 3.2×10^{-3} torr vacuum. Particle sizes will vary between 20 and 100 microns. Relative humidity levels will be from 0 (at vacuum) to 75% (at 1 atm). Nominal surface acceleration levels will be 2,000 to 25,000 G. The test matrix is shown in Table 4-1.

Table 4-1. Force model verification test matrix

Variables	1	2	3	4	5
Particle size	20 μm	40 μm	60 μm	80 μm	10 μm
Vacuum	1 atm	3.2×10^{-3} torr			
Accel level g pk	2,000	5,000	10,000	25,000	
Relative humidity %	0 (at 3.2×10^{-3} torr)	25 (at 1 atm)	50 (at 1 atm)	75 (at 1 atm)	

Statistical analysis techniques will be applied to the data to define the appropriate distribution and confidence level associated with the results.

4.2.1.2 Test Facility. This section describes the test facility constructed at the Jet Propulsion Laboratory (JPL) and presents the capabilities of that facility. Figure 4-1 shows a schematic drawing of the test facility. The central part of the facility is a 4 in. "T" vacuum chamber which has a circular plate attached to each flange. These plates provide the vacuum seal and allow for a set of operational functions. One plate is employed to induce the acceleration environment. Another will be used to mount electrical connectors and a relative humidity sensor. The third plate contains the vacuum system connections and appropriate gages.

The test plate supports the load application assembly which includes the hinge post, load application level, notched bolt, and a hydraulic cylinder. In addition, an accelerometer is mounted inside the chamber which, via the connector, is wired into the appropriate conditioners, monitoring scopes, and a magnetic tape recorder.

No system for controlling or monitoring the relative humidity of the chamber has been designed.

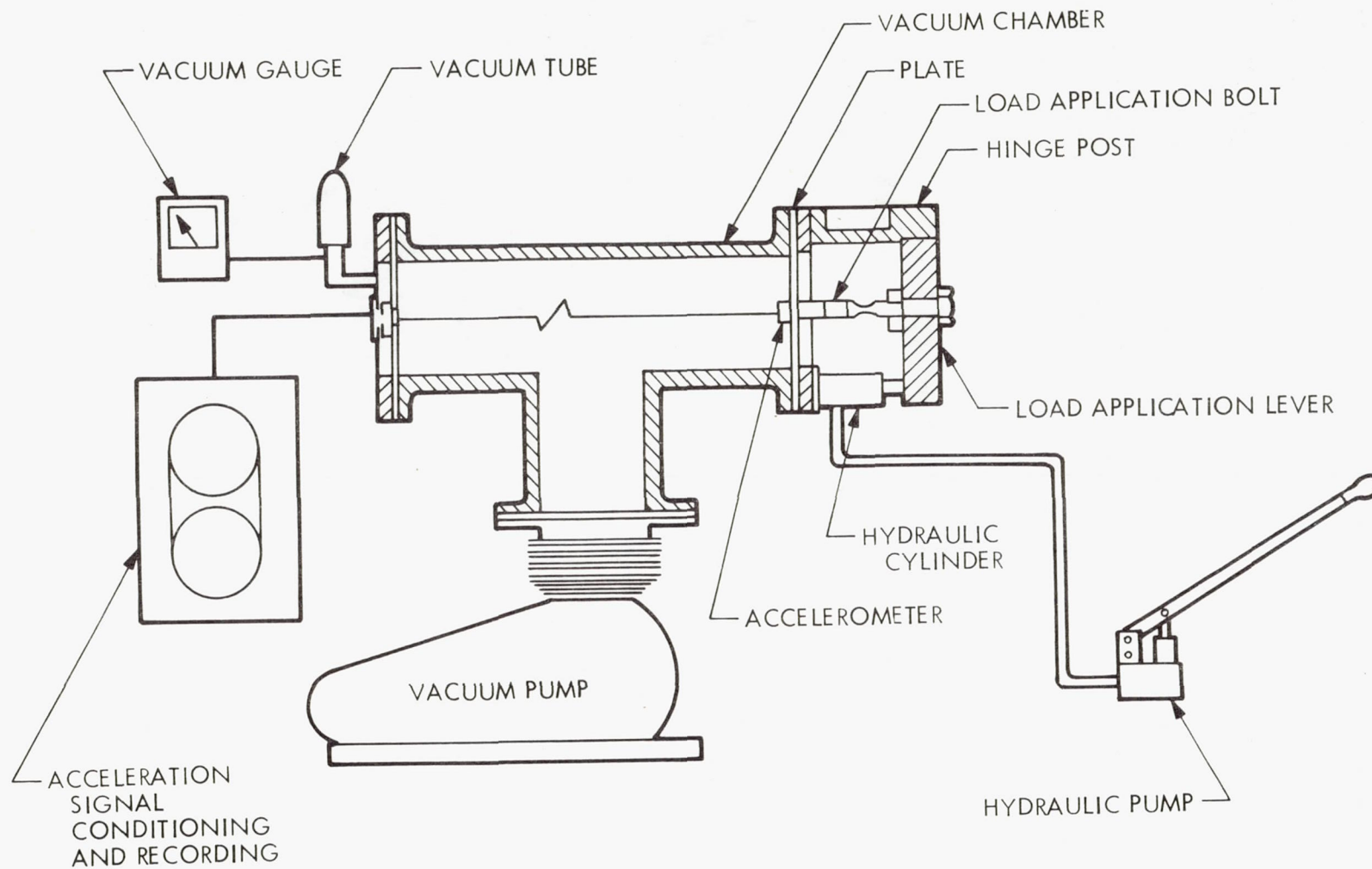


Fig. 4-1. Schematic diagram of test set-up

1. Facility operation. Initially a sample of particles is placed on the accelerometer head, which is then mounted in the chamber. Vacuum is established in the chamber at the desired level using the vacuum pump and the vacuum monitoring equipment. The production of the desired peak acceleration is accomplished as follows.

Stored deformation energy is imparted to the test plate on which the accelerometer is mounted by the load application assembly. Initially the notched bolt is connected to the test plate and the load lever with a tensile pre-load. The hydraulic cylinder is employed (with the hydraulic pump) to gradually increase the load in the bolt until failure. When the bolt fails, the strain energy of the plate causes an acceleration to be imparted to the accelerometer. The diameter of the bolt notch and the test plate thickness may be altered to attain environments of varying acceleration levels and frequency content. For example, the time for the acceleration rise will depend on the speed of failure of the bolt material.

High resolution photographs of the particles on the accelerometer head will be made before and after the test and the percent of particles released for each size of particles will be noted as function of the relative humidity, vacuum, and dynamic environments.

2. Facility capability. In order to obtain the operational characteristics and capabilities of the test system, several test runs were conducted. The characteristics of the facility are shown in Table 4-2. A sample of

Table 4-2. Test facility capabilities

Environment	Facility capability
Acceleration -G	130, 000
Frequency response	100, 000 Hz
Vacuum level	6.8×10^{-5} Torr
Particle size resolution	5 Micron

digitized acceleration data for one run is shown in Figs. 4-2 and 4-3. Figure 4-2 is the acceleration time history with a maximum acceleration level shown of 130,000 Gs. Figure 4-3 is the shock spectrum ($Q = 20$) obtained for the same shock pulse. The frequency of the plate at which the maximum acceleration level occurs is seen to be about 60,000 Hz. The peaks above 100,000 Hz are accelerometer resonances and not true plate acceleration response data.

4.2.1.3 Preliminary Data. Data obtained for the first six test runs is presented in Table 4-3. This is an insufficient amount of information from which to make statistical inferences as there is some scatter. This may be due to variations in the cleaning technique used on the accelerometer head. The cleaning technique is now standardized to eliminate that possible problem.

Statistics are also poor for a given particle size because a mixture of sizes (10 - 100 μm) was employed. In order to eliminate this problem as well as simplify the counting procedure, the availability of closely sized beads is being investigated. The test plan (Table 4-1) has been changed to reflect this goal.

4.2.2 Meteoroid Impact Study

The meteoroid impact study logically consists of a series of analyses for different conditions and geometry, providing surface acceleration predictions, and an experimental verification task. The analyses have been completed and are reported below. No effort has been made in the test phase because a related experimental program is being conducted at LRC.

4.2.2.1 Meteoroid Impact Analysis. Meteoroid impact on a surface is an extremely complicated phenomenon. Involved are the surface and meteoroid melting, crater formation, shockwave propagation, plastic wave propagation, etc. Since the maximum surface acceleration and velocity outside the crater area (usually small compared to the total area subjected to significant excitation) are of main concern, the idealized model ignores the detail of crater formation and only elastic wave propagation is taken into account. In addition,

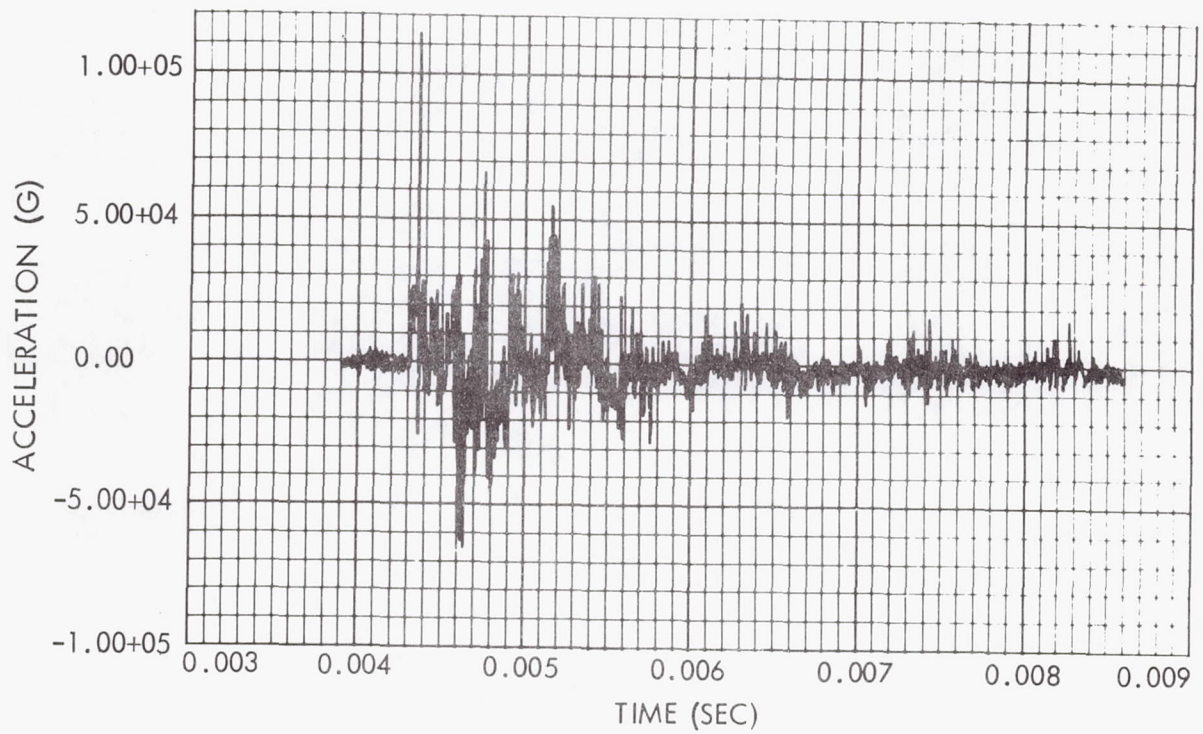


Fig. 4-2. Acceleration time history

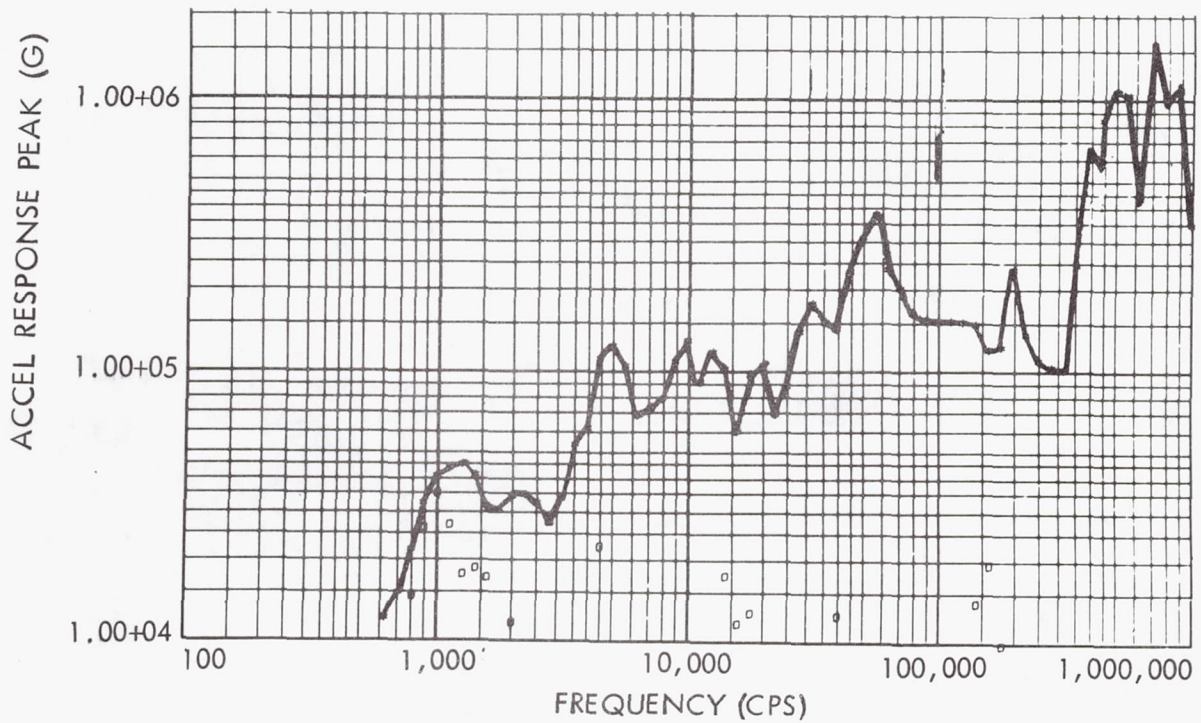
Fig. 4-3. Shock spectrum ($Q = 20$)

Table 4-3. Particle adhesion force model verification experiment (preliminary data)

Run No.	Ambient		Vacuum (Torr)	Peak acceleration (Gs)	Particle size (μm)	Particle count before	Particle count after	Percent removed
	T°F	R. H.						
18	70	37	4×10^{-3}	7,500	25	18	13	28
					60	2	1	50
19	70	37	2.5×10^{-3}	6,000	25	13	0	100
					40	5	0	100
					60	1	0	100
20	70	37	2.0×10^{-3}	24,000	25	23	0	100
					40	15	0	100
					60	9	0	100
					75	6	0	100
					100	2	0	100
21	75	42	1.8×10^{-4}	7,500	25	27	12	56
					40	21	3	86
					75	16	0	100
					90	6	0	100
					100	2	0	100
					110	2	0	100
22	75	42	3.2×10^{-3}	5,500	25	19	1	95
					40	14	0	100
					70	5	0	100
					90	9	0	100
					100	5	0	100
					110	3	0	100
23	75	42	6.8×10^{-5}	5,000	15	32	20	38
					25	51	14	73
					40	36	4	89
					60	5	0	100
					75	8	0	100
					90	2	0	100
					100	1	0	100

since available statistical data indicates a predominance of small meteoroids (implying small craters), the precise geometry of the struck surface is not important.

Since it is anticipated that the maximum acceleration and velocity will occur shortly after the impact as the result of outgoing waves (as opposed to the reflected waves from the boundary) the surface of the structure is considered infinite. It is further expected that a meteoroid impact at normal incidence will produce higher surface acceleration and velocity than other impacts. Hence, only the meteoroid impact at normal incidence will be considered.

Based on these assumptions, three idealized mathematical models, designated as Model I, II, and III, are given. Model I represents the semi-infinite solid with surface pressure loading; Model II, infinite plate with surface pressure loading (thin plate); and Model III, infinite punctured plate with shear loading (thin plate).

Given that the depth of the crater is of the same order as the crater diameter D , Model III holds when the ratio of D to the target thickness h is greater than unity. Model I holds when $D/h \ll 1.0$, and Model II covers the rest of the situation.

While the analytical solution for Model I may be found in the literature, the analytical solutions for Models II and III represent new technology. In this section, the models are described, the available analytical solution for Model I is summarized, and the new analytical solutions for Models II and III are presented.

For Model I, let a_0 be the radius of the surface pressure $P(t)$ and $W(r, t)$ be the surface displacement of a point at the distance r from the center of the loading. This problem has been solved by M. Mitra (Ref. 2) when the loading $P(t)$ is an impulse; i. e., $P(t) = \delta(t)$ for $r \leq a_0$.

With the application of Laplace and Hankel transform techniques and inversion by Cagniard's method, Mitra's results can be expressed, when the Poisson ratio $\nu = 1/4$, is as follows:

$$W(r, t) = \frac{-a_0}{\pi^2 \sqrt{G\rho}} \int_0^\pi \frac{r \cos \phi - a_0}{R^2} U(\tau) d\phi \quad (1)$$

where

ρ = density

G = shear modulus

$$R = (r^2 + a_0^2 - 2a_0 r \cos \phi)^{1/2}$$

$$\tau = \frac{t}{R} \sqrt{\frac{G}{\rho}}$$

$U(\tau)$ = algebraic function of τ (see Ref. 2 for detailed expressions)

The surface displacement $W(r, t)$ under impulsive loading for the case $\nu \neq 1/4$ has also been obtained by Mitra. However, the expressions and the numerical effort involved in computation are much more complicated than Eq. (1), and they are not given here (see Ref. 2).

The surface displacement $W^*(r, t)$ due to an arbitrary loading history $P(t)$ can be obtained from the convolution integral

$$W^*(r, t) = \int_0^t W(r, \xi) P(t - \xi) d\xi \quad (2)$$

In order to find the velocity $\dot{W}^*(r, t)$ and the acceleration $\ddot{W}^*(r, t)$, differentiation w.r.t. t may be performed.

Model II, the surface motion of an infinite plate under point loading, has been examined in detail, both analytically and experimentally, by Medick (Ref. 3) using the classical plate theory.

Good agreement has been observed between the analytical and experimental displacement-time history for the time $t > 2r/\sqrt{E/\rho}$ where E denotes the elastic modulus. The surface acceleration and velocity can be written in simple forms for special cases of loading history $P(t)$, such as a step function and a Dirac delta. Unfortunately, however, the analytical solution leads to an infinite acceleration at the time $t = 0$ for these cases. Since the maximum acceleration is expected to occur at small t , considerable error may be introduced by the classical plate theory if the loading function has discontinuities.

The same problem was solved by Miklowitz (Ref. 4) who used Mindlin's plate theory (Ref. 5). Unlike the classical plate theory, the Mindlin plate theory takes into account the shear deformation and the rotatory inertia. An immediate consequence is that the displacement $W(r, t)$ is zero before the P-wave arrives (see Ref. 4). In contrast, the classical plate theory predicts that $W(r, t)$ changes instantaneously with the impact since the velocity of shear wave is assumed to be infinite. Therefore, the Mindlin plate theory should lead to better results than the classical plate theory, as far as the velocity and acceleration are concerned.

In what follows, solutions for the surface loading over a circle of radius a_0 will be presented for both plate theories. It should be mentioned that if the velocity and acceleration are needed only in the far field zone; i. e., $r \gg a_0$, the solutions will be very close to those obtained under the point loading condition. However, since the maximum velocity and acceleration are expected to occur near the loading area, solutions must be obtained for the problem of loading over a finite area. The solutions are converted into the form of sine or cosine Fourier transform, so that the efficient method of Fourier transform technique, called FFT (Refs. 6 and 7) can be applied.

According to the classical plate theory, the transverse deflection $W(r, t)$ of a thin, homogeneous, isotropic elastic plate of thickness h and density ρ is governed by the equation

$$D \left(\frac{\partial^2}{\partial r^2} + \frac{1}{r} \frac{\partial}{\partial r} \right)^2 W(r, t) + \rho h \ddot{W}(r, t) = Z(r, t) \quad (3)$$

$$D = Eh^3/12(1 - \nu^2) \quad (4)$$

where

D is the plate stiffness

E is the Young's modulus

ν is the Poisson ratio.

The surface loading $Z(r, t)$ over a circle of radius a_0 is an impulse where E is the Young's modulus and ν is the Poisson ratio. The surface loading $Z(r, t)$ over a circle of radius a_0 is an impulse

$$\begin{aligned} Z(r, t) &= \delta(t)/\pi a_0^2 & r \leq a_0 \\ &= 0 & r > a_0 \end{aligned} \quad (5)$$

Let $\bar{W}(\xi, t)$ be the Hankel transform of $W(r, t)$ (Ref. 8); i.e.,

$$\bar{W}(\xi, t) = \int_0^\infty r J_0(\xi r) W(r, t) dr \quad (6)$$

where J_0 is the zero order Bessel function.

Multiplying by $r J_0(\xi r)$ on both sides of Eq. (3) and integrating from zero to infinity, one can obtain an expression for $\bar{W}(\xi, t)$. Then with the inverse Hankel transform and other appropriate transforms, the solution $W(r, t)$ can be written in form of Fourier sine transform

$$W(r, t) = \frac{1}{\pi a_0 \rho h} \int_0^\infty J_0\left(r \sqrt{\frac{\omega}{b}}\right) J_1\left(a_0 \sqrt{\frac{\omega}{b}}\right) \frac{\sin \omega t}{2\omega \sqrt{\omega b}} d\omega \quad (7)$$

$$= \frac{1}{2\pi a_0 \rho h} S_\omega \left[\frac{J_0(r \sqrt{\omega/b}) J_1(a_0 \sqrt{\omega/b})}{\omega \sqrt{\omega b}} \right] \quad (8)$$

in which $S_\omega [\]$ indicates the Fourier sine transform of the bracketed quantity and

$$b = D/2\rho h \quad (9)$$

By expanding $J_1(a_0 \sqrt{\omega/b})$ into a series and taking $a_0 \rightarrow 0$, one can easily show that the solution of Eq. (7) reduces to the closed form solution given in Ref. 2.

The governing differential equations of motion associated with the Mindlin plate theory (see Refs. 9 and 10) can be written as

$$\left(\frac{\partial^2}{\partial r^2} + \frac{1}{r} \frac{\partial}{\partial r} - \frac{1}{r^2} \right) \phi - v v_2^2 \phi - v v_2^2 \frac{\partial W}{\partial r} = \frac{1}{v_1^2} \ddot{\phi} \quad (10)$$

$$Z(r, t) + \left(\frac{\partial^2}{\partial r^2} + \frac{1}{r} \frac{\partial}{\partial r} \right) W + \left(\frac{\partial}{\partial r} + \frac{1}{r} \right) \phi = \frac{1}{v_2^2} \ddot{W} \quad (11)$$

in which $W = W(r, t)$ is the transverse displacement, and $\phi = \phi(r, t)$ is the rotation. The loading function $Z(r, t)$ is unchanged (Eq. (5)) and

$$\begin{aligned} v_1^2 &= \frac{E}{\rho(1 - \nu^2)} & ; & & v_2^2 &= \frac{K^2 G}{\rho} \\ V &= \frac{12}{h^2 v_1^2} & ; & & K^2 &= 0.76 + 0.3\nu \end{aligned} \quad (12)$$

where E , ρ , ν , G , and h are the same quantities as before.

Let $\bar{\phi}(\xi, t)$ and $\bar{W}(\xi, t)$ be the Hankel transforms of $\phi(r, t)$ and $W(r, t)$, respectively (see Eq. (12)). Multiplying Eqs. (10) and (11) by $rJ_1(\xi r)$ and $rJ_0(\xi r)$, respectively, and integrating from zero to infinity, one can solve for $\bar{\phi}(\xi, t)$ and $\bar{W}(\xi, t)$ in closed form. Then, with the Hankel inversion of $\bar{W}(\xi, t)$ and with appropriate transformations, $W(r, t)$ can be obtained as

$$\begin{aligned} W(r, t) &= \frac{1}{a_0 \pi} S_\omega \left[\frac{\left(v_1^2 \eta_1^2 + V v_1^2 v_2^2 - \omega^2 \right) J_1(\eta_1 a_0) J_0(\eta_1 r)}{v_1^2 \eta_1 \left(2\eta_1^2 - M^2 \omega^2 \right)} \right] \\ &+ \frac{1}{a_0 \pi} \bar{S}_\omega \left[\frac{v_2^4 J_0(\eta_3 r) J_1(\eta_3 a_0)}{\left(v_1^2 - v_2^2 \right) \left(\omega^4 + a^2 \omega^2 \right)^{1/2}} \right] \end{aligned} \quad (13)$$

in which $\bar{S}_\omega [\]$ indicates the Fourier transform from $\omega = V v_1 v_2$ to $\omega = \infty$, and

$$\begin{bmatrix} \eta_1 \\ \eta_3 \end{bmatrix} = \frac{M}{\sqrt{2}} \left[\omega^2 \pm N \sqrt{\omega^4 + a^2 \omega^2} \right]^{1/2} \quad (14)$$

where

$$\begin{aligned}
 M^2 &= \frac{v_1^2 + v_2^2}{v_1^2 v_2^2} \geq 0 \\
 N &= \frac{v_1^2 - v_2^2}{v_1^2 + v_2^2} \geq 0 \\
 a &= \frac{2 \sqrt{V} v_1^2 v_2^2}{v_1^2 - v_2^2} \geq 0
 \end{aligned} \tag{15}$$

The differential equations of motion for both the classical plate theory and the Mindlin plate theory are given, respectively, by Eqs. (3), (10), and (11). However, the difference in loading and boundary conditions makes it impossible to derive the solutions for Model III, infinite punctured plate with shear loading, from the solutions of Model II. In Model III, the loading function $Z(r, t)$ is zero and a_0 denotes the radius of the punctured hole.

For the Mindlin plate theory, the problem has been solved by Chou, et. al, by using the method of characteristics coupled with a finite-difference numerical procedure (Refs. 9 and 10). The general computer program is also available for the numerical computation of the displacement and velocity responses. With appropriate modifications, it is expected that the computer program that has been obtained, can be used to obtain the acceleration response. In this work, closed form analytical solutions for the frequency response function $\bar{W}(r, \omega)$ or impedance have been obtained. $\bar{W}(r, \omega)$ is related to the displacement $W(r, t)$ by

$$W(r, t) = \bar{W}(r, \omega) e^{-i\omega t} \tag{16}$$

where the shear loading is $e^{-i\omega t}$. The frequency response function $\bar{W}(r, \omega)$ is highly desirable since it provides information on the response at any frequency ω . The response $W^*(r, t)$ due to an arbitrary loading $P(t)$ can then be obtained by the complex Fourier inversion

$$W^*(r, t) = \frac{1}{2\pi} \int_{-\infty}^{\infty} \bar{W}(r, \omega) \bar{P}(\omega) e^{-i\omega t} d\omega \quad (17)$$

where $\bar{P}(\omega)$ is the complex Fourier transform of $P(t)$,

$$\bar{P}(\omega) = \int_0^{\infty} P(t) e^{i\omega t} dt \quad (18)$$

In the classical plate theory, the substitution of Eq. (16) into Eq. (3) obtains a solution for $\bar{W}(r, \omega)$ of the form

$$\bar{W}(r, \omega) = A_1 J_0(kr) + A_2 Y_0(kr) + A_3 I_0(kr) + A_4 K_0(kr) \quad (19)$$

where

J_j and Y_j are the j th order Bessel functions of the first kind and the second kind, respectively

I_j and K_j are the j th order modified Bessel functions of the first kind and the second kind, respectively

A_1 , A_2 , A_3 , and A_4 are arbitrary constants

and

$$k^4 = V\omega^2 \quad (20)$$

The boundary conditions at $r \rightarrow \infty$ are as follows:

- (1) the displacement should be finite; i. e., condition of finiteness.
- (2) there is no incoming wave, i. e.; condition of radiation.

Making an appropriate asymptotic expansion as $r \rightarrow \infty$ for Eq. (19) and applying the boundary conditions, one obtains

$$\bar{W}(r, \omega) = A_1 H_0(kr) + A_4 K_0(kr) \quad (21)$$

in which $H_0(r)$ is the zero order Hankel function, defined by

$$H_j(kr) = J_j(kr) + iY_j(kr) \quad (22)$$

The boundary conditions at $r = a_0$ are that the bending moment $M_r(a_0, t)$ is zero and shear force $Q_r(a_0, t) = e^{-i\omega t}$; i. e.,

$$M_r(r, t) = -D \left(\frac{\partial^2 W}{\partial r^2} + \frac{\nu}{r} \frac{\partial W}{\partial r} \right) = 0 \quad (23)$$

$$Q_r(r, t) = D \frac{\partial}{\partial r} (\nabla^2 W) = e^{-i\omega t} \quad (24)$$

Arbitrary constants A_1 and A_4 appearing in Eq. (21) are determined from the boundary conditions at $r = a_0$ with the results

$$A_1 = \frac{-1}{\Lambda k^3 D} \left[\frac{1-\nu}{\lambda_0} K_1(\lambda_0) + K_0(\lambda_0) \right] \quad (25)$$

$$A_4 = \frac{1}{\Lambda k^3 D} \left[\frac{1-\nu}{\lambda_0} H_1(\lambda_0) - H_0(\lambda_0) \right] \quad (26)$$

where

$$\lambda_0 = k a_0 \quad (27)$$

$$\Lambda = H_0(\lambda_0) K_1(\lambda_0) - K_0(\lambda_0) H_1(\lambda_0) - \frac{2(1-\nu)}{\lambda_0} K_1(\lambda_0) H_1(\lambda_0) \quad (28)$$

In the Mindlin plate theory, the differential equation of motion with which it is associated (Ref. 3) can also be written as

$$\frac{1}{v_1^2} \left(-v_1^2 \nabla^4 + \frac{\partial^2}{\partial t^2} \nabla^2 \right) W_b - v_2^2 \nabla^2 W_s = 0 \quad (29)$$

$$- \frac{\partial^2 W_b}{\partial t^2} + \left(v_2^2 \nabla^2 - \frac{\partial^2}{\partial t^2} \right) W_s = 0 \quad (30)$$

where

$$W(r, t) = W_b(r, t) + W_s(r, t) \quad (31)$$

Analogously to Eq. (16), one may write

$$W_b(r, t) = \bar{W}_b(r, \omega) e^{-i\omega t} \quad (32)$$

$$W_s(r, t) = \bar{W}_s(r, \omega) e^{-i\omega t}$$

The general solution can therefore be written as

$$\bar{W}_b(r, \omega) = A H_0(\eta r) \quad (33)$$

$$\bar{W}_s(r, \omega) = B H_0(\eta r)$$

The characteristic equations for the eigenvalues η , A and B can be obtained by substituting Eqs. (32) and (33) into Eqs. (29) and (30). Then

$$\bar{W}_b(r, \omega) = \sum_{j=1}^4 A_j H_0(\eta_j r)$$

and

$$\bar{W}_s(r, \omega) = \sum_{j=1}^4 A_j \phi_j H_0(\eta_j r) \quad (34)$$

in which A_j , $j = 1, 2, 3, 4$ are arbitrary constants to be determined by the boundary conditions and

$$\phi_j = -\frac{1}{v_2^2 V} \left(\frac{\omega^2}{v_1^2} - \eta_j^2 \right) \quad (35)$$

$$\eta_2 = -\eta_1 \quad \eta_4 = -\eta_3$$

where η_1 and η_3 are given in Eqs. (14) and (15).

With the application of the boundary conditions at $r \rightarrow \infty$; i.e., finiteness and radiation conditions, it can be shown that $A_2 = A_4 = 0$. The boundary conditions at $r = a_0$

$$M_r(r, t) = -D \left(\frac{\partial^2 W_b}{\partial r^2} + \frac{\nu}{r} \frac{\partial W_b}{\partial r} \right) = 0 \quad (36)$$

$$Q_r(r, t) = K^2 G h \frac{\partial W_s}{\partial r} = e^{-i\omega t}$$

allow A_1 and A_3 to be determined, with the results

$$A_1 = \frac{\eta_3^2}{K^2 Gh \Lambda} \left[H_0(\lambda_{30}) - \frac{1-\nu}{\lambda_{30}} H_1(\lambda_{30}) \right]$$

$$A_3 = \frac{-\eta_1^2}{K^2 Gh \Lambda} \left[H_0(\lambda_{10}) - \frac{1-\nu}{\lambda_{10}} H_1(\lambda_{10}) \right] \quad (37)$$

where

$$\lambda_{10} = \eta_1 a_0$$

$$\lambda_{30} = \eta_3 a_0$$

$$\Lambda = \eta_1^2 \eta_3 \phi_3 H_1(\lambda_{30}) \left[H_0(\lambda_{10}) - \frac{1-\nu}{\lambda_{10}} H_1(\lambda_{10}) \right]$$

$$- \eta_3^2 \eta_1 \phi_1 H_1(\lambda_{10}) \left[H_0(\lambda_{30}) - \frac{1-\nu}{\lambda_{30}} H_1(\lambda_{30}) \right] \quad (38)$$

Hence, it follows from Eq. (31) that the solution $\bar{W}(r, \omega)$ can be written as

$$\bar{W}(r, \omega) = A_1(1 + \phi_1) H_0(\eta_1 r) + A_3(1 + \phi_3) H_0(\eta_3 r) \quad (39)$$

4.2.2.2 Verification Test. The LRC test program has not as yet produced reportable results. When available, however, the LRC data will be used to obtain a general verification of the analyses discussed above.

The LRC experimental setup consists of two test chambers, a light gas gun, and an electrostatic firing device. These employ large and small projectiles, respectively, at speeds to 15 Km/sec. Particle removal as a

function of radius will be obtained as well as holographic data enabling released particle speed determinations to be made. The latter information is an essential adjunct to the data obtained from the particle adhesion force study.

4.2.3 Spaceflight Recontamination Analysis

The spaceflight recontamination analysis is intended to provide the probability for the transport of particles released during spaceflight. A complete analysis must consider the transfer probability from any surface area of the spacecraft to any other selected surface area. In general, such quantities depend on particle size, mass, and velocity of ejection. Since these latter parameters will be accounted for by distributions resulting from other areas of this program and other research, the analysis here has been concentrated on a deterministic calculation for specific values of them.

The calculation of the trajectory of a particle depends on the previously mentioned parameters plus the net force acting on it. Order of magnitude estimates of the forces, including gravitational, magnetic, electrostatic, and electromagnetic radiation, show that the electrostatic force is expected to dominate among the forces acting radially in the spacecraft particle reference frame (Ref. 11). The e-m radiation force is much smaller, but should be considered since it acts in the anti-Sun direction rather than radially. Fortunately, its value is known in terms of known parameters. On the other hand, the electrostatic force is a much more difficult problem, upon which the major effort in this area has been expended.

4.2.3.1 Surface Potential of Spacecraft. In order to determine the forces on a particle near the spacecraft, the potentials on the surface of the spacecraft must be determined. The analysis of this problem was discussed (Ref. 12). To calculate the potential of a surface it is necessary to know what portion of the surface is in the Sun and the angle with which the Sun's rays strike the surface.

A model spacecraft geometry has been previously defined (Ref. 13) to be used in the recontamination computer model. The model chosen has no curved surfaces because computer calculations are simpler when only flat surfaces are used. The model is made up of several polygons. Figure 4-4 shows this model in perspective.

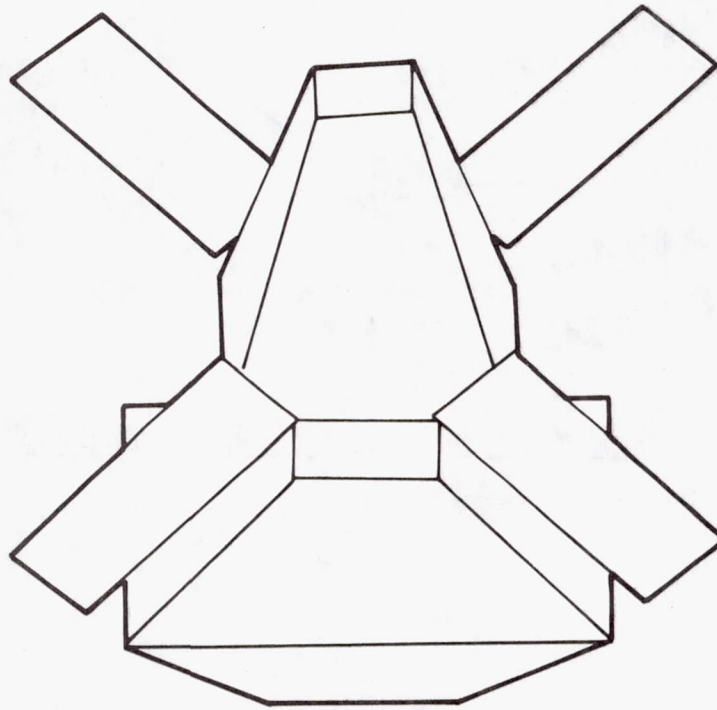


Fig. 4-4. Sample spacecraft geometry

The geometry of a typical spacecraft, even in simplified form is generally complicated enough to preclude the calculation of shaded portions by hand. A computer program was developed by Skladony and Rochkind (Ref. 14) to calculate the net thermal energy incident on a spacecraft by the determination of the projected area of a surface shaded by a number of other surfaces. The program computes the surface areas, total projected area, and net projected area (non-shaded portion) of a number of common geometrical surfaces. The projected area is the area of the object projected on a plane normal to the Sun, which is how the object would appear to the Sun (Fig. 4-5). The analytical procedure used is described in the article mentioned above. The program was obtained and then adapted to the Univac 1108 computer. It will become a subroutine in the overall recontamination analysis program.

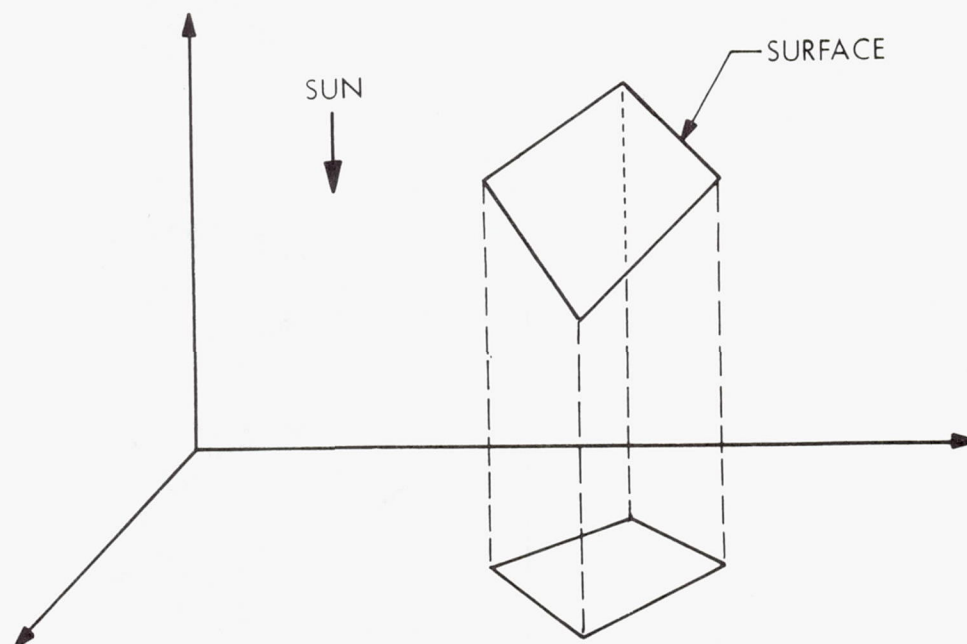


Fig. 4-5. Projected surface area

The equilibrium potential on the surface of the spacecraft may be determined (Ref. 12) by setting the sum of the input currents to a point equal to zero.

$$J_- + P(J_+ + J_p) = 0 \quad (40)$$

In Eq. (40), Ref. 12, J_+ and J_- are due to the ions and electrons in the solar wind plasma and are defined by the following equations:

$$J_+ = nev_0 \quad (41)$$

$$J_- = \frac{-ne\bar{v}}{4} \exp\left(\frac{\phi e}{kT_e}\right) \quad (42)$$

where

n = electron and ion density

e = electronic charge

v_0 = velocity of plasma

\bar{v} = average electron thermal speed

ϕ = potential

T_e = electron temperature

k = Boltzmann's constant

J_p is the photoelectron current and is obtained from empirical data in the form of a plot like the one in Fig. 4-6 (Ref. 15). When light of sufficiently short wavelength falls on a surface, electrons are emitted. This causes the surface to have a more positive potential. As shown in Fig. 4-6, the current resulting decreases rapidly as the surface potential becomes more positive. The photoelectric current is dependent on the surface potential as well as the surface material.

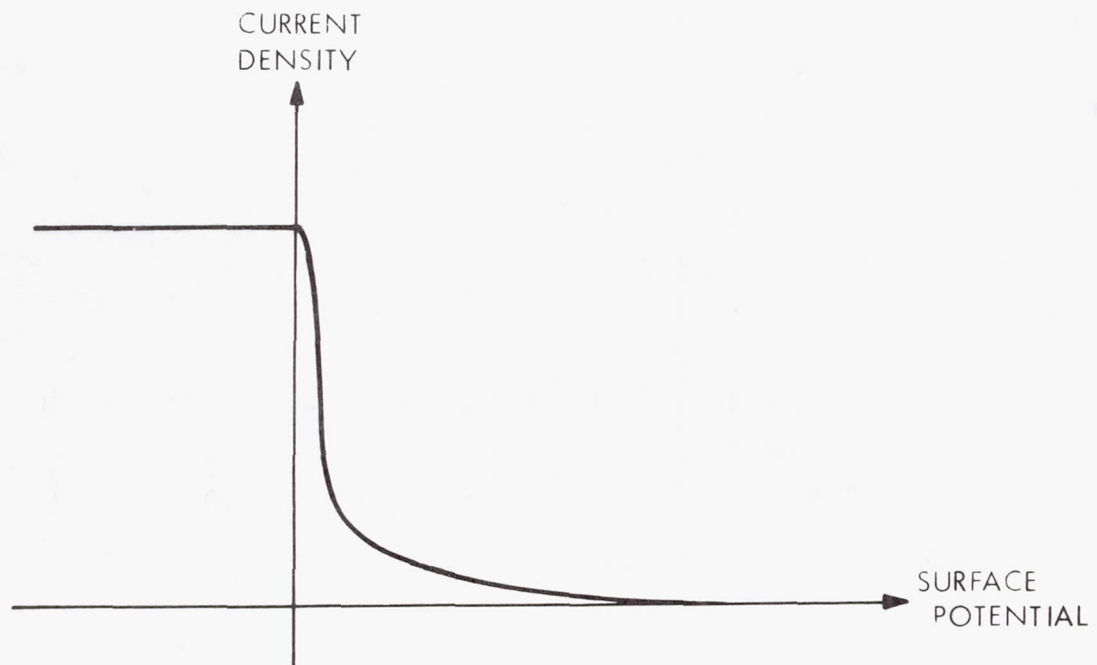


Fig. 4-6. Photoelectric current density

To calculate the surface potential, it is assumed that the photoelectron effect and the positive ion current J_+ can only occur in the nonshaded portions of the spacecraft. J_- , the electron current, is assumed to reach the entire spacecraft due to the higher thermal velocity of the electrons.

For conducting surfaces on the spacecraft, the resulting potential will be a constant over the entire connected conducting surface, including the shaded parts. The factor P in Eqs. (40) and (43) account for this by including both the percentage of the conducting surface in the Sun and the direction of the incident light on the surface. Equation (43) is derived from Eqs. (40), (41), and (42):

$$\phi = \frac{kT_e}{e} \ln \left\{ \frac{(J_p + nev_0)}{\frac{ne}{4} \bar{v}} P \right\} \quad (43)$$

A computer subroutine, SURPOT, computes ϕ based on the factor P for any surface. Any dielectric surfaces are assumed to be perfect non-conductors resulting in the same equation being applied to the separate regions of Sun and shade. In a shaded region, $P = 0$, and in a sunlight region, P is equal to the cosine of the Sun vector normal to the surface. Equation (43) cannot be solved when P goes to zero, so a limiting negative value for ϕ is chosen.

4.2.3.2 Particle Transport. Particles moving through space from one part of the spacecraft to another are also charged and have a surface potential. A particle leaving the spacecraft has a similar potential to that in the region of the spacecraft from which it left. Since there is a limit on the amount of charge a small particle can carry, the particle may not have a potential as great as that of the spacecraft. A maximum value has not been chosen as yet, but it could be much less than that of the spacecraft.

Particles change their surface potential at a given rate. The rate in the shade (Ref. 12) is

$$\frac{d\phi}{dt} = \frac{4\pi a^2}{4\pi a \epsilon_0} \cdot -\frac{nev}{4} \exp \left[\frac{\phi e}{kT_e} \right] = -\frac{nev a}{4\epsilon_0} \exp \left[\frac{\phi e}{kT_e} \right] \quad (44)$$

In the Sun it is

$$\frac{d\phi}{dt} = \frac{-4\pi a^2 \frac{ne\bar{v}}{4} \exp\left[\frac{\phi e}{kT_e}\right] + (nev_0 + J_p) \pi a^2}{4\pi a \epsilon_0} = \frac{-ne\bar{v}a}{4\epsilon_0} \exp\left[\frac{\phi e}{kT_e}\right] + \frac{(nev_0 + J_p)a}{4\epsilon_0} \quad (45)$$

until their respective charge limits are reached. The terms are defined in Table 4-1 except for "a" which represents the radius of the particle. These differential equations can be solved along with the equations describing the particle trajectory. Since there is a change in the sign of the charging rate as the particle moves from Sun to shade or shade to Sun, it would be desirable to restart the differential equation calculation at those points in the trajectory.

At each step of a particle's trajectory it must be determined whether the particle has hit the spacecraft or gone far enough away from it to be considered out of its influence. If a particle is within the vicinity of the spacecraft, then the particle is either in the sunlight or the shade of the spacecraft. Two subroutines, SHDHIT and CHKHIT, calculate this information. At the beginning of the program a third subroutine, INITSH, initializes information used in SHDHIT. INITSH increases computational efficiency by doing certain calculations once and storing the information for later use. The particle is tested with each surface polygon to determine if it is in the shade or has hit the spacecraft. A flowchart of this procedure is shown in Fig. 4-7.

The vector running from the origin of the spacecraft geometry system to the Sun is defined by input to the computer program and is called the Sun vector (Fig. 4-8, line A). The subroutine SHDHIT considers a line parallel to the Sun vector starting from the position of the particle (Fig. 4-8, line B). If that line is parallel to the plane of the polygon being tested, then the polygon of the plane could not possibly shade the particle.

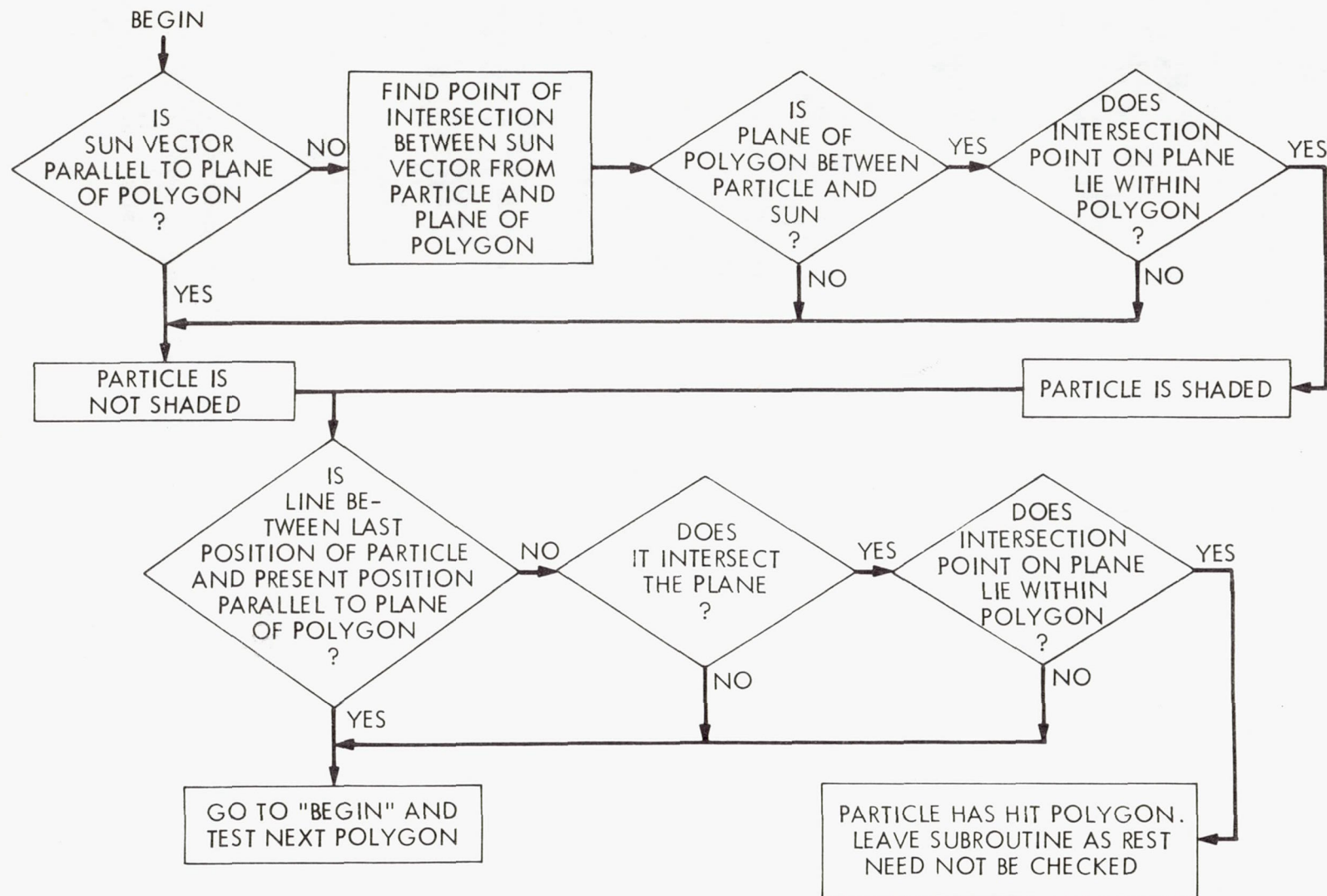


Fig. 4-7. Flow diagram of sun/shade and particle impact

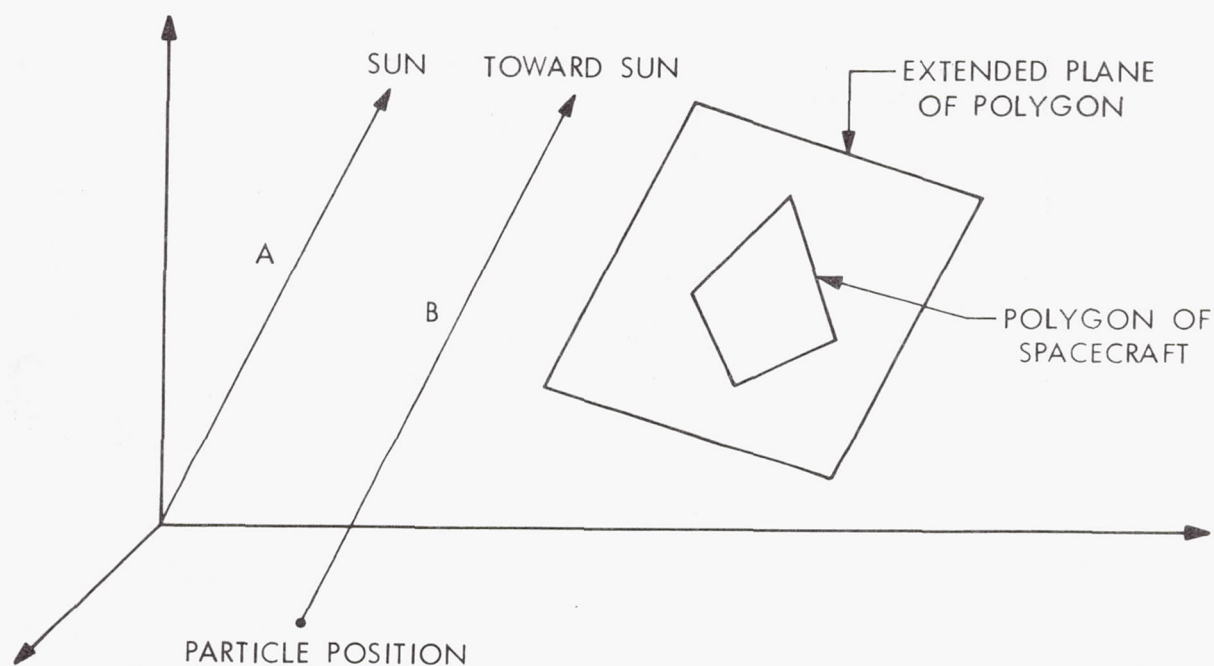


Fig. 4-8. Sun vector paralleled to polygon of spacecraft

When the line is not parallel to the plane of the polygon, its intersection point with the plane is found (Fig. 4-9). If the distance to the plane along the line from the particle is negative, the plane could not shade the particle (as at point D). If the distance is positive (as at point C), the intersection point is considered in CHKHIT to determine whether it lies in the polygon. If the intersection point is within the polygon, the particle is shaded.

To determine if a point on a plane lies within a polygon, the Cauchy integral formula is used. This is calculated by summing the angles between adjacent vectors from the point to each vertex of the polygon. The sum equals 2π when the point lies inside the polygon (Fig. 4-10).

Whether or not a particle is shaded, it must be tested for a possible "hit". First the line from the previous position of the particle to the present position is tested to determine if it is parallel to the plane of the polygon

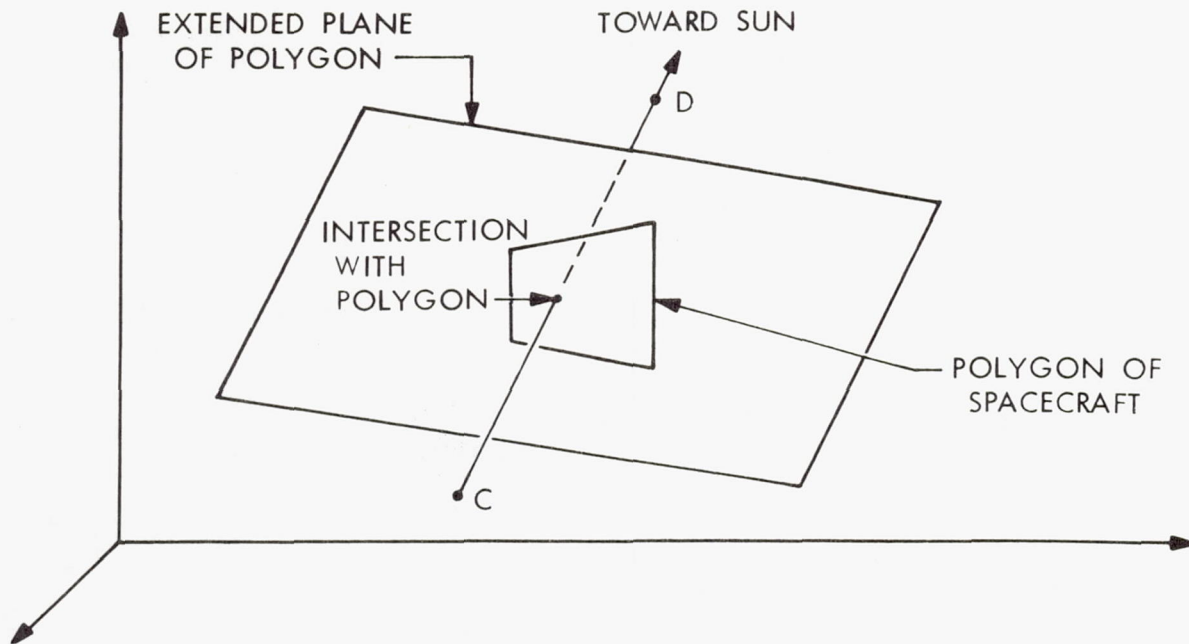


Fig. 4-9. Particles in the Sun and shade

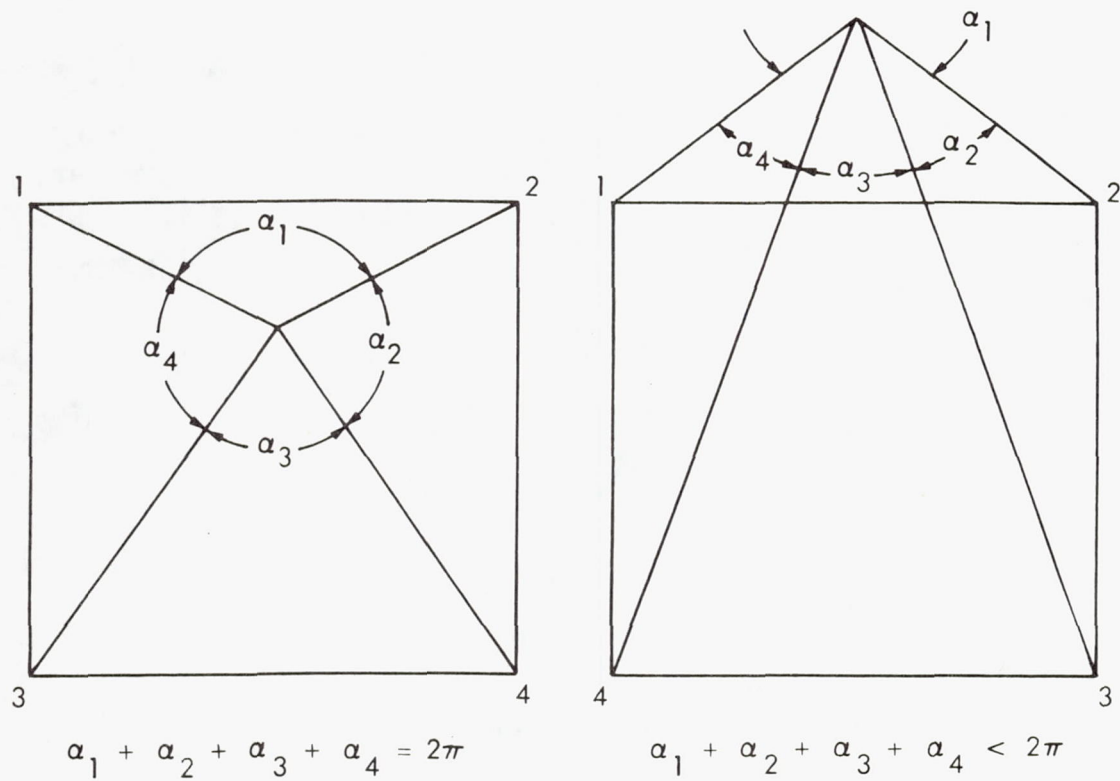


Fig. 4-10. Cauchy integral formula

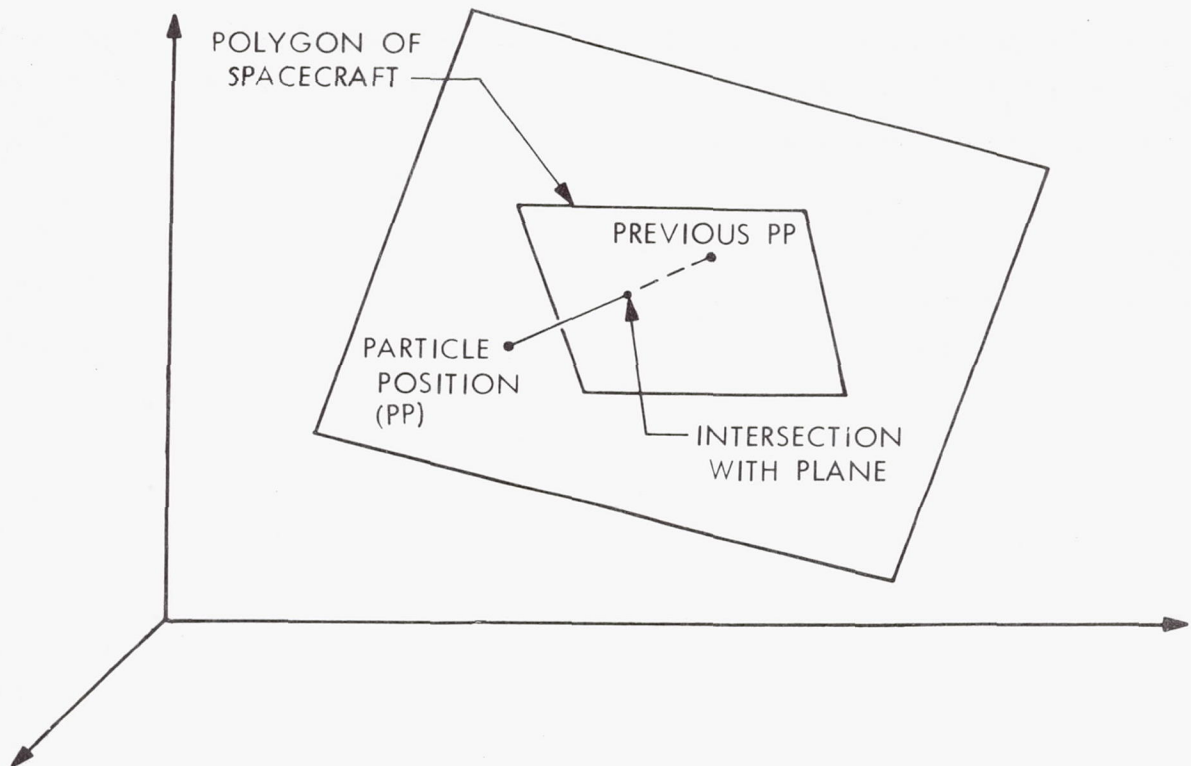


Fig. 4-11. Particle "hit" test

(Fig. 4-11). If not, then that line segment between the particle positions is tested to determine whether it intersects the plane. If it does, the intersection point is tested to determine whether it lies within the polygon. If all these tests are met, a "hit" has occurred.

The above subroutines check each polygon making up the spacecraft. Even if the particle is already shaded, the rest of the polygons must still be tested for a possible "hit".

The main program will trace the trajectory of a particle from the time it leaves the spacecraft until it either hits the spacecraft or leaves the vicinity of the spacecraft. A subroutine is available for the Univac 1108 to numerically integrate the differential equation of the trajectory.

4.3 FUTURE ACTIVITIES

The next year's effort will be to complete the analyses and tests currently underway, to resolve the problems and eliminate some of the approximations in them, to construct the results in a form suitable for the prediction

of the recontamination probability, to devise methods to relate the outputs of one subtask to the inputs of the next phase, and to integrate all of these components into a complete analysis package.

There are problems to be resolved in the particle adhesion force study, the meteoroid impact study, and the particle recontamination analysis. As mentioned previously, the poor statistics and data scatter in the particle release tests are expected to be improved by the use of closely sized beads. However, the surface cleaning parameter and the importance of the other physical parameters of the particles (such as material and shape) should be investigated. There is also reason to believe that the pre-shock humidity history may be more important than the humidity. The present model has no flexibility to account for this mechanism.

The meteoroid impact analyses must be converted into numerical solutions. Efficient numerical techniques employing fast Fourier transform are being developed. In addition, the computer program for Chou's method of characteristics and finite - difference numerical procedure (Ref. 10) is being tested to compare results with the Fourier analysis approach where possible. Finally, the gap between meteoroid impact parameters (mass, speed, and size) and the pressure history and crater diameter must be eliminated.

In the particle transport area, limiting bounds on surface potentials must be predicted, the photoelectric effect for spacecraft materials must be characterized, and the electric field in the vicinity of the spacecraft determined. The electric field is a complex theoretical problem which includes the spacecraft surface potential as only a part; the plasma of solar ions and electrons and photoelectrons form a sheath which must be considered.

By the end of the next year, a working deterministic recontamination analysis program will be completed. This code will then be exercised to determine parameter sensitivity, especially where approximations or assumptions were required.

4.4 PRESENTATIONS

Kazares, R. E., "Post Launch Recontamination Studies," presented at the NASA Semiannual Planetary Quarantine Technology Seminar, San Francisco, California, July, 1972.

REFERENCES

1. Haudenschild, C.; "Mathematical Model of Particle Adhesion Force to Surfaces"; IOM 2945-2152; March 9, 1971.
2. Mitra, M.; "Disturbance Produced in an Elastic Half-Space by Impulsive Normal Pressure"; Proc. Camb. Phil. Soc., Vol. 60; 683-696; 1964.
3. Medick, M. A.; "On Classical Plate Theory and Wave Propagation"; J. of Appl. Mech., ASME; 223-228; 1961.
4. Miklowitz, J.; "Flexural Stress Wave in an Infinite Elastic Plate Due to a Suddenly Applied Concentrated Transverse Load"; J. of Appl. Mech., ASME, Paper No. 60-APMW-11, 1960.
5. Mindlin, R. D.; "Influence of Rotatory Inertia and Shear on Flexural Motions of Isotropic, Elastic Plates"; J. of Appl. Mech., ASME, Vol. 18; 31-38; 1951.
6. Cooley, J. N., and Takey, J. W.; "An Algorithm for Machine Calculation of Complex Fourier Series"; Mathematics of Computation, Vol. 19; 297-301; 1965.
7. Krough, F. T.; "CFT--Multi-Dimensional Complex Fourier Transform"; Section 314 Subroutine Write-Up, Jet Propulsion Laboratory, Pasadena, California, October 1969.
8. Sneddon, I. N.; Fourier Transforms; McGraw-Hill, New York, 1951.
9. Chou, P. C., and Koenig, H. A.; "Flexural Waves in Elastic Circular Plates by Method of Characteristics"; NASA Contractor Report 69703, August 1965.
10. Mortimer, R. W. and Hoburg, J. F.; "MCDIT 21--A Computer Code for One-Dimensional Elastic Wave Problems"; NASA CR-13006, April 1969.
11. Haudenschild, Chris; "Order of Magnitude Analysis of Particle Force in Space"; IOM 171; July 6, 1971.
12. Haudenschild, Chris; "Spacecraft Surface and Ejected Particle Potentials in Space"; IOM 2945-71-46; October 12, 1971.
13. Bauerle, Charlotte; "Recontamination Analysis - Spacecraft Geometry"; IOM 120; March 30, 1972.
14. Skladany, Joseph T. and Rochkind, Allen B.; "Determination of Net Thermal Energy Incident on a Satellite"; Contributed by ASME for presentation at ASME-AICHE Heater Transfer Conference and Exhibit, Seattle, Washington, August 6-9, 1967.

15. Whipple, E. C., Jr.; The Equilibrium Electric Potential of a Body in the Upper Atmosphere and in Interplanetary Space; NASA X-615-65-296; 42; June 6, 1965.

900-597

SECTION V
SPACECRAFT MICROBIAL BURDEN
ESTIMATION AND PREDICTION

SECTION V

SPACECRAFT MICROBIAL BURDEN ESTIMATION AND PREDICTION

NASA No. 193-58-63-01

Cognizance: Alan R. Hoffman

Associate Personnel: D. Winterburn (Bionetics), R. Koukol,
B. Efron (Stanford U.)

5.1 INTRODUCTION

The objective of the spacecraft microbial burden prediction and estimation task is twofold: 1) to develop mathematical tools for estimation and prediction of microbial burden on spacecraft; and 2) to determine relationships and interactions between environmental data and spacecraft data.

This task is a follow-on for FY'72, which combined two tasks from the previous year: the Microbial Burden Prediction Model and Spacecraft Monitoring Methods and Procedures.

The approaches to meet the objectives are:

- 1) To complete the verification of the microbial burden prediction model and write a final report and User's Manual.
- 2) Analyze the Mariner '71 microbial data in order that bioburden estimation techniques from direct assays can be refined.
- 3) Correlate the environmental cleanliness and the spacecraft bioburden.

5.2 SIGNIFICANT ACCOMPLISHMENTS

5.2.1 Microbial Burden Prediction Model

The Mariner 71 microbiological data was used to update the environmental and initial burden histograms for the model. Good agreement between the predictions and direct bioassays has resulted (Fig. 5-1). A series of

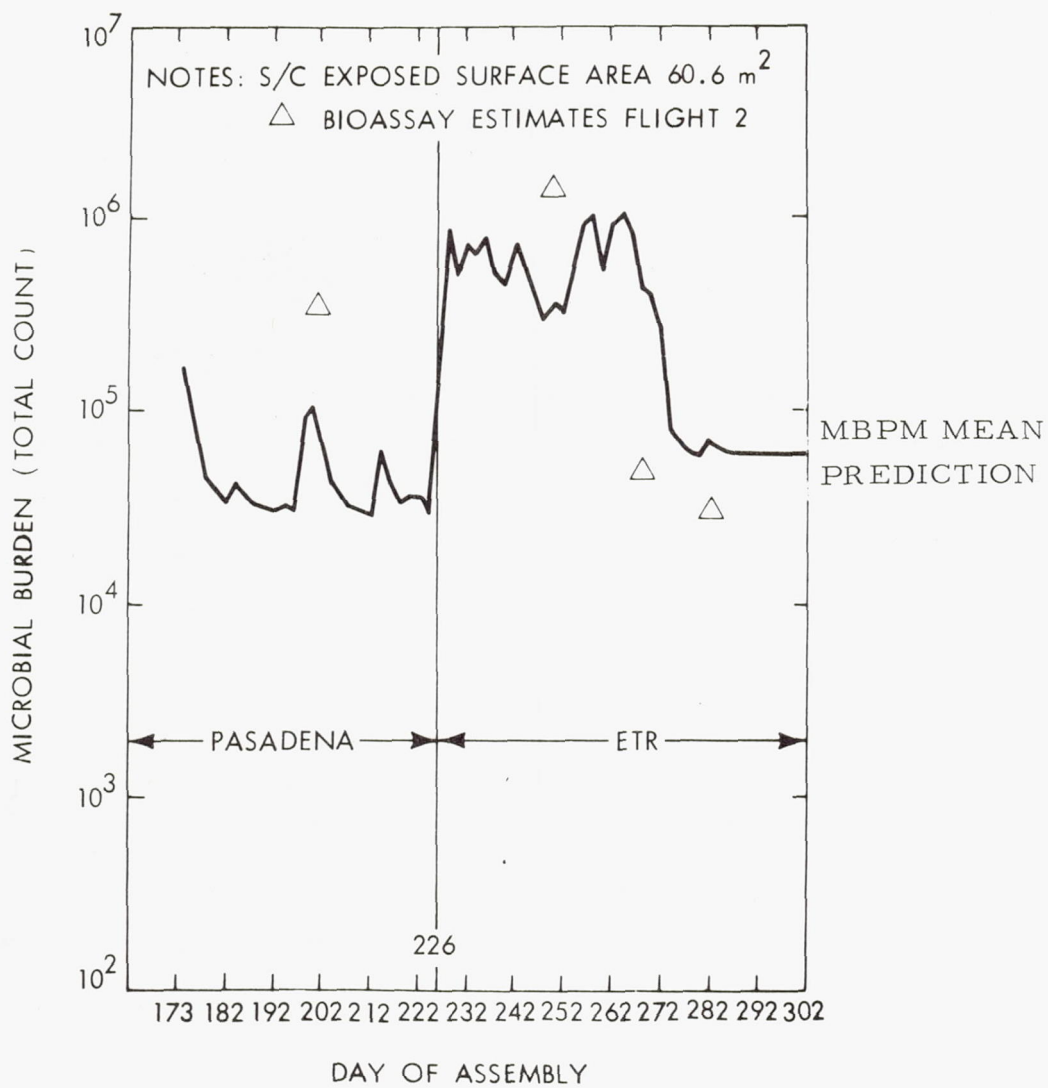


Fig. 5-1. Comparison between estimates and prediction - total count - Mariner '71-2

computer runs were performed to determine the increase in predicted burden when selected input parameters were increased by a factor of 10 (an order of magnitude). The parameters observed to be the most important input in affecting a change in the predicted burden were the average lifetime of an organism, and the environmental fallout in the facilities at the Air Force Eastern Test Range (AFETR). A final report detailing the technical development of the model has been published (JPL Report No. 900-566). A User's Manual is in publication.

5.2.2 Analysis of the Mariner '71 Microbial Data

The data gathered during the course of the Mariner 71 program was analyzed in detail during this reporting period.

The two hundred and fifty samples taken during each assay were broken down so that 43 were taken on the octagon structure; 13 on the High Gain Antennas; 40 on the Thermal Blankets (27 on Propulsion Blanket, 7 on Lower Blanket, 5 on Scan Platform Blanket, and 1 on the Rocket Engine Blanket); and the remaining 154 samples taken on two solar panels (36 on each front or cell side and 41 on each rear).

These specific number of samples were selected by prorating the percentage of total spacecraft surface area for each part to the total of 250 samples. These particular pieces of hardware were selected because they represent over 70% of the total spacecraft exposed surface area.

Table 5-1 shows the nonheat shocked colony counts for the assays performed on flight hardware. The chart shows the number of samples that had counts of zero, one, two, three, four, and five or larger. The total microbial count for samples showing five or more organisms are given.

The data on the Flight 1 spacecraft shows a consistent level of "zero" samples for the last 3 bioassays (Pre-shipment 2-12-71, AO Mechanical Prep 4-5-71, and Pre-Encapsulation 4-16-71, and 5-1-72 - 5-2-72). The large increase in "zero" counts from the Post Environmental Inspection (PEI) Assay and the decline in the number of counts 5 or larger, is possibly due to the cleaning of the spacecraft hardware during disassembly. The bioburden at

Table 5-1. Number of samples with given non-heat shocked colony count

Location		Flight 1				Flight 2				
		Pasadena		AFETR		Pasadena		AFETR		
Building		SAF	SAF	AO	ESF	SAF	SAF	AO	ESF	
Event		PEI	Preship	Mech Prep	Encap	PEI	Preship	Mech Prep	Encap 1	Encap 2
Date(s)		1/5/71	2/12/71	4/5/71	4/16/71 5/1/71 5/2/71	1/28/71	2/19/71	4/8/71	4/19/71 4/26/71	4/21/71 5/10/71 5/16/71
Colony Count	0	151	215	220	212	162	214	157	230	236
	1	40	27	19	22	46	9	29	16	12
	2	12	4	0	5	13	4	27	1	0
	3	7	2	6	4	4	3	3	0	0
	4	9	1	2	0	1	1	6	1	0
	≥5	31	1	3	7	24	16	28	2	2
	Values for Counts ≥5	195, 6, 21, 97, 6, 5, 7, 198, 7, 15, 7, 5, 16, 9, 5, 60, 62, 196, 84, 19, 41, 8, 7, 6, 9, 8, 16, 40 18, 6, 14	66	452, 5, 8	21, 7, 8, 5, 63, 11, 5	10, 5, 33, 22, 16, 8, 16, 6, 8, 9, 21, 14, 16, 21, 11, 8, 12, 6, 66, 48, 7, 6, 8, 91	7, 9, 7, 9, 11, 31, 12, 9, 9, 17, 5, 22, 7, 222, 71, 6	9, 8, 7, 5, 8, 6, 6, 5, 8, 5, 5, 5, 9, 7, 5, 8, 15, 8, 160, 12, 19, 58, 5, 1052, 100, 5, 7, 41	18, 18	18, 12
Total Number of Samples		250	250	250	250	250	250 (247 + 3 Lab Accidents)	250	250	250

the 1, 2, 3, and 4 colony levels also stayed at approximately the same level through the Air Force Eastern Test Range (AFETR) operations. There was an increase in the number of samples which recorded a count of 5 or larger. However, while these counts are more prevalent, the individual counts on the final Explosive Safe Facility (ESF) encapsulation assay are lower than in the other assays considered.

The Flight 2 data shows the same improvement as Flight 1 when the PEI assay (1-28-71) is compared with the Pre-shipment assay (2-19-71). The spacecraft bioburden did show an increase in the AO Mechanical Prep assay (4-8-71). This rapid increase showed the necessity of cleaning the hardware. The spacecraft was thoroughly cleaned before the first encapsulation assay. The large drop in burden and the large increase in the number of zero samples may indicate the effectiveness of the cleaning. The second ESF encapsulation assay was consistent with the results of the first.

Table 5-2 shows the heat shocked results for those assays performed on the flight hardware. The Flight 1 data indicates the low level contamination recorded. The Flight 2 data also reflects the low level of nonheat shocked organisms on the spacecraft throughout the program. The extremely low counts (only one organism each) for the two encapsulation assays, possibly reflect the intensive cleaning which occurred before these assays were performed. An extensive cleaning was implemented to offset the increase in microbial count detected on the AO Mechanical Prep assay (4-8-71).

Bacteria isolated from the flight spacecraft microbiological assays were identified by the United States Public Health Services Spacecraft Bioassay Unit at the AFETR (personal communication M. Favero). The resulting relative percentages as well as the genera of the organisms tested are given in Tables 5-3 and 5-4.

Figure 5-2 shows the spacecraft configuration during the first ESF encapsulation assay on Flight 2. Included in the picture is the back of one of the flight solar panels. A comparison of the sampling sites and associated microbial burden of a portion of the back side is also given.

The center portion of the solar panel as shown in Fig. 5-2 is represented schematically in Fig. 5-3. The random nature of the bacterial population is also shown in the drawings. An interesting situation arises in this comparison.

Table 5-2. Number of samples with given heat shocked colony count

		Flight 1				Flight 2				
Location		Pasadena		AFETR		Pasadena		AFETR		
Building		SAF	SAF	AO	ESF	SAF	SAF	AO	ESF	
Event		PEI	Preship	Mech Prep	Encap	PEI	Preship	Mech Prep	Encap 1	Encap 2
Date(s)		1/5/71	2/12/71	4/15/71	4/16/71 5/1/71 5/2/71	1/28/71	2/12/71		4/26/71	
Colony Count	0	223	244	246	247	226	233	211	249	249
	1	15	5	3	2	15	8	27	1	1
	2	3	1	0	0	5	4	5	0	0
	3	4	0	0	0	0	0	4	0	0
	4	4	0	0	0	1	1	1	0	0
	≥5	1	0	1	1	3	1	2	0	0
Values for Counts ≥5		7		306	17	88, 16, 55	8	6, 7		
Total Number of Samples		250	250	250	250	250	250 (247 + 3 lab accidents)	250	250	250

Table 5-3. Comparison of the numbers and types of microorganisms detected on Mariner-Mars 1971 spacecraft

Bacteria	Number	Percent
<u>Staphylococcus</u> spp.		
Subgroup I	1	0.2
Subgroup II	11	2.7
Subgroup III	5	1.2
Subgroup IV	7	1.7
Subgroup V	40	9.8
Subgroup VI	23	5.6
<u>Micrococcus</u> spp.		
Subgroup 1	2	0.5
Subgroup 3	1	0.2
Subgroup 6	1	0.2
Subgroup 7	1	0.2
Subgroup 8	1	0.2
<u>Bacillus</u> spp.		
<u>B. badius</u>	1	0.2
<u>B. brevis</u>	2	0.5
<u>B. cereus</u>	2	0.5
<u>B. circulans</u>	9	2.2
<u>B. coagulans</u>	17	4.1
<u>B. firmus</u>	12	2.9
<u>B. lentus</u>	5	1.2
<u>B. licheniformis</u>	5	1.2
<u>B. macerans</u>	12	2.9
<u>B. megaterium</u>	4	1.0
<u>B. polymyxa</u>	11	2.7
<u>B. pulvifaciens</u>	2	0.5
<u>B. pumilus</u>	1	0.2
<u>B. sphaericus</u>	3	0.7
<u>B. subtilis</u>	8	2.0

Table 5-3. Comparison of the numbers and types of microorganisms detected on Mariner-Mars 1971 spacecraft (contd)

Bacteria	Number	Percent
<u>Corynebacterium-</u> <u>Brevibacterium</u> Group	131	32.0
Actinomycetes	6	1.5
Yeasts	4	1.0
Molds	24	5.9
Atypical <u>Micrococcus</u> spp.	2	0.5
Atypical <u>Bacillus</u> spp.	52	12.7
No growth on subculture	4	1.0
Number Isolated	410	

Identification of microorganisms provided by USPHS Bioassay Unit at AFETR.

Table 5-4. Identification of heat shock cultures isolated from
Mariner-Mars 1971 spacecraft

Culture identification	Number	Percent
<u>B. brevis</u>	3	5.8
<u>B. circulans</u>	7	13.5
<u>B. coagulans</u>	3	5.8
<u>B. firmus</u>	5	9.6
<u>B. licheniformis</u>	2	3.8
<u>B. macerans</u>	3	5.8
<u>B. polymyxa</u>	2	3.8
<u>B. pulvifaciens</u>	1	1.9
<u>B. subtilis</u>	3	5.8
Atypical <u>Bacillus</u> spp.	14	26.9
Streptomycete	1	1.9
No growth on subculture	8	15.4
Number isolated	52	

Identification of microorganisms provided by USPHS Bioassay Unit at AFETR.

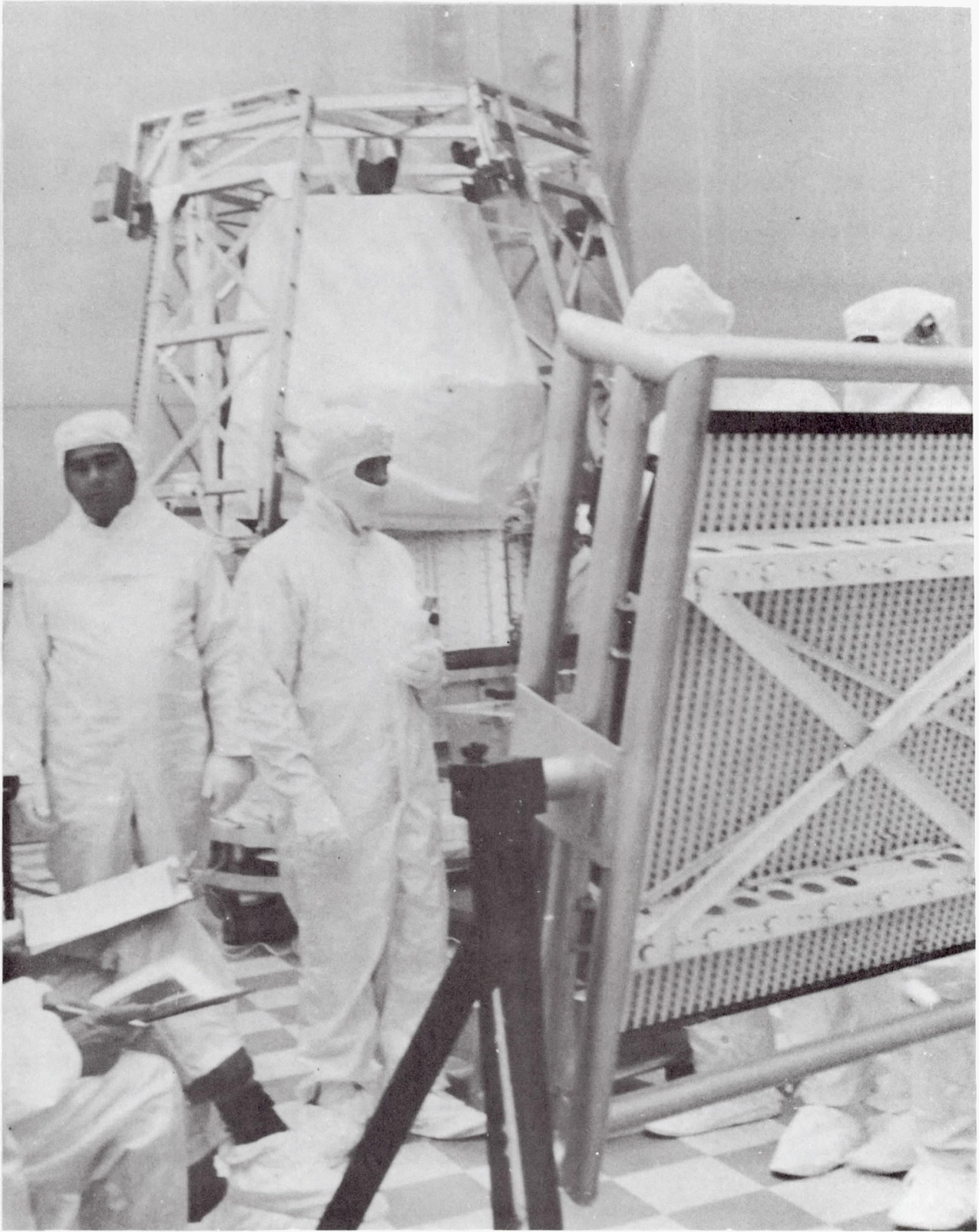
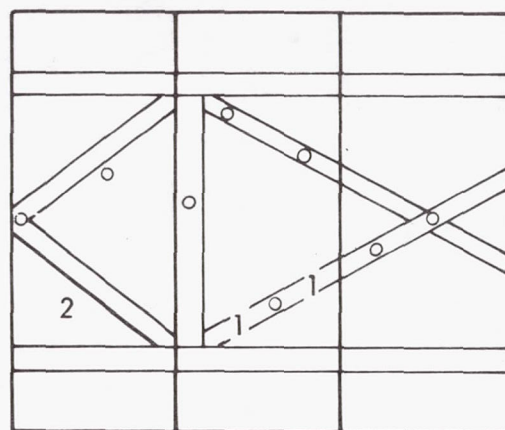
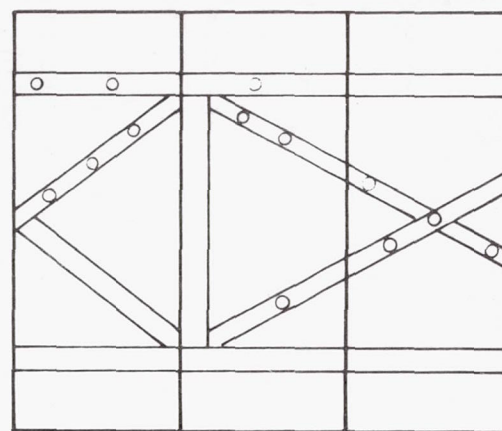


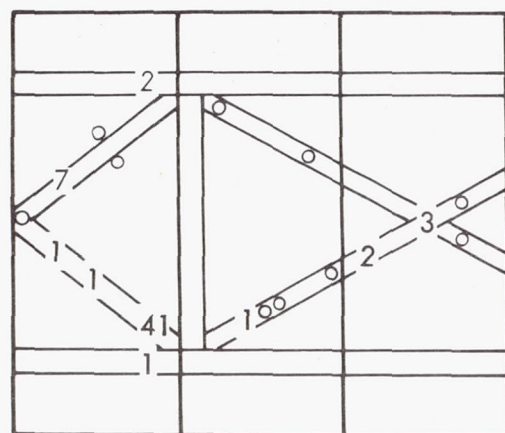
Fig. 5-2. Spacecraft configuration during first ESF encapsulation assay (Flight 2)



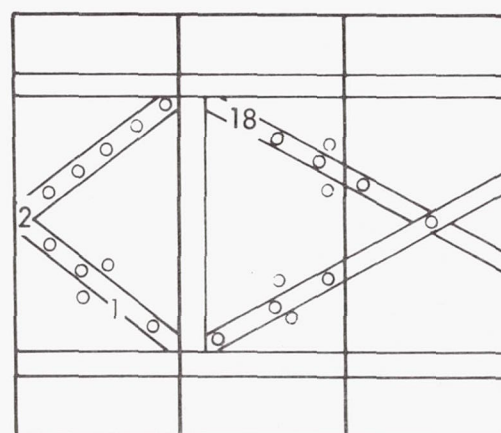
PEI 1/28/71



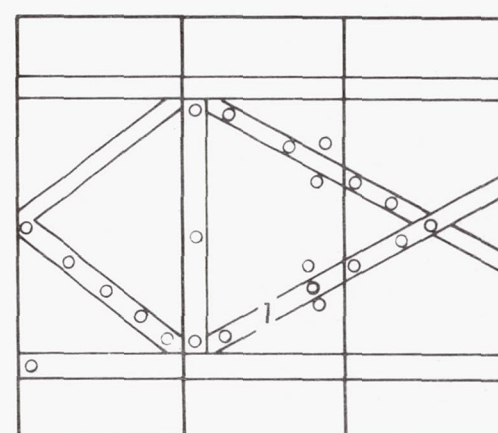
PRE-SHIP 2/19/71



AO MECH PREP 4/8/71



ENCAPS No. 1-4/26/71



ENCAPS No. 2-5/10/71

Fig. 5-3. Distribution of microorganisms on back of Mariner 71 panel

In the first three assays (PEI, Pre-ship, and AO Mechanical Prep), a count of zero is recorded in that area just to the upper right of the cross brace. In the first encapsulation assay, however, a count of 18 was recorded. Counts, such as this 18 and 41 which was recorded during the AO Mechanical Prep assay, bring up the possibility of clumping.

Clumping refers to the grouping of organisms in a specific spot or sample, which is surrounded by counts of very low numbers or zeros. A more extreme example of the clumping phenomena occurred in the sampling of the solar panel cell; i.e., front side (Fig. 5-4). One sample in column C depicts a count of 160 colonies surrounded by counts of zero. The actual sampling of a flight solar panel is shown in Fig. 5-5. It is apparent that these large counts are real data. Thus with the large size of the solar panels in relation to the total area of the spacecraft, the necessity of maintaining a low level of contamination is shown.

The results of the environmental monitoring are shown in Figs. 5-6 through 5-12. Figures 5-6 and 5-7 show the mean particle level in the Spacecraft Assembly Facility (SAF) as detected by the Royco Particle sampler. Figures 5-8 and 5-9 show the microbial level recorded in SAF through the use of Reyneirs. Figures 5-10 and 5-11 show both the nonheat and heat shocked results recorded per week in SAF using the fallout strips. Figure 5-12 is a composite graph showing the interrelationships between the two types of Millipore data and the fallout strips. This data was collected during the AFETR operations.

Dr. Bradley Efron, a consultant from Stanford University, assisted in the analysis and interpretation of the data (Appendix A). His report details these significant conclusions: 1) the large colony counts which appear infrequently in the data are real and are not artifacts of the assay procedures; 2) the compound Poisson model does not fit the Mariner 71 data very well; and 3) the arithmetic mean is not necessarily a very good estimator for spacecraft burden estimates.

During the entire MM 71 Program, environmental samples were taken to try and correlate spacecraft bioburden with total particulate sizes and quantity as well as biological particles.

[illegible]

Fig. 5-4. Solar panel front raw count distribution
Flight 2, panel all samples

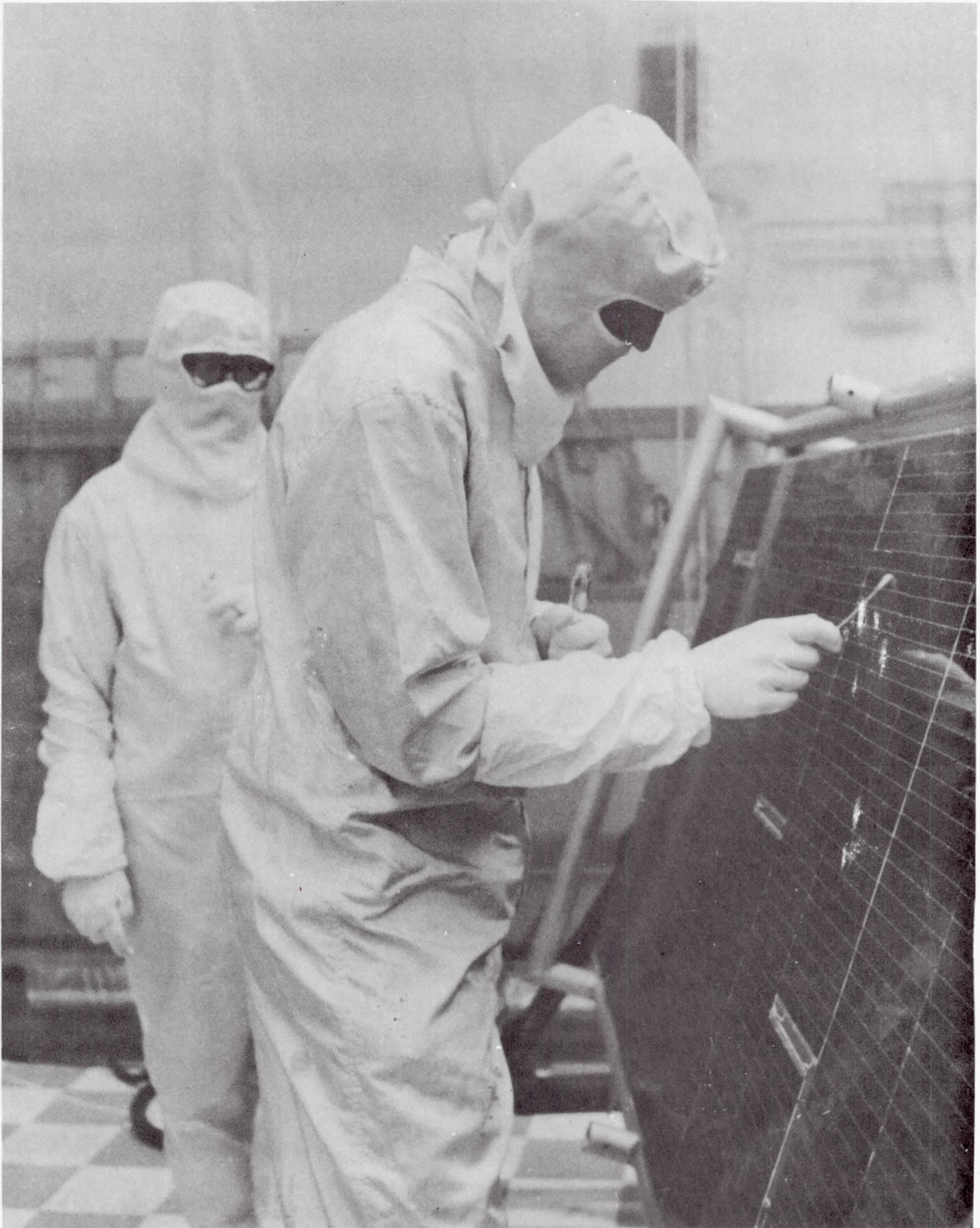


Fig. 5-5. Sampling of flight solar panel

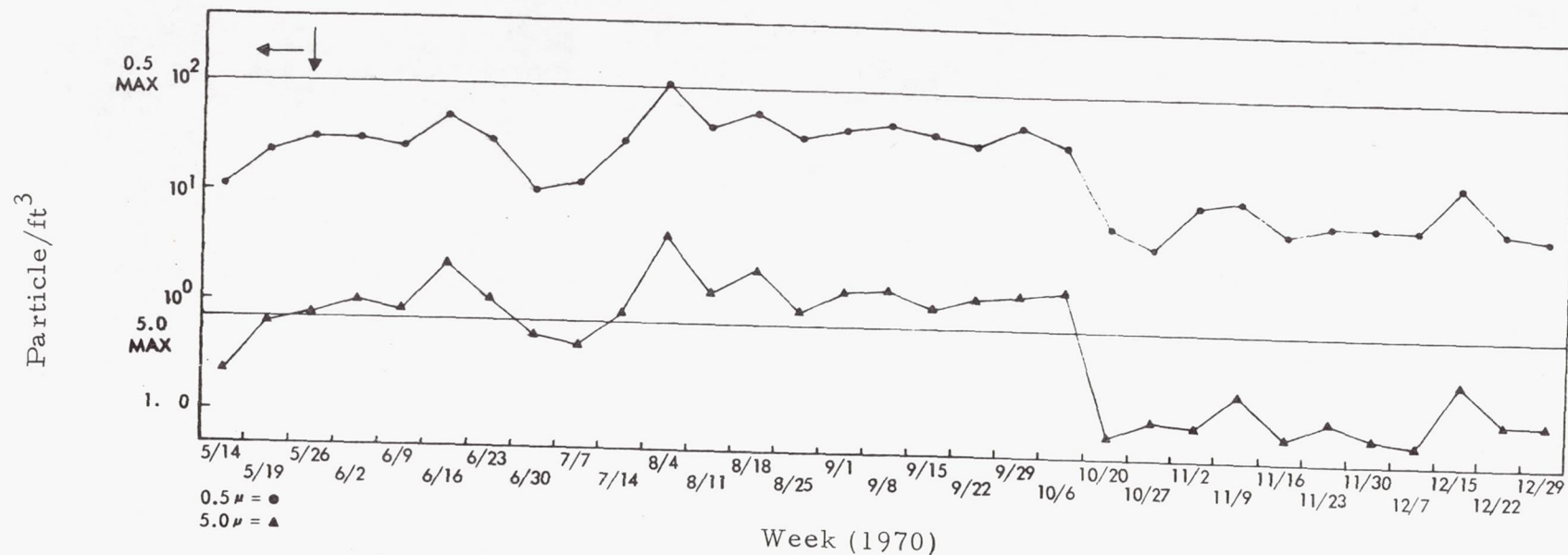


Fig. 5-6. Mean particle levels in SAF high bay. Particle/Ft³/Week

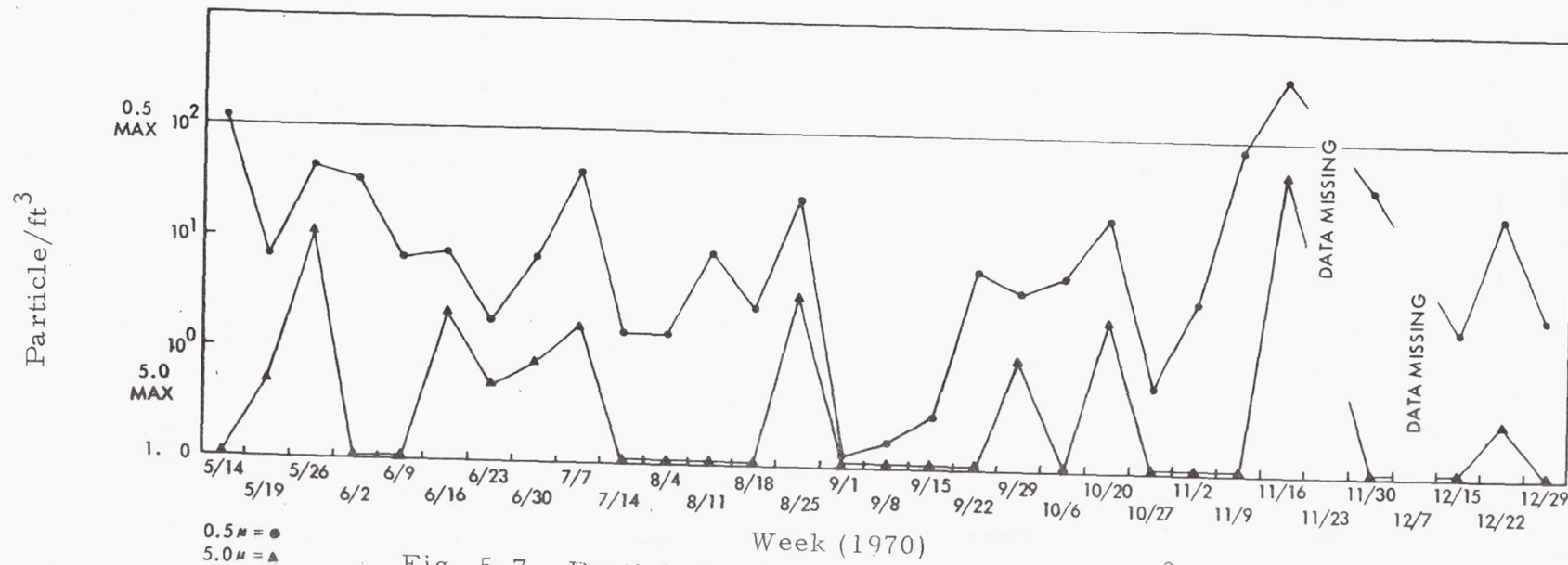


Fig. 5-7. Particle level in SAF tent. Particle/Ft³/Week

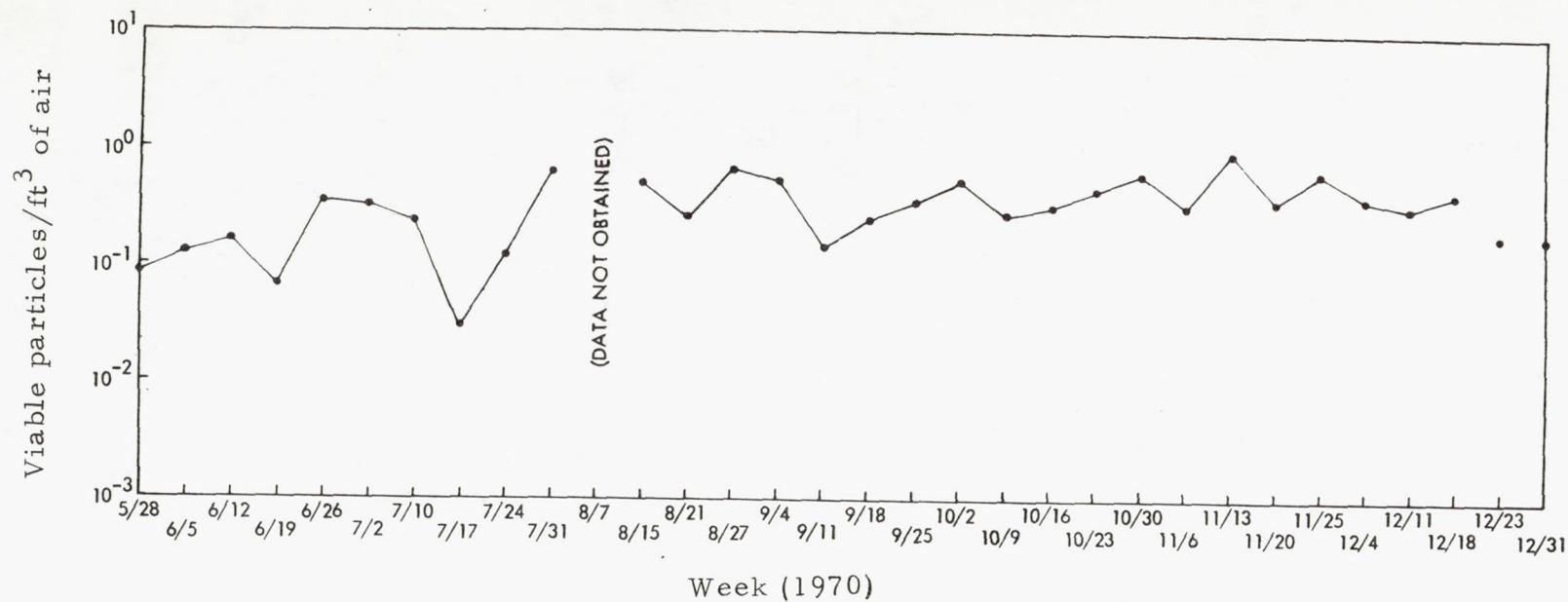


Fig. 5-8. Reyneirs tent, high bay. Viable particles/ft³ of air/week

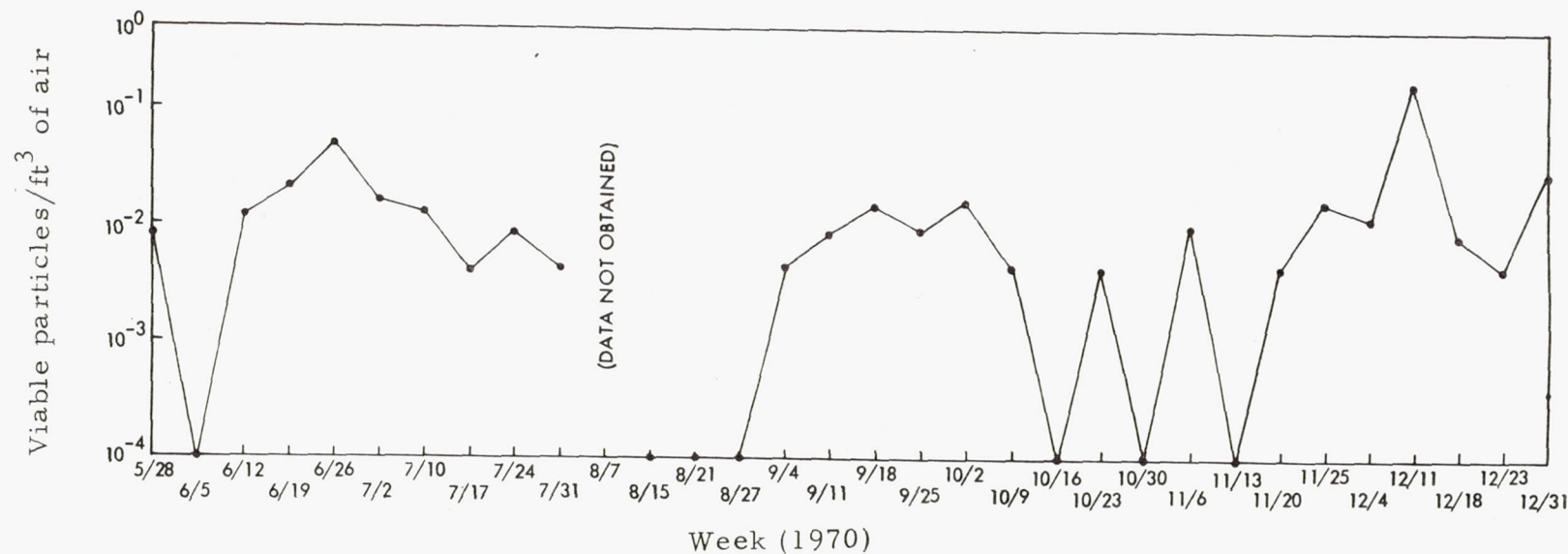


Fig. 5-9. Reyneirs tent. Viable particles/ft³ of air/week

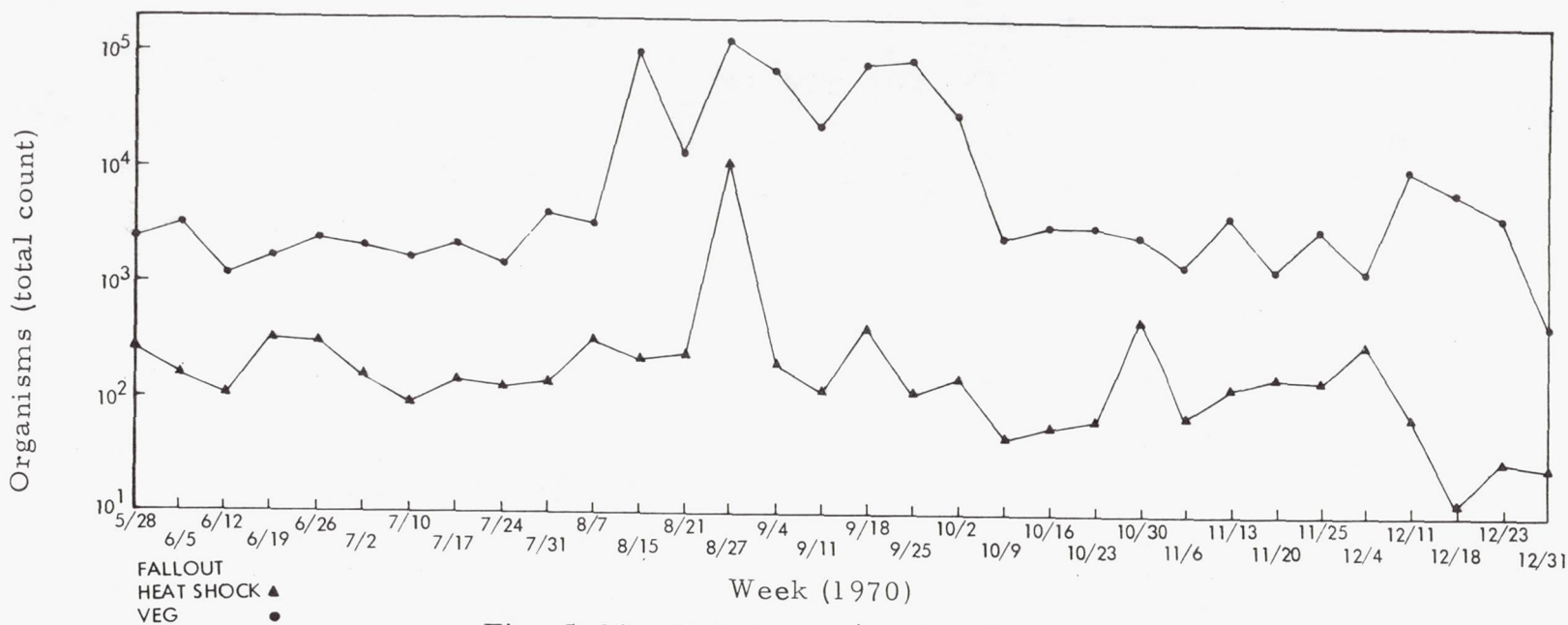


Fig. 5-10. Total count/week in high bay

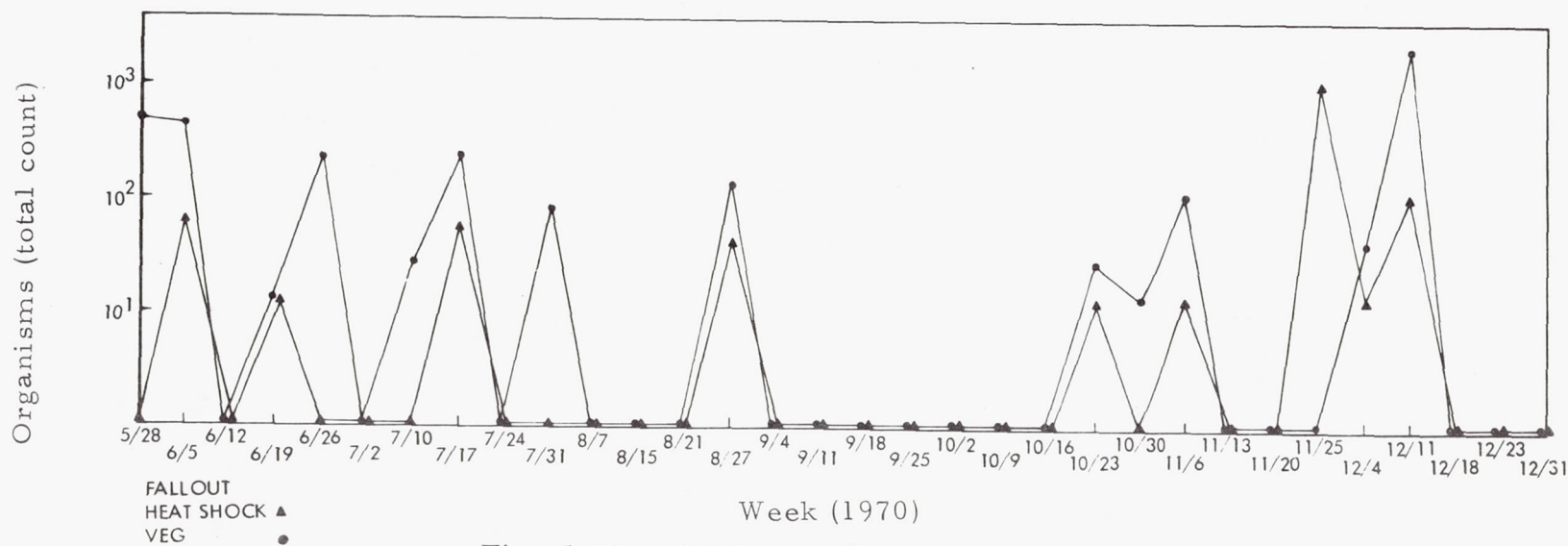


Fig. 5-11. Total count/week in SAF tent

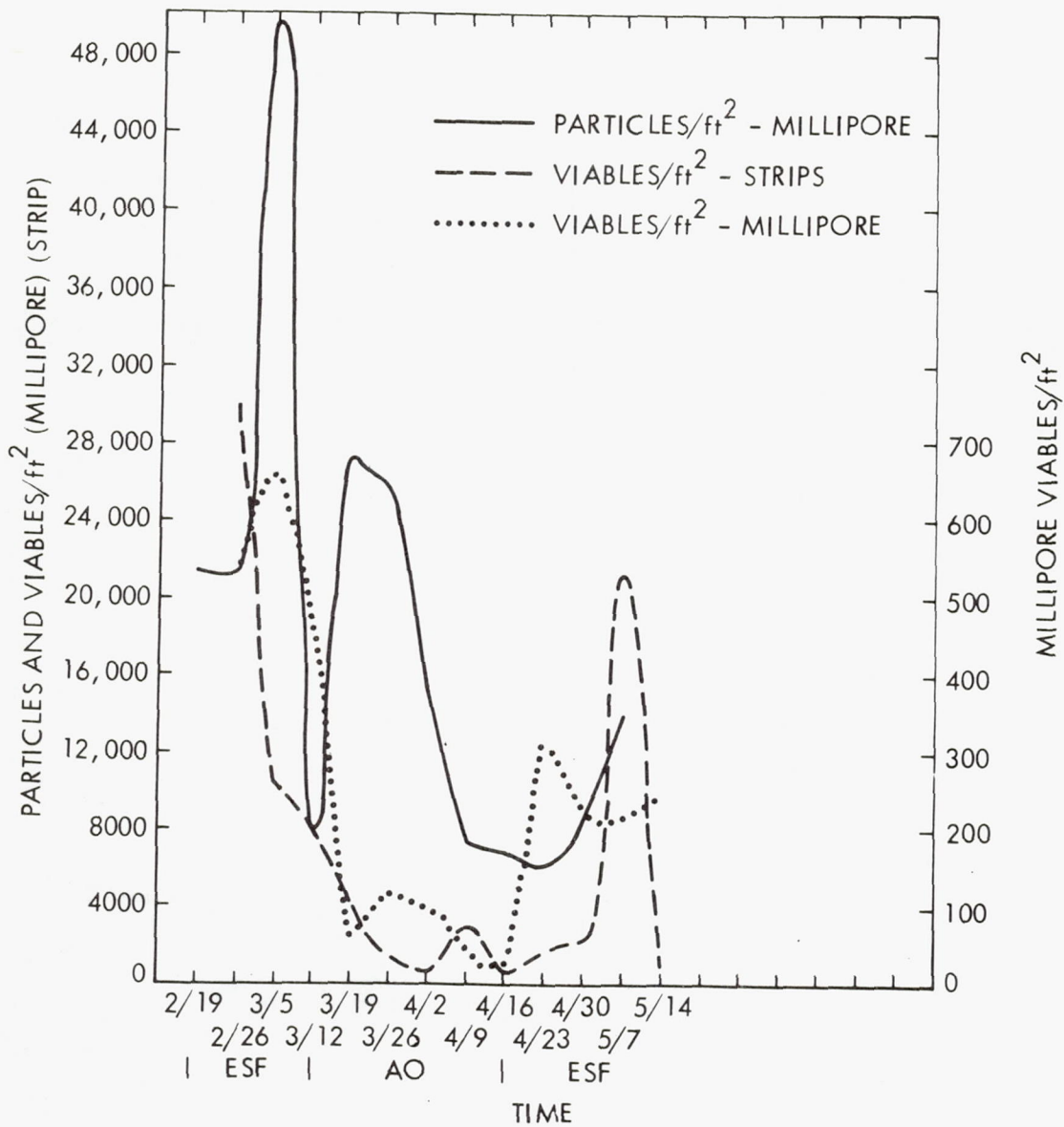


Fig. 5-12. Relationship between viable and nonviable environmental fallout data.

During both the Pasadena and AFETR operations, the Millipore field monitors and fall-out strips were taken once a week (Friday). The Royco and Reyneir data were taken twice a week (Tuesday and Thursday).

The environmental data (Fig. 5-12) does not show any consistent correlation between the viable and nonviable fallout data.

The data from AFETR operations reinforces the data gathered during Pasadena operations.

5.3 PROBLEM AREAS

The analysis of the Mariner 71 microbiological data indicated that it will be very difficult to establish a functional relationship between environmental data and spacecraft data. In Appendix A, Dr. Efron proposes some follow-up work to obtain insight into this problem.

5.4 FUTURE ACTIVITIES

No further activities are planned under this task.

5.5 PUBLICATIONS

Hoffman, A. R., and Winterburn, D. A., "Microbial Burden Prediction Model for Unmanned Planetary Spacecraft (Final Report), " JPL Report 900-566, June 30, 1972.

Winterburn, D. A., "Microbial Burden Prediction Model for Unmanned Planetary Spacecraft, Users Manual" (in publication).

5.6 PRESENTATIONS

Hoffman, A. R., "Spacecraft Microbial Burden Estimation and Prediction, " presented at the NASA Semiannual Planetary Quarantine Technology Seminar, Cape Kennedy, Florida, January, 1972.

900-597

SECTION VI
SPACECRAFT CLEANING
AND
DECONTAMINATION TECHNIQUES

SECTION VI

SPACECRAFT CLEANING AND DECONTAMINATION TECHNIQUES

NASA No. 193-58-63-02

To maintain the detailed scopes of this task, Section VI is discussed as four individual subtasks under four distinct subsections designated as paras. 6.1, 6.2, 6.3, and 6.4, respectively. Each paragraph corresponds to the subtask number and title listed below.

<u>Subtask</u>	<u>Title</u>
I	Mechanical Removal of Spacecraft Microbial Burden
II	Thermal Resistance of Microbial Populations Occurring in Spacecraft Assembly Areas
III	Verification of USSR Hydrogen Peroxide Decontamination Data
IV	Plasma Cleaning and Decontamination Techniques

SUBTASK I

MECHANICAL REMOVAL OF SPACECRAFT MICROBIAL BURDEN

Cognizance: H. W. Schneider

Associate Personnel: R. Gildersleeve (Bionetics)

SUBTASK I

MECHANICAL REMOVAL OF SPACECRAFT MICROBIAL BURDEN

6.1.1 INTRODUCTION AND SCOPE

The primary objective of this study is to establish guidelines for the design of mechanical cleaning tools that are capable of controlling spacecraft microbial burden by removing viable particles from exposed surfaces. The effort is primarily concentrated on the use of aero or gas dynamical, and on physical mechanical actions (brushes) to detach and to remove particulates from the surface. Potential means to decrease particle adhesion prior to or during cleaning, will also be investigated.

The principal difficulty with decontaminating spacecraft structures is providing feasibility through final assembly without impairing the functional integrity of the spacecraft structures or any of its components. A most critical condition exists if a final biological cleaning should be necessary to meet the planetary quarantine requirements prior to encapsulation. Then the propellants and pressurants have been loaded, the pyrotechnics installed, and all systems electrically connected. Operations within the facility are governed by stringent electrical and explosive safe requirements. Schedules are usually restricted during this time and constrain further decontaminating corrective. For these reasons, spacecraft engineers are extremely conservative in approving any decontamination.

As a general rule, only decontamination methods that are compatible with all surfaces are eligible. When the liquids are used, all surfaces that may potentially come in contact with the liquid and its vapors due to spill, capillary action, diffusion, or condensation, are to be considered for compatibility. Unfortunately, effective sporicidal liquids and gases such as ethylene oxide, are not compatible with many surfaces used on present generation spacecraft, and thus, do not meet the above requirements. Wiping selected areas with isopropyl is being applied, but this also has to be used selectively because the vapors released may potentially degrade certain printed circuitry aboard the spacecraft.

Cold plasma techniques have proven successful in restoring the reflective and optical properties of thermal surfaces and of lenses, and, at the present time, are being studied with regard to their biological effectiveness. Since organic materials are used on present generation spacecraft, such techniques may not be feasible for the cleaning of assembled hardware. Thus, it follows that there exists a strong dependence on particulate cleanliness and cleaning to control microbial burden.

Although a general relation between microorganisms and particulate matter has not been cohesively determined, it can be reasonably assumed, based on past spacecraft experience, that particulate cleanliness is a prerequisite for biological cleanliness. Indications are that a particulate cleaning to the ten micron size or less is necessary to effect an efficient burden reduction on a surface with microbial burden density. An increasing demand for a particulate cleanliness on the same order also exists because of the growing size of space hardware. If contamination control constraints become more stringent, the large size spacecraft mean more particles may be present which potentially can interfere with spacecraft functions. Particulate interferences during flight - already a problem in earlier missions - may well become a major problem leading to a loss of mission objectives or a total failure if the particulate load per unit area can not be reduced.

The particulate cleaning method in use is a low vacuum cleaning with cup-type brushes capable of removing visible dust of approximately 50 μm sizes or larger. The brushes contaminate quickly and become a shedding source if not cleaned frequently. Sable hair is the only brush material approved for the cleaning of large area contributors to the microbial burden, such as the solar panels, thermal surfaces, and dish-antennas. Also, the brushes in existence are not compatible with heat sterilization procedures.

Design changes of the existing equipment have introduced some improvement involving the shedding and flow-clogging of the brushes. But the potential for improving the removal capability of smaller particle size ranges is practically exhausted. Completely new and fundamental approaches have to be taken to develop a 10 μm level (or less) cleaning capability. The mechanical removal of one micron spore-size particle is the far goal of this effort.

6.1.2 APPROACH

6.1.2.1 Test Apparatus

For study purposes, a device called a vacuum flow simulator (Fig. 6.1-1) was designed to simulate the mechanical removal of particulates in a controllable and repeatable manner, while observing the behavior of the particulates under a 100 x microscope. The device was described in detail in the previous program report (900-556). The vacuum flow simulator was installed in a laminar flow bench.

6.1.2.2 Experimental Techniques

6.1.2.2.1 Environmental Conditions. The air temperature and relative humidity existing at the laminar flow bench were measured before and after each daily working period. Both varied between 22 - 28° C and 40 - 45% RH, respectively, during the entire test period. The ambient atmospheric pressure varied between 730 and 734 mm Hg. The static pressure changes generated by the facility air conditioning system and the laminar flow bench itself were on the order of 1 - 2 mm H₂O.

6.1.2.2.2 Sample Preparation. Optical 50 x 50 mm glass slides proved to be most suitable because they had to cover the one inch diameter hole in the center of the stage, and still leave enough room for sealing and off-center movements in the sample plane. The slides were thoroughly cleaned with Freon TF, and wiped with 90% isopropyl alcohol prior to seeding. For the seeding with dust, the slides were vertically placed into a vacuum cleaner which was used for a prolonged time in a class 100,000 spacecraft facility. Seeding was then accomplished by switching the vacuum on for a short moment to stir the dust inside, which would then settle fairly evenly on the rack-mounted slides.

The dust in the vacuum cleaner was identified as 90% silicon materials, with the remainder approximately equal parts of non-magnetic and ferrus materials, cellulose, teflon, and some unidentified colored materials. (This composition is very representative of the type of contamination generated during spacecraft operations.) Glass beads were seeded by dipping a chromed metal

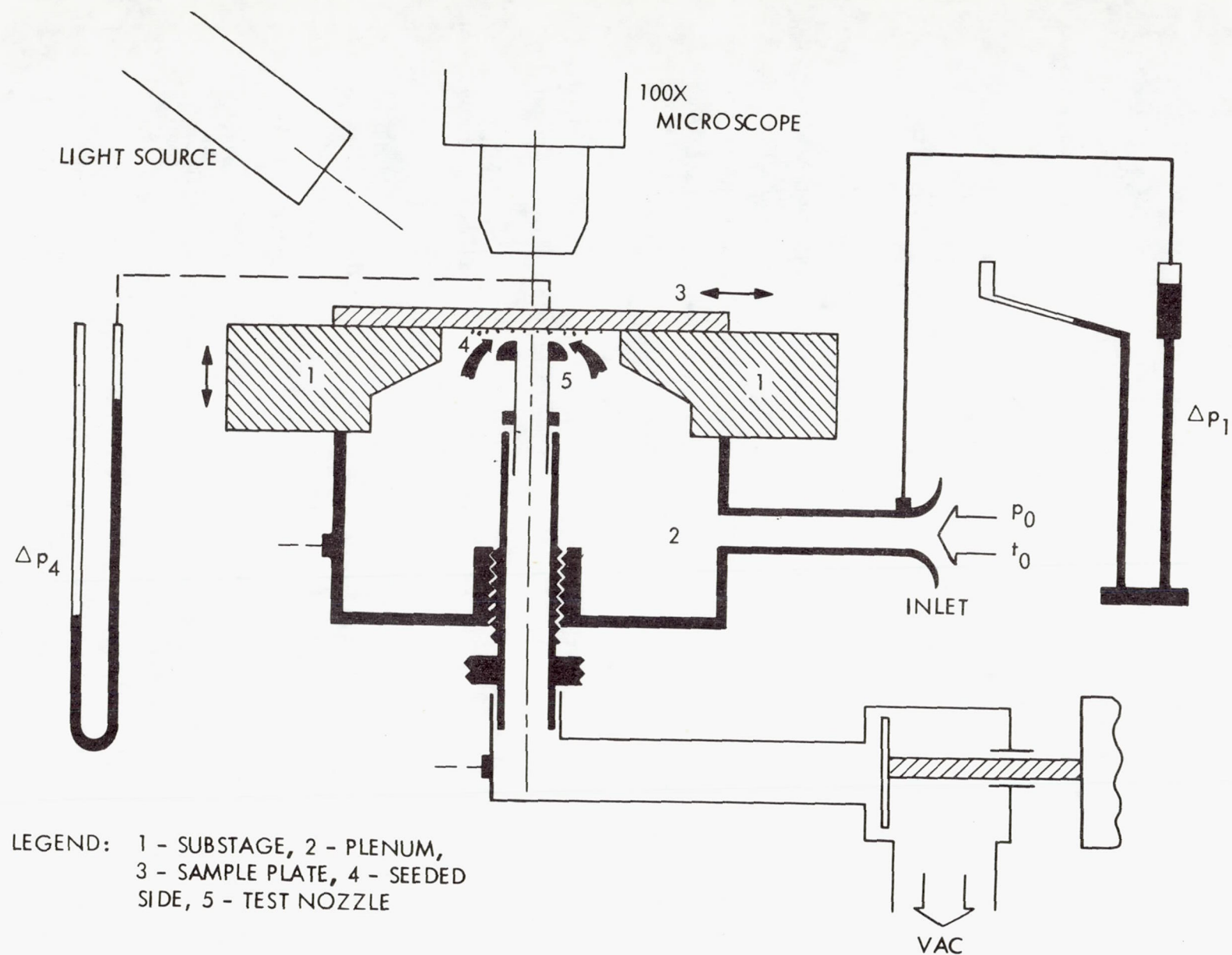


Fig. 6.1-1. Schematic of vacuum flow simulator

stick into the beads and holding it approximately 1 in. over the samples while tapping it with another metal item. With some practice, a fairly even and controllable particle spacing could be achieved with both the above described methods. After seeding, the samples were stored on the laminar flow bench for further treatment or tests.

To simulate moisture condensation - a condition that occurs during spacecraft prelaunch operations when the air conditioning fails - seeded samples were placed into a refrigerator for 15 minutes to induce fogging when the samples were returned to room atmosphere. The fogged samples were then dried on the laminar flow bench for a specified length of time. To simulate oiliness, cleaned slides were fingerprinted, by rolling the middle finger over them, prior to seeding.

6.1.2.2.3 Test Techniques. To evaluate the effect of flow velocity, particle size and surface conditions, the following technique proved to be most practical: 1) acquiring an individual particle under the microscope at zero flow; 2) determine its major dimension and the dimension normal to the flow by means of the ocular scale; 3) moving the particle into the nozzle throat; 4) opening the throttling valve slowly; and 5) recording the manometer reading at which the particle would detach from the surface and move.

This procedure was repeated for each data point. Care had to be taken to select only those particles from the area outside the outer nozzle radius where the flow velocities are very low if the same sample was to be used for more than one test. To prevent a testing of particles that might have touched the inner edge of the stage center hole, the sample movement was restricted to a 1 cm square about the center. The stage center was greased with vaseline to prevent air from bypassing the calibrated plenum inlet. To evaluate the effect of surface conditions and nozzle standoff from the surface at a constant velocity, and to study brush-cleaning problems, full counts taken before and after the test proved to be most useful. Unless otherwise indicated, the test always consisted of one double stroke with the glass slide over 10 mm distance to and from the operator.

6.1.2.2.4 Definitions and Derivations.

1. Removal Efficiency. For tests with individual particles, the removal (or cleaning) efficiency is defined as the number of particles detached out of the number of particles selected for test. In this case, there is only one determination for each data point shown.

For tests where actual cleaning was simulated by sweeping the sample with the test nozzle or brush, the removal efficiency is defined as the difference between counts taken before and after the test, compared to the initial count. Unless indicated otherwise, there are two determinations for each data point shown.

2. Particle Dimensions. All particle sizes indicated represent the particle width normal to the flow, determined with an accuracy of approximately $\pm 2 \mu\text{m}$. Only particles that appeared to be fairly uniform across the major axis were selected. Where particle break-up occurred prior to detachment, the original dimension was recorded. The partial detachment of a broken-up particle was not counted.

3. Nozzle Flow. The flow velocity \bar{v} as indicated in relation to the removal efficiencies determined by the test, represents the mean velocity in the nozzle throat cylinder plane normalized to standard atmospheric conditions, $P_o = 10,330 \text{ kg/m}^3$ and $T_o = 288^\circ\text{C}$. The factor $\bar{\lambda}$ where indicated, is the ratio between this velocity and the critical velocity as defined by

$$v_{\text{crit}} = \sqrt{2g \frac{k}{k-1} \cdot R \cdot T^*} = \bar{v}/\bar{\lambda} \quad (1)$$

where

k = the adiabatic constant

R = the gas constant

T^* = the absolute total air temperature

g = the standard gravity acceleration

The factor $\bar{\lambda}$ is computed from the continuity relations between the calibrated system inlet A_1 and the flow controlling plane (nozzle throat A_4). Assuming perfect continuity; i.e., no leaks, the states in these two planes are governed by the equation

$$\sigma = \bar{V} \cdot \frac{A_1}{A_4} \sqrt{\frac{k+1}{k}} = \frac{P_4/P_o}{\sqrt{\Delta P_1/P_o}} \cdot \frac{\bar{\lambda}}{1 - \frac{k-1}{k+1} \bar{\lambda}^2} = \text{constant} \quad (2)$$

where ΔP_1 is the measured inlet pressure drop, and

$$\bar{V}_1 = A_1 \frac{V_1}{\sqrt{\frac{2 \Delta P_1}{\rho}}}$$

the flow constant of the inlet determined by measuring the volume flow rate V_1 and the correlated pressure drop ΔP_1 . The flow through the inlet is practically incompressible under test conditions and the density of the air ρ is a constant. P_4 represents the static pressure in the nozzle cylinder plane, and P_o as mentioned earlier, is the ambient pressure.

For a given configuration, the value σ is a system constant, and the nozzle expansion ratio P_4/P_o depends upon the measurable ratio $\Delta P_1/P_o$. The relation between these two ratios had to be empirically established. Inserting for the relationship into Eq. (2), the factor λ then remains the only unknown that has to be determined.

6.1.3 ACCOMPLISHMENTS

6.1.3.1 Vacuum Cleaning with Brushes

Because of the problems encountered in sampling directly from the spacecraft, the efficiency of the cup-type brushes in use could not be established. However, observations made indicate that the equipment in existence has barely the capability to remove readily visible dust, and tends to recontaminate the cleaned surface, if the brushes are not cleaned frequently.

Earlier tests conducted on typical full-size nylon and sable hair brushes by means of small size (hyperdermic needle) pitot tubes (Planetary Quarantine 900-484) have shown that the flow-resistance across the brush hair is very high and increases progressively with the vacuum as the pressure differential across the brush builds up. The hair becomes solidly packed and blocks the flow completely. The re-entrainment of particles broken loose by the brush into the vacuum flow is practically zero under such circumstances and the brush becomes saturated with particles very quickly (Fig. 6.1-2).

In earlier tests it also appeared that the brushes would sweep the dust aside rather than remove it. Tests conducted with a small sable brush on the described apparatus substantiate this observation. For this test, a glass slide seeded with dust was swept once with the test brush (Fig. 6.1-3). The U-shaped arrow parallel to the abscissa represents the distance swept. The brush was in a fixed position with the hair-tips just touching the surface. The vacuum across the brush was 57 in. H_2O - approximately the vacuum producible without sucking the hair into the center.

The counts taken across the sample in the direction of the sweep are plotted on the ordinate. The right side of the plot, then, represents the cleaned surface; the left side, the uncleaned surface. A pile-up of particles is very evident in the transition zone between these two areas where the brush motion was reversed.

After the count, the cleaned surface was tapped once with the used brush which resulted in the recontamination indicated by the dotted line (approximately 40% of the count on the uncleaned side). The test brush was thoroughly cleaned by means of a small vacuum nozzle prior to this test.

Figure 6.1-4 shows the removal efficiencies achieved on a practically dry and on a fogged sample with the cleaned test brush in one double sweep. To account for the potential recontamination of the cleaned surface and pile-up demonstrated in Fig. 6.1-3, these data would have to be reduced by a factor of two for each succeeding wipe with the contaminated brush. The study indicates that the brush-cleaning equipment and the methods used to clean spacecraft are very inefficient and do not meet the requirements for future particulate and biological cleaning.



Fig. 6.1-2. Sable brush seen through sample plate (100x view)

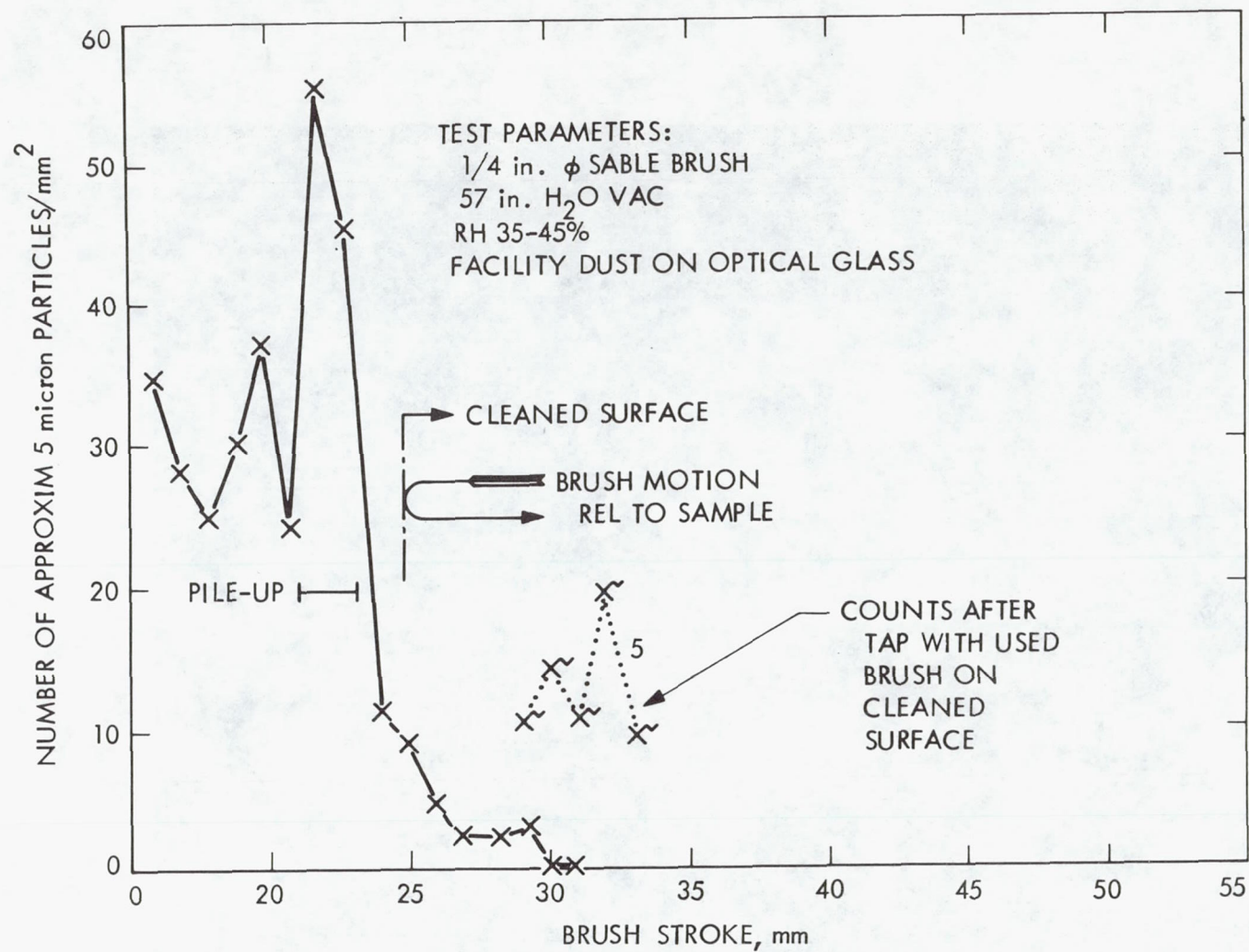


Fig. 6.1-3. Particulate surface load vs brush stroke

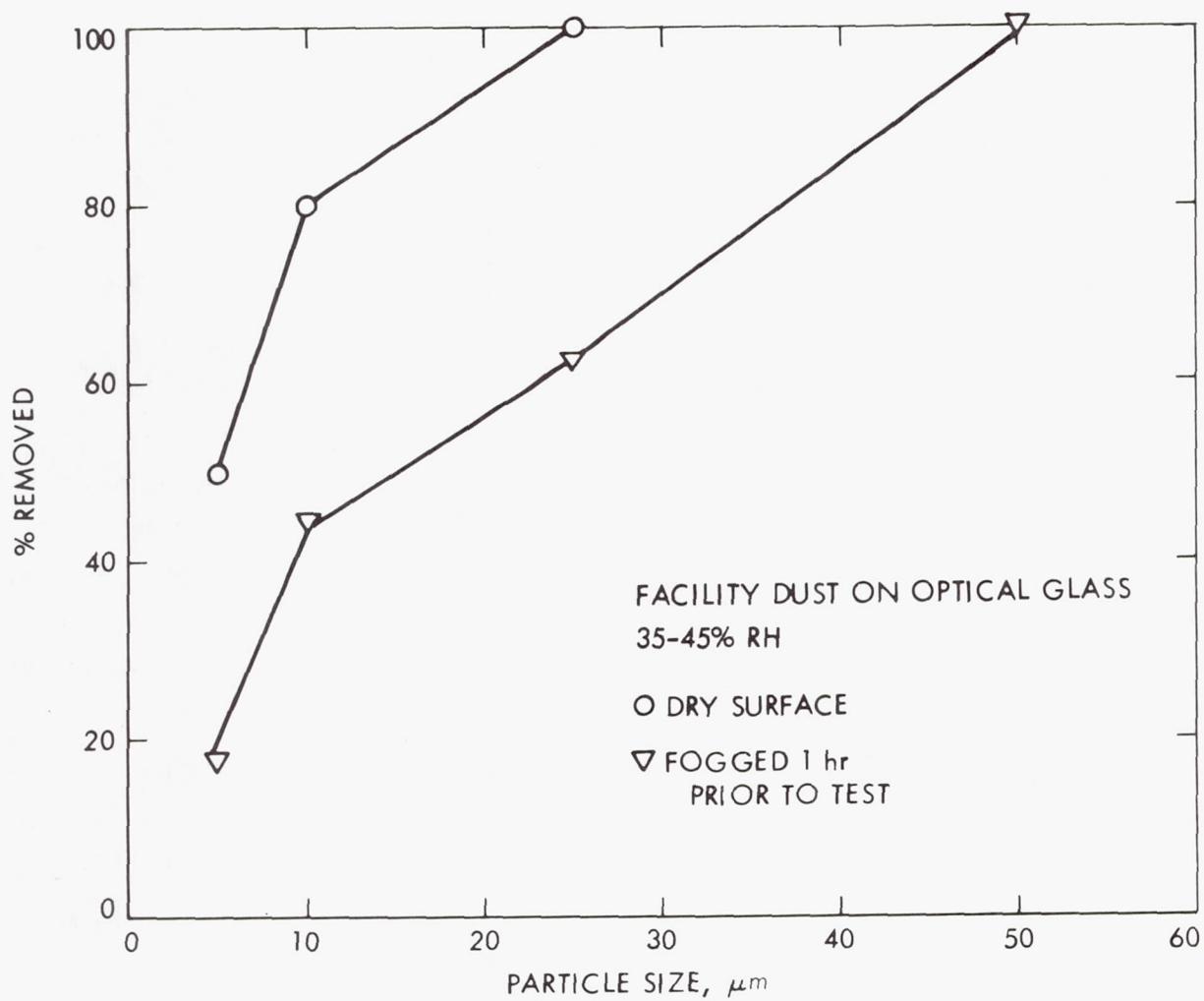


Fig. 6.1-4. Removal efficiency of 1/4 in. sable brush at 57 in. H_2O vacuum (count before and after one cm double stroke cleaned with brush)

6.1.3.2 Vacuum Cleaning with Air Flow Only

The objective of the first series of tests conducted was to establish the relation between some of the main parameters effecting the removal efficiency; i. e., the flow velocity, the nozzle geometry and certain surface conditions typical for spacecraft operations, such as a relatively dry (40% RH) surface, a fogged (100% RH) surface, and an oily (fingerprinted) surface. Efficiency determination was made for samples seeded with dust and glass beads, using the rounded lip convergent nozzle at a constant 0.008 in. (~ 230 microns) distance from the surface. The results are shown in Figs. 6.1-5, 6.1-6, and 6.1-7. Since the individual particle observation method described was used, each data point shown represents one determination.

It is obvious that the glass beads are not representative for real dust. The adhesion of the beads appears to be one tenth or less than that of dust on dry and oily surfaces, whereas the effect of moisture seems to be much more pronounced with the beads. Nevertheless, the glass beads have definite experimental advantages in studying flow-effects. Having fairly uniform spherical dimensions, they are easier to size and to count than dust. Thus, larger numbers of data can be obtained.

Flow velocities on the order of the critical velocity ($\lambda = 1$) are necessary to remove small particle sizes efficiently (10 microns and smaller). Commercial vacuum cleaners and associated attachments have just the capability to remove readily visible dust, 50 microns and larger. Moisture and oiliness have a very strong effect on the adhesion of dust and render the surface practically uncleanable by means of vacuum flow alone.

The sudden rise in removal efficiency between 100 and 200 m/s noticeable for all particle sizes and surface conditions, have been identified as a Reynolds number effect (see para. 6.1.4.1).

The maximum removal efficiencies achieved with dust during these tests are compared in Fig. 6.1-8. The comparison shows that larger dust particles are more effected by moisture and oiliness than smaller ones. The larger ones, however, seem to dry up faster. This tendency may be attributed to their exposure to room currents that enhance the evaporation of the moisture absorbed. This tendency also can be explained with the surface-to-volume ratio

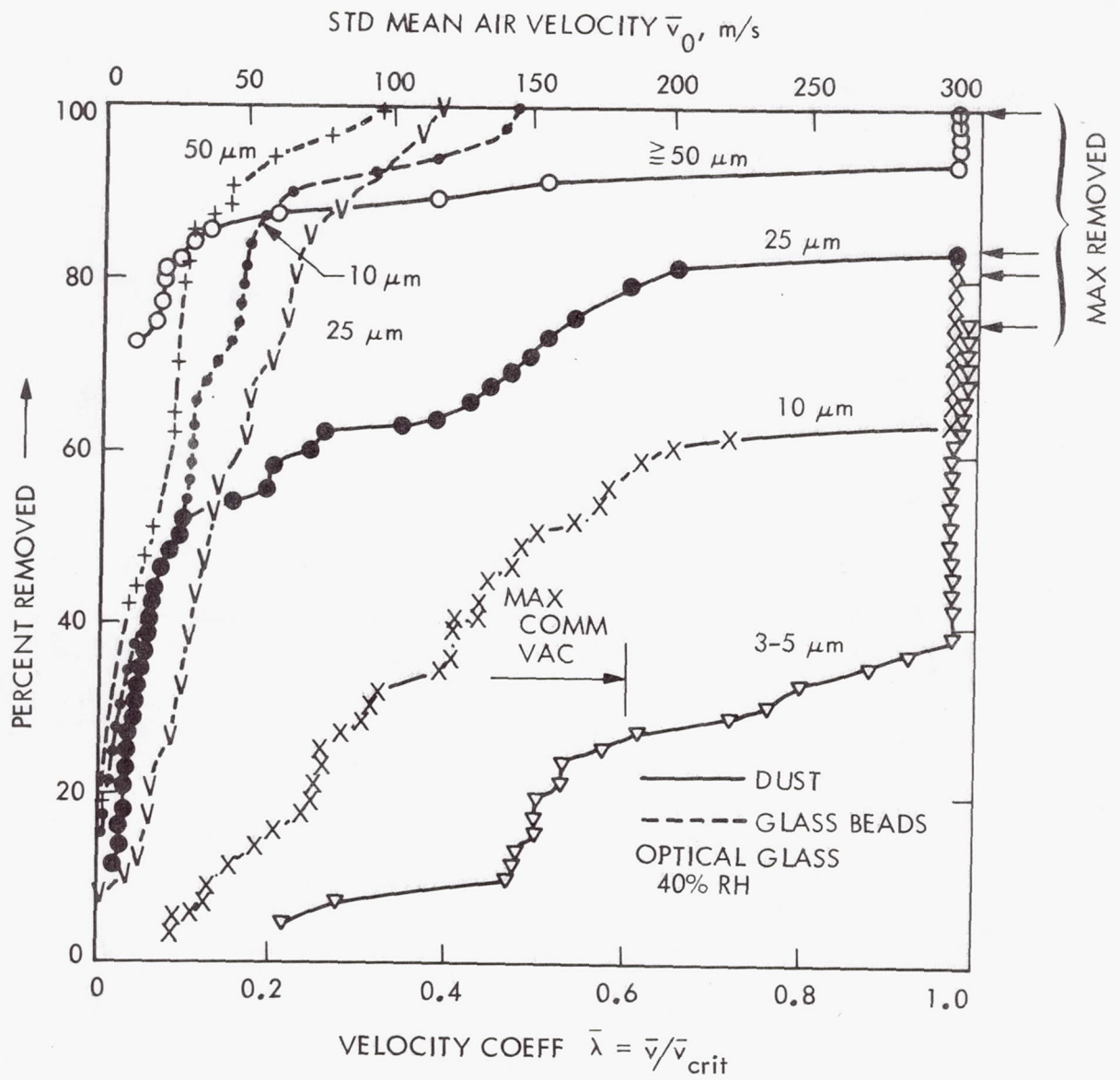


Fig. 6.1-5. Removal efficiency vs particle size and flow velocity

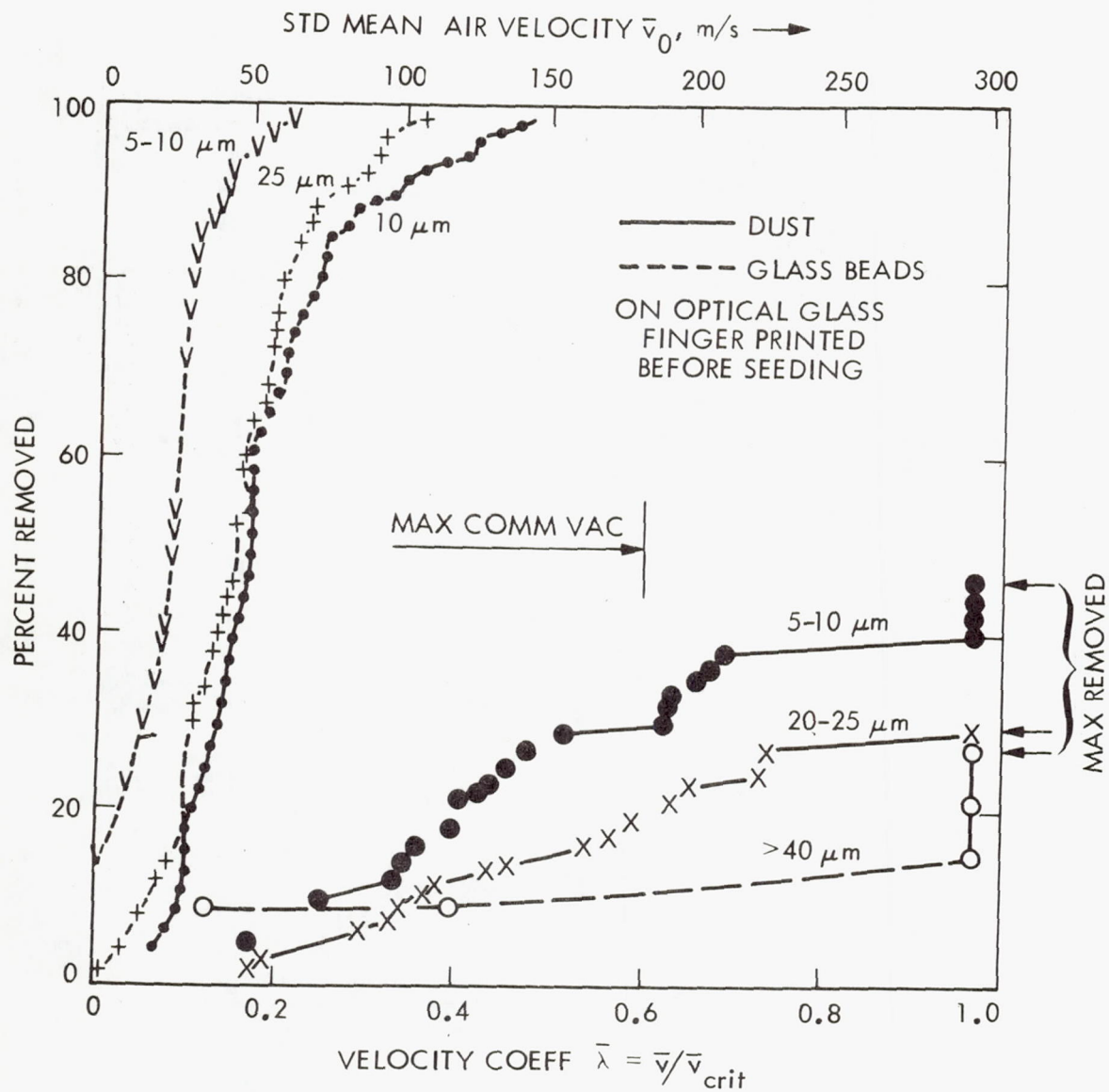


Fig. 6.1-6. Removal efficiency vs particle size and flow velocity

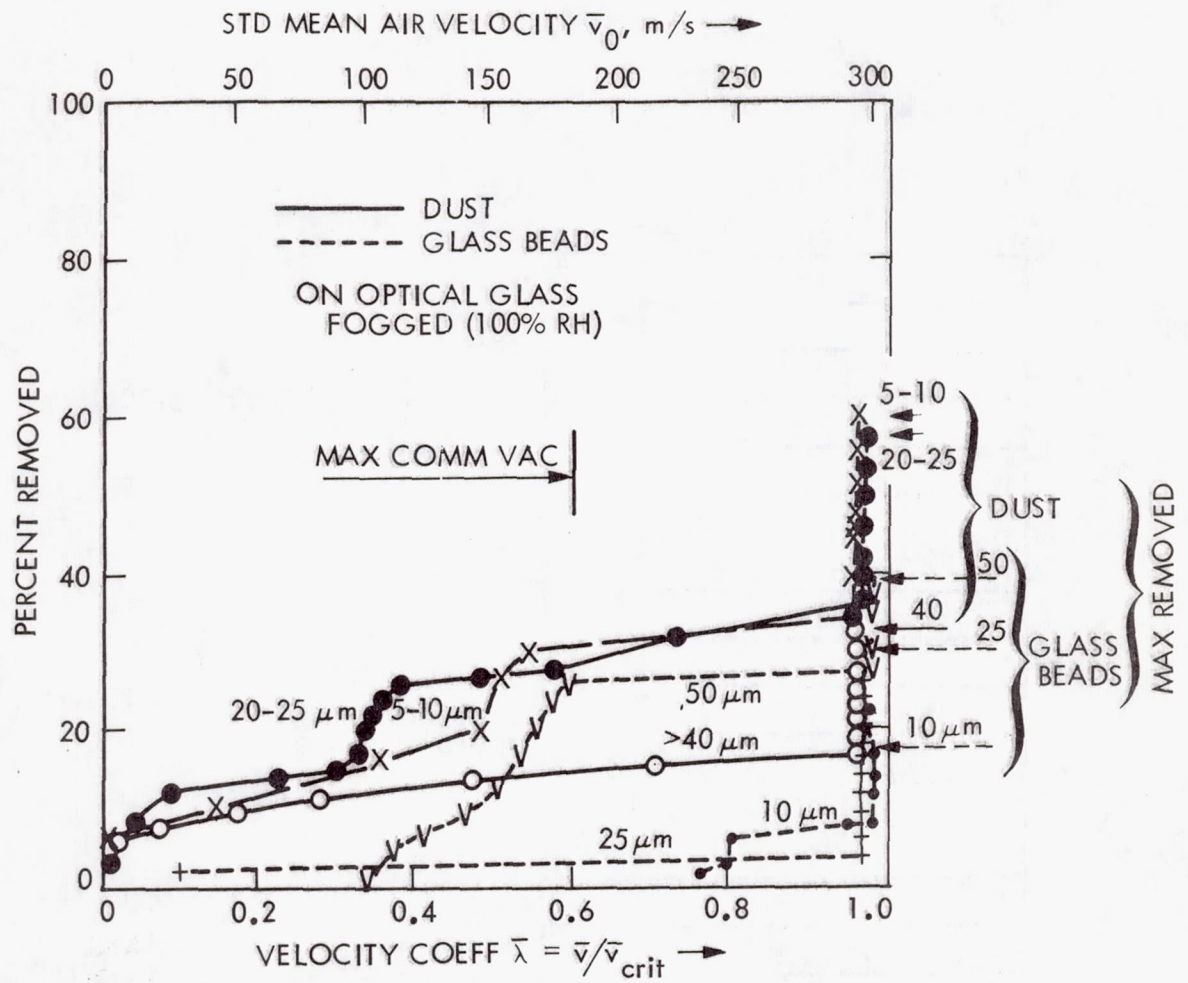


Fig. 6.1-7. Removal efficiency vs particle size and flow velocity

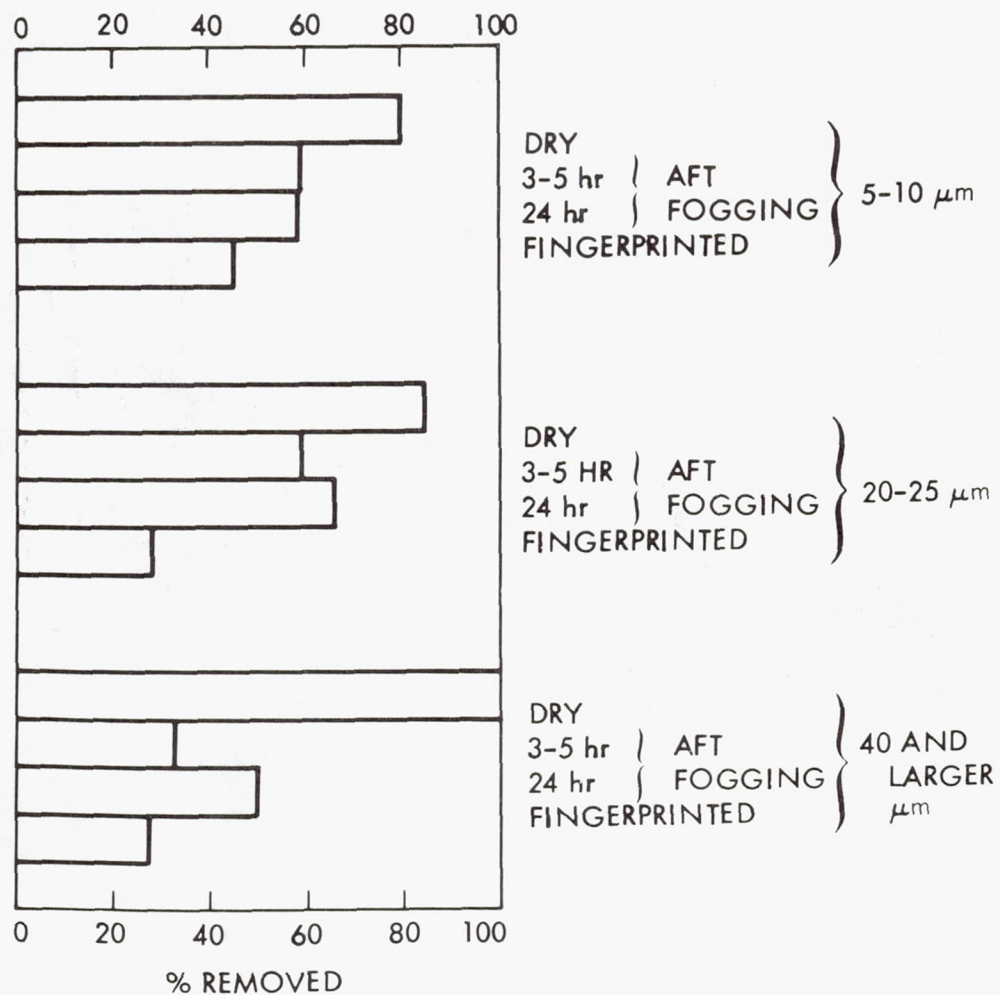


Fig. 6.1-8. Maximum removal efficiencies at 0.02 mm stand-off and choked nozzle flow

of the particles: larger dust particles are predominantly flakes, fibers, and porous materials, whereas smaller ones are composed of more compact and crystalline materials that retain the moisture trapped underneath much longer.

Other tests were conducted to demonstrate the effect of nozzle geometry, which is mainly determined by the stand-off from the surface and the nozzle radius. Two nozzles were tested, one with a sharp edge and the other with a rounded tip and a straight radial section of 0.3 mm. The inner diameter of both nozzles was 5 mm. The stand-off from the surface was varied between 50 and 300 microns in 75 micron (0.003 in.) increments. These tests were conducted at maximum flow on dry samples seeded with dust. The removal efficiencies were established from counts before and after the test. As mentioned earlier, two determinations were made for each data point.

The results (Fig. 6.1-9) indicate that the stand-off from the surface has a strong effect. Efficiencies drop off sharply at stand-off larger than 200 and smaller than 100 microns from the surface mainly because of boundary layer effects (see para. 6.1.4).

As expected, the sharp edged nozzle is more efficient, particularly for smaller particle sizes. This efficiency is enhanced by two factors: 1) the edge effect and the resulting contraction of the flow having the same effect as a smaller stand-off; and 2) less boundary layer buildup and friction.

The maximum removal efficiencies achieved with vacuum cleaning on dry samples seeded with dust are summarized and compared in Fig. 6.1-10. It is obvious that cleaning with flow only is more efficient than in a synergistic mode with a brush. The removal efficiency achieved with any of the tested techniques begins to decrease at particle sizes below 10 microns and is virtually non-existent below 5 microns.

6.1.3.3 Injection of Solvents into the Vacuum Flow

Since accidents causing moisture condensation and/or oiliness cannot be completely prevented during spacecraft operations, the problem of restoring cleanability in such cases was investigated. Vacuum cleaning with heated extra dry high purity GN_2 was the selected method. Isopropyl alcohol (or freon TF) was injected into the flow to reduce excessive particle adhesion due to moisture and oiliness.

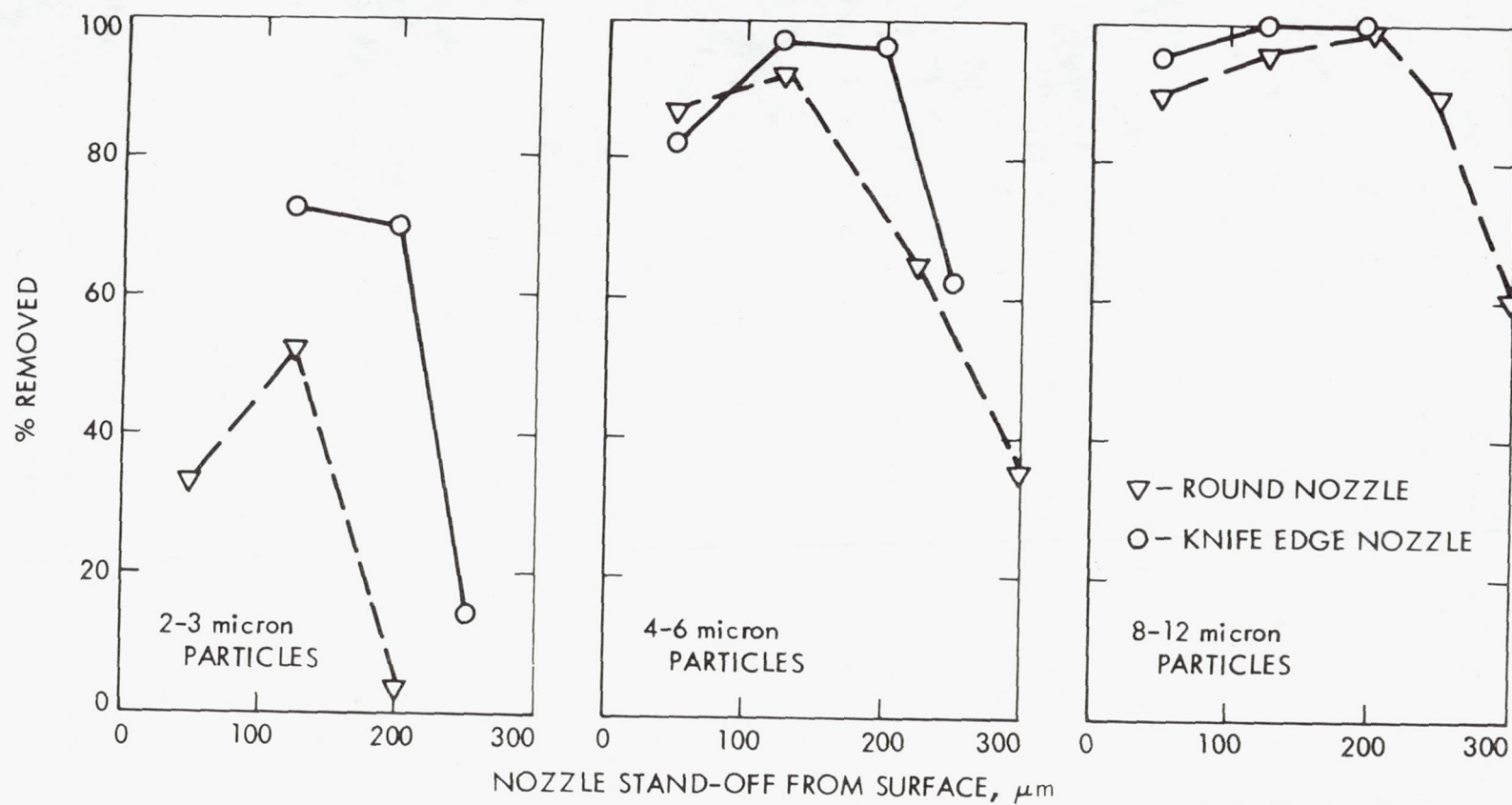


Fig. 6.1-9. Effect of stand-off from surface on removal efficiency at choked nozzle flow. Facility dust on glass, 35-45% RH

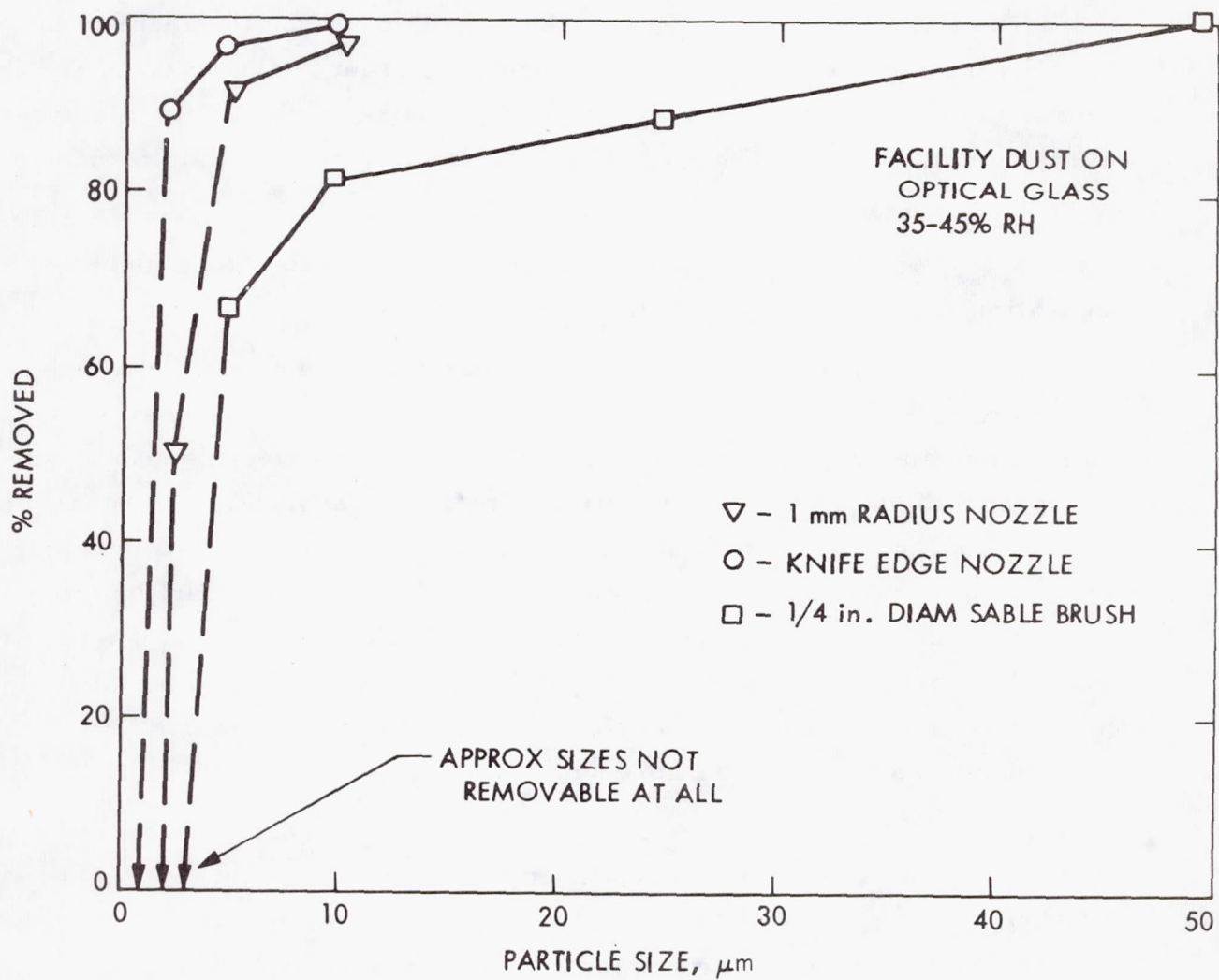


Fig. 6.1-10. Maximum removal efficiencies achieved

For this test, the inlet of the test apparatus was removed, the plenum was connected to a pressure source feeding GN_2 into the system through a heater, and the rounded tip test nozzle was installed 230 microns from the sample surface. The vacuum flow through the nozzle was critical; the GN_2 flow was adjusted to maintain a slight positive pressure on the order of 50 mm H_2O in the plenum chamber.

The liquids were injected into the plenum chamber by means of an artist's airbrush driven with 2 atm GN_2 pressure from the same source. The brush venturi was installed at a 45° angle to the nozzle axis 40 mm distance from the sample surface. The test was conducted in the following manner:

Three sample sets in 3×3 batches were seeded with dust. The first group was practically dry, the second group was fogged to induce moisture condensation, and the last group was fingerprinted prior to seeding.

One set of dry and moist samples were then swept with GN_2 , increasing the plenum temperature up to 80°C in 10° increments between sweeps. The remaining dry and fogged samples, divided into two sets, were sprayed with 90% isopropyl alcohol: one set by introducing a wide angle fine mist that just would not produce a liquid film at the sample surface; the other set by applying a narrow angle spray against the sample that would produce a film but no running liquid on the surface. The fingerprinted samples were treated in the same manner, but sprayed with freon TF instead of alcohol. All samples were swept with five double strokes of critical flow air prior to test to remove loosely attached particles that did not represent a problem.

The spray was always applied with the vacuum nozzle during the first double sweep, and sweeping was continued until the sample surface was dry. The plenum temperature was kept at about 50°C , to prevent icing. The behavior of selected particles and of the sample surface was observed during all procedural steps through a 100 X microscope. The following observations were made:

(1) Sweeping with heated or unheated GN_2 and fine spray with either of the liquids into the plenum chamber did not have any effect on particle detachment. At temperatures above 50°C , some particles appeared to change color, transparency and/or contour, suggesting tackiness.

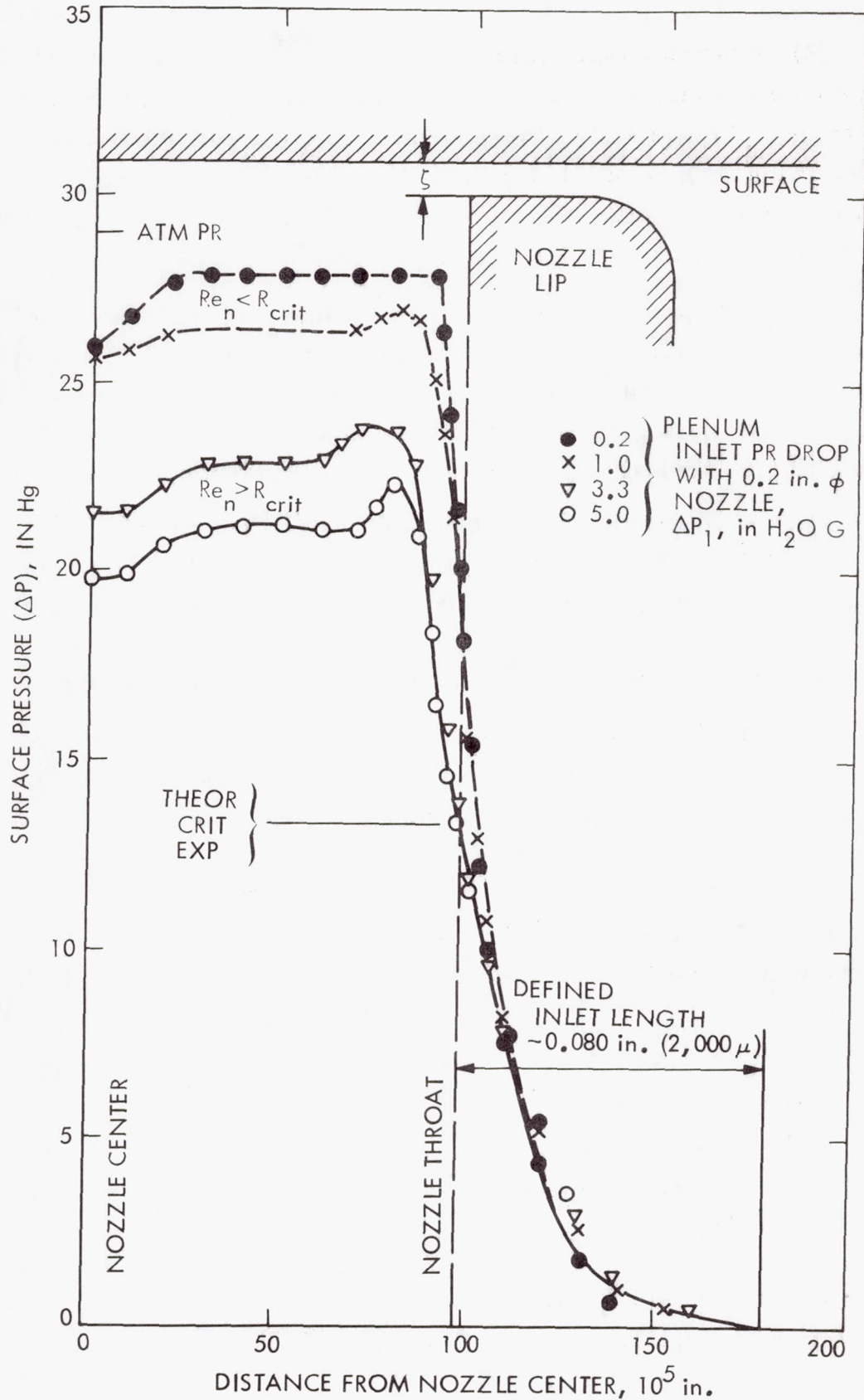


Fig. 6.1-11. Typical surface pressure profile with rounded test nozzle at choked flow condition

(2) A narrow angle spray producing film with either liquids caused an immediate detachment of most particles and downstream migration through the nozzle throat. Immediately after passing the throat cylinder plane, the film would surge into a violently boiling annular puddle. Some particles could be seen to re-entrain into the flow with the splash, but this did not seem to be enough to make a quantitative evaluation worthwhile.

According to these observations, an injection of liquids during cleaning is not a suitable method for restoring cleanability, especially for a type of contamination that is not compatible with temperatures required for instant drying. Also, the film thickness had to be controlled within a much narrower tolerance than was possible with the existing test setup.

Because of limited resources, this test was not pursued further. However, additional study of this effort is warranted. It should then be investigated as a pre-cleaning treatment rather than a synergistic mode with cleaning.

6.1.4 AERODYNAMICAL CONSIDERATIONS AND DISCUSSIONS

Prior to the cleaning tests, a series of systematical aerodynamical surveys were conducted on the test apparatus to establish its capability and to obtain pertinent data necessary to compute the referenced velocity, \bar{v} (see para. 6.1.2.2.4, item 3). These surveys consisted mainly of static pressure measurements across the nozzle radius by means of a tapped precision ground sample plate. The total pressure across the inlet throat plane was measured by hyperdermic needle pitot tubes. (Measuring the pressure distributions normal to the sample surface was not feasible because of the small distance between the nozzle lip and the sample.)

The typical pressure profile of the round lip test nozzle at critical flow for the indicated stand-offs from the surface is shown in Fig. 6.1-11. For analytical reasons, the radial mean velocity in the throat cylinder plane was primarily used as a criterion to evaluate removal capability. As can be seen from Fig. 6.1-11, the expansion is not terminated at the nozzle throat but continues into the inner cavity. The tendency of the profile indicates the existence of a Prandle-Mayer flow (a fan of refraction waves) disrupted by a

compression shock 0.8 to 0.9 radially inward from the nozzle throat radius where the pressure drop reaches a maximum.

The flow velocities in this point are super critical (supersonic), explaining four phenomena: 1) why some particles that did not detach in the nozzle throat would come loose if moved further downstream; 2) why efficiencies achieved in tests that accomplished cleaning by means of a sweep were slightly higher than those obtained from observing the particle detachment in the nozzle throat plane; 3) why all detached particles would blitz radially inward after detachment and suddenly disappear at a certain radius downstream the nozzle throat; and 4) why, during spray tests, the liquid film would surge at the same radius.

These phenomena are attributable to sudden boundary layer growth and the disturbance associated with the compression shock that actually accomplishes the re-entrainment of the detached particles into the flow.

Another observation that also supports the above hypothesis should be mentioned: if the laminar bench was shut off and a cleaned sample exposed to critical flow without changing the position of the sample relative to the nozzle, a readily visible halo would form right at the radius where, as hypothesized above, the compression shock takes place. Under the 100X microscope, this halo appeared to be micron size particulate matter densely packed against the surface, suggesting the existence of an intensive annular vortex and boundary layer detachment in this area. These results are extremely desirable for removal and re-entrainment; however, they also demonstrate that high velocity cleaning with flow can also be contaminating if the flow is not filtered accordingly.

6.1.4.1 Effect of the Reynolds Number

A useful tool to normalize and to interpret flow effects is the relation between the Reynolds number and the frictional resistance. For the flow through a narrow slot, the Reynolds number is defined as

$$\text{Re} = \frac{2s \bar{v} \rho}{\mu} \quad (3)$$

where

s = the stand-off; i. e., the distance between the nozzle lip and the surface

\bar{v} = the mean velocity in the nozzle throat cyclinder plane as determined from Eqs. (1) and (2)

ρ = the air density

μ = the viscosity of the air

The frictional resistance can be expressed as

$$C_F = \frac{2 \cdot s}{\ell} \left[\left(\frac{v_{ad}}{\bar{v}} \right)^2 - 1 \right] \quad (4)$$

where

v_{ad} = the adiabatic flow velocity resulting from the measured expansion ratio between the plenum chamber and the nozzle throat

ℓ = the reference length - defined in this case as the radial distance from the throat plane where a measurable pressure drop starts to exist (Fig. 6.1-11)

representing the relative friction losses per unit length along the flow path. Figure 6.1-12 shows the relation between these factors for the two typical conditions tested (constant stand-off at variable velocity, and critical velocity at variable stand-off) compared with literature data for flow through a narrow slot.

From numerous tests conducted by a variety of investigators, it is fundamentally known that, for the left portion of the curve, indicated by the steep slope, the flow is laminar; whereas in the right portion of the curve indicated by the flatter slope, turbulent mixing takes place. In between the two there is a transition zone where the flow changes from one state into the other. The Reynolds number that separates the laminar regime from the rest of the spectrum is usually referred to as the critical Reynolds number.

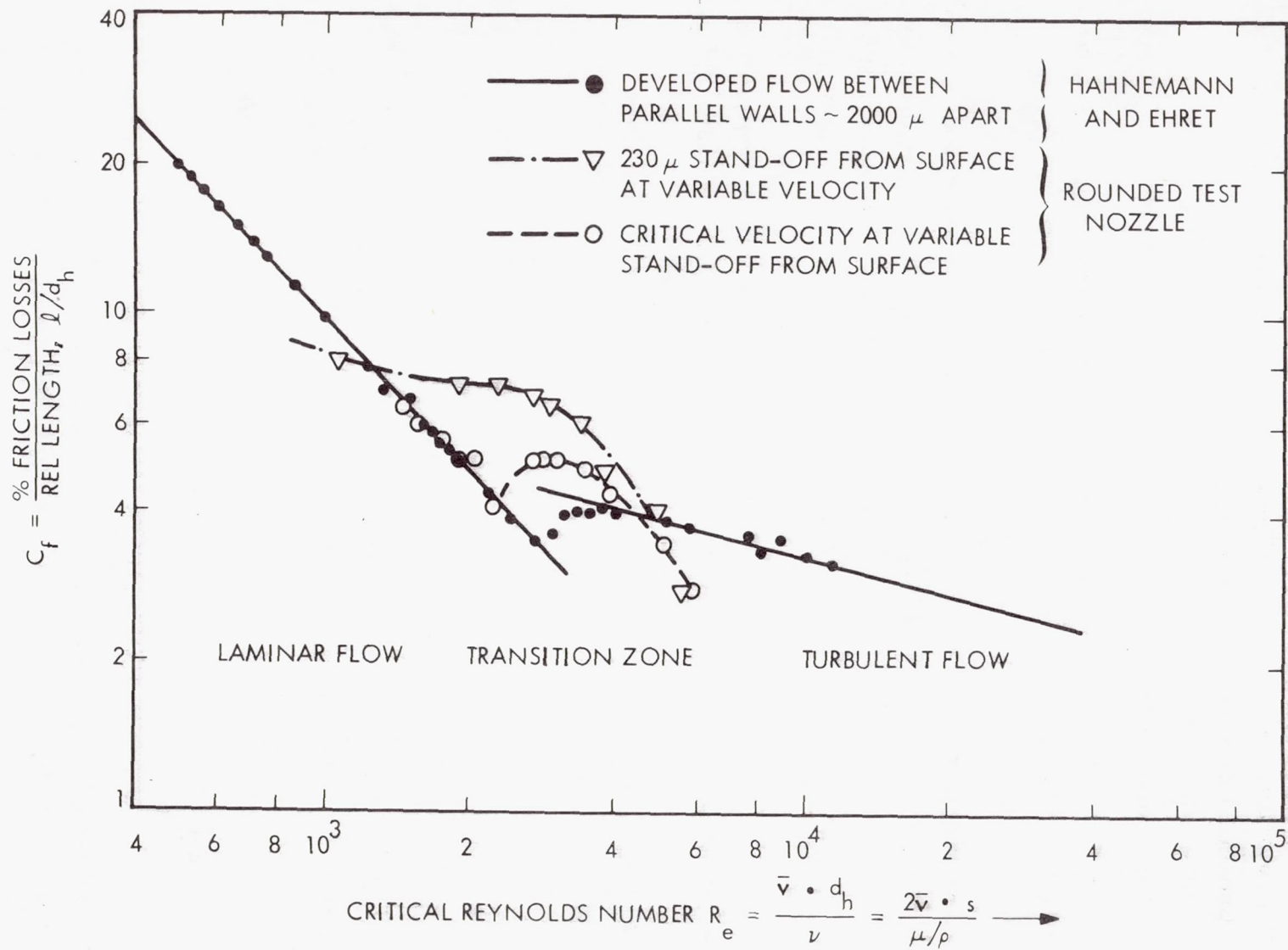


Fig. 6.1-12. Frictional resistance vs Reynolds number

One might ask now, 'What does this have to do with vacuum cleaning? ' The data discussed in para. 6.1.3.2 provides the answer. The data show that for a given velocity, best removal efficiencies were always achieved at Reynolds numbers that fall into this transition zone.

6.1.4.2 Assessment of the Drag Force

The following simple approach was employed to assess the near surface aerodynamics and the detachment force and to identify areas for potential improvement:

It is fundamentally known that viscous forces dominate near the wall. Disregarding those typical conditions (laminar, turbulent, or transient) that may prevail in the core flow, a thin layer referred to as the laminary sub-layer exists where the flow is always in laminar motion. Rough calculations show that, for the conditions tested, the sublayer is on the order of 60 microns or more, and the drag on the particle sizes of interest is primarily governed by viscous relations. In this case, Stokes equation for viscous drag applies.

$$F_d = 3\pi\mu d_p \cdot v_p \quad (5)$$

where

d_p = the particle diameter

v_p = the velocity acting on the particle

Since the velocity gradient near the wall is practically constant, for a wall attached particle, the distance from the wall y equals to particle radius of the form

$$\frac{v}{y} = 2 \frac{v}{d_p} = k = \text{constant} \quad (6)$$

With good approximation, it can also be assumed that the shearing stress τ between adjacent laminar layers is constant. Then, with Newton's law of friction, and with Hagen-Poiseulles equation for laminar flow, the shearing stress becomes

$$\tau = \mu \frac{dv}{dy} = C_F \rho \cdot v^2 / 8 \quad (7)$$

Substituting Eq. (7) for v_p in Eq. (5), the particle drag force is finally obtained as

$$F_d = \frac{3\pi}{8} C_F \left(\frac{\rho}{2} v^2 \right) \cdot d_p^2 \quad (8)$$

It can be seen that, for the wall attached particle, Eq. (5), has assumed a square character, though viscous relations still rule. Although greatly simplified, Eq. (5) shows, in a very illustrative manner, the relations between the main factors involved and the area most instrumental to further increases of the detachment force. The main factors effecting the particle drag are the friction coefficient C_F (which reflects the shearing stresses and the velocity gradient imposed to the sublayer by the core flow), the mean dynamic pressure, and the particle projected area.

Plotted in Figs. 6.1-13 and 6.1-14 are particle drag data calculated in Eq. (8) using the test data discussed earlier (para. 6.1.4.1). Figure 6.1-13 shows the relation between the mean flow velocity, particle drag, and the Reynolds number for a constant stand-off. The same pronounced changes of the force-velocity gradient, comparable to the changes of the efficiency-velocity gradient observed in test with dust and glass beads, are evident. The relation between the friction coefficient C_F and the Reynolds number shown in Fig. 6.1-12 are primarily responsible for this. The continuous rise beyond $\lambda \approx .4$ is attributed to velocity increase alone.

Figure 6.1-14 compares the calculated data with test results obtained with dust and glass beads for maximum flow velocity at variable stand-offs from the surface. Because, as mentioned earlier, the test beads would detach too easily, the samples were fogged to obtain conclusive results. As can be seen, the calculated data show a pronounced optimum at about the same stand-off from the surface.

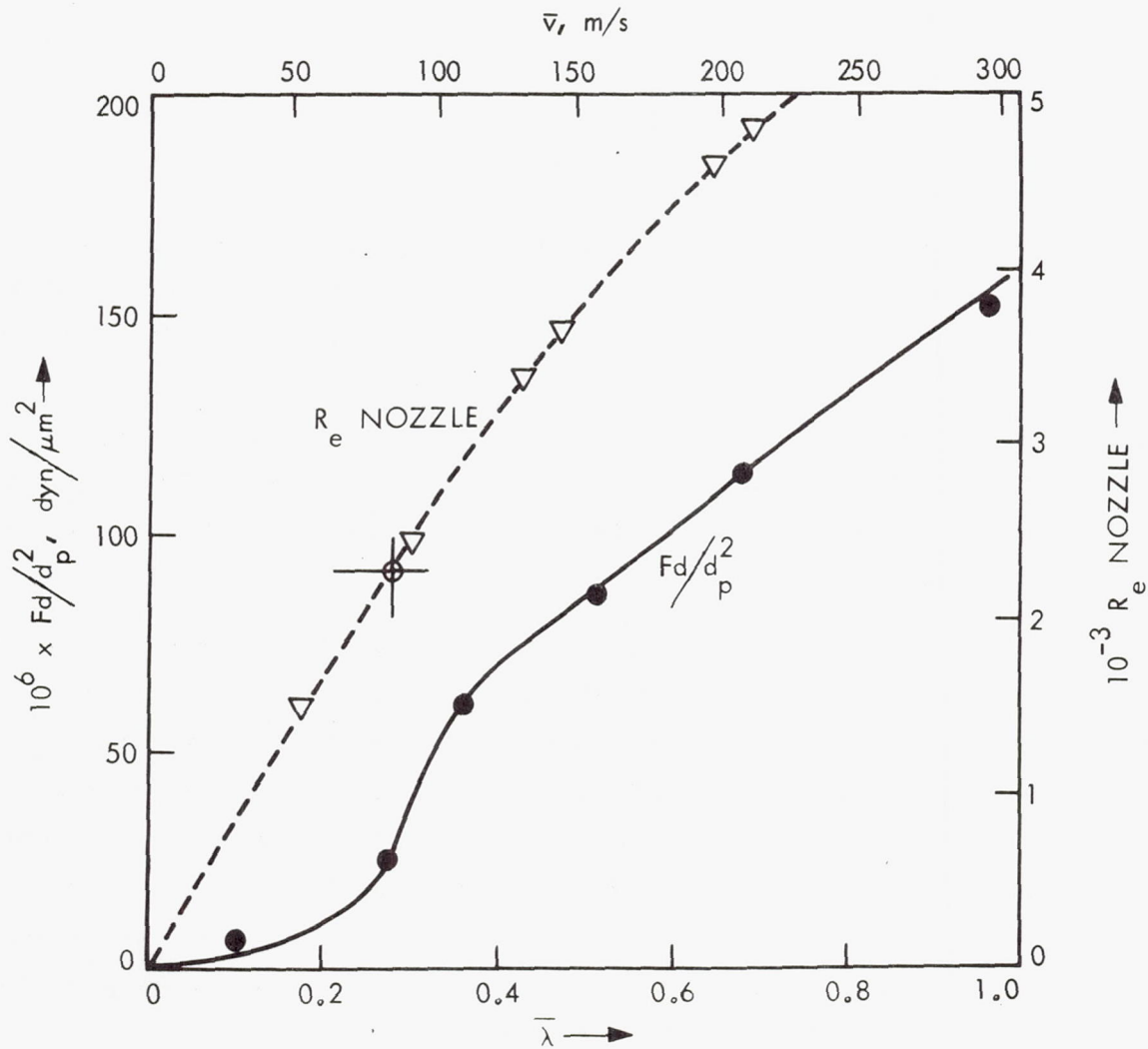


Fig. 6.1-13. Calculated Stokes- drag at constant 230 microns stand-off from surface

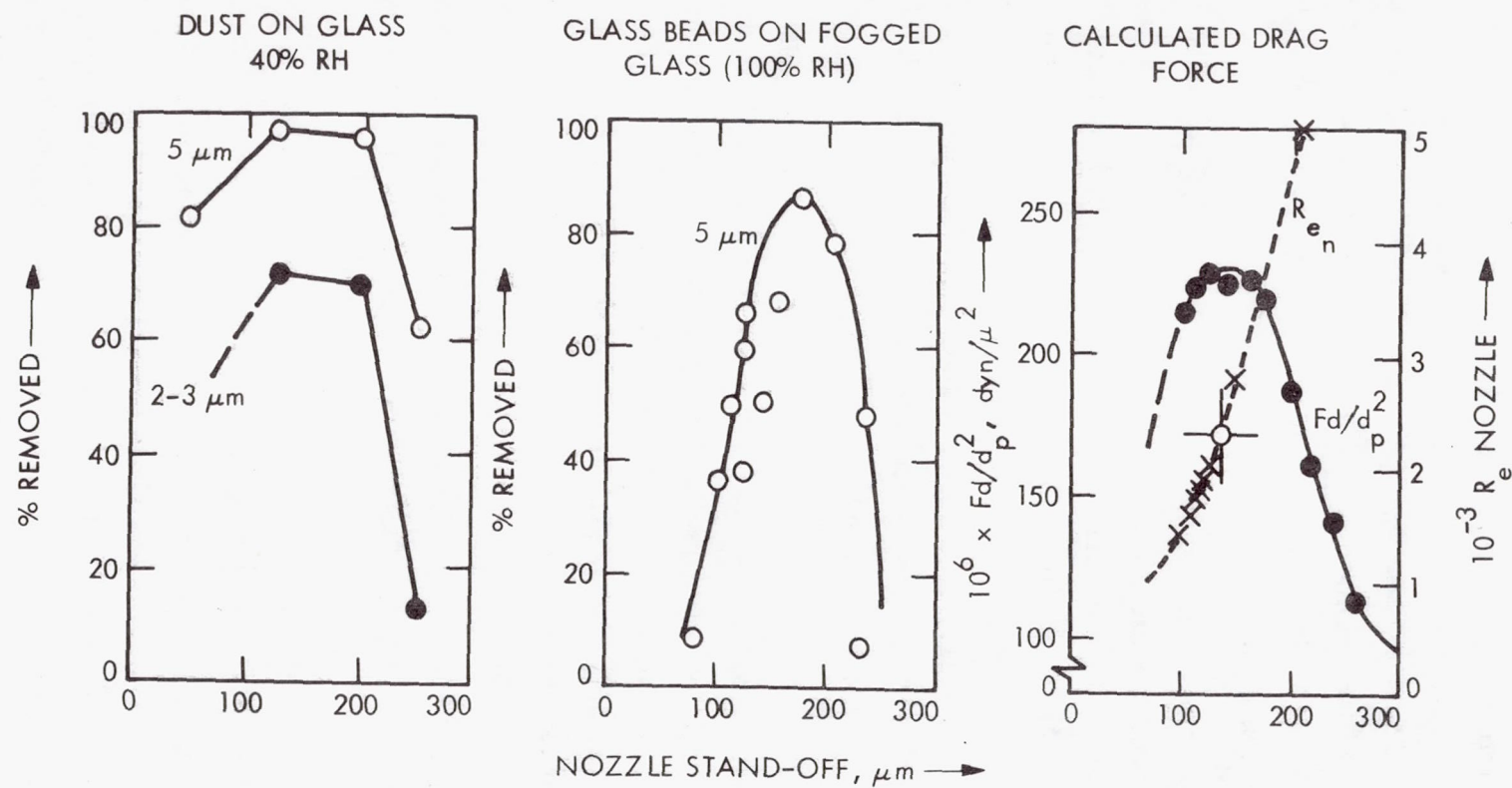


Fig. 6.1-14. Effect of nozzle stand-off from surface on removal efficiency and drag force at critical expansion (choked flow)

The Reynolds number and C_F relation are once again primarily responsible for the results. The force reaches its maximum slightly above the critical Reynolds number (approximately in the center of the transition zone) between the laminar and the turbulent state. Above that, the flow is all turbulent and the drop-off to the right (i. e. ; to higher stand-offs), is mainly caused by the decrease of the friction coefficient C_F . This decrease indicates that the shearing stress, the velocity gradient in the sublayer, and the velocity acting on the particle are going down.

The mechanics of the drop-off to the left (i. e., to smaller stand-offs from the optimum), which are much more complicated, also appear to be steeper. The friction coefficient C_F (see Fig. 6.1-12) goes up steeply at sub-critical Reynolds numbers and, one would assume that the drag force should also. This, however, does not occur because the back pressure, and consequently the density ρ had to be lowered drastically to maintain critical core-flow through the nozzle throat, which, in this case, dominates the rise of the C_F value.

In addition to maintaining a constant core velocity, the mean velocity is also subject to drop-off as the flow changes from the turbulent into the laminar state. This drop-off results from the ratio of core to mean velocity in both states. As can be derived, the mean velocity of turbulent flow equals 14/15 of the core velocity, whereas the mean velocity of the laminar flow equals 2/3 of the maximum core velocity. Thus, the mean velocity drops in a ratio of 10 to 14 or 35%.

In conclusion then, all available data establishes the Reynolds number as the most essential criterion for the layout of a cleaning tool, if flow is the primary source used to generate the detachment force.

6.1.5 PULSATORY EFFECTS

Although the tendency of the test data can be explained by means of steady state flow relations alone, indications are that pulsatory effects are also involved. Chugging of the flow was observed at certain positions of the throttling valve controlling the flow rate through the system (see Fig. 6.1-1). It also appeared that some of the particles tested would detach more easily

under these conditions. Unfortunately, however, this state was not very reproduceable, nor was enough data collected to substantiate this observation in a quantitative manner.

It is also fundamentally known that the flow in the transition zone (para. 6.1.4.2) is of an intermittent nature alternating between laminar and turbulent states. This, as can be derived, is associated with periodic changes of the mean velocity and with lateral velocity components that possibly extend into the sublayer and thus enhance the particle drag-force — the reason removal efficiencies were best achieved at the critical Reynolds number. This evidence also suggests that the use of pulsatory effects to enhance particle drag should be investigated further.

6.1.6 SUMMARY AND CONCLUSIONS

The findings made and the conclusion drawn from this study can be summarized as follows:

- (1) Brush action efficiently loosens particulates, but because brushes contaminate quickly and become a shedding source, the re-entrainment of the particles into the flow is poor. For more efficient cleaning, brushes should be cleaned after each single sweep. Even then, however, the efficiency that can be achieved cannot compete with vacuum cleaning.
- (2) The efficient removal of particles by means of vacuum flow only requires the highest possible (i.e., critical) flow velocities. The Reynolds number has a strong effect. Maximum efficiency is achieved at Reynolds numbers that bracket the transition zone between the laminar and the turbulent regime, between 2,300 and 3,000. A narrow stand-off from the surface on the order of 100 to 200 microns is necessary to satisfy such Reynolds numbers at critical velocities.
- (3) Moisture and oiliness have an effect on particle adhesion that renders the surface practically uncleanable by means of flow and/or brush. Methods to restore cleanability in cases of accidental fogging or contamination from oily constituents

(fingerprints) have to be developed. The method tested - the injection of detergents into the vacuum flow during cleaning - is not recommended.

- (4) Two potential measures developed to further increase the removal capability and to make vacuum cleaning more forgiving where stand-off is concerned are: 1) increase the density of the medium sweeping the surface; and 2) introduce pulsatory effects to enhance sublayer disturbance. These measures call for the concept of a blow-vacuum device where the jet-blow generates the detachment force, and the vacuum flow accomplishes only the re-entrainment and removal of the particles into the system.
- (5) Although less efficient, the brush is still an important tool to clean irregular surfaces such as cable bundles. The problem associated with the use of brushes in a synergistic mode with vacuum flow are inherent and there is practically no potential to improve the efficiencies demonstrated with a clean brush. There ought to be possibilities, however, to eliminate the entrapment and shedding problem and to achieve such efficiencies under practical operational conditions. Possible means to clean the brush are the application of flow and/or electrostatical means in a simultaneous or consecutive mode with surface cleaning.

Running the existing brushes over a cleaning tool between sweeps would be an improvised but possible approach. The concept of a self-cleaning rotary brush might be the solution for the future.

- (6) A need for improvement also exist in the area of brush materials. Natural sable hair is the only brush material generally approved for use on spacecraft. The hair, and also the potting compounds used to fasten the hair roots to the brush body, are not compatible with heat - sterilization or effective chemical decontaminants. Sterilizable substitute materials having essentially the same mechanical properties where surface compatibility is concerned, have to be found. A resilient hollow fiber material that can be

tapered into an approximately 2 micron diameter tip, may provide the solution to the problem.

6.1.6.1 Potential for Improvement

Two basic approaches can be taken to improve the removal efficiency: 1) decrease the adhesion to the surface; and 2) increase the particle drag that has to accomplish detachment. The capability to re-entrain the particles detached has to be improved accordingly.

The effects of moisture and oiliness, and the procedure used to reduce excessively high adhesion caused by such conditions, (para. 6.1.3.3) illustrate that the means or any apparatus necessary to reduce adhesion should not be an integral part of the cleaning tool. Thus, it shall be assumed that the cleaning method and the tools necessary to accomplish cleaning have only to cope with the adhesion in existence under normal cleanroom conditions ($22^{\circ}\text{C} \pm 2$ and 30-45% RH). (The restoration of the surface to these conditions in cases of accidental moisture condensation or fingerprinting shall be considered as a separate problem.)

Fortunately, the mechanics of particle drag and re-entrainment are closely linked together. According to Eq. (8) (see para. 6.1.4.1), the main factors having an effect on particle drag are the friction coefficient C_F , the mean flow velocity, the density of the medium, and the particle projected area. The final question now is twofold: "How can we improve, and how much can we improve"?

As discussed earlier, the maximum possible velocity producible in a convergent nozzle is already in operation. Since the friction coefficient C_F is primarily governed by the Reynolds number, it was concluded that the transition zone above the critical Reynolds number is best.

Particle size is essentially something that has to be accepted although lumping (coagulation) of particles to increase drag and weight-to-drag-ratio can be accomplished by exciting the medium with a frequency that produces particle oscillation and collision. These techniques require that the particles are freely suspended in the medium and are not applicable to enhance detachment from the surface. However, as discussed in the previous paragraph, pulsatory (or

vibratory) effects may potentially be used to enhance detachment. The modes and frequencies applied will have to be different than those necessary to effect lumping. A combination of both techniques into the same cleaning tool to enhance detachment and re-entrainment appears to be an attractive approach.

From the static force standpoint the density of the flow remains the primary factor to work on. To increase density we have to blow against the particle with a jet expending from a high pressure source. The particles then loosened, still have to be transported away by means of vacuum flow. However, less vacuum and a larger stand-off will be sufficient to accomplish this.*

To determine the needs for improvements, the particle drag forces have to be compared to the adhesive forces. Figure 6.1-15 shows the comparison and the relation between force and size.

The upper line in the figure (-.-) represents the force necessary to detach a particle from a wet surface, based upon the surface tension of water. (These data are very conservative and are primarily used as a reference level.) The symbols plotted are literature data on particle adhesion for the indicated conditions, included here to illustrate the wide spread between data. The dotted lines bracket the detachment force for humidity conditions between 40 and 95° RH, the range of primary interest. It can be seen that most of the data are concentrated between these margins. The steeply sloped solid line represents the calculated drag force achieved with vacuum flow under the tested conditions.

It can be seen that the detachment force is in a linear (or less) relation to the particle size, whereas the drag force diminishes with the square of the particle size. This is the main reason why the removal of small particles is a problem. Assuming, as discussed earlier, that the surface will always be brought to 40% RH conditions before cleaning, according to these data, the capability exists to remove all particles larger than 30 microns. To remove 10 micron size particles, the drag force would at least have to be doubled; to remove one micron sizes, the drag force would have to be increased by a factor of 10 or more. Whether this can be done by increasing density alone is questionable. All the discussed potential means combined may have to be applied to achieve such a goal.

*The use of a jet to effect detachment also opens up the possibility for further velocity increases beyond the critical velocity, if compatible with the surface to be cleaned.

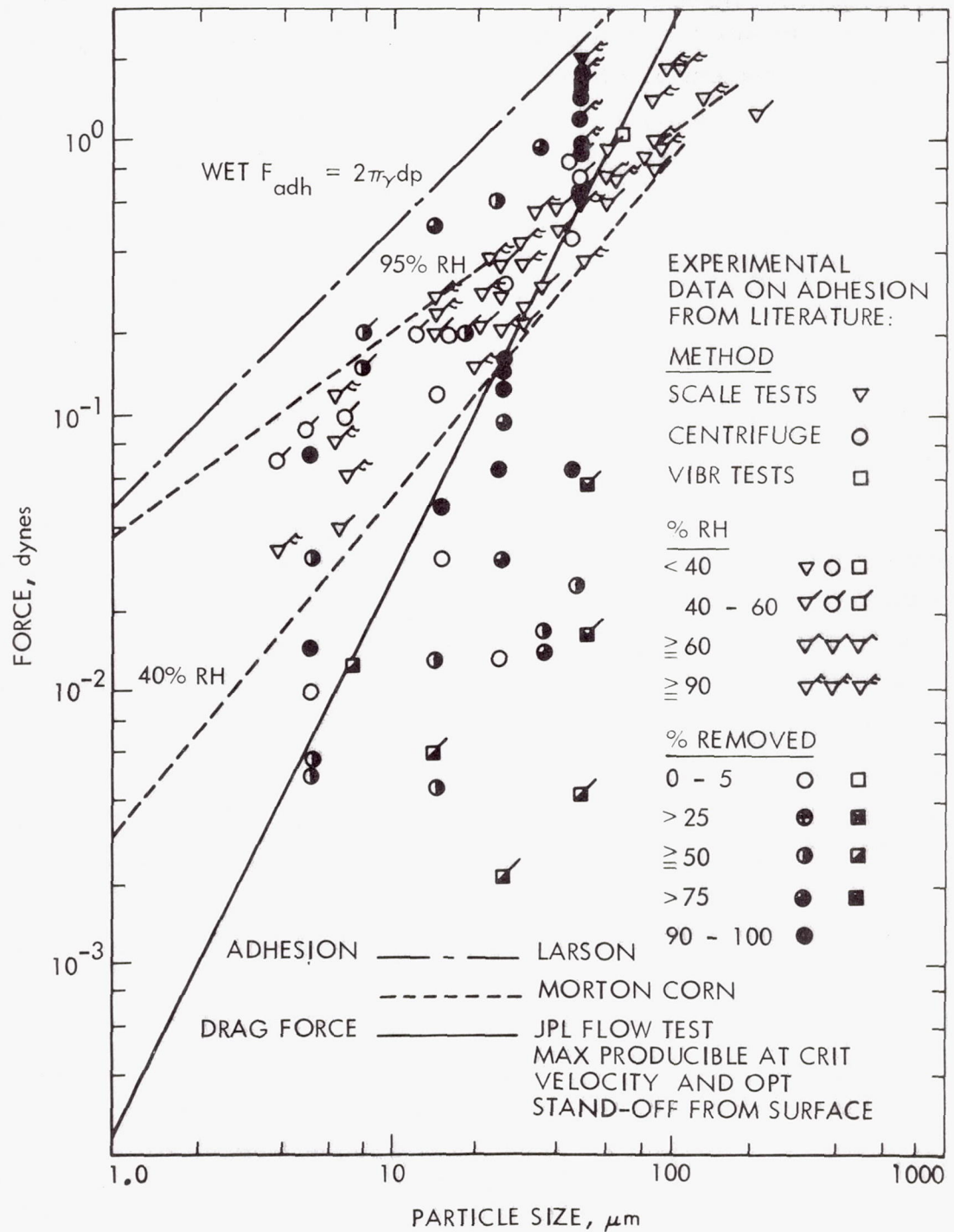


Fig. 6.1-15. Particle adhesion and drag force vs size

Since compatibility with the surface is also an important part of the problem, compromising solutions will probably have to be sought. At this point, the development of a hand-operated device that removes all particles larger than 10 microns from a smooth surface (such as solar panels) should be feasible.

6.1.7 PROBLEMS ENCOUNTERED

The main problem encountered during the tests was to keep the system parameters constant. Vibrations imparted to the system from the vacuum pump through the relatively stiff high vacuum hose, effecting a slow change of the setting of the throttling valve and of the test nozzle, made frequent readjustments between tests necessary.

At tests with very small stand-offs from the surface bowing of the sample plate and other structural deflections due to pressure had a noticeable effect on the critical flow rate, if compared to data obtained with the ridged steel-plate used for calibration. The data obtained for stand-offs below 100 microns, therefore, have not been very repeatable, though still conclusive.

Problems were also encountered in finding appropriate lighting conditions. Lighting from underneath with a shallow angle would have been best for contrast and preventing reflection from the test nozzle. This however, was not possible because of the plenum chamber installed underneath the microscope stage. A lighting angle from the top had to be found that would minimize unavoidable reflections and still produce enough contrast for particle observation and counting. The lighting conditions achieved allowed to discriminate and to count particles on the order of 3 to 5 microns in size. The observation and counting of particles on the order of one to two microns would have been feasible, but was very eye-straining and therefore omitted from the test.

A major problem represented the measuring of the surface pressures in the sample plane across the test nozzle. For the accurate measuring of static pressures, the pressure tap has to be rectangular to the surface and free of burrs. The diameter of the tap-hole also had to be relatively small if compared to the dimension of the flow normal to the wall. For the dimensions tested (50 to 300 microns), this was hard to achieve. The smallest hole that could be

produced was still in the order of 0.002 in.; i.e., 50 microns. To obtain conclusive data, a special measuring device had to be designed that measured the pressure in the nozzle throat plane by means of a 20 to 25 micron wide annular slot formed by a plug insert worked flushed with the surface. The use of the device then created a new problem; namely, the long times required for equilibrium before readings could be taken.

6.1.8 FUTURE ACTIVITIES

The primary objective of the FY 73 period will be the improvement of flow-cleaning in the direction of a larger stand-off from the surface, and an efficient removal of all particles larger than 10 microns. The effort will mainly concentrate on the evaluation of various techniques of jet - impingement on the detachment of particulates. The re-entrainment of detached particles by means of selected vacuum flow concepts will be pursued later.

A new test device will have to be designed that allows the simulation of steady state, single pulse, and oscillatory free flow and deflected jet impingement while observing particulates under a 100X microscope. Modified components of the apparatus, and similar test techniques will be used for re-entrainment studies.

A secondary objective is to investigate the possibility of the swift cleaning of the existing brush attachment between sweeps, using high velocity vacuum and jet-blow techniques for this purpose also. The concept of a controlled line, or rotary scanning of the contaminated surface by means of a high velocity needle jet to effect detachment is an attractive concept for an operational cleaning tool.

SUBTASK II

THERMAL RESISTANCE OF MICROBIAL POPULATIONS
OCCURRING IN SPACECRAFT ASSAY AREAS

Cognizance: M. D. Wardle

Associate Personnel: G. Simko (Bionetics)

SUBTASK II

THERMAL RESISTANCE OF MICROBIAL POPULATIONS
OCCURRING IN SPACECRAFT ASSAY AREAS

6.2.1 INTRODUCTION

The primary objective of this task area is to acquire the necessary parametric information to define optimum flight acceptance and sterilization processes for space hardware. In line with this goal, the dry heat resistances of microorganisms representative of those found on flight spacecraft are characterized.

6.2.2 SIGNIFICANT ACCOMPLISHMENTS

The Mariner - Mars 1971 Microbiological Monitoring Programs provided a large number of flight hardware bacterial isolates from which a random selection of candidate organisms for dry heat testing was made. These isolates were then subjected to a screening process to provide representative sporeformers for dry heat resistance studies at 125°C. The frequency distribution of $D_{125^{\circ}\text{C}}$ values for these Mariner '71 spore isolates is shown in Fig. 6.2-1. Comparison of these results with those for the Mariner '69 spore isolates (Table 6.2-1) shows a similarity in distributions, with the possible exception of the 0-30 minute range. These differences may have been influenced by the difference in sample size (70 vs 31).

6.2.3 FUTURE ACTIVITIES

Work in this area has been completed.

6.2.4 PUBLICATIONS

Simko, G. J., Devlin, J. D. and Wardle, M. D.; "Dry-Heat Resistance of Bacillus subtilis var. niger Spores on Mated Surfaces"; Applied Microbiology 22: 491-496; 1971.

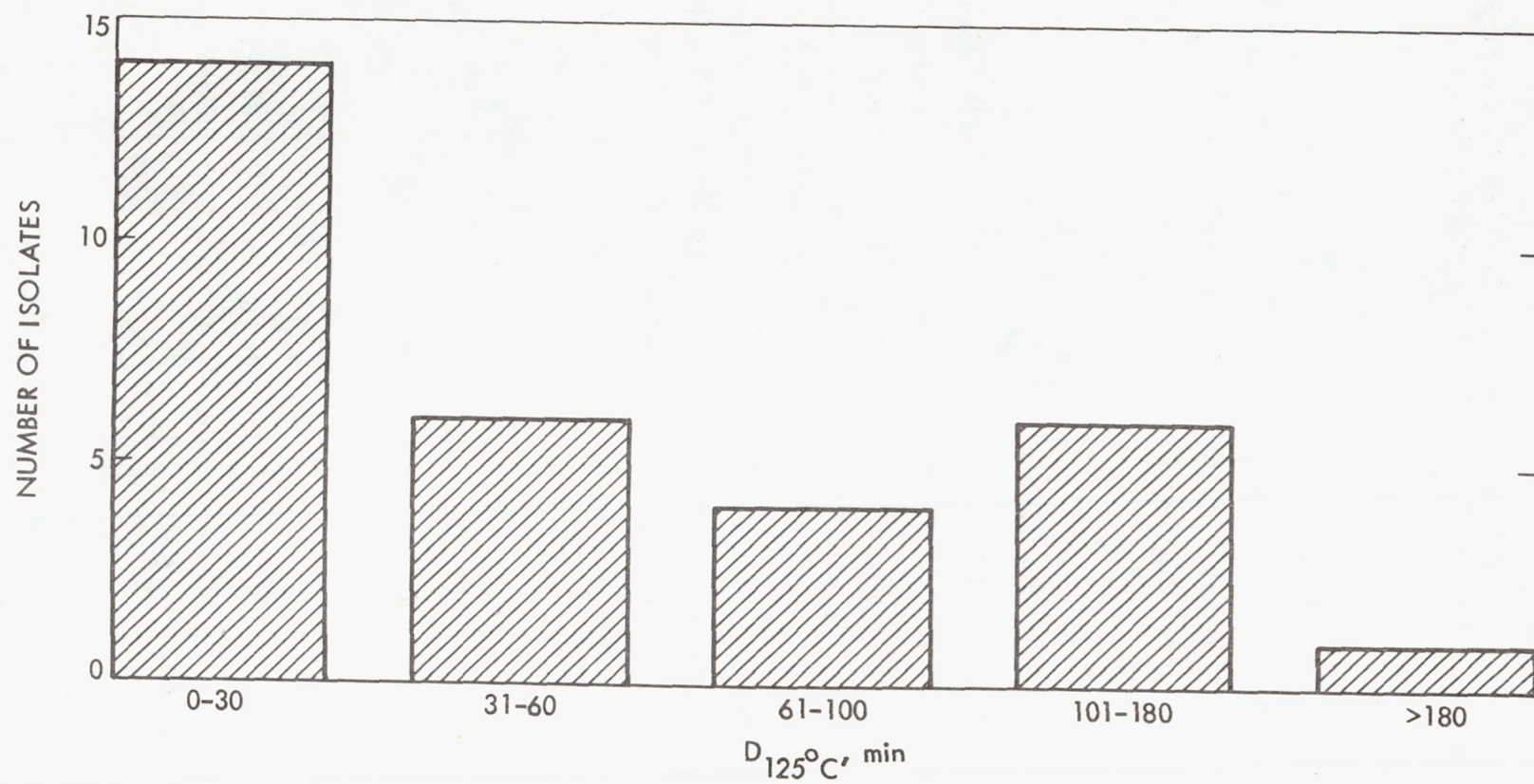


Fig. 6.2-1. Frequency distribution of $D_{125^{\circ}\text{C}}$ values for Mariner '71 spore isolates

Table 6.2-1. Comparison of Mariner '69 and '71 spore isolate $D_{125^{\circ}\text{C}}$ values

$D_{125^{\circ}\text{C}}$ (min)	Percent of total	
	'69 (70 total)	'71 (31 total)
0-30	24	45
31-60	24	19
61-100	19	13
101-180	23	19
180	10	3

6.2.5 PRESENTATIONS

Wardle, M. D.; "Thermal Resistance of Microbial Populations Occurring in Spacecraft Assembly Areas"; presented at the NASA Semiannual Planetary Quarantine Technology Seminar, Cape Kennedy, Florida, 1972.

900-597

SUBTASK III

VERIFICATION OF USSR HYDROGEN PEROXIDE DECONTAMINATION

Cognizance: M. D. Wardle

Associate Personnel: G. Renninger (Bionetics)

SUBTASK III

VERIFICATION OF USSR HYDROGEN PEROXIDE DECONTAMINATION

6.3.1 INTRODUCTION

The primary objective of this task is to evaluate hydrogen peroxide as a bactericidal agent for use on spacecraft hardware. Such an application of hydrogen peroxide appears warranted in light of recent investigations in the USSR. The Russian work, as reported in a recent NASA technical translation (No. F-13, 769), indicates that 3-5% hydrogen peroxide was effective in killing vegetative cells while 6-15% rendered spores nonviable. The effectiveness of the peroxide was a function of temperature and surface cleanliness and could be augmented through the addition of anionic surfactants. Its compatibility with a majority of materials and complete breakdown leaving no harmful sideproducts were cited as being beneficial to its spacecraft application. However, its use as a spacecraft microbial decontaminant must be evaluated in the context of the requirements and objectives of the United States space program.

6.3.2 APPROACH

Initial work in this task area will entail a review of pertinent literature and obtainment of necessary baseline data on the efficacy of hydrogen peroxide as a bactericidal agent. The next step will be to ascertain any problems associated with its application to spacecraft. With a sound understanding of the above factors, a test plan will be generated for the evaluation of the spacecraft usage of hydrogen peroxide. The plan will dictate different methods of application; i.e., immersion, wiping, and spraying, and a study of bactericidal effects on both pure bacterial cultures and heterogeneous, naturally-occurring populations representative of those found on spacecraft surfaces.

6.3.3 SIGNIFICANT ACCOMPLISHMENTS

A study was performed to identify the time-concentration effects of hydrogen peroxide on selected bacteria. A total of twelve MM '71 isolates — 9 spores and 3 nonsporeformers — were tested. Bacillus subtilis and Staphylococcus epidermidis were chosen as comparative species. Challenge

cultures were prepared for inoculation into concentrations of 3, 8 and 14% hydrogen peroxide. Surviving bacteria were cultured in Trypticase Soy Broth (TSB) using a loop transfer method from the peroxide suspensions. This technique provided for the determination of time-concentration combinations that rendered cells nonviable. Results were recorded as either growth or no growth.

Tests were performed to check for inhibitory concentrations of peroxide in the TSB by inoculation of control tubes at the time of transfer from the suspensions, and of test samples that proved negative following appropriate incubation. These tests indicated no significant growth inhibition for the 3% runs, but that an inhibitory amount of peroxide was transferred to the TSB in the 8 and 14% tests (as little as 4 $\mu\text{g}/\text{ml}$ can be inhibitory). The need for a dissipator of peroxide (e.g., catalase) was apparent.

6.3.4 FUTURE ACTIVITIES

Future work in this will entail a repeat of the time-concentration study that will generate survivor curves for the test organisms. Procedures will be invoked to remove inhibitory concentrations of peroxide. Following these studies, an evaluation will be made of application techniques for spacecraft surfaces.

6.3.5 PRESENTATIONS

"Verification of USSR Hydrogen Peroxide Decontamination Data" presented at the NASA Semiannual Planetary Quarantine Technology Seminar, San Francisco, California, July, 1972.

SUBTASK IV

PLASMA CLEANING AND DECONTAMINATION TECHNIQUES

Cognizance: D. M. Taylor

Associate Personnel: R. L. Olson (Boeing)

S. J. Fraizer (Boeing)

R. B. Gillette (Boeing)

SUBTASK IV

PLASMA CLEANING AND DECONTAMINATION TECHNIQUES

6.4.1 INTRODUCTION

The objectives of this task are to provide preliminary evaluation of:
1) the feasibility of plasma cleaning of surfaces; and 2) the applicability of low-energy (AUGER) spectroscopy for monitoring organic contamination on surfaces.

6.4.2 SIGNIFICANT ACCOMPLISHMENTS

A contract (JPL No. GU-561461) was placed with the Boeing Company, Seattle, Washington, to conduct a feasibility study. This effort was completed in May, 1972 and submitted as a final report entitled "Evaluation of Plasma Cleaning and Electron Spectroscopy for Reduction of Organic Contamination. Copies of this final report have been previously distributed.

6.4.3 FUTURE ACTIVITIES

Future activities in this task area will involve investigation into plasma cleaning in terms of material compatibility, penetration characteristics, and lethality effects.

900-597

APPENDIX A
ANALYSIS OF MICROBIAL BURDEN DATA

APPENDIX A

ANALYSIS OF MICROBIAL BURDEN DATA

Dr. Bradley Efron, Stanford University

A.1 ASSAY COUNTS

Assay counts from the Mariner Mars 1971 (MM71) Project display the same general nature as those previously observed in highly controlled assembly conditions: a predominance of zero counts, up to 90 percent, but also a small percentage of very large counts in the 100-2000 range. It is well known that the sample mean can be a very unstable estimator of the true population mean in such conditions. In order to find a better estimation, it will be necessary to model the distributions observed. A successful model would consist of a family of probability distributions depending on a small number of parameters such that some member of the family would fit the data observed in any particular situation. Once such a model is agreed upon, it is usually straightforward to devise an efficient estimation scheme. The model would also facilitate the evaluation of the Microbial Burden Prediction Program. This discussion is concerned solely with the problem of developing a suitable model.

A.2 MM71 SPACECRAFT DATA

The data from the MM 71 spacecraft, Flight 1, Flight 2, and PTM was used.

Let us call a "case" any situation where at least 20 samples were obtained for one piece of equipment at one time. Flight 1 provides 24 cases, Flight 2, 30 cases, and PTM, 41 cases.

Figure A-1 separates the 91 cases into five categories depending on the proportion of zero counts observed. Category 1 is the "cleanest", averaging 90 percent zeroes. For each category, a histogram of the nonzero counts is shown.

The histograms show a general trend: the more dirty cells there are, the dirtier they tend to be. This is reasonable behavior and lends credence to the belief that something real is being measured by the assay method. The details of these histograms provide some useful information about the observed counts.

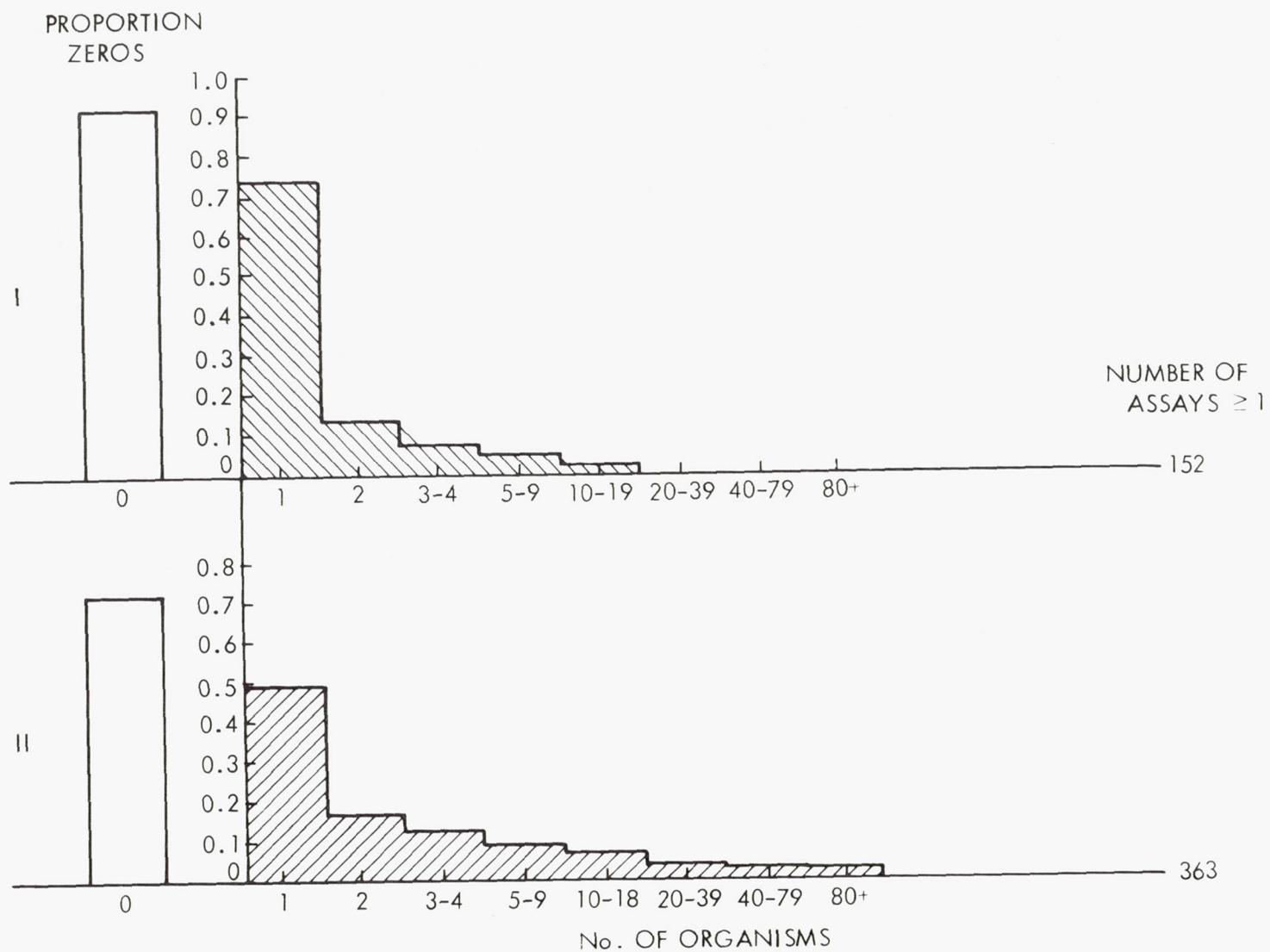


Fig. A-1. Histograms of burden distribution on non-zero assays categorized by percent zero cells

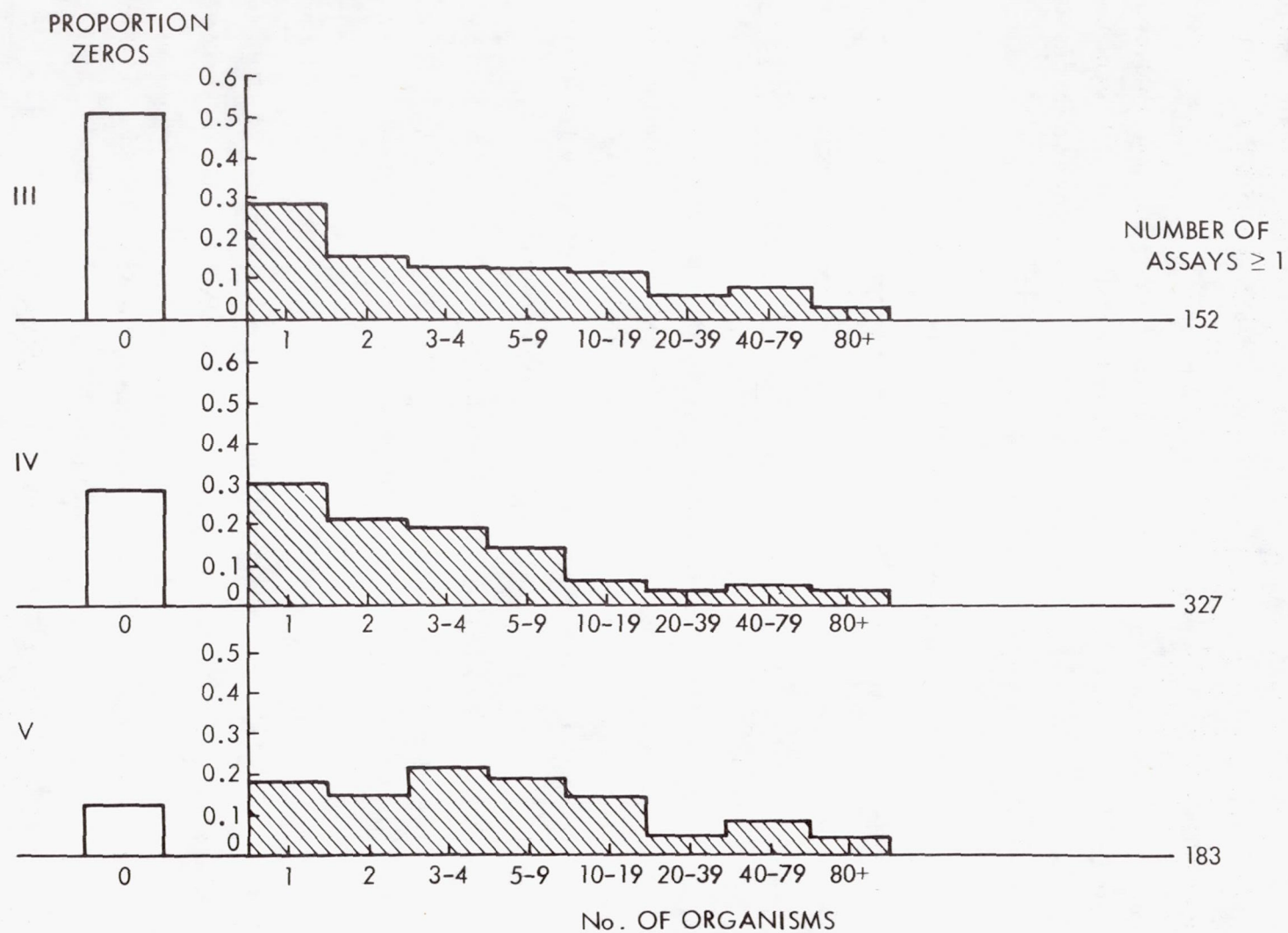


Fig. A-1. Histograms of burden distribution of non-zero assays categorized by percent zero cells (contd)

A.3 ARE THE LARGE COUNTS REAL?

A possible explanation of the large counts is that they are produced by the fractionation of single counts during the ultrasonication phase of the assay procedure. This would make the large counts "non-real", and they could be discounted in estimating the true burden.

Suppose it is assumed that counts less than 20 are real, but that counts greater than 20 are produced by the "busting" of individual counts. It can then be calculated that the number of counts greater than 20 should occur in the following proportions in the five shown in Table A-1.

Table A-1. Theoretical count proportions

Category	1	2	3	4	5
Proportion of Counts >20 (Relative to Category 1)	1.00	1.58	1.91	1.75	2.29

However Fig. A-1 does not show nearly a large enough proportion of counts greater than 20 for Category 1 or Category 2. Changing the number 20 in the above calculation will not affect the conclusion that the large counts are indeed real, and not artifacts of the assay procedure. The histogram of the large counts from the MM71 data (Fig. A-2), confirms this impression.

The histogram shows a rather smooth decline to zero toward the large end of the scale, rather than any sharp discontinuities. It is hard to believe that any artificial production of counts induced by the assay would fit in so well with the genuine data.

A.4 THE COMPOUND POISSON MODEL

B. A. Nelson, in Martin Marietta report number PR-3701051, discusses a compound Poisson model for count data. In this model, the microbes occur in clumps; the number of clumps in an individual assay being a Poisson random variable with p_j ; and the probability of j clumps, being $e^{-\lambda} \lambda^j / j!$. Each clump consists of a random number N of microbes with $\text{Prob}(n = i) = q_i$ for $i = 1, 2, \dots$. The important point is that the probability distribution $q = (q_1, q_2, \dots)$ is the same for all the clumps, and independent from clump to clump.

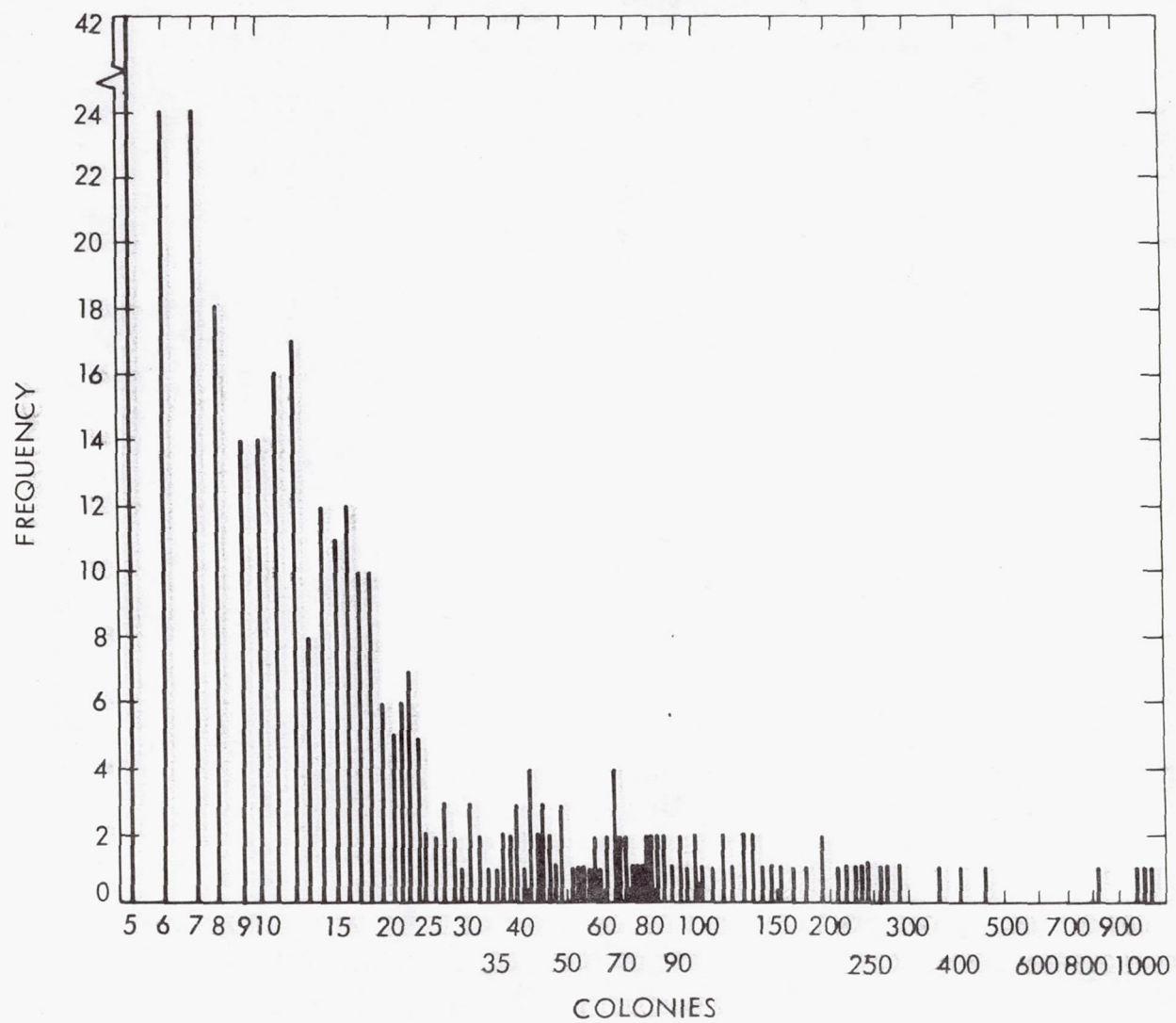


Fig. A-2. Distribution of large counts

Unfortunately, the compound Poisson model does not fit the data shown in Fig. A-1. If 90 percent of all counts are zero, as in Category 1, then Table A-2 shows that 94.8 percent of the assays must be counting only one clump.

Table A-2. Proportion of assays containing one or two clumps

Category	$p_0 = e^{-\lambda}$	Resultant λ	$p_1/(p_1 + p_2 + \dots)$	$p_2/(p_1 + p_2 + \dots)$
1	0.90	0.105	0.948	0.050
2	0.70	0.357	0.832	0.149
3	0.50	0.693	0.693	0.240
4	0.30	1.204	0.516	0.311
5	0.10	2.302	0.256	0.295

This means that the histogram for Category 1 must be a close approximation to the q distribution. However, when the q distribution in the compound Poisson model is used, theoretical distributions looking like the histograms in Categories 2 thru 5 are not generated. For example, the theoretical proportion of counts greater than 10 is much too small in Category 2 and much too large in Category 5.

These calculations do not totally discredit the compound Poisson model. The histograms probably reflect a complicated superposition of various processes which disguise the Poisson component observed by Nelson. One peculiar feature of the data is that the large counts, those greater than 20, do not increase in proportion from Category 3 to Category 5. This suggests that the really bad dirt is deposited in a single disaster of limited duration, rather than being laid down steadily over the entire assembly period. A "plateau" phenomenon may also be in effect.

A.5 ARE THE MICROBES IN CLUMPS?

A high count, say 17, in an assay might be the result of 17 individual microbes spread uniformly over the sampled area, or a single clump of 17 essentially a point on the spacecraft, or might be two lumps of 7 and 10 microbes, etc. To help settle this question, maps of the spacecraft showing the

position of the assayed areas and the corresponding number of counts recorded were prepared.

Under the uniform spread theory, a high degree of geometrical continuity in the observed counts would be expected. That is, a sample taken right next to an area with 108 counts should not show zero counts itself. The clump theory would mitigate against geometrical continuity.

The maps do not provide a clear-cut decision. There are some regions that seem to be smears; for example, the lower third of solar panel 5, rear, Flight 2, A0 Phase. However, the large counts seem to be very discontinuous (for example, the front of solar panel 1, PTM Pre-encapsulation phase). Overall, the maps seem to favor the clump theory, particularly for the large counts.

The sampling scheme used on the spacecraft is not well suited for answering this question since there are few adjacent samples taken. Even where adjacent samples do exist, as on the solar panels, the large sampling area of four square inches limits the resolution of the size of clumps that could be detected.

A simple experiment that could be very informative on this point would be to deliberately sample small adjacent areas of an assembly constructed under realistic conditions, at about the cleanliness level of the PTM.

The clump question is related to the problem of particle size raised by Dr. Dan Taylor in relation to the vacuum cleaning of the spacecraft. This problem is also best approached by direct experimentation, and the experiments could probably be run simultaneously without great difficulty.

A.6 HOW MANY MICROBES IN A CLUMP?

If it could be assumed that all large counts are from single clumps, then Fig. A-2 would be a histogram of clump size. Of course it is not expected that no assay involved 2 or more clumps, but if it was rare for an assay to involve more than one large clump, then Fig. A-2 should still be a reasonable approximation to the distribution of clump sizes. Figure A-1 makes the assumption quite plausible if "large" is defined as greater than 10 or 20. Of course, the experiment suggested above would give a direct answer to the question.

Figure A-3 was constructed to test the uniformity of the size of large counts from case to case. Each count x equal or greater than 5 was transformed into $y = F(x)$, where F is the CDF in Fig. A-2. The points y for each case were plotted on a line from 0 to 1. If the distribution of large counts for the particular case was the same as the overall distribution shown (Fig. A-2), then the y points would be distributed uniformly on $(0, 1)$. This uniformity is actually observed for most of the spacecraft data, though there are some exceptions.

The observed uniformity is evidence for the single clump theory. If large counts were made up of many smaller clumps then one would expect the large counts to be larger in dirtier situations and smaller in cleaner situations.

A.7 HOW ARE THE MICROBES DEPOSITED ON THE SPACECRAFT?

There are two obvious vectors of delivery - airborne fallout and handling. To build a successful model of the spacecraft data, the individual contributions of each vector must be assessed.

A.7.1 Airborne Fallout

Some of the maps discussed above seem to offer strong evidence of airborne deposit because of the uniform distribution of high counts over large areas (see the front of the high gain antenna, Flt. 2 PEI). The uniform results for the large count data also argue for airborne delivery. However, some of the maps do seem to show handling smudges, as mentioned in para. A.5.

There exists a large amount of data on pure airborne dirt, unaffected by handling, in the cultures taken from the steel strips for the assessment of environmental cleanliness. The log book for the Pasadena operations of MM71 was examined. It was found that the strip assays taken in the tent were generally far too clean to account for the spacecraft counts. However, the strips in the high bay showed large counts similar to those observed on the craft (see Fig. A-3). Since the spacecraft was occasionally exposed to the high bay environment, it seems possible that the major burden observed could be caused by airborne fallout.

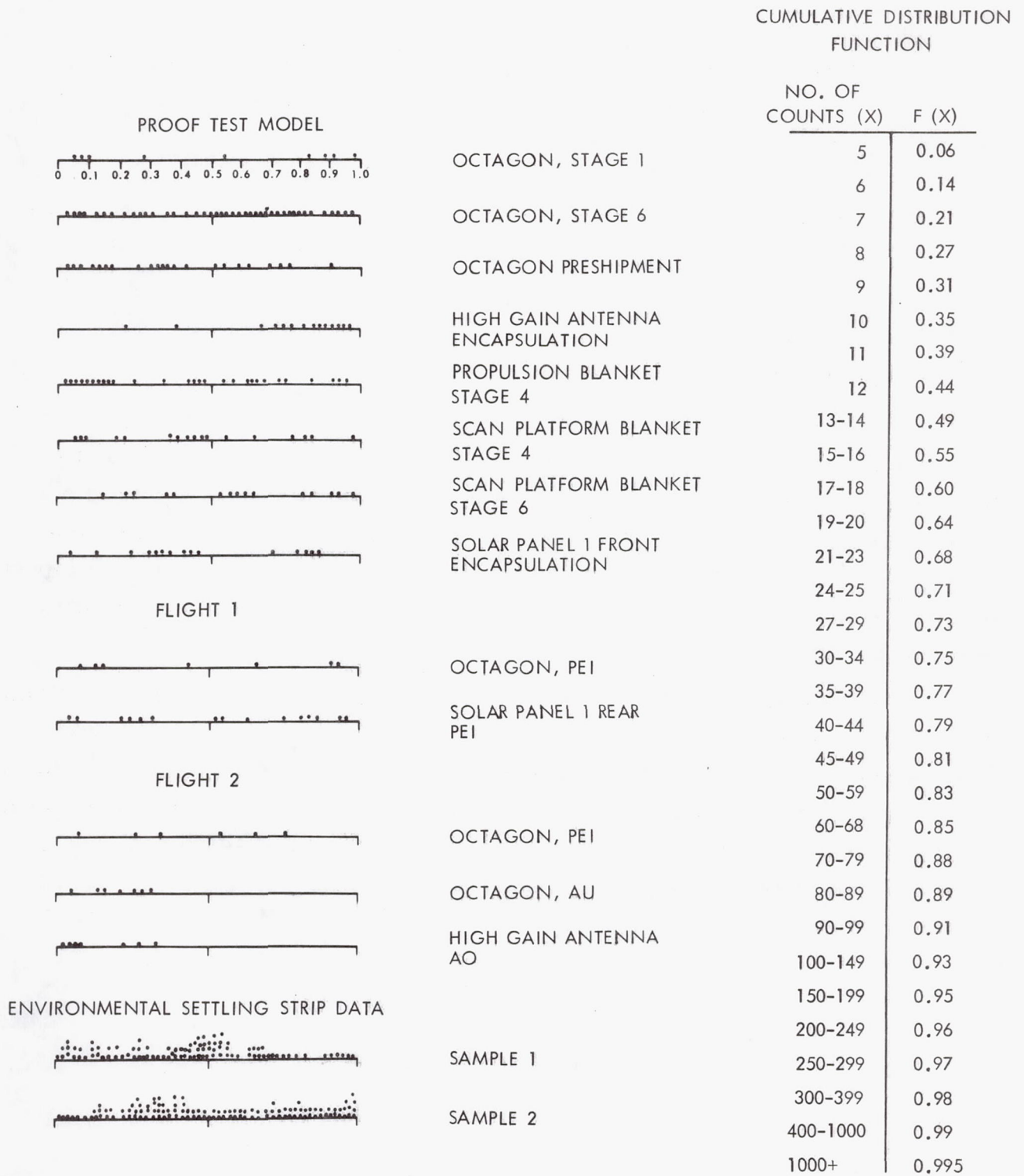


Fig. A-3. Large counts in different cases compared to total cumulative distribution function (CDF)

A. 7.2 Handling

Unfortunately there is no spacecraft data where only handling dirt could be present, airborne fallout having been eliminated or at least strictly controlled. The CMTM experiment provides such data, but under cleaner handling conditions than are realistic for actual assembly. A preliminary look at the data seemed to show no major effect due to handling, and it would be worthwhile to make more extensive comparisons within this body of data. However, a planned handling experiment may very well be the only way to obtain satisfactory information.

A. 8 MODELING THE AIR DEPOSITED BURDEN

A major effort should be made to model the counts obtained from samples of areas not subjected to handling. The CMTM data seems ideal for this purpose since: 1) strict environmental controls were maintained; 2) non-handled areas of the spacecraft were identified; and 3) there is considerable repetition of similar situations. There are good a priori reasons for believing that the compound Poisson model should fit this data, given the general nature of airborne dirt.

The modeling would begin by first identifying groups of samples obtained under comparable conditions of exposure. Within each group, a compound Poisson model would be fitted to observe how good the fit was and how homogeneous the fitted parameters were from case to case. If this modeling procedure performed satisfactorily, then the model obtained would be fitted to the other environmental data available.